Series in BioEngineering

Clara Mihaela Ionescu

The Human Respiratory System

An Analysis of the Interplay between Anatomy, Structure, Breathing and Fractal Dynamics

Springer

Series in BioEngineering

For further volumes:
www.springer.com/series/10358

Clara Mihaela Ionescu

The Human Respiratory System

An Analysis of the Interplay between Anatomy, Structure, Breathing and Fractal Dynamics

Springer

Clara Mihaela Ionescu
Department of Electrical Energy, Systems
and Automation
Ghent University
Gent, Belgium

ISSN 2196-8861 ISSN 2196-887X (electronic)
Series in BioEngineering
ISBN 978-1-4471-5387-0 ISBN 978-1-4471-5388-7 (eBook)
DOI 10.1007/978-1-4471-5388-7
Springer London Heidelberg New York Dordrecht

Library of Congress Control Number: 2013947158

© Springer-Verlag London 2013
This work is subject to copyright. All rights are reserved by the Publisher, whether the whole or part of the material is concerned, specifically the rights of translation, reprinting, reuse of illustrations, recitation, broadcasting, reproduction on microfilms or in any other physical way, and transmission or information storage and retrieval, electronic adaptation, computer software, or by similar or dissimilar methodology now known or hereafter developed. Exempted from this legal reservation are brief excerpts in connection with reviews or scholarly analysis or material supplied specifically for the purpose of being entered and executed on a computer system, for exclusive use by the purchaser of the work. Duplication of this publication or parts thereof is permitted only under the provisions of the Copyright Law of the Publisher's location, in its current version, and permission for use must always be obtained from Springer. Permissions for use may be obtained through RightsLink at the Copyright Clearance Center. Violations are liable to prosecution under the respective Copyright Law.
The use of general descriptive names, registered names, trademarks, service marks, etc. in this publication does not imply, even in the absence of a specific statement, that such names are exempt from the relevant protective laws and regulations and therefore free for general use.
While the advice and information in this book are believed to be true and accurate at the date of publication, neither the authors nor the editors nor the publisher can accept any legal responsibility for any errors or omissions that may be made. The publisher makes no warranty, express or implied, with respect to the material contained herein.

Printed on acid-free paper

Springer is part of Springer Science+Business Media (www.springer.com)

"To raise new questions, new possibilities, to regard old problems from a new angle, requires creative imagination and marks the real advance in science"
A. Einstein

As a result of the above thought, I dedicate this book to all those who are curious, critical, and challenging.

Foreword

Fractional Calculus (FC) was originated in 1695 based on the genial ideas of the German mathematician and philosopher Gottfried Leibniz (1646–1716). Up to the end of the 19th century, this topic remained mainly abstract with progress centered in pure mathematics. The application of FC started with Oliver Heaviside (1850–1925), an English electrical engineer, mathematician, and physicist. Heaviside applied concepts of FC in is operational calculus and electrical systems. Nevertheless, FC remained a mathematical tool unknown for most researchers. In the area of life sciences the first contributions are credited to the American scientists Kenneth Stewart Cole (1900–1984) and Robert Hugh Cole (1914–1990), who published several papers by the end of the 1930s. They proposed the so-called Cole–Cole empirical model, which has been successfully applied up to today, in a large variety of tissues.

These pioneering applications of FC were apparently forgotten in the decades that followed. There is no historical record, social event, or scientific explanation, for the 'oblivium' phenomenon. Three decades later Bertram Ross organized the First Conference on Fractional Calculus and its Applications at the University of New Haven in 1974. Also, Keith Oldham and Jerome Spanier published the first monograph devoted to FC. Again, these important contributions remained with FC focused on pure mathematics, but in 1983 the French engineer Alain Ousaloup developed the CRONE (acronym for 'Commande Robuste d'Ordre Non Entier') method, which is used since then in control and identification algorithms. We can say that the modern era of application of FC in physics and engineering started there. In 1998 Virginia Kiryakova initiated the publication of the journal Fractional Calculus & Applied Analysis. We should mention the vision of Ali Nayfeh and Murat Kunt, editors-in-chief of journals 'Nonlinear Dynamics' and 'Signal Processing', respectively, that supported a sustained growth of the new–old field by means of several special issues.

In the area of biology and medicine the first book, authored by Richard Magin, was published in 2006. By 2004 a young researcher, Clara Ionescu, started an intensive work in modeling respiratory systems using FC. I called her the 'atomic woman' given the intensity of her work that culminated with her Ph.D. by the end of 2009. Clara continued improving the models, getting more results and publishing her research. This book formulates, in a comprehensive work, her vision on the application of FC in the modeling of respiratory systems. I am certain that the book will constitute a novel landmark in the progress in the area and that its readers will be rewarded by new perspectives and wider conceptual avenues.

Porto J.A. Tenreiro Machado
May 2013

Preface

The objective of the book is to put forward emerging ideas from biology and mathematics into biomedical engineering applications in general with special attention to the analysis of the human respiratory system. The field of fractional calculus is mature in mathematics and chemistry, but still in infancy in engineering applications. However, the last two decades have been very fruitful in producing new ideas and concepts with applications in biomedical engineering. The reader should find the book a revelation of the latest trends in modeling and identification of the human respiratory parameters for the purpose of diagnostic and monitoring. Of special interest here is the notion of fractal structure, which tells us something about the biological efficiency of the human respiratory system. Related to this notion is the fractal dimension, relating the adaptation of the fractal structure to environmental changes (i.e. disease). Finally, we have the dynamical pattern of breathing, which is then the result of both the structure and the adaptability of the respiratory system.

The distinctive feature of the book is that it offers a bottom-up approach, starting from the basic anatomical structure of the respiratory system and continuing with the dynamic pattern of the breathing. The relations between structure (or the specific changes within it) and fundamental working of the system as a whole are pinned such that the reader can understand their interplay. Moreover, this interplay becomes crucial when alterations at the structural level in the airway caused by disease may require adaptation of the body to the functional requirements of breathing (i.e. to ensure the necessary amount of oxygen to the organs). Adaptation of the human body, and specially of the respiratory system, to various conditions can be thus explained and justified in terms of breathing efficiency.

The motivation for putting together this book is to give by means of the example chosen (i.e. the respiratory system) an impulse to the engineering and medical community in embracing these new ideas and becoming aware of the interaction between these disciplines. The net benefit of reading this book is the advantage of any researcher who wants to stay up to date with the new emerging research trends in biomedical applications. The book offers the reader an opportunity to become aware of a novel, unexplored, and yet challenging research direction.

My intention was to build a bridge between the medical and engineering worlds, to facilitate cross-fertilization. In order to achieve this, I tried to organize the book in the traditional structure of a textbook.

A brief introduction will present the concept of fractional signals and systems to the reader, including a short history of the fractional calculus and its applications in biology and medicine. In this introductory chapter, the notions of fractal structure and fractal dimension will be defined as well.

The second chapter describes the anatomy of the respiratory system with morphological and structural details, as well as lung function tests for evaluating the respiratory parameters with the aim of diagnosis and monitoring. The third chapter will present the notion of respiratory impedance, how it is measured, why it is useful and how we are going to use it in the remainder of the book.

A mathematical basis for modeling air-pressure and air-flow oscillations in the airways is given in the fourth chapter. This model will then be used as a basis for further developments of ladder network models in Chap. 5, thus preserving anatomy and structure of the respiratory system. Simulations of the effects of fractal symmetry and asymmetry on the respiratory properties and the evaluation of respiratory impedance in the frequency domain are also shown.

Chapter 6 will introduce the equivalent mechanical model of the respiratory tree and its implications for evaluating viscoelasticity. Of special importance is the fact that changes in the viscoelastic effects are clearly seen in patients with respiratory insufficiency, hence markers are developed to evaluate these effects and provide insight into the monitoring of the disease evolution. Measurements on real data sets are presented and discussed.

Chapter 7 discusses models which can be used to model the respiratory impedance over a broad range of frequencies, namely ladder network model and a model existing in the literature, for comparison purposes. The upper airway shunt (not part of the actual respiratory system with airways and parenchyma) and its bias effect in the estimated values for the respiratory impedance is presented, along with a characterization on healthy persons and prediction values. Measurements on real data sets are presented and discussed.

Chapter 8 presents the analysis of the breathing pattern and relation to the fractal dimension. Additionally, a link between the fractal structure and the convergence to fractional order models is shown, allowing also a link between the value of the fractional order model and the values of the fractal dimension. In this way, the interplay between structure and breathing patterns is shown. A discussion of this interplay points to the fact that with disease, changes in structure occur, these structural changes implying changes in the work necessary to breath at functional levels. Measurements on real data sets are again presented and discussed.

Chapter 9 introduces methods and protocols to investigate whether moving from the theory of linear system to nonlinear contributions can bring useful insight as regards diagnosis. In this context, measuring frequencies close to the breathing of the patient is more useful than measuring frequencies outside the range of tidal breathing. This also implies that viscoelasticity will be measured in terms of nonlinear effects. The nonlinear artifacts measured in the respiratory impedance, are then linked to the viscous and elastic properties in the lung parenchyma. Measurements on real data sets are presented and discussed. Chapter 10 summarizes the contributions of the book and point to future perspectives in terms of research and diagnosis methods. In the Appendix, some useful information is given to further support the reader in his/her quest for knowledge.

Finally, I would like to end this preface section with some words of acknowledgment.

I would like to thank Oliver Jackson for the invitation to start this book project, and Ms. Charlotte Cross of Springer London for her professional support with the review, editing, and production steps.

Part of the ideas from this book are due to the following men(tors): Prof. Robin De Keyser (Ghent University, Belgium), Prof. Jose-Antonio Tenreiro Machado (Institute of Engineering, Porto, Portugal), Prof. Alain Oustaloup (University of Bordeaux1, France) and Prof. Viorel Dugan (University of Lower Danube, Galati, Romania). Clinical insight has been generously provided to me by Prof. Dr. MD Eric Derom (Ghent University Hospital, Belgium) and Prof. Dr. MD Kristine Desager (Antwerp University Hospital, Belgium). I thank them cordially for their continuous support and encouragement.

Further technical support is acknowledged from the following Master and Ph.D. students throughout the last decade: Alexander Caicedo, Ionut Muntean, Niels Van Nuffel, Nele De Geeter, Mattias Deneut, Michael Muehlebach, Hannes Maes, and Dana Copot.

Next, I would like to acknowledge the persons who supported my work administratively and technically during the clinical trials.

- For the measurements on healthy adult subjects, I would like to thank Mr. Sven Verschraegen for the technical assistance for pulmonary function testing at the Department of Respiratory Medicine of Ghent University Hospital, Belgium.
- For the measurements on healthy children, I would like to thank Mr. Raf Missorten from St. Vincentius school in Zwijnaarde, Principal, for allowing us to perform tests and to Mr. Dirk Audenaert for providing the healthy volunteers. I would also like to thank Nele De Geeter and Niels Van Nuffel for further assistance during the FOT (Forced Oscillations Technique) measurements.
- For the measurements on COPD patients: many thanks to Prof. Dr. Dorin Isoc from Technical University of Cluj-Napoca and to Dr. Monica Pop for the assistance in the University of Pharmacy and Medicine "Iuliu Hatieganu" in Cluj-Napoca, Romania.
- For the measurements on asthmatic children, I would like to thank Rita Claes, Hilde Vaerenberg, Kevin De Sooner, Lutje Claus, Hilde Cuypers, Ria Heyndrickx and Pieter De Herdt from the pulmonary function laboratory in UZ Antwerp, for the professional discussions, technical and amicable support during my stay in their laboratory.
- For the measurements on kyphoscoliosis adults, I would like to thank Mrs. Hermine Middendorp for the assistance with the Ethical Committee request; to Philippe De Gryze, Frank De Vriendt, Lucienne Daman, and Evelien De Burck

  for performing the spirometry tests and to Dr. Robert Gosselin for calculating the Cobb angles on the RX photos.
- For the measurements on healthy children during the Science Week event, I would like to thank Stig Dooms, Hannes Maes, Gerd Vandersteen, and Dana Copot for their technical support with the device and for performing measurements.

Last but not least, I would like to acknowledge the moral support and care received from my grandma, Buna, my aunt, Victoria, and my two cousins, Florina and Petrica. I would also like to thank Nathalie for her friendship during the strenuous times of writing this book, and to thank Robin, Amelie, Cosmin, and Dana for their critical comments to improve the content of the book.

Gent, Belgium Clara M. Ionescu
June 2013

Acknowledgements

This monograph on the respiratory impedance and related tools from fractional calculus is based on a series of papers and articles that I have written in the past 10 years. Therefore, parts of material has been re-used. Although such material has been modified and rewritten for the specific focus of this monograph, copyright permissions from several publishers is acknowledged as follows.

Acknowledgement is given to the Institute of Electrical and Electronic Engineers (IEEE) to reproduce material from the following papers:

© 2009 IEEE. Reprinted, with permission, from Clara Ionescu and Robin De Keyser, "Relations between fractional order model parameters and lung pathology in chronic obstructive pulmonary disease". *IEEE Transactions on Biomedical Engineering*, 978–987 (material found in Chaps. 4 and 7).

© 2009 IEEE. Reprinted, with permission, from Clara Ionescu, Patrick Segers, and Robin De Keyser, "Mechanical properties of the respiratory system derived from morphologic insight". *IEEE Transactions on Biomedical Engineering*, 949–959 (material found in Chap. 4).

© 2010 IEEE. Reprinted, with permission, from Clara Ionescu, Ionut Muntean, Jose Antonio Tenreiro Machado, Robin De Keyser and Mihai Abrudean, "A theoretical study on modelling the respiratory tract with ladder networks by means of intrinsic fractal geometry". *IEEE Transactions on Biomedical Engineering*, 246–253 (material found in Chap. 5).

© 2013 IEEE. Reprinted, with permission, from Clara Ionescu, Jose Antonio Tenreiro Machado and Robin De Keyser, "Analysis of the respiratory dynamics during normal breathing by means of pseudo-phase plots and pressure volume loops". *IEEE Transactions on Systems, Man and Cybernetics: Part A: Systems and Humans*, 53–62 (material found in Chap. 8).

© in print IEEE. Reprinted, with permission, from Clara Ionescu, Andres Hernandez and Robin De Keyser, "A recurrent parameter model to characterize the high-frequency range of respiratory impedance in healthy subjects". *IEEE Transactions on Biomedical Circuits and Systems*, doi:10.1109/TBCAS.2013.2243837 (material found in Chap. 8).

Acknowledgement is given to Elsevier to reproduce material from the following papers:

Clara Ionescu, Jose Antonio Tenreiro Machado and Robin De Keyser, “Fractional order impulse response of the respiratory system”. *Computers and Mathematics with Applications*, 845–854, 2011 (material found in Chap. 8).

Clara Ionescu, Robin De Keyser, Jocelyn Sabatier, Alain Oustaloup and Francois Levron, “Low frequency constant-phase behaviour in the respiratory impedance”. *Biomedical Signal Processing and Control*, 197–208, 2011 (material found in Chap. 7).

Clara Ionescu, Kristine Desager and Robin De Keyser, “Fractional order model parameters for the respiratory input impedance in healthy and asthmatic children”. *Computer Methods and Programs in Biomedicine*, 315–323, 2011 (material found in Chap. 7).

Clara Ionescu, Eric Derom and Robin De Keyser, “Assessment of respiratory mechanical properties with constant phase models in healthy and COPD lungs”. *Computer Methods and Programs in Biomedicine*, 78–85, 2009 (material found in Chap. 7).

Contents

Acronyms

FOT	Forced Oscillation Technique
PV	Pressure Volume
FC	Fractional Calculus
FO	Fractional Order
FEV1	Forced Expiratory Volume in one second
FVC	Forced Vital Capacity
PT	Pressure Transducer
PN	Pneumotachograph
I2M	Input Impedance Device Logo
LS	Loudspeaker
BT	Bias Tube
bf	biological filter
CT	Computer Tomography
MDS	Multi-Dimensional Scaling
QF	Quality Factor
NE	Normal-to-Exam
CI	Confidence Intervals
RLC	Resistance–Inductance–Capacitance Series
CP4, CP5	Constant Phase Model in four, respectively in five elements
RLCES	RLC Series with Extended Shunt element
VC	Vital Capacity
SD	Standard Deviation
KS	Kyphoscoliosis
COPD	Chronic Obstructive Pulmonary Disease
GOLD	Global Initiative for COPD—guidelines
CF	Cystic Fibrosis
BTPS	Body Temperature and Pressure, Saturated air conditions
VC	Vital Capacity in percent (spirometry)
FEF	Forced Expiratory Flow (spirometry)
MEF75/25	Mean Expiratory Flow at 75/25 percent ratio (spirometry)
BLA	Best Linear Approximation

Nomenclature

Defined in Chap. 1:

P	pressure
Q	flow
Z_r	respiratory impedance
R_r	respiratory resistance
L_r	respiratory inertance
C_r	respiratory capacitance
β_r	fractional order
n	fractional order
j	the imaginary number $= \sqrt(-1)$
ω	angular frequency $= 2\pi f$, f the frequency in Hz
E^*	complex modulus of elasticity
σ	stress
ε	strain
E_S, E_D	storage and dissipation moduli, respectively
E	spring/elastic constant
η	damper/viscous constant
t	time
τ	time delay, time shift
F_d	fractal dimension
L	length
d	diameter, distance
$\varepsilon_{\mathrm{FD}}$	box size
$N(\varepsilon_{\mathrm{FD}})$	number of boxes of size $\varepsilon_{\mathrm{FD}}$

Defined in Chap. 2:

m	airway level
$\varDelta$	degree of asymmetry
ℓ	airway length

h	airway wall thickness
κ	airway cartilage fraction

Defined in Chap. 3:

U_g	generated input/signal
U_r	breathing input/signal
Z_1	impedance describing voltage-pressure conversion
Z_2	impedance describing the loudspeaker and bias tube
Z_3	impedance describing the pneumotachograph effect
S_{PU}, S_{QU}	cross-correlation spectra between various signals
E_R	error calculated from the real part of impedance
E_X	error calculated from the imaginary part of impedance
E_T	total error
Re	the values of the real part of the impedance
Im	the values of the imaginary part of the impedance
α_r, β_r	fractional orders
$CP4$	the constant-phase model from literature in four parameters
$CP5$	the proposed constant-phase model in five parameters
N_S	total number of samples

Defined in Chap. 4:

δ	Womersley parameter $= R\sqrt{\omega\rho/\mu}$
ε_0, ε_1, ε_2	phase angles of the complex Bessel functions of the first kind and order 0 and 1
ϕ_P	phase angle for pressure
γ	complex propagation coefficient
κ	cartilage fraction
μ	dynamic viscosity
ν_P	coefficient of Poisson (= 0.45)
θ	contour coordinate
ρ, ρ_{wall}, ρ_s, ρ_c	density of air at BTPS, respectively of the airway wall, of the soft tissue, and of the cartilage
ω	angular frequency
ζ	radial deformation
ϕ_b	angle of bifurcation
ΔP	pressure drop
b	bifurcation length
c_x	capacity per distance unit
d_x	distance unit
$\tilde{c}$, $\acute{c}_0$	the complex velocity of wave propagation, the effective/corrected Moens–Korteweg velocity
f	frequency in Hz

g_x	conductance per distance unit
h	wall thickness
j	complex unit $= \sqrt{-1}$
l_x	inductance per distance unit
ℓ	airway length
ℓ_m	length of an airway in a level m
m	airway depth or airway level
p	pressure
q	flow
r	radial direction, radial coordinate
r_x	resistance per distance unit
t	time
u	velocity in radial direction
v	velocity in contour direction
w	velocity in axial direction
z	axial direction, longitudinal coordinate
y	ratio of radial position to radius $= r/R$
R	airway radius
A_p, C_1	amplitude of the pressure wave
A_u	amplitude of the radial velocity wave
A_w	amplitude of the axial velocity wave
A_m^*, A_m	the cross sectional area in an airway, and in the level m, respectively
Q_m^*, Q_m	the air-flow in an airway, and in the level m, respectively
w_m^*, w_m	the axial velocity in an airway, and in the level m, respectively
E, E_c, E_s	effective, cartilage and soft tissue elastic modulus, respectively
F_r, F_θ, F_z	forces in the radial, contour and axial directions
M_p	modulus of pressure wave
J_1, J_0	Bessel functions of first kind and order 1 and 0
M_0, M_1, M_2	the modulus of the complex Bessel functions of the first kind and order 0 and 1
$\varDelta$	asymmetry index
R_e	electric resistance
L_e	electric inductance, inertance
C_e	electric capacitance, compliance
Zl, Zt, Z_0	the longitudinal, transversal and characteristic impedances
$\lvert E\rvert$, ϕ_E	the modulus and angle of the elastic modulus
N_{RE}	Reynolds number

Defined in Chap. 5:

λ	ratio for resistance
$1/\alpha$	ratio for inertance
χ	ratio for capacitance
o	ratio for conductance

R_m	radius of an airway in a level m
R_{em}	electrical resistance in the level m
L_{em}	electrical inertance in the level m
C_{em}	electrical capacitance in the level m
R_{UA}, L_{UA}, C_{UA}	upper airway resistance, inertance and capacitance, respectively
R_{CG}, L_{CG}, C_{CG}	gas compression resistance, inertance and capacitance, respectively
Zl, Zt	longitudinal and transversal impedances, respectively
Z_N, Y_N	the total ladder network impedance, respectively admittance
N	total number of levels, total number of cells
I_m	current in cell m
U_m	voltage in cell m

Defined in Chap. 6:

n	fractional order
F	force
A	cross sectional area
σ	stress
ε	strain
$\Delta\ell$	longitudinal deformation
E_S, E_D	storage and dissipation moduli, respectively
τ	relaxation time
V	volume
B	damping constant (dashpot) from electrical equivalence
K	elastic constant (spring) from electrical equivalence
E	spring constant
η	damper constant
v	velocity
x	axial displacement
E_d, φ_d	dynamic modulus and its angle
W	energy
σ_c	constant stress
$\tan\delta$	loss tangent

Defined in Chap. 7:

R_{aw}	total airway resistance (body plethysmography)
C_{cw}	chest wall compliance calculated from Cobb angle
$\underline{h}$, $\underline{a}$, $\underline{w}$	height (m), age (years) and weight (kg)
$QF6$	quality factor at 6 Hz
$R6$	real part of impedance at 6 Hz
$PF6$	power factor at 6 Hz
$Frez$	resonant frequency

G_r	tissue damping
H_r	tissue elastance
η_r	tissue hysteresivity
ε_r	tissue permittivity
ϕ_z	phase angle at 6 Hz
Z_{PAR}	high-frequency interval parametric impedance model
Z_{REC}	high-frequency interval recurrent parametric impedance model

Defined in Chap. 8:

p, z	poles, zeros
K	gain
N_{pz}	number of pole-zero pairs
ω_u	unit angular frequency
ω_b, ω_h	low, respectively high-frequency limit interval
d_{ij}, D_1, D_2	distance
δ_{ij}	dissimilarity
τ	delay

Defined in Chap. 9:

$b(t)$	breathing signal
i	harmonic
β	polynomial order
T_s	sampling period
F_0	breathing frequency
U_{FOT}	optimized multisine excitation signal for FOT testing
$E\{\}$	expected value
T	index of nonlinear distortions
P_{even}	non-excited pressure values at even frequency points
P_{odd}	non-excited pressure values at odd frequency points
P_{exc}	excited pressure values at odd frequency points
U_{even}	non-excited pressure values at even frequency points
U_{odd}	non-excited pressure values at odd frequency points
U_{exc}	excited pressure values at odd frequency points

Chapter 1
Introduction

1.1 The Concept of Fractional Signals and Systems in Biomedical Engineering

The seminal concepts risen from two mathematicians, the bourgeois L'Hopital and the philosopher Leibnitz, have proven yet again that old ideas have long shadows. Three hundred years after this cross-fertilization, modern sciences are plucking its fruits at a logarithmically ever-increasing speed. About half a century ago, fractional calculus has emerged from the shadows of its abstract form into the light of a very broad application field, varying from ecology, economics, physics, biology, and medicine. Of course, it all became possible with a little aid from the revolution in computer science and microchip technology, allowing to perform complex numerical calculations in a fraction of a millisecond. Nowadays, it turns out that Mother Nature has a very simple, yet extremely effective design tool: the fractal. For those not yet aware of this notion, the concise definition coined by Mandelbrot is that a fractal structure is a structure where its scale is invariant under a(ny) number of transformations and that it has no characteristic length [97]. Fractals and their relative dimensions have been shown to be natural models to characterize various natural phenomena, e.g. diffusion, material properties, e.g. viscoelasticity, and repetitive structures with (pseudo)recurrent scales, e.g. biological systems.

The emerging concepts of fractional calculus (FC) in biology and medicine have shown a great deal of success, explaining complex phenomena with a startling simplicity [95, 167]. For some, such simplicity may even be cause for uneasiness, for what would the world be without scepticism? It is the quest to prove, to show, to sustain one's ideas by practice that allows progress into science and for this, one must acknowledge the great amount of results published in the last decades and nicely summarized in [149–152].

To name a few examples, one cannot start without mentioning the work of Mandelbrot, who, in his quest to decipher the Geometry of Life, showed that fractals are ubiquitous features [97]. An emerging conclusion from his investigations was that in Nature there exists the so called "magic number", which allows to generically describe all living organisms. Research has shown fractal properties from cellular

C.M. Ionescu, *The Human Respiratory System*, Series in BioEngineering,
DOI 10.1007/978-1-4471-5388-7_1,

metabolism [144] to human walk [50]. Furthermore, the lungs are an optimal gas exchanger by means of fractal structure of the peripheral airways, whereas diffusion in the entire body (e.g. respiratory, metabolic, drug uptake, etc.) can be modeled by a fractional derivative.[1] Based on similar concepts, the blood vascular network also has a fractal design, and so do neural networks, branching trees, seiva networks in a leaf, cellular growth and membrane porosity [50, 74, 81].

It is clear that a major contribution of the concept of FC has been and remains still in the field of biology and medicine [151, 152]. Is it perhaps because it is an intrinsic property of natural systems and living organisms? This book will try to answer this question in a quite narrow perspective, namely (just) the human lungs. Nevertheless, this example offers a vast playground for the modern engineer since three major phenomena are interwoven into a complex, symbiotic system: fractal structure, viscoelastic material properties, and diffusion.

1.2 Short History of Fractional Calculus and Its Application to the Respiratory System

From the 1970s, FC has inspired an increasing awareness in the research community. The first scientific meeting was organized as the First Conference on Fractional Calculus and its Applications at the University of New Haven in June 1974 [151, 152]. In the same year appeared the monograph of K.B. Oldham and J. Spanier [113], which has become a textbook by now together with the later work of Podlubny [126].

Signal processing, modeling, and control are the areas of intensive FC research over the last decades [146, 147]. The pioneering work of A. Oustaloup enabled the application of fractional derivatives in the frequency domain [118], with many applications of FC in control engineering [20, 117].

Fractional calculus generously allows integrals and derivatives to have any order, hence the generalization of the term *fractional order* to that of *general order*. Of all applications in biology, linear viscoelasticity is certainly the most popular field, for their ability to model hereditary phenomena with long memory [9]. Viscoelasticity has been shown to be the origin of the appearance of FO models in polymers (from the Greek: *poly*, many, and *meros*, parts) [2] and resembling biological tissues [30, 68, 143].

Viscoelasticity of the lungs is characterized by compliance, expressed as the volume increase in the lungs for each unit increase in alveolar pressure or for each unit decrease of pleural pressure. The most common representation of the compliance is given by the pressure–volume (PV) loops. Changes in elastic recoil (more, or less: stiffness) will affect these pressure–volume relationships. The initial steps undertaken by Salazar to characterize the pressure–volume relationship in the lungs by

---

[1] The reader is referred to the appendix for a brief introduction to FC.

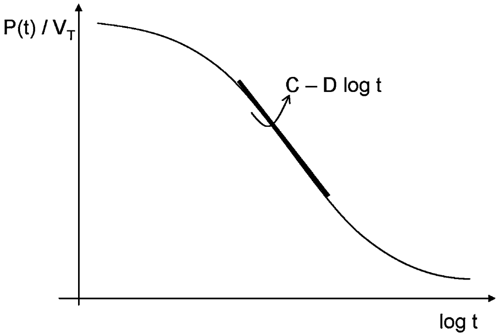

Fig. 1.1 Schematic representation of the quasi-linear dependence of the pressure–volume ratio with the logarithm of time

means of exponential functions suggested a new interpretation of mechanical properties in lungs [134]. In their endeavor to obtain a relation for compliance which would be independent on the size of the lungs, they concluded that the pressure–volume curve is a good tool in characterizing viscoelasticity. Shortly afterwards, Hildebrandt used similar concepts to assess the viscoelastic properties of a rubber balloon [61] as a model of the lungs. He obtained similar static pressure–volume curves by stepwise inflation in steps of 10 ml (volume) increments in a one minute time interval. He then points out that the curves can be represented by means of a power-law function (see Fig. 1.1).

Instead of deriving the compliance from the PV curve, Hildebrandt suggests to apply sinusoidal inputs instead of steps and he obtains the frequency response of the rubber balloon. The author considers the variation of pressure over total volume displacement also as an exponentially decaying function:

$$\frac{P(t)}{V_T} = At^{-n} + B, \qquad \frac{P(t)}{V_T} = C - D\log(t) \tag{1.1}$$

with A, B, C, D arbitrary constants, V_T the total volume, t the time, and n the power-law constant. The transfer function obtained by applying Laplace to this stress relaxation curve is given by

$$\frac{P(s)}{V_T} = A\frac{\Gamma(1-n)}{s^{1-n}} + \frac{B}{s} \tag{1.2}$$

with Γ the Gamma function. If the input is a step $v(t) = V_T u(t)$, then $V(s) = V_T/s$ and the output is given by $P(s) = T(s)V_T/s$ with $T(s)$ the unknown transfer function. Introducing this into (1.2) one obtains

$$T(s) = \frac{P(s)}{V(s)} = As^n\Gamma(1-n) + B \tag{1.3}$$

By taking into account the mass of air introduced into the balloon, an extra term appears in the transfer function equation:

$$T(s) = \frac{P(s)}{V(s)} = As^n\Gamma(1-n) + B + L_r s^2 \tag{1.4}$$

with L_r the inductance. The equivalent form in frequency domain is given by

$$T(j\omega) = A\Gamma(1-n)\omega^n \cos\left(\frac{n\pi}{2}\right) - L_r\omega^2 + B + j\left[A\Gamma(1-n)\omega^n \sin\left(\frac{n\pi}{2}\right)\right] \tag{1.5}$$

This function describes the behavior of the balloon in a plethysmograph, while undergoing sinusoidal forced oscillations. One year later, in 1970, he published the results obtained by identifying such a model on excised cat lungs [62]. He then suggests to do the PV approximation with a transfer function which has an imaginary part independent on frequency. This special property gives a phase angle which decreases slightly with frequency (quasi-constant). Playing with these models on the data for the PV curves, he discusses the viscoelastic properties of the rubber balloon versus the excised cat lungs. In doing so, he combines several idealized mechanical elements to express viscoelasticity in a mechanical context. Some fragile steps are then directed towards concepts of stress relaxation and dynamic hysteresis of the lungs.

Two decades later, Hantos and co-workers in 1992 revised the work of Hildebrandt and introduced the impedance as the ratio of pressure and flow, in a model structure containing a resistance R_r, inertance L_r and compliance C_r element, as in (3.9) [57]. This model proved to have significant success at low frequencies and has been used ever since by researchers to characterize the respiratory impedance.

In the same context of characterizing viscoelasticity, Suki provided an overview of the work done by Salazar, Hildebrandt and Hantos, establishing possible scenarios for the origin of viscoelastic behavior in the lung parenchyma [143]. The authors acknowledge the validity of the models from (1.1) and the FO impedance from [57]:

$$Z_r(s) = \frac{1}{C_r s^{\beta_r}} \tag{1.6}$$

in which the real part denotes elastance and the imaginary part the viscance of the tissue. This model was then referred to as *the constant-phase model* because the phase is independent of frequency, implying a frequency-independent mechanical efficiency. Five classes of systems admitting power-law relaxation or constant-phase impedance are acknowledged [143].

- *Class 1*: *systems with nonlinear constitutive equations*; a nonlinear differential equation may have a At^{-n} solution to a step input. Indeed, lung tissue behaves nonlinearly, but this is not the primary mechanism for having constant-phase behavior, since the forced oscillations are applied with small amplitude to the mouth of the patient to ensure linearity. Moreover, the input to the system is not a step, but rather a multisine.
- *Class 2*: *systems in which the coefficients of the constitutive differential equations are time-varying*; the linear dependence of the pressure–volume curves in logarithmic time scale does not support this assumption. However, on a larger time interval, the lungs present time-varying properties.
- *Class 3*: *systems in which there is a continuous distribution of time constants that are solutions to integral equations*. By aid of Kelvin bodies and an appropriate

distribution function of their time constants, a linear model has been able to capture the hysteresis loop of the lungs, capturing the relaxation function decreasing linearly with the logarithm of time [49]. This is a class of systems which may be successful in acknowledging the origin of the constant-phase behavior, but there is no clearly defined micro-structural basis. Some attempts to establish this origin have been made [9].

- *Class 4*: *complex dynamic systems exhibiting self-similar properties* (*fractals*). This class is based on the fact that the scale-invariant behavior is ubiquitous in nature and the stress relaxation is the result of the rich dynamic interactions of tissue strips independent of their individual properties [8, 91]. Although interesting, this theory does not give an explanation for the appearance of constant-phase behavior.
- *Class 5*: *systems with input–output relationships including fractional-order equations*; borrowed from fractional calculus theory, several tools were used to describe viscoelasticity by means of fractional-order differential equations [8, 23, 143].

Referring to the specific application of respiratory mechanics, Classes 3–5 are most likely to characterize the properties of lung parenchyma. The work presented in this book deals primarily with concepts from Class 4, but addresses also several items from Class 5.

Following the direction pointed out hitherto, several studies have been performed to provide insight on fiber viscoelasticity at macro- and microscopic levels, using tissue strips from animals [162]. For instance, Maksym attempted to provide a model based on Hookean springs (elastin) in parallel with a nonlinear string element (collagen) to fit measurements of stress–strain in tissue strips in dogs [96]. Their theory is based on the seminal work of Salazar and Hildebrandt and the results suggest that the dominant parameter in (1.1) is n. This parameter has been found to increase in emphysema and decrease in fibrosing alveolitis. They interpret the changes in this variable as related to alterations in collagen and elastin networks.

About a decade later, Bates provided another mechanistic interpretation of the quasi-linear viscoelasticity of the lung, suggesting a model consisting of series spring-dashpot elements (Maxwell bodies) [8]. He also suggests the genesis of power-law behavior arising from:

- the intrinsic complexity of dynamic systems in nature, ubiquitously present;
- the property of being self-organized critically, posing an avalanche behavior (e.g. sandpile);
- the rich-get-richer mechanism (e.g. internet links).

whereas the common thread which sews all them together is *sequentiality*. By allowing two FO powers in the model of Maxwell bodies arranged in parallel (a spring in parallel with a dashpot), he discussed viscoelasticity in simulation studies. Similar attempts have been done by Craiem and Armentano in models of the arterial wall [23].

Hitherto, the research community focused on the aspect of viscoelasticity in soft biological tissues. The other property of the lungs which can be related to fractional-order equations is diffusion and some papers discuss this aspect [91], but current state-of-art lacks a mathematical basis for modeling diffusion in the lungs. The subject in itself is challenging due to its complexity and requires an in-depth study of alveolar dynamics. This is not treated in this book, but the reader is encouraged to check the provided literature for latest advances in this topic.

The study of the interplay between fractal structure, viscoelasticity, and breathing pattern did not capture the attention of both medical and engineering research communities. This is surprising, since interplay clearly exists and insight into its mechanisms may assist diagnosis and treatment. This book will address this issue and will establish several relations between recurrent geometry (symmetric and asymmetric tree) and the appearance of the fractional-order models, viscoelasticity, and effects of pulmonary disease on these properties.

1.3 Emerging Tools to Analyze and Characterize the Respiratory System

1.3.1 Basic Concepts of Fractional Calculus

The FC is a generalization of integration and derivation to non-integer (fractional) order operators. At first, we generalize the differential and integral operators into one fundamental operator D_t^n (n the order of the operation) which is known as *fractional calculus*. Several definitions of this operator have been proposed (see, e.g. [126]). All of them generalize the standard differential–integral operator in two main groups: (a) they become the standard differential–integral operator of any order when n is an integer; (b) the Laplace transform of the operator D_t^n is s^n (provided zero initial conditions), and hence the frequency characteristic of this operator is $(j\omega)^n$. The latter is very appealing for the design of control systems by using specifications in the frequency domain [117].

A fundamental D_t^n operator, a generalization of integral and differential operators (*differintegration* operator), is introduced as follows:

$$D_t^n = \begin{Bmatrix} \frac{d^n}{dt^n}, & n > 0 \\ 1, & n = 0 \\ \int_0^t (d\tau)^{-n}, & n < 0 \end{Bmatrix} \tag{1.7}$$

where n is the fractional order and $d\tau$ is a derivative function. Since the entire book will focus on the frequency-domain approach for fractional-order derivatives and integrals, we shall not introduce the complex mathematics for time-domain analysis. The Laplace transform for integral and derivative order n are, respectively:

$$L\{D_t^{-n} f(t)\} = s^{-n} F(s) \tag{1.8}$$

$$L\{D_t^{n} f(t)\} = s^{n} F(s) \tag{1.9}$$

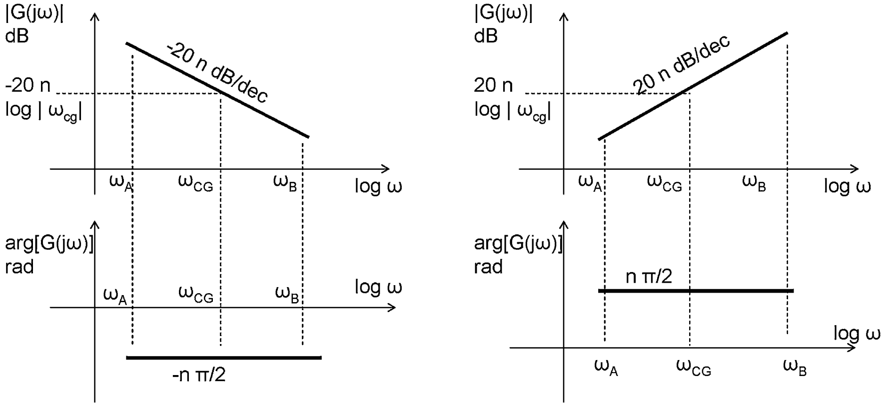

Fig. 1.2 Sketch representation of the FO integral and derivator operators in frequency domain, by means of the Bode plots (magnitude, phase)

where $F(s) = L\{f(t)\}$ and s is the Laplace complex variable. The Fourier transform can be obtained by replacing s by $j\omega$ in the Laplace transform and the equivalent frequency-domain expressions are

$$\frac{1}{(j\omega)^n} = \frac{1}{\omega^n}\left(\cos\frac{\pi}{2} + j\sin\frac{\pi}{2}\right)^{-n} = \frac{1}{\omega^n}\left(\cos\frac{n\pi}{2} - j\sin\frac{n\pi}{2}\right) \tag{1.10}$$

$$(j\omega)^n = \omega^n\left(\cos\frac{\pi}{2} + j\sin\frac{\pi}{2}\right)^{n} = \omega^n\left(\cos\frac{n\pi}{2} + j\sin\frac{n\pi}{2}\right) \tag{1.11}$$

Thus, the modulus and the argument of the FO terms are given by

$$\text{Modulus (dB)} = 20\log\left|(j\omega)^{\mp n}\right| = \mp 20n\log|\omega| \tag{1.12}$$

$$\text{Phase (rad)} = \arg\left((j\omega)^{\mp n}\right) = \mp n\frac{\pi}{2} \tag{1.13}$$

resulting in:

- a Nyquist contour of a line with a slope $\mp n\frac{\pi}{2}$, anticlockwise rotation of the modulus in the complex plain around the origin according to variation of the FO value n;
- magnitude (dB) vs. log-frequency: straight line with a slope of $\mp 20n$ passing through 0 dB for $\omega = 1$;
- phase (rad) vs. log-frequency: horizontal line, thus independent of frequency, with value $\mp n\frac{\pi}{2}$.

The respective sketches can be seen in Fig. 1.2.

1.3.2 Fractional-Order Dynamical Systems

Let us consider the rheological properties of soft biological tissue, i.e. viscoelasticity. Typical cases are the arterial wall [23] and lung parenchyma [8], which clearly show viscoelastic behavior. In these recent reports, the authors acknowledge that integer-order models to capture these properties can reach high orders and that fractional derivative models with fewer parameters have proven to be more efficient in describing rheological properties. Both of these authors define the complex modulus of elasticity as being determined by a real part, i.e. the storage modulus, capturing the elastic properties, and, respectively, by an imaginary part, i.e. the dissipation modulus, capturing the viscous properties:

$$E^*(j\omega) = \frac{\sigma(\omega)}{\varepsilon(\omega)} = E_S(\omega) + jE_D(\omega) \tag{1.14}$$

with σ the stress and ε the strain, E_S and E_D the real and imaginary parts of the complex modulus. This complex modulus $E^*(j\omega)$ shows partial frequency dependence within the physiologic range in both soft tissue examples. A typical example of an integer-order lumped rheological model is the Kelvin–Voigt body, consisting of a perfectly elastic element (spring) in parallel with a purely viscous element (dashpot):

$$\sigma(t) = E\varepsilon(t) + \eta\frac{d\varepsilon(t)}{dt} \tag{1.15}$$

with E the elastic constant of the spring and η the viscous coefficient of the dashpot. One of the limitations of this model is that it shows creep but does not show relaxation, the latter being a key feature of viscoelastic tissues [2, 68]. The classical definition of fractional-order derivative (i.e. the Riemann–Liouville definition) of an arbitrary function $f(t)$ is given by [113, 126]

$$\frac{d^n f}{dt^n} = \frac{1}{\Gamma(1-n)}\frac{d}{dt}\int_0^t \frac{f(\tau)}{(t-\tau)^n}\,d\tau \tag{1.16}$$

where Γ is the Euler gamma function. Hence, the FO derivative can be seen in the context of (1.15) as the convolution of $\varepsilon(t)$ with a t^{-n} function, anticipating some kind of memory capability and power-law response. It follows that the *spring–pot element* can be defined based on (1.16) as

$$\sigma = \eta\frac{d^n\varepsilon}{dt^n}, \quad 1 \geq n \geq 0 \tag{1.17}$$

in which the value for n can be adjusted to incorporate either a purely elastic component ($n = 0$), either a pure viscous one ($n = 1$). Both Bates and Craiem acknowledged the fact that the soft biological tissue follows both elastic and viscous behavior under baseline and stimulated case. Therefore, if one needs to derive a general model for characterizing soft tissue rheological properties, two instead of one spring–pot elements may be necessary.

Now, let us consider the diffusive properties; e.g. heat transfer [91], gas exchange [66] and water transfer through porous materials [12, 91]. Diffusion is of fundamental importance in many disciplines of physics, chemistry, and biology. It is well known that the fractional-order operator $\frac{d^{0.5}}{dt^{0.5}} \to s^{0.5}$ appears in several types of problems [10]. The transmission lines, the heat flow, or the diffusion of neutrons in a nuclear reactor are examples where the half-operator is the fundamental element. Diffusion is in fact a part of transport phenomena, being one of the three essential partial differential equations of mathematical physics. Molecular diffusion is generally superimposed on, and often masked by, other transport phenomena such as convection, which tend to be much faster. However, the slowness of diffusion can be the reason for its importance: diffusion is often encountered in chemistry, physics, and biology as a step in a sequence of events, and the rate of the whole chain of events is that of the slowest step. Transport due to diffusion is slower over long length scales: the time it takes for diffusion to transport matter is proportional to the square of the distance. In cell biology, diffusion is a main form of transport for necessary materials such as amino acids within cells. Metabolism and respiration rely in part upon diffusion in addition to bulk or active processes. For example, in the alveoli of mammalian lungs, due to differences in partial pressures across the alveolar–capillary membrane, oxygen diffuses into the blood and carbon dioxide diffuses out. Lungs contain a large surface area to facilitate this gas exchange process. Hence, the spreading of any quantity that can be described by the diffusion equation or a random walk model (e.g. concentration, heat, momentum, ideas, price) can be called diffusion, and this is an ubiquitously present property of nature.

Finally, let us consider the fractal geometry; e.g. self-similarity and recurrence. Much work has been done on the fundamental property of percolation using self-similar fractal lattices such as the Sierpinski gasket and the Koch tree [91, 97, 118, 130]. Examples from real life include the coastline, invasion-front curve, lightning, broccoli and cauliflower, and several human organs such as lungs, vascular tree, and brain surface [9]. Other studies involve the temporal dynamics of biological signals and systems, which also pose recurrence [37, 144].

It is generally acknowledged that dynamical systems (e.g. electrical circuits) involving such geometrical structures would lead to the appearance of a fractional-order transfer function [118]. Although this topic has been investigated for the respiratory tree, in this book the relation to viscoelasticity will be made, to offer a broader image of their interplay.

1.3.3 Relation Between Fractal Structure and Fractal Dimension

A fractal is a set of points which at smaller scales resembles the entire set. Thus the essential characteristic of the fractal is self-similarity. Its details at a certain scale are similar to those at other scales, although not necessarily identical. The textbook example of such a fractal is the Koch curve, depicted in Fig. 1.3.

The concept of fractal dimension (F_d) originates from fractal geometry and it emerges as a measure of how much space an object occupies between Euclidean dimensions, e.g. the fractal structure from Fig. 1.3. In practice, the Fd of a waveform

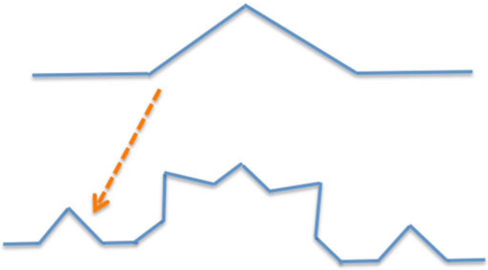

Fig. 1.3 An example of repetitive pattern at the origin of fractals

(e.g. respiratory, circadian, cardiac, electroencephalogram, etc.) represents a powerful tool for transient detection. Several algorithms are available; here we discuss only two: (i) the Katz algorithm and (ii) the box-counting method.

The definition introduced by Katz is given as[50]

$$F_d^K = \frac{\log(L)}{\log(d)} \tag{1.18}$$

where L is the total length of the curve or sum of distances between successive points, and d is the diameter estimated as the distance between the first point of the sequence and the most distal point of the sequence. Hence, d can be expressed as

$$d = \max \left\| x(1) = x(i) \right\|, \quad \forall i. \tag{1.19}$$

The F_d compares the actual number of units that compose a curve with the minimum number of units required to reproduce a pattern of the same spatial extent. Consequently, F_d depends on the measurement units. Naturally, if units will be different, so will F_d values. The solution is to create a general unit, e.g. the average step or average distance between successive points, denoted by a. Normalization applied to (1.18) results in a new definition:

$$F_d^K = \frac{\log(L/a)}{\log(d/a)} \tag{1.20}$$

There is also a relationship between the length, area or volume of an object and its diameter. If one tries to cover the unit square with little squares (i.e. boxes) of side length $\varepsilon_{\mathrm{FD}}$, then one will need $1/\varepsilon_{\mathrm{FD}}^2$ boxes. To cover a segment of length 1, there is need only for $1/\varepsilon_{\mathrm{FD}}$ boxes. If we need to cover a $1 \times 1 \times 1$ cube, then we need $1/\varepsilon_{\mathrm{FD}}^3$ boxes. The general rule emerges as

$$N(\varepsilon_{\mathrm{FD}})(S) \approx 1/\varepsilon_{\mathrm{FD}}^d, \quad \text{for } \varepsilon_{\mathrm{FD}} \to 0 \tag{1.21}$$

where $\varepsilon_{\mathrm{FD}}$ is the length of the box, S is the full data set, $N(\varepsilon_{\mathrm{FD}})(S)$ is the minimum number of n-dimensional boxes needed to cover S entirely and d is the dimension of S. Using this, one can define F_d as

$$F_d^{\mathrm{box}} = -\lim_{\varepsilon_{\mathrm{FD}} \to 0} \frac{\ln N(\varepsilon_{\mathrm{FD}})(S)}{\ln \varepsilon_{\mathrm{FD}}} \tag{1.22}$$

Usually, for systems whose dynamics is intrinsic fractal, the graphic representation of F_d will be a line and its slope denotes the value of the fractal dimension.

1.4 Summary

In this introductory chapter, the background has been set for the pioneer concepts further introduced by this book. A definition of fractional calculus and fractional signals has been given before proceeding in the quest for novel landmarks in biomedical engineering applications. A brief history of fractional calculus and how these abstract concepts became emerging tools in biology and medicine has been given, providing also a motivation as to why these tools are now of great interest to the research community. Two of the most common concepts used to characterize biological signals have been introduced, namely those of fractal structure and of fractal dimension. With these basic concepts at hand, the reader is now ready for the quest of this book.

Chapter 2
The Human Respiratory System

2.1 Anatomy and Structure

Respiration is the act of breathing, namely inhaling (inspiration) oxygen from the atmosphere into the lungs and exhaling (expiration) into the atmosphere carbon dioxide [53]. The respiratory system is made up of the organs involved in breathing, and consists of the nose, pharynx, larynx, trachea, bronchi, and lungs, as depicted in Fig. 2.1.

The respiratory system can be divided into two major parts: the upper airways part and the lower airways part. The upper respiratory tract includes the nose, with its nasal cavity, frontal sinuses, maxillary sinus, larynx, and trachea. The lower respiratory tract includes the lungs, bronchi and the alveoli.

The lungs take in oxygen, which is required by all the cells throughout the body to live and carry out their normal functions. The lungs also get rid of carbon dioxide, a waste product of the body's cells. The lungs are a pair of cone-shaped organs made up of spongy, pinkish-gray tissue. They take up most of the space in the chest, or the thorax (the part of the body between the base of the neck and diaphragm).

The lungs are separated from each other by the mediastinum, an area that contains the following:

- heart and its large vessels;
- trachea;
- esophagus;
- thymus;
- lymph nodes.

The right lung has three sections, called lobes. The left lung has only two lobes. When one breaths, the air enters the body through the nose or the mouth, travels down the throat through the larynx (voice box) and trachea (windpipe) and goes into the lungs through the tubes called main-stem bronchi. One main-stem bronchus leads to the right lung and the other one leads to the left lung. In the lungs, the main-stem bronchi divide into smaller bronchi and then into even smaller tubes called bronchioles, which finally end in tiny air sacs called alveoli. At this level, the act of

C.M. Ionescu, *The Human Respiratory System*, Series in BioEngineering,
DOI 10.1007/978-1-4471-5388-7_2,

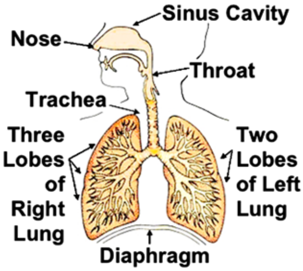

Fig. 2.1 Schematic representation of the respiratory system and its main components

diffusion takes place. Diffusion allows the oxygen from the alveoli to pass through the alveolar walls into the blood and the carbon dioxide to pass through the capillary walls into the alveoli.

In order to move air in and out of the lungs, the volume of the thoracic cavity is increased (or decreased). The lungs do not contract but increase or decrease in volume. Muscles like intercostals or diaphragm contract during inspiration. Normally, the expiration is passive, the inspiration is active (= contraction of muscles). By increasing the thoracic cavity, the pressure around the lungs decreases, the lungs expand, and air is sucked in.

2.2 Morphology

In the literature, there are two representative sets of airway morphological values: the symmetric case and the asymmetric case of the respiratory tree, schematically depicted in Fig. 2.2. The *symmetric* case assumes a dichotomously equivalent bifurcation of the airways in subsequent levels and is agreed by a group of authors e.g. [97, 135, 164] as in Table 2.1. The *asymmetric* case is when the bifurcations are still dichotomous, but they occur in non-sequent levels, as given in Table 2.2. The parameter Δ denotes the asymmetry index. In this case, a parent airway will split into two daughters: one of subsequent level $m+1$ and one of level $m+1+\Delta$. This latter anatomical context is agreed by another group of authors: [54, 65].

2.3 Specific Pulmonary Abnormalities

Chronic Pulmonary Emphysema refers to a class of respiratory disorders which implies the existence of excess air in the lungs [6, 53, 64]. It results from three major pathophysiological events in the lungs:

- chronic infection, caused by inhaling smoke or other substances that irritate the bronchi and bronchioles;
- the infection, the excess of mucus, and inflammatory edema of the bronchiolar epithelium together cause chronic obstruction of smaller airways;

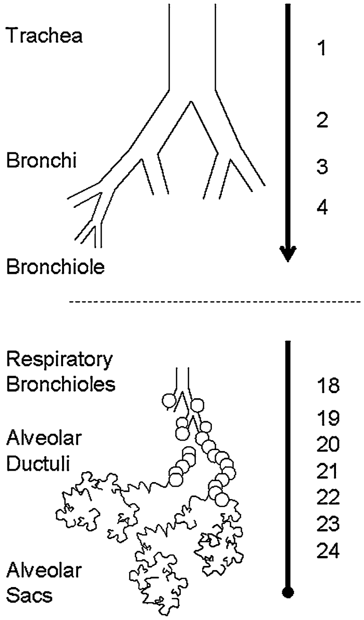

Fig. 2.2 A very brief schematic representation of the bronchial tree: generations 1–16 transport gas and 17–24 provide gas exchange [97, 135, 164]. This is not an accurate anatomical representation and it is modified with respect to numbering from the original Weibel model [164]. The notation implies here the number of levels and, as described later in this book, the number of elements in an analogy to electrical ladder networks

Fig. 2.3 A schematic representation of alveolar tissue in normal lungs (*left*) and disrupted alveolar walls in emphysematous lungs (*right*)

- the obstruction of the airways makes it especially difficult to expire, causing entrapment of air in the lungs (i.e. barrel chest effect) and over-stretching the alveoli.

The physiological effects of chronic emphysema are extremely varied, depending on the severity of the disease and on the relative degree of bronchiolar obstruction versus parenchymal destruction at the alveolar level. A schematic representation of tissue samples can be observed in Fig. 2.3.

The bronchiolar obstruction causes increased airway resistance and results in greatly increased work of breathing. It is especially difficult for the person to move air through the bronchioles during expiration, because the compressive force on the alveoli acts also on the bronchi, further increasing their resistance during expiration. Another physiological effect is that of a decreased diffusive capacity, from the marked loss of lung parenchyma (see Fig. 2.3 on the right). This will reduce the ability of the lungs to oxygenate the blood and to remove the carbon dioxide. Another effect is that of abnormal ventilation-perfusion ratio, i.e. portions of the lungs will be well ventilated, while others will be poorly ventilated, depending on the degree of the obstructive process. Chronic emphysema progresses slowly over many years, leading to necessity of ventilatory assist devices and finally to death.

Table 2.1 The tube parameters for the sub-glottal airways depths, whereas depth 1 denotes the trachea and depth 24 the alveoli, as used in [59, 66, 85, 97, 100, 164]

Depth m	Length ℓ (cm)	Radius R (cm)	Wall thickness h (cm)	Cartilage fraction κ
1	10.0	0.80	0.3724	0.67
2	5.0	0.6	0.1735	0.5000
3	2.2	0.55	0.1348	0.5000
4	1.1	0.40	0.0528	0.3300
5	1.05	0.365	0.0409	0.2500
6	1.13	0.295	0.0182	0.2000
7	1.13	0.295	0.0182	0.0922
8	0.97	0.270	0.0168	0.0848
9	1.08	0.215	0.0137	0.0669
10	0.950	0.175	0.0114	0.0525
11	0.860	0.175	0.0114	0.0525
12	0.990	0.155	0.0103	0.0449
13	0.800	0.145	0.0097	0.0409
14	0.920	0.140	0.0094	0.0389
15	0.820	0.135	0.0091	0.0369
16	0.810	0.125	0.0086	0.0329
17	0.770	0.120	0.0083	0.0308
18	0.640	0.109	0.0077	0.0262
19	0.630	0.100	0.0072	0.0224
20	0.517	0.090	0.0066	0.0000
21	0.480	0.080	0.0060	0.0000
22	0.420	0.070	0.0055	0.0000
23	0.360	0.055	0.0047	0.0000
24	0.310	0.048	0.0043	0.0000

Asthma is characterized by spastic contraction of the bronchioles, which causes extremely difficult breathing [17, 53]. The usual cause is bronchial hyperresponsiveness towards a variety of specific and a-specific stimuli. In fact, in younger patients, under the age of 30, the asthma is in about 70 % of the cases caused by allergic hypersensitivity (i.e. plant pollen, dust mite, cats, dogs). In elder persons, the hypersensitivity is to non-allergic types of irritants in air, such as smog.

As a result of the irritants, the allergic person has a tendency to produce a high amount of antibodies, which attach to specific cells in the bronchioles and small bronchi. As a result of the antibodies reaction with the irritant, some substances are released (e.g. histamine). The combined effect of all these factors will produce:

- localized edema in the walls of the small bronchioles as well as secretion of thick mucus into bronchiolar airways, and
- spasm of the bronchiolar smooth muscle.

Table 2.2 The tube parameters for the sub-glottal airways depths, whereas depth 1 denotes the trachea and depth 35 the alveoli, as used in [54, 65]

Depth m	Length ℓ (cm)	Radius R (cm)	Wall thickness h (cm)	Cartilage fraction κ	Bifurcation Δ
1	10.0	0.80	0.3724	0.67	1
2	5.0	0.6	0.1735	0.5000	2
3	2.2	0.55	0.1348	0.5000	3
4	1.1	0.40	0.0528	0.3300	3
5	1.05	0.365	0.0409	0.2500	3
6	1.13	0.295	0.0244	0.2000	3
7	1.13	0.295	0.0244	0.0926	3
8	0.97	0.270	0.0205	0.0851	3
9	1.08	0.215	0.0149	0.0671	3
10	0.860	0.175	0.0126	0.0526	3
11	0.950	0.175	0.0126	0.0525	3
12	0.990	0.155	0.0118	0.0450	3
13	0.800	0.145	0.0114	0.0410	3
14	0.920	0.140	0.0112	0.0389	3
15	0.820	0.135	0.0111	0.0370	3
16	0.810	0.125	0.0107	0.0329	3
17	0.770	0.120	0.0105	0.0309	3
18	0.640	0.109	0.01	0.0262	3
19	0.630	0.100	0.0096	0.0224	3
20	0.517	0.090	0.0091	0.0000	3
21	0.480	0.080	0.0085	0.0000	3
22	0.420	0.070	0.0079	0.0000	3
23	0.360	0.055	0.0067	0.0000	2
24	0.310	0.048	0.0060	0.0000	2
25	0.250	0.038	0.0050	0.000	1
26	0.11	0.0315	0.0042	0.000	0
27	0.131	0.0265	0.0036	0.000	0
28	0.105	0.024	0.0032	0.000	0
29	0.075	0.0215	0.0029	0.000	0
30	0.059	0.04	0.0052	0.000	0
31	0.048	0.04	0.0052	0.000	0
32	0.048	0.04	0.0052	0.000	0
33	0.048	0.04	0.0052	0.000	0
34	0.048	0.04	0.0052	0.000	0
35	0.048	0.04	0.0052	0.000	0

There may be a wheezing or whistling sound, which is typical of asthma. Wheezing occurs because muscles that surround the airways tighten, and the inner lining of the airways swells and pushes inward. It also occurs because membranes that line the airways secrete extra mucus and furthermore the mucus can form plugs that may block the air passages. As a result, the rush of air through the narrowed airways produces the wheezing sounds. Usually, the asthmatic person can inspire quite easily, but has difficulty to expire air from the lungs. Also here the long-term effect of barrel chest will occur, similarly to chronic obstructive emphysema.

Although anyone may have an asthma attack, it most commonly occurs in children, by the age of 5, adults in their 30s, adults older than 65, and people living in urban communities (smog or allergic reactions). Other factors include: family history of asthma and personal medical history of allergies.

Cystic Fibrosis is an inherited disease characterized by an abnormality in the glands that produce sweat and mucus [35, 132]. It is chronic, progressive, and may be fatal. Cystic fibrosis affects various systems in children and young adults, including the following: respiratory system, digestive system, and the reproductive system.

Approximately 1 in 20 people in the US and Europe are carriers of the cystic fibrosis gene. They are not affected by the disease and usually do not know that they are carriers. Abnormalities in the glands that produce sweat and mucus can cause:

- excessive loss of salt, which in turn can cause an upset in the balance of minerals in the blood, abnormal heart rhythms and possibly, shock;
- thick mucus that accumulates in lungs and intestines, which in turn can cause malnutrition, poor growth, frequent respiratory infections, breathing difficulties and in general, lung disease;
- other medical problems.

Under the item of medical problems one can enumerate: sinusitis, nasal polyps, clubbing of fingers and toes, pneumothorax—rupture of lung tissue, hemoptysis—coughing blood, enlargement of right side of the heart, abdominal pain, gas in the intestines, liver disease, diabetes, pancreatitis and gallstones.

Kyphoscoliosis is a deformation of the spine, as a combination effect of scoliosis and kyphosis [103]. An example of an X-ray is given in Fig. 2.4, courtesy of Prof. Derom from Ghent University Hospital. The patient was hospitalized for severe breathing insufficiency.

Scoliosis, is a medical condition in which a person's spine is curved from side to side, shaped like an *S* or *C*, and may also be rotated. To adults it can be very painful. It is an abnormal lateral curvature of the spine. On an X-ray, viewed from the rear, the spine of an individual with a typical scoliosis may look more like an *S* or a *C* than a straight line. It is typically classified as congenital (caused by vertebral anomalies present at birth), idiopathic (sub-classified as infantile, juvenile, adolescent, or adult according to when onset occurred) or as neuromuscular, having developed as a secondary symptom of another condition, such as spina bifida, cerebral palsy, spinal muscular atrophy or due to physical trauma. Scoliotic curves of 10 degrees or less affect 3–5 out of every 1000 people.

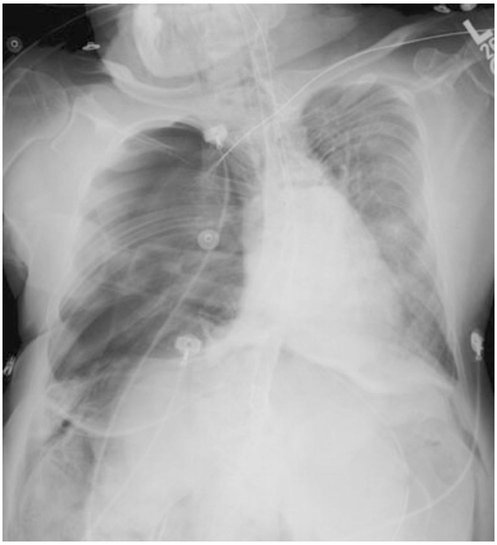

Fig. 2.4 X-ray of a patient presenting kyphoscoliosis. Courtesy of Prof. Dr. MD Eric Derom from Ghent University Hospital, Belgium

Kyphosis, also called hunchback, is a common condition of a curvature of the upper (thoracic) spine. It can be either the result of degenerative diseases (such as arthritis), developmental problems, osteoporosis with compression fractures of the vertebrae, and/or trauma. In the sense of a deformity, it is the pathological curving of the spine, where parts of the spinal column lose some or all of their normal profile. This causes a bowing of the back, seen as a slouching back and breathing difficulties. Severe cases can cause great discomfort and even lead to death.

As a result of these deformities at the spinal level, the thorax cannot perform its normal function, leading to changes in airway resistance and total lung compliance.

2.4 Structural Changes in the Lungs with Disease

The term *airway remodeling* refers to the process of modification and sustained disruption of structural cells and tissues leading to a new airway-wall structure with implicit new functions. Airway remodeling is supposed to be a consequence of long-term airway diseases. Some studies suggest that the remodeling may be a part of the primary pathology rather than simply a result of chronic inflammation [9]. Of crucial importance in this quest to understand airway remodeling is the composition and structure of the lung tissue [82, 153]. The composition and structure determines the mechanical properties of the lungs. Structural changes will induce alternations in tissue elasticity and viscosity. Structural alternations introduced by pathological processes are traditionally divided into three layers: the inner wall, the outer wall and the smooth-muscle layer. The inner wall consists of the epithelium, basement membrane and submucosa, while the outer layer consists of cartilage and loose connective tissue between the muscle layer and the surrounding lung parenchyma.

In COPD, major structural alternations occur in the small bronchi and membranous bronchiole (airway diameter $<$ 2 mm). Changes occur around the supporting cartilage and bronchial glands in the peripheral airways ($\approx$2 mm diameter). Here, the thickening occurs mainly in the inner wall area of the large airways [9, 82, 86].

The most important changes in asthma are located in the conducting airways, which can thicken up to 300 %. Asthma patients have thickened segmental and subsegmental bronchial walls over their entire size rage. This thickening is dependent on the degree of the disease, more severe and older patients will depict these characteristics more than young patients [9, 85]. In asthma, the inflammatory reactions takes place in the higher part of the airways than in COPD. Unfortunately for COPD patients, the airway obstruction that accompanies these changes is resistant to medication which makes the changes persistent. By contrast, in asthma the inflammatory processes can be controlled by the use of corticosteroids. There are also important differences in the remodeling of the extracellular matrix and the role of proteolytic enzymes and growth factors which lead to specific airway remodeling results by disease. More clinical information about inflammation mechanics in airway remodeling can be found in [13]. For remodeling effects in asthma, an important role is played by the degree to which the smooth muscle surrounds the airway lumen. These muscles are located within the posterior membranous sheath in the trachea and main-stem bronchi, whereas they surround the entire lumen of the airway in the bronchioles [53]. Consequently, the same degree of muscle shortening in asthma patients has a smaller effect on the central airways than on the lower situated bronchioles [53].

In COPD, hyperplasia and mucous metaplasia are observed in central and peripheral airways which ends in a more even distribution of secretary cells. This leads to a state where the smaller airways (diameter $<$ 400 μm), which are normally populated with very little goblet cells, become large contributors to the excess of mucous which characterizes COPD [64]. Mucous, produced in both asthma as COPD, is quantitatively and qualitatively abnormal with alternations in its molecular and cellular composition. The elevated ratio of mucous/serous acini provides a secretion of a thicker, gel-like mucus in COPD. Partial or complete occlusion of the small airways occurs.

The lungs consist of large surface areas with small diffusion distances to guarantee proper gas exchange. The 3D structure of the alveoli can be compared to a honeycomb structure of thin-walled septa which form a fractal network [64, 71]. This structure is unstable at low inflating pressures and would collapse if there would not be a mechanical stress at the end of expiration. This ‘pre-stress’ is generated by the pleural pressure around the lung. Changes in mechanical properties of the lung tissue by pathology will influence the response on this pre-stress. Once an alveolar wall starts to rupture, the stress the original wall carried is redistributed to the neighboring walls. These areas will experience a increased pre-stress which will result in a relentless increase of the unbinding and cleavage rate and the unfolding of new binding sites. A single rupture will induce a cascade of ruptures and serves as a positive feedback for further breakdown. It is obvious that there must be a kind of ‘tipping point’ beyond which the structure–function relationship cannot return to the healthy condition. The rupturing process develops in time and depends on sudden exacerbations. After the rupture of (one) septal wall(s), a new stable mechanical equilibrium can be reached. However, exacerbations triggered by bacterial or viral infections or tissue fatigue due to hard breathing or forceful coughing can lead to physical failure of the walls.

It is clear that mechanical forces invoked during breathing on enzyme-injured lungs have an important role in the breakdown of the septal walls of the alveoli. Changes in network topology will influence the macroscopic elasticity which may be detectable by the FOT (Forced Oscillations Technique) lung function test. When pressure oscillations are applied to this injured and mechanical adapted tissue, a significantly higher amount of nonlinear dynamics will be present.

2.5 Non-invasive Lung Function Tests

Normal quiet breathing (such as during the FOT lung function test) is accomplished by contraction of the diaphragm, the parasternal muscles and the scaleni. During inspiration, the diaphragm pulls the lower surfaces of the lung downwards. Expiration results from simple relaxation of these muscles. Changes in the elastic recoil of the lungs (more, or less, stiffness) will affect their normal function, in particular total lung volume and pressure–volume relationships.

Some measurements are performed during forced inspirations and forced expirations, i.e. the spirometry lung function test. A person's vital capacity can be measured by a spirometer [109]. In combination with other physiological measurements, the vital capacity (VC) can help make a diagnosis of underlying lung disease. Vital capacity is the maximum amount of air a person can expel from the lungs after a maximum inspiration. It is equal to the inspiratory reserve volume plus the tidal volume plus the expiratory reserve volume. Forced vital capacity (FVC) is the maximum volume of air that a person can exhale after maximum inhalation. It can also be the maximum volume of air that a person can inhale after maximum exhalation. Another important measure during spirometry is the forced expired volume in one second (FEV1). The FEV1/FVC ratio is used in the diagnosis of obstructive and restrictive lung disease, and normal values are approximately 80 %. In obstructive lung disease, the FEV1 is reduced due to obstruction to air escape. Thus, the FEV1/FVC ratio will be reduced. In restrictive lung disease, the FEV1 and FVC are equally reduced due to fibrosis or other lung pathology (not obstructive pathology). Thus, the FEV1/FVC ratio should be approximately normal.

The compliance is expressed as the volume increase in the lungs for each unit of trans-pulmonary pressure (which is the difference between the alveolar and pleural pressures). For instance, the compliance of the normal lungs and thorax combined is 0.13 liter per centimeter of water pressure (l/cmH_2O). This means that every time the alveolar pressure is increased by 1 cmH_2O, the lungs expand 130 ml. The most common representation of the compliance is given by the pressure–volume (PV) loops. The area between the inspiratory and expiratory PV curve is called the work of breathing; this will again vary with pathology.

Factors that cause abnormal compliance can be in fact anything which destroys the lung tissue, causing it to become fibrotic or edematous, blocks the bronchioli or in any other way impedes lung expansion and contraction. When considering the compliance of the lungs and thorax together, one should keep in mind any abnormality of the thoracic cage (e.g. kyphosis, scoliosis).

2.6 Summary

The purpose of this chapter was to provide a basic knowledge of anatomy and structure of the lungs, necessary to understand further developments in this book. The morphology plays an important role here, so a great deal of attention has been given to its implications in fractal analysis. The mechanical properties of the lungs are the result of a dynamic interplay between structure, active and passive breathing, all due to variations in pressure between the mouth and the alveoli. An overview of the spirometry non-invasive lung function test is also provided, since it helps the reader understand the clinical significance of the mechanical work of respiration.

Chapter 3
The Respiratory Impedance

3.1 Forced Oscillation Technique Lung Function Test

Although standardized and currently used in clinical environment, spirometry has several limitations. It requires maximal, reproducible efforts, which in turn requires several measurement sessions from the patient, resulting in fatigue and time consumption. The maximal expiratory flow is dependent on the lung recoil pressure, the dynamic airway resistance and the airway properties at the flow limiting segment (i.e. flow plateau) [112, 125]. Spirometry has also difficulties to clearly evaluate obstructive lung diseases. Even paired with bronchoprovocation, spirometry cannot reliably differentiate patients with both asthma and COPD (chronic obstructive pulmonary disease) features from either asthma or either COPD, and it is rather insensitive to early airway changes [38, 88]. Additionally, neither spirometry nor body plethysmography can provide information upon the resonance and anti-resonance frequencies in the lungs.

The forced oscillation technique (FOT) is defined as superimposing external pressure signals on spontaneous breathing (tidal breathing) [32, 116, 141, 158]. The effect of these oscillations on the airways and lungs provides an effort-independent assessment of respiratory mechanics. There is a significant amount of literature in pediatric applications [15, 25, 27, 123, 140] and there is an increasing interest in adult lung function testing [19, 28]. Typically, the forced oscillations can employ a mono- or a multi-frequency excitation signal, typically in the range 4 Hz to 30–50 Hz. It can be continuous (e.g. pseudo random noise, optimized multisine), or time discrete (e.g. impulse oscillations) [78, 79, 141]. FOT has been broadly used for screening purposes: upper airway obstruction, small airways disease in COPD [64], for bronchoprovocation testing [36], vocal cord dysfunction evaluation [106], with bronchodilator response, and respiratory mechanics in obstructive sleep apnea [110].

The measurements of the signals analyzed in this book have been performed using the device depicted in Fig. 3.1: the FOT standard setup, modified from a commercially available device, able to assess the respiratory mechanics in the range

C.M. Ionescu, *The Human Respiratory System*, Series in BioEngineering,
DOI 10.1007/978-1-4471-5388-7_3, © Springer-Verlag London 2013

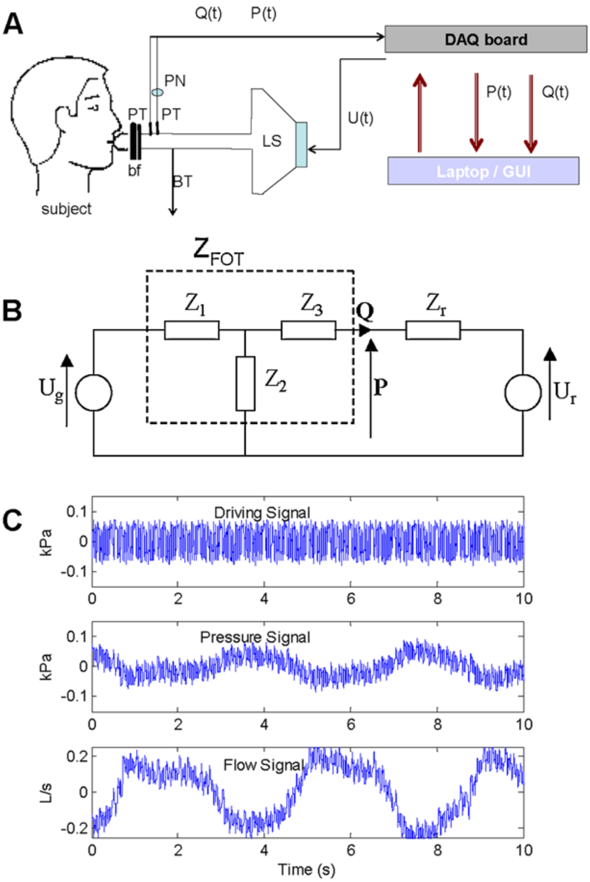

Fig. 3.1 A schematic overview (**A**) and an electrical analogy of the FOT setup (**B**). Typical measured signals (**C**) from one subject: oscillatory driving air flow; air pressure and air flow. The breathing of the patient (low frequency) can be observed superimposed on the multisine signals. Symbols: *LS* loudspeaker; *PT* pressure transducer; *PN* pneumotachograph; *BT* bias tube; *bf* biological filter; $U(t)$ generated pressure oscillations (4–48 Hz); $P(t)$ measured pressure oscillations; $Q(t)$ measured flow; pressure unit conversion: 1 kPa = 10 cmH$_2$O. See text for further symbol explanation

4–250 Hz. However, in this book we will see applications of FOT over three different frequency intervals: the low frequency range, from 0.01–5 Hz, mid-frequency range, from 4–50 Hz and high frequency range, from 7–250 Hz. Due to limitations implied by the loudspeaker, we have used two prototypes for the low frequency range, described later in the book. These prototypes kept the same principle of superimposing oscillations on the tidal breathing of the patient, so they used the same FOT lung function test.

The commercially available I2M (Input Impedance Measurement) device produced by Chess Medical Technologies, The Netherlands (2000) was used for pulmonary testing. The specifications of the device are: 11 kg, 0.50 × 0.50 × 0.60 m, 8 s measurement time, European Directive 93/42 on Medical devices and safety standards EN60601-1. Because the standard measurement time (8 seconds) is too short, a second measurement line has been connected to a data acquisition card and the signals recorded for 30–40 seconds, in order to provide better estimates. The subject is connected to the typical setup as in Fig. 3.1 via a mouthpiece, suitably designed to avoid flow leakage at the mouth and dental resistance artifact.

In the commercial device, the oscillation pressure is generated by a loudspeaker (LS) connected to a chamber [112, 116, 141, 158]. The LS is driven by a power amplifier fed with the oscillating signal generated by a computer (U_g). The movement of the LS cone generates a pressure oscillation inside the chamber, which is applied to the patient's respiratory system by means of a tube connecting the LS chamber and the bacterial filter (bf). A side opening of the main tubing (BT) allows the patient to have fresh air circulation. This pipeline has high impedance at the frequencies above 5 Hz to avoid the loss of power from the LS pressure chamber.

It has been shown that in some patients, using a nose clip causes the first anti-resonance peak in respiratory impedance to be distorted, resulting also in splitting of the anti-resonance peak into two smaller peaks [154, 155]. This is mainly because the use of a nose clip frequently results in velum opening and biased anti-resonance parameters. During the measurements performed for this study, the patient wears a nose clip and keeps the cheeks firmly supported to counteract this influence. Before starting the measurements, the frequency response of the transducers (PT) and of the pneumotachograph (PN) are calibrated. The measurements of air pressure, P, and air flow, $Q = dV/dt$ (with V the air volume), during the FOT lung function test is done at the mouth of the patient. The FOT lung function tests were performed according to the recommendations described in [116, 159]. The FOT excitation signal was kept within a range of a peak-to-peak size of 0.1–0.3 kPa, in order to ensure optimality, patient comfort, and linearity. Averaged measurements from three technically acceptable tests (i.e. no artifacts and coherence values above 0.8) were taken into consideration for each subject, with typical time records depicted in Fig. 3.1-C. The time records were sampled at a sampling time of 1 ms. All patients were tested in the sitting position, with cheeks firmly supported and elbows resting on the table. The posture is important in estimating values for respiratory impedance and, therefore a straight back was as much as possible applied (some patients who were too tall for the adjusted maximum height of the device, were excluded from the database). Each and every group of patients and volunteers has been tested in its unique location, using the same FOT device, and under the supervision of the same FOT team.

3.2 Frequency Response of the Respiratory Tissue and Airways

The global experimental setup from Fig. 3.1-A can be modeled by the electrical analogy from Fig. 3.1-B, where U_g denotes the generator test signal (known); U_r denotes the effect of spontaneous breathing (unknown); Z_r denotes the total respiratory impedance (to be estimated); Z_1 denotes the impedance (unknown) describing the transformation of driving voltage (U_g) to chamber pressure; Z_2 denotes the impedance (unknown) of both bias tubes and loudspeaker chamber; Z_3 denotes the impedance (unknown) of tube segment between bias tube and mouth piece (effect of pneumotachograph essentially).

Using the basic laws for analyzing electrical networks, the following relationships can be derived:

$$P = \frac{(Z_m - Z_3)Z_r}{(Z_m + Z_r)Z_1} \cdot U_g + \frac{Z_m}{Z_m + Z_r} \cdot U_r \tag{3.1}$$

$$Q = \frac{(Z_m - Z_3)}{(Z_m + Z_r)Z_1} \cdot U_g - \frac{1}{Z_m + Z_r} \cdot U_r \tag{3.2}$$

with $Z_m = Z_3 + \frac{Z_1 \cdot Z_2}{Z_1 + Z_2}$.

This can be written as a system

$$\begin{bmatrix} P(s) \\ Q(s) \end{bmatrix} = H(s) \cdot \begin{bmatrix} U_g(s) \\ U_r(s) \end{bmatrix} \tag{3.3}$$

with two *inputs* U_g and U_r, two *outputs* P and Q and transfer matrix:

$$H = \begin{bmatrix} \frac{(Z_m - Z_3)Z_r}{(Z_m + Z_r)Z_1} & \frac{Z_m}{Z_m + Z_r} \\ \frac{(Z_m - Z_3)}{(Z_m + Z_r)Z_1} & \frac{-1}{Z_m + Z_r} \end{bmatrix} \tag{3.4}$$

(all impedances in Z being also a function of s, the Laplace operator). Define now the vectors:

$$S_{YU} = \begin{bmatrix} S_{PU_g} \\ S_{QU_g} \end{bmatrix} \quad \text{and} \quad S_{UU} = \begin{bmatrix} S_{U_gU_g} \\ S_{U_rU_g} \end{bmatrix} \tag{3.5}$$

containing cross-power spectra $S_{YU}(j\omega)$ between two signals $y(t)$ and $u(t)$ and auto-power spectra $S_{UU}(\omega)$ of a signal $u(t)$. From well-known identification and signal-processing theory it then follows that [136]

$$S_{YU}(j\omega) = H(j\omega) S_{UU}(j\omega) \tag{3.6}$$

In the case of *absence of breathing* ($U_r = 0$) (3.6) reduces to

$$\begin{bmatrix} S_{PU_g} \\ S_{QU_g} \end{bmatrix} = \begin{bmatrix} \frac{(Z_m - Z_3)Z_r}{(Z_m + Z_r)Z_1} \\ \frac{(Z_m - Z_3)}{(Z_m + Z_r)Z_1} \end{bmatrix} \cdot S_{U_gU_g} \tag{3.7}$$

It follows that the respiratory impedance Z_r can be defined as their spectral (frequency domain) ratio relationship [24, 67]:

$$Z_r(j\omega) = \frac{S_{PU_g}(j\omega)}{S_{QU_g}(j\omega)} \tag{3.8}$$

where $\omega = 2\pi f$ is the angular frequency and $j = \sqrt{-1}$, the result being a complex variable.

However, it is supposed that the test is done under *normal breathing conditions*, which may result in an interference between the (unknown) breathing signal U_r and the test signal U_g, making the identification exercise more difficult. From the point of view of the forced oscillatory experiment, the signal components of respiratory origin (U_r) have to be regarded as pure noise for the identification task! Nevertheless, if the test signal U_g is designed to be uncorrelated with the normal respiratory breathing signal U_r, then $S_{U_rU_g} \cong 0$, and the approach (3.8) is still valid, based on (3.6) with $S_{U_rU_g} \cong 0$ [24, 67].

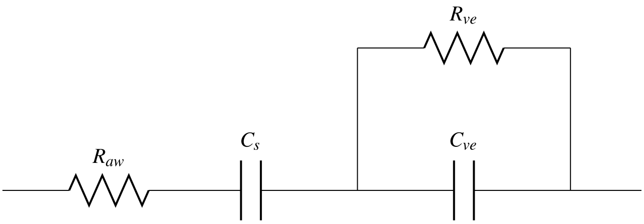

Fig. 3.2 Structure of the viscoelastic model from [111]. R_{aw} airway resistance; C_s static compliance; R_{ve} viscoelastic tissue resistance; C_{ve} viscoelastic tissue compliance

3.3 Lumped Models of the Respiratory Impedance

3.3.1 Selected Parametric Models from Literature

With the real (Re) and imaginary (Im) parts of the complex impedance from (3.8) at hand, parametric identification can be further employed to characterize the respiratory impedance. Unlike non-parametric modeling, parameterization has the advantage of providing concise values for the variables of interest. With the frequency-dependent impedance curves at hand, by means of identification algorithms [136], the non-parametric data may be correlated with the models consisting of electrical components that are analogous to the resistances, compliances, and inertances inherent in the respiratory system [116]. For this study, we selected several reported models closely related to the physiology of human lungs. If not mentioned explicitly, the units of model parameters are given for resistance in $cmH_2O/(l/s)$; for inertance in $cmH_2O/(l/s^2)$ and for compliance in l/cmH_2O.

One of the first models reported in the literature and also the simplest is based on analogy of the respiratory system as a tube denoting the central airways and a balloon accounting for the inspiration and expiration changes in volume of the lungs. This pipe–balloon analogy can be described as a RLC series electrical circuit [32]. In his initial attempts to characterize input impedance with a series RLC model structure, DuBois observed that over the 1–15 Hz frequency range, the inertance is a factor which must be negligible at ordinary breathing frequencies ($\approx 0.0004\ cmH_2O/(l/s^2)$), but that inertia and compressibility of alveolar air become factors of increasing importance as the test frequency is increased. He also found rather high values for the airway resistance ($3.8\ cmH_2O/(l/s)$) in the 2–10 Hz frequency range. He concluded that the mechano-acoustical (equivalent) system must be more complex in order to be able to capture the true properties of chest and lungs. This simple model is unable to represent the frequency-dependent real part of the complex impedance (resistance) found later by other authors and therefore it has not been included in the consequent discussions.

To characterize the respiratory mechanical properties at low frequencies, Navajas proposed the model from Fig. 3.2, including a linear viscoelastic component for the tissues [111], with R_{aw} airway resistance; C_s static compliance; R_{ve} viscoelastic

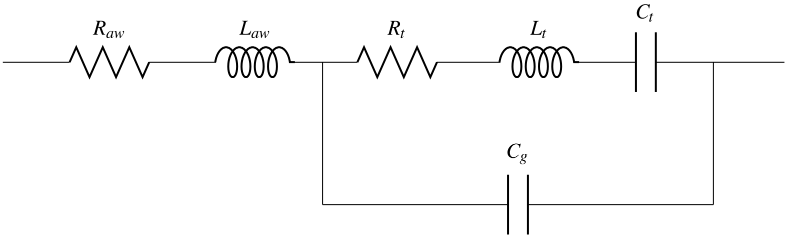

Fig. 3.3 Structure of the "DuBois" model from [32]. R_{aw} airway resistance; L_{aw} airway inertance; R_t tissue resistance; C_t tissue compliance; L_t tissue inertance; C_g gas compression compliance

tissue resistance; C_{ve} viscoelastic tissue compliance. They assessed the impedance in seven anesthetized paralyzed patients with no respiratory disease. The advantage of this scenario is that the influences from upper airway shunt and muscular activity are not significant and therefore do not bias the estimates. The R_{aw} is hypothesized to represent airways resistance plus a purely viscous component of tissue resistance, presumably in the chest wall. The C_s is the static compliance of the respiratory system. The R_{ve} and C_{ve} are related to viscoelastic properties of the tissue. However, there is virtually no inertance (air mass) quantified in this model, one may expect that this model will provide biased estimates at relative higher frequencies.

All patients exhibited a marked frequency dependence of effective respiratory resistance (real part of impedance) at low frequencies. The resistance fell sharply from 6.2 ± 2.1 $cmH_2O/(l/s)$ at 0.25 Hz to 2.3 ± 0.6 $cmH_2O/(l/s)$ at 2 Hz and decreased moderately with frequency, such that its value at 32 Hz was 1.5 ± 0.5 $cmH_2O(l/s)$. The imaginary part of the impedance was -22.2 ± 5.9 $cmH_2O/(l/s)$ at 0.25 Hz and increased with frequency, crossing zero line around 14 Hz and reached 2.3 ± 0.8 $cmH_2O/(l/s)$ at 32 Hz. They observed that the inertance becomes important as early as with 4 Hz, which rather contradicts DuBois [32, 93]. The strong negative dependence in the vicinity of spontaneous breathing frequencies in the real part of impedance in anesthetized patients agreed with studies in awaken subjects. The authors agree that this dependence at low frequencies can hardly be attributed to regional inhomogeneities of tissues. They suggest that the mechanical behavior of the respiratory system at spontaneous breathing frequencies is largely determined by intrinsic features of tissues, such as plasto-elastic properties. They also report an average value of ≈ 9 $cmH_2O/(l/s)$ for total resistance, mainly influenced by tissue properties at very low frequencies. The authors suggest that a nonlinear plastic model should be considered to account for the mechanical behavior of the respiratory system.

A relatively good model structure, dividing the airway tissue and alveolar properties into different compartments, is the one proposed by DuBois and schematically depicted in Fig. 3.3 [32]. This model has the following elements: R_{aw}, airway resistance; L_{aw}, airway inertance; R_t, tissue resistance; C_t, tissue compliance; L_t, tissue inertance; C_g, gas compression compliance.

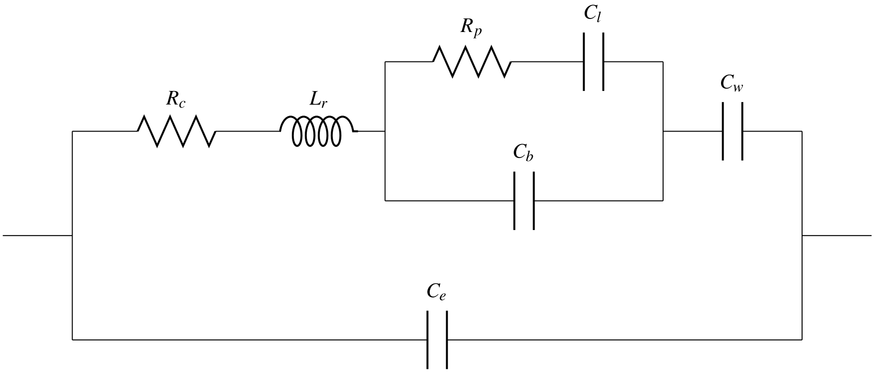

Fig. 3.4 Structure of the "Mead" model from [102]. R_c central resistance, L_r the total inertance, R_p peripheral resistance, C_l lung compliance, C_b bronchial tube compliance, C_w wall compliance, and C_e extrathoracic compliance

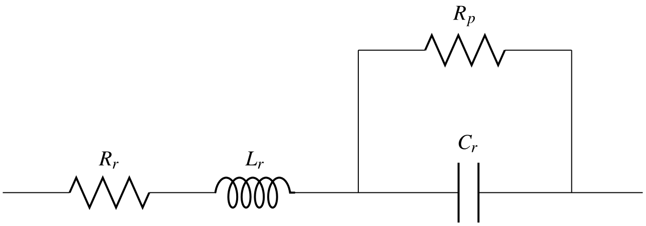

Fig. 3.5 Structure of the 'extended' model from [29]. R_r airway and lung resistance; R_p peripheral resistance; L_r lung inertance; C_r alveolar compliance

Mechanical properties in lung and chest wall are described by the model developed originally by Mead and described later in [9, 158]. Mead's model is an extended one-compartment model that does not allow the simulation of uneven alveolar ventilation (Fig. 3.4). In this model, R_c is the central resistance, L_r the total inertance, R_p peripheral resistance, C_l lung compliance, C_b bronchial tube compliance, C_w wall compliance, and C_e extrathoracic compliance.

The Mead model [102] from Fig. 3.4 allows the simulation of different influences on the respiratory mechanics (e.g. extrathoracic compliance by the mouth and the face mask, properties of the chest wall, air leaks around face mask or endotracheal tubes). The model is used to investigate different causes of airway obstructions and to assess the influence of the equipment on measurements.

Recently, an *extended RLC* model was proposed in [29], which can be viewed either as a simplification of the DuBois's or Mead's model, either an improvement of the simple series RLC circuit. The model allows characterization of small airways resistance. For the *extended RLC* model from Fig. 3.5 we have R_r, airway and lung resistance; R_p, peripheral resistance; L_r, lung inertance; C_r, alveolar compliance. This model provides a theoretical support for the observations made in experimental

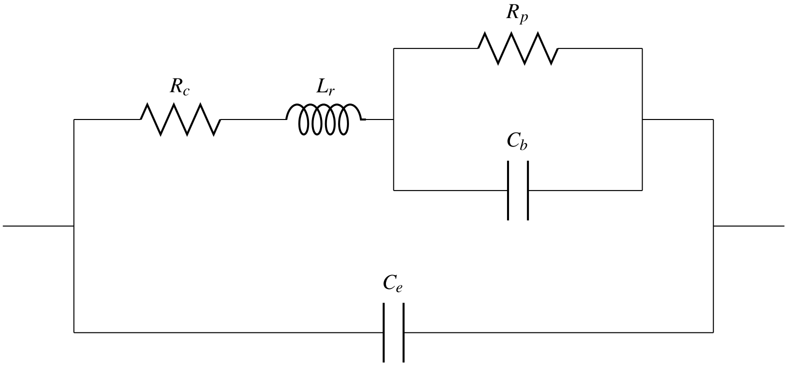

Fig. 3.6 Structure of the ‘RLCES’ proposed model [69]. R_c the central resistance, L_r the total inertance, R_p the peripheral resistance, C_b the bronchial tube compliance, and C_e the extrathoracic compliance

studies upon the frequency dependence of respiratory resistance at low frequencies. The added peripheral resistance R_p allows for the frequency dependence observed of the typical real impedance data, which is beyond the RLC series model’s capability. The physical justification for adding this additional component is that it models the resistance presented by the respiratory system’s small airways.

Finally, another lumped parametric model proposed recently in the literature is based on the observations from [29] on the influence of the upper airway shunt: RLCES (**RLC E**xtended with **S**hunt). In Mead’s model, the influence of upper airway shunt is taken into account by the extrathoracic compliance C_e. The proposed model is then an extension from the Extended RLC proposed in [29] combined with the extrathoracic compliance from Mead [102]. The corresponding electrical scheme of the RLCES model is given in Fig. 3.6. This model is a simplification of Mead model, with similar variables: R_c, the central resistance, L_r, the total inertance, R_p, the peripheral resistance, C_b, the bronchial tube compliance, and C_e, the extrathoracic compliance [69].

Hitherto, integer-order parametric models for characterizing the respiratory input impedance have been broadly developed and tested in various lung pathologies. Although they succeed to characterize in a clinically useful manner the mechanical properties of the lungs, there is a major drawback: accuracy increases with the model order and so does numerical complexity. The impedance varies significantly with frequency, requiring high order dynamical models. This problem has been tackled by introducing the concept of fractional calculus from mathematics, leading to FO models.

Some of the proposed FO models in the literature are

$$Z_r(s) = \frac{P(s)}{Q(s)} = R_r + L_r s + \frac{1}{C_r s^{\beta_r}} \tag{3.9}$$

Table 3.1 Biometric and spirometric parameters of the investigated (male) subjects. Values are presented as mean ± SD; % pred: predicted according to the asymptomatic males of the present study; VC: vital capacity; FEV1: forced expiratory volume in 1 s

	Healthy (7)	Asthma (5)	COPD (14)
Age (yrs)	55 ± 3	65 ± 2	51 ± 6
Height (m)	1.74 ± 0.15	1.62 ± 0.12	1.73 ± 0.14
Weight (kg)	82 ± 4	78 ± 5	71 ± 5
VC % pred	100 ± 3	80 ± 8	89 ± 7
FEV1 % pred	100 ± 4	53 ± 7	44 ± 6

and

$$Z_r(s) = \frac{P(s)}{Q(s)} = R_r + L_r s^{\alpha_r} + \frac{1}{C_r s^{\beta_r}} \tag{3.10}$$

with P pressure in cmH$_2$O; Q flow in l/s; Z_r the impedance in cmH$_2$O/(l/s); R_r airway resistance in cmH$_2$O/(l/s), L_r inductance in cmH$_2$O/(l/s^2); C_r capacitance in l/cmH$_2$O; $0 \leq \alpha_r \leq 1$ and $0 \leq \beta_r \leq 1$ fractional orders and s the Laplace operator. Using the definition of complex numbers, (3.10) becomes

$$\begin{aligned} Z_r(j\omega) &= R_r + L_r\omega^{\alpha_r}\cos\left(\frac{\alpha_r\pi}{2}\right) + \frac{1}{C_r\omega^{\beta_r}}\cos\left(\frac{\beta_r\pi}{2}\right) \\ &\quad + j\cdot\left[L_r\omega^{\alpha_r}\sin\left(\frac{\alpha_r\pi}{2}\right) - \frac{1}{C_r\omega^{\beta_r}}\sin\left(\frac{\beta_r\pi}{2}\right)\right] \end{aligned} \tag{3.11}$$

It is possible to see that, contrary to a RLC series system, the real part of the impedance in (3.11) will vary with frequency and comprises both inductance and compliance effects. Therefore, it allows to characterize both increase and decrease with frequency in the real part of impedance, without requiring a high integer-order system.

3.3.2 The Volunteers

In this chapter, we are dealing with subjects evaluated with the classical FOT non-invasive lung function test. There are three (averaged) data sets from groups of Caucasian healthy, asthmatic and COPD patients. Table 3.1 presents the corresponding biometric and spirometric details.

The choice of these representative cases is motivated by the general aim of the study: to evaluate the parametric models on the input impedance of these three sets of subjects. The physiological differences between these sets of subjects are clearly visible in the complex impedance values and we expect that the parametric models proposed in this section will be able to quantify their specific properties.

3.3.3 Identification Algorithm

For the purpose of this example, the model parameters were estimated using a nonlinear least squares optimization algorithm, making use of the `MatLab` function `lsqnonlin`. The optimization algorithm is a subspace trust region method and is based on the interior-reflective Newton method described in [21]. The large-scale method for `lsqnonlin` requires that the number of equations (i.e., the number of elements of cost function) is at least as great as the number of variables. Every iteration involves the approximate solution using the method of preconditioned conjugate gradients, for lower and upper bounds. In this application, the lower bounds were set to 0 (negative values are meaningless) and no upper bounds. The optimization stopped either when a high number of iterations reached 100 times the number of variables (i.e. 500), or a termination tolerance value of $10e^{-8}$. In all cases we obtained a correlation coefficient between data and model estimates above 80 %.

Along with the corresponding model estimates, the error on the real and imaginary part respectively and the total error between the real patient impedance and the model estimated impedance are calculated according to the formula:

$$\begin{aligned} E_R &= \frac{1}{N_S}\sqrt{\sum_{1}^{N_S}(\mathrm{Re}-\hat{\mathrm{Re}})^2} \\ E_X &= \frac{1}{N_S}\sqrt{\sum_{1}^{N_S}(\mathrm{Im}-\hat{\mathrm{Im}})^2} \\ E_T &= \sqrt{E_R^2+E_X^2} \end{aligned} \tag{3.12}$$

with Re denoting the real part of the impedance, Im denoting the imaginary part of the impedance, and N_S the total number of excited frequency points.

3.3.4 Results and Discussion

We apply the input impedance identification methods described initially in [24] and revisited in [67, 69] on the data measurements from FOT. By using (3.8), we obtain complex input impedances for each group from Table 3.1 from 4–48 Hz frequency range.

The reported values are given for resistance in $cmH_2O/(l/s)$; for inertance in $cmH_2O/(l/s^2)$ and for compliance in l/cmH_2O. The corresponding averaged values for each model parameter and their standard deviations are reported. The results were tested using the one way analysis of variance (in Matlab, `anova1`). All reported values were statistically significant ($p < 0.001$, where p is the probability of obtaining a result at least as extreme as the one that was actually observed, assuming that the null hypothesis is true).

Fig. 3.7 The performance of the RLCES model (*star line*), the CP4 model (*dashed line*) and the CP5 model (*dotted line*), against measured data (*continuous line*) in healthy subjects

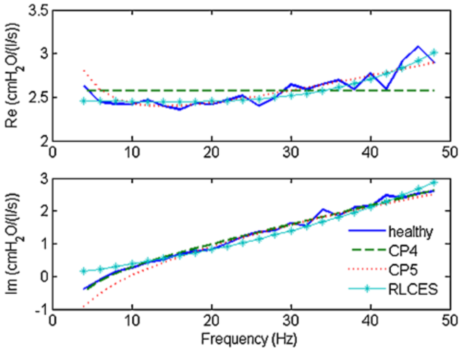

Fig. 3.8 The performance of the RLCES model (*star line*), the CP4 model (*dashed line*) and the CP5 model (*dotted line*), against measured data (*continuous line*) in asthmatic patients

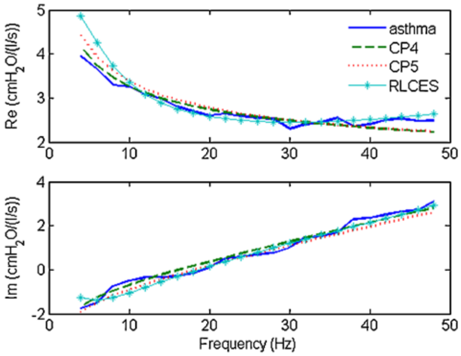

The error values calculated with (3.12) for each case are also reported, in terms of their averaged values and a standard deviation $>5\ \%$. For those model parameters for which no standard deviation is reported, the standard deviation varied with $<5\ \%$.

In the remainder of this chapter, CP4 and CP5 will denote the constant-phase model in four parameters from (3.9), respectively, the constant-phase model in five parameters from (3.10).

The performance of the models from (3.9), (3.10) and RLCES on the impedance complex data is depicted in Figs. 3.7, 3.8 and 3.9. It can be observed that these models characterize sufficiently well the frequency-dependent behavior of the impedance. It is also clear that the FO model in four parameters from the literature, given by (3.9), is unable to capture the real part of impedance, which is increasing with frequency. This model is then only valid in the low frequency range where the real part of the impedance is decreasing as frequency is increasing.

As observed from the results given in Tables 3.2, 3.3, 3.4, 3.5, 3.6, 3.7 and 3.8, the viscoelastic model has the poorest performance in terms of total error, explained by the absence of inductance in the model structure. Within the integer-order models, Mead's model has the least total error results in all subject groups. Notice that Extended RLC is a (simplified) special case of Mead's model, and therefore it will never provide better results. For the case of a healthy subject, peripheral resistance

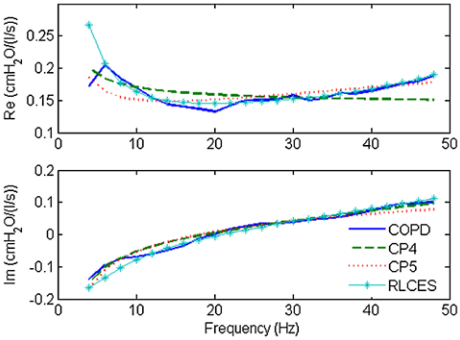

Fig. 3.9 The performance of the RLCES model (*star line*), the CP4 model (*dashed line*) and the CP5 model (*dotted line*), against measured data (*continuous line*) in COPD patients

Table 3.2 Identified values for the *viscoelastic model* parameters and modeling errors. Ref. Fig. 3.2

	R_{aw}	C_s	R_{ve}	C_{ve}	E_R	E_X	E_T
Healthy	2.458±0.83	1.477e+9	0.117±0.012	2.04e−13	0.185	1.551	1.562
Asthma	1.925±0.61	0.291±0.04	0.817±0.23	6.37e−12	0.423	1.580	1.636
COPD	0.160±0.03	0.390±0.07	4.892e−4	1.43e−11	0.017	1.636	1.636

is very high (910.5778 cmH_2O/(l/s)). As reported in [29], in trying to minimize the error by not having the real part of the impedance decrease too rapidly (with respect to frequency), R_p will tend to have larger values. Diong et al. suggest that it is not entirely reliable to use any individual value of the model parameter to discriminate between pathologic and healthy cases. However, the authors point to the possibility of using two-parameter combinations for discriminating between healthy volunteers and diagnosed patients.

It is also worth noticing that the estimated values of the RLCES model parameters are close to the ones estimated in the Mead model, leading to the conclusion that the absence of wall compliance does not affect significantly the total impedance of the human respiratory system.

Generally, the values for the model parameters in the three subject groups were significantly different, allowing a separation (necessary for screening or for diagnosis). The airway resistance in models Viscoelastic, DuBois, and RLCES were fairly close to each other, indicating good correlation between the various models for this specific parameter. The same is valid for the central resistance values in models Mead and CP5.

As referring to the specific values in each case (healthy, asthma, and COPD), the resistance indicated correctly the possible variations with pathology. As expected, the viscoelastic resistance R_{ve} in Viscoelastic was significantly lower in COPD than in Healthy and Asthma groups. The peripheral resistance R_p in models Mead, Extended and RLCES had similar order of magnitude in each group, but their values did not correlate. Since the highest values are reported by the Extended model, which also has the least number of parameters of the above mentioned three model

Table 3.3 Identified values for the *DuBois model* parameters and modeling errors. Ref. Fig. 3.3

	R_{aw}	L_{aw}	R_t	C_t	L_t	C_g	E_R	E_X	E_T
Healthy	2.573±0.58	0.009±0.001	1.247±0.21	0.00064	0.019±0.008	0.033±0.012	0.183	0.121	0.219
Asthma	2.181±0.51	0.011±0.03	3.413±0.45	0.014±0.004	0.00063	0.004±0.0007	0.107	0.232	0.255
COPD	0.199±0.06	3.4e−4	0.55±0.08	0.267±0.075	0.007±0.001	0.087±0.009	0.028	0.015	0.032

Table 3.4 Identified values for the *Mead model* parameters and modeling errors. Ref. Fig. 3.4

	R_c	L_r	R_p	C_l	C_b	C_w	C_e	E_R	E_X	E_T
Healthy	2.37±0.08	0.009±0.001	0.21±0.095	13.16±2.64	0.13±0.013	0.05±0.006	1.2e−4	0.087	0.115	0.145
Asthma	1.85±0.64	0.012±0.001	2.12±0.086	21.71±1.87	0.004±0.001	0.02±0.003	1.0e−4	0.095	0.203	0.225
COPD	0.13±0.02	5e−5	0.11±0.013	1.86±0.5	0.17±0.01	0.31±0.02	4.3e−3	0.010	0.009	0.013

Table 3.5 Identified values for the *Extended RLC model* parameters and modeling errors. Ref. Fig. 3.5

	R_r	R_p	L_r	C_r	E_R	E_X	E_T
Healthy	2.57±0.04	910.57±50	0.009±0.001	0.034±0.006	0.185	0.092	0.207
Asthma	2.35±0.01	4.02±0.3	0.010±0.003	0.007±0.0005	0.114	0.247	0.272
COPD	0.19±0.02	0.68±0.07	3.77e−4	0.073±0.004	0.029	0.012	0.032

Table 3.6 Identified values for the *RLCES model* parameters and modeling errors. Ref. Fig. 3.6

	R_c	L_r	R_p	C_b	C_e	E_R	E_X	E_T
Healthy	1.78±0.09	0.01±0.002	0.77±0.08	0.0077±0.001	2.50e−4	0.091	0.197	0.217
Asthma	2.11±0.46	0.011±0.003	3.52±0.22	0.0059±0.001	9.42e−5	0.127	0.241	0.273
COPD	0.13±0.017	4.77e−4	0.34±0.012	0.1382±0.01	0.0044±0.0003	0.011	0.010	0.014

Table 3.7 Identified values for the CP4 model and its modeling errors. Ref. (3.9)

	R_r	L_r	C_r	β	E_R	E_X	E_T
Healthy	2.5757	0.0089±0.0002	0.0577±0.005	1	0.1817	0.0902	0.2028
Asthma	0.6588±0.001	0.012±0.005	0.0872±0.008	0.3248±0.005	0.1345	0.2077	0.2474
COPD	0.1427	0.0004±0.0001	0.59±0.06	0.7818±0.02	0.0175	0.0102	0.0202

Table 3.8 Identified values for the CP5 model and its modeling errors. Ref. (3.10)

	R_r	L_r	C_r	α	β	E_R	E_X	E_T
Healthy	2.33e−14	0.088±0.0012	0.109±0.05	0.654±0.002	0.36±0.001	0.081	0.116	0.142
Asthma	0.0077±0.001	0.014±0.005	0.077±0.08	0.976±0.015	0.30±0.005	0.124	0.226	0.258
COPD	2.22e−14	0.006±0.0004	0.557±0.04	0.591±0.003	0.546±0.004	0.012	0.008	0.015

structures, we may suspect that this is due to the lumped characterization in model Extended as opposed to Mead or RLCES, where part of this resistance's effects are transmitted to other model parameters.

In DuBois, tissue compliance correlated well with physiologically expected values and pathology. Bronchial compliance C_b correlated well between models Mead and RLCES for asthma and COPD cases, but not in healthy subjects. We suspect this may be due to inaccurate partitioning of wall and lung compliance. Nevertheless, the values for C_b in asthma are very close to the reported values by Van Noord, where $C_b = 0.005$ l/cmH$_2$O and although the values for C_e are somewhat lower than expected, they are similar to what other authors report [29, 39, 93]. Airway inertance correlated well between model structures DuBois, Mead, Extended, RLCES, as well as in relation to expected pathology.

From the point of view of reported total errors, we may add that for all subject groups the best performance was given by Mead's model and highest errors for viscoelastic model. We may conclude that Mead's model is still the structure with least errors in parametric estimations. However, the newly proposed integer-order model RLCES gives similar total errors with less number of model parameters. This is indeed an advantage when a specific characterization is not intended, but merely a clear-cut within subject population for preliminary diagnosis. It is clear that if more specific information is required, the Mead model must be employed. Nonetheless, the model structure in Mead may not necessarily be optimal, for it over-estimates lung compliance (in healthy and asthmatic).

It is also noticeable that the total errors given by the CP5 model are comparable to the ones given by the Mead model. The main advantage of the CP5 model structure over the Mead model structure is its reduced number of parameters to be identified. The reason for giving such good estimations is that the fractional order captures in a more accurate and flexible way the frequency dependence of the complex impedance. It also seems that the model from (3.10) gives most accurate estimates for the COPD case. For healthy persons, the airway resistance is very low. The reason for such low values is that part of dissipation properties are captured by the fractional orders [118]. This observation suggests eliminating the term R_r from (3.10), but this issue will be revisited later in this book.

3.4 Summary

This chapter introduced the basic principles of estimating the respiratory impedance from measurements performed with the forced oscillation lung function test. The non-parametric identification of the respiratory impedance has been derived and presented by means of spectral analysis. Next, a comparison of most representative parametric models from literature for assessing respiratory input impedance shows that FO models are more efficient than integer-order models in capturing frequency-dependent impedance values variations. This motivates the development of the next chapters, where theoretical models will be derived and it is shown that convergence of these models for many airways will lead to the appearance of FO terms in the lumped model structure.

Chapter 4
Modeling the Respiratory Tract by Means of Electrical Analogy

4.1 Modeling Based on a Simplified Morphology and Structure

Since the fractal geometry is characterized by recurrent geometry, the respiratory system is an ideal application. Lung geometry and morphology have been studied using CT scans in 3D form [135]. Already since the work of Weibel, the fractal geometry present in the lung morphology has been employed in studies on airway aerodynamics [163]. The self-similarity is related to the optimality of ventilation and asymmetry exists in the healthy lung as well. By contrast, a diseased lung parenchyma contains significant heterogeneities and the optimality conditions are no more fulfilled [66].

One of the most comprehensive and earliest overviews on the mechanical properties of lungs is given by Mead, describing the initial attempts to quantify static and dynamic resistive, inertial and compliant properties of lungs. His review covers both the inspiratory and the expiratory phase, at laminar and turbulent flow conditions, in terms of a single variable: air volume. Another important study has been reported in [114] for tube-entrance flow and pressure drop during inspiration in spontaneous ventilation. While breathing at rest, the airflow remains laminar [66, 114, 120]. A decade later, Franken developed a model for oscillating flow of a viscous and compressible fluid in a rigid tube [41]. It is one of the first applications of dynamic models to the conditions of the forced oscillations technique as applied for lung function testing. They modified the standard measurement device for pressure and flow at the mouth of the patient replacing it with a 2 m rigid tube and based on the tube model, the flow was estimated (thus the pneumotachograph is replaced by this 2 m rigid tube). They included a one dimensional model of the propagating waves and the true thermal properties of the tube wall and found that quantitative differences between models with and without thermal variations are negligible.

Technological and computational progress allowed to perform studies of CT scans from the 3D topology and morphology of a human (cast) lung [135]. Mean gravity and branching angles up to level 9 bifurcations for the right and the left lobe (asymmetric morphology due to heart location) were also reported, allowing

C.M. Ionescu, *The Human Respiratory System*, Series in BioEngineering,
DOI 10.1007/978-1-4471-5388-7_4, © Springer-Verlag London 2013

detailed simulations in flow analysis studies. Such a detailed analysis, however, involves complex numerical computations and the effort may be justified only by the need for aerosol deposition models, etc. This is obviously out of the scope of this book.

From the zoo of literature reports on pulmonary function, one may distinguish two mainstreams:

- a symmetrical structure of the lung [163, 164] and
- an asymmetrical [54, 65] representation of the airways in the respiratory tree.

In this book, a symmetric flow bifurcation pattern is assumed in order to derive the pressure–flow relationship in the airways. However, both symmetric and asymmetric airway networks will be discussed in the next chapter, by means of their electrical analogues.

Womersley theory has been previously applied to circulatory system analysis, considering the pulsatile flow in a circular pipeline for sinusoidally varying pressure-gradients [168]. Taking into account that the breathing is periodic with a certain period (usually, for normal breathing conditions, around 4 seconds), we address the airway dynamics problem making use of this theory. Usually, when sinusoidal excitations are applied to the respiratory system [69, 116], they contain ten times higher frequencies than the breathing, which permits analyzing oscillatory flow. To find an electrical equivalent of the respiratory duct, one needs expressions relating pressure and flow with properties of the elastic tubes, which can be done straightforward via Womersley theory [3, 115, 139].

The periodic breathing can be analyzed in terms of periodical functions, such as the pressure gradient: $-\frac{\partial p}{\partial z} = M_P \cos(\omega t - \Phi_P)$, where z is the axial coordinate, $\omega = 2\pi f$ is the angular frequency (rad/s), with f the frequency (Hz), M_P the modulus and Φ_P is the phase angle of the pressure gradient. Given its periodicity, it follows that also the pressure and the velocity components will be periodic, with the same angular frequency ω. The purpose is to determine the velocity in radial direction $u(r, z, t)$ with r the radial coordinate, the velocity in the axial direction $w(r, z, t)$, the pressure $p(r, z, t)$ and to calculate them using the morphological values of the lungs. In this study, we shall make use of the Womersley parameter from the Womersley theory developed for the circulatory system, with appropriate model parameters for the respiratory system, defined as the dimensionless parameter $\delta = R\sqrt{\frac{\omega\rho}{\mu}}$ [139, 168], with R the airway radius. The air in the airways is treated as Newtonian, with constant viscosity $\mu = 1.8 \times 10^{-5}$ kg/m s and density $\rho = 1.075$ kg/m^3, and the derivation from the Navier–Stokes equations is done in cylinder coordinates [165]:

$$\begin{aligned}
&\rho\left(\frac{\partial u}{\partial t} + u\frac{\partial u}{\partial r} + \frac{v}{r}\frac{\partial u}{\partial \theta} + w\frac{\partial u}{\partial z} - \frac{v^2}{r}\right) \\
&\quad = -\frac{\partial p}{\partial r} + \rho F_r + \mu\left[\frac{1}{r}\frac{\partial}{\partial r}\left(r\frac{\partial u}{\partial r}\right) - \frac{u}{r^2} + \frac{1}{r^2}\frac{\partial^2 u}{\partial \theta^2} - \frac{2}{r^2}\frac{\partial v}{\partial \theta} + \frac{\partial^2 u}{\partial z^2}\right] \qquad (4.1)
\end{aligned}$$

for the radial direction r, and

$$\rho\left(\frac{\partial v}{\partial t}+u\frac{\partial v}{\partial r}+\frac{v}{r}\frac{\partial v}{\partial \theta}+w\frac{\partial v}{\partial z}+\frac{uv}{r}\right)$$
$$=-\frac{1}{r}\frac{\partial p}{\partial \theta}+\rho F_\theta+\mu\left[\frac{1}{r}\frac{\partial}{\partial r}\left(r\frac{\partial v}{\partial r}\right)-\frac{v}{r^2}+\frac{1}{r^2}\frac{\partial^2 v}{\partial \theta^2}-\frac{2}{r^2}\frac{\partial u}{\partial \theta}+\frac{\partial^2 v}{\partial z^2}\right] \tag{4.2}$$

for the contour θ, and

$$\rho\left(\frac{\partial w}{\partial t}+u\frac{\partial w}{\partial r}+\frac{v}{r}\frac{\partial w}{\partial \theta}+w\frac{\partial w}{\partial z}\right)$$
$$=-\frac{\partial p}{\partial z}+\rho F_z+\mu\left[\frac{1}{r}\frac{\partial}{\partial r}\left(r\frac{\partial w}{\partial r}\right)+\frac{1}{r^2}\frac{\partial^2 w}{\partial \theta^2}+\frac{\partial^2 w}{\partial z^2}\right] \tag{4.3}$$

in the axial direction z. If we have the simplest form of axi-symmetrical flow in a cylindrical pipeline, the Navier–Stokes equations simplify by $\frac{\partial}{\partial\theta}=\frac{\partial^2}{\partial\theta^2}=0$ and with the contour velocity $v=0$; it follows that (4.2) can be omitted. Let us consider no external forces F_r, F_z. Since we have very low total pressure drop variations, i.e. $\approx$0.1 kPa [114], we can divide by density parameter ρ. Next, we introduce the dimensionless parameter $y=r/R$, with $0\le y\le 1$ in the relation $\frac{d}{dy}=\frac{d}{dr}\frac{dr}{dy}=R\frac{d}{dr}$, and $\frac{d}{dr}=\frac{1}{R}\frac{d}{dy}$. The simplifying assumptions are applied: (i) the radial velocity component is small, as well as the ratio u/R and the term in the radial direction; (ii) the terms $\frac{\partial^2}{\partial z^2}$ in the axial direction are negligible, leading to the following system:

$$\frac{\partial u}{\partial t}=-\frac{1}{\rho R}\frac{\partial p}{\partial y}+\frac{\mu}{\rho}\left[\frac{1}{yR^2}\frac{\partial u}{\partial y}+\frac{1}{R^2}\frac{\partial^2 u}{\partial y^2}-\frac{u}{R^2y^2}\right] \tag{4.4}$$

$$\frac{\partial w}{\partial t}=-\frac{1}{\rho}\frac{\partial p}{\partial z}+\frac{\mu}{\rho}\left[\frac{1}{yR^2}\frac{\partial w}{\partial y}+\frac{1}{R^2}\frac{\partial^2 w}{\partial y^2}\right] \tag{4.5}$$

$$\frac{u}{Ry}+\frac{1}{R}\frac{\partial u}{\partial y}+\frac{\partial w}{\partial z}=0 \tag{4.6}$$

Studies on the respiratory system using similar simplifying assumptions can be found in [41, 114, 120]. Given that the pressure gradient is periodic, it follows that also that the pressure $p(y,z,t)$ and the other velocity components $u(y,z,t)$, $w(y,z,t)$ are periodic, as in

$$\begin{aligned} p(y,z,t)&=A_P(y)e^{j\omega(t-z/\tilde{c})}\\ u(y,z,t)&=A_U(y)e^{j\omega(t-z/\tilde{c})}\\ w(y,z,t)&=A_W(y)e^{j\omega(t-z/\tilde{c})} \end{aligned} \tag{4.7}$$

where $\tilde{c}$ denotes the complex velocity of wave propagation and $j = \sqrt{-1}$. Further simplifications lead to the following system of equations:

$$\begin{aligned} u &= \frac{j\omega R}{\mu \tilde{c}} \left\{ C_1 \frac{2}{\delta j^{3/2}} J_1\left(\delta j^{3/2} y\right) + \frac{A_P}{\rho \tilde{c}} y \right\} e^{j\omega\left(t - \frac{z}{\tilde{c}}\right)} \quad \text{or} \\ u &= C_1 \frac{j\omega R}{\delta j^{3/2} \tilde{c}} J_1\left(\delta j^{3/2} y\right) e^{j\omega\left(t - \frac{z}{\tilde{c}}\right)} + \frac{R}{2\rho \tilde{c}} M_P e^{j(\omega t - \Phi_P)} \end{aligned} \tag{4.8}$$

$$\begin{aligned} w &= \left\{ C_1 J_0\left(\delta j^{3/2} y\right) + \frac{A_P}{\rho \tilde{c}} \right\} e^{j\omega\left(t - \frac{z}{\tilde{c}}\right)} \quad \text{or} \\ w &= C_1 J_0\left(\delta j^{3/2} y\right) e^{j\omega\left(t - \frac{z}{\tilde{c}}\right)} + \frac{M_P}{\omega \rho} e^{j\left(\omega t - \Phi_P - \frac{\pi}{2}\right)} \end{aligned} \tag{4.9}$$

$$p(t) = A_P e^{j\omega\left(t - \frac{z}{\tilde{c}}\right)} \quad \text{or} \quad -\frac{dp}{dz} = M_P e^{j(\omega t - \Phi_P)} \tag{4.10}$$

with $C_1 = -\frac{A_P}{\rho \tilde{c}} \frac{1}{J_0(\delta j^{3/2})}$, A_P the amplitude of the pressure wave, J_0 the Bessel function of the first kind and zero degree, J_1 the Bessel function of the first kind and first degree [1], and where

$$-\frac{dp}{dz} = \frac{j\omega}{\tilde{c}} A_P e^{j\omega\left(t - \frac{z}{\tilde{c}}\right)} = M_P e^{j(\omega t - \Phi_P)} \tag{4.11}$$

such that

$$A_P e^{j\omega\left(t - \frac{z}{\tilde{c}}\right)} = \frac{\tilde{c}}{\omega} M_P e^{j(\omega t - \Phi_P - \pi/2)} \tag{4.12}$$

It is supposed that the movement of the (relatively short) elastic airway ducts is limited to the radial movement $\zeta(z,t)$ of the tube, being dependent only on the longitudinal coordinate and the time. This supposition is valid for short segments ($\ll$ wavelength of the pressure wave) in which the longitudinal movement is negligible compared to the radial. The wavelength corresponding to the tracheal tube is about 2.5 m long, much longer than the length of the tube itself; hence, the supposition is valid in our case. Although the inspiratory and expiratory movements of the airways involve both radial as well as longitudinal movement, we restrict our analysis to the radial elongation only. The Poisson coefficient is denoted by ν_P; it equals 0.45 [85]. The problem now contains four unknowns: $u(y,z,t)$, $w(y,z,t)$, $p(z,t)$, and $\zeta(z,t)$; therefore we need an extra equation in order to solve the system: the pipeline equation. The movement equation of the wall follows from the dynamical equilibrium of the forces applied on the wall, similar to the work reported in [115]. Denoting with ζ the elongation of the tube radius from R to $R + \zeta$, we have the dynamic equilibrium equation in the radial direction:

$$p(R + \zeta)\, d\theta\, dz + h \frac{E}{1 - \nu_P^2} \frac{\zeta}{R}\, d\theta\, dz = h \rho_{\text{wall}} (R + \zeta)\, d\theta\, dz \frac{d^2 \zeta}{dt^2} \tag{4.13}$$

where R is the initial (steady-state) radius, h is the thickness of the wall, E is the effective modulus of elasticity, ρ_{wall} is the effective density of the wall, and ν_P is the Poisson coefficient. The modulus of elasticity and the wall density have to take into account that the airways are a combination of soft tissue and cartilage, the percent of which varies with the airway levels.

In this model, the effective elastic modulus and wall density, respectively, are considered in function of the airway tissue structure:

$$\begin{aligned} E &= \kappa E_c + (1-\kappa) E_s \\ \rho_{\text{wall}} &= \kappa \rho_c + (1-\kappa)\rho_s \end{aligned} \tag{4.14}$$

taking into account at each level the fraction amount κ of corresponding cartilage tissue (index c) and soft tissue (index s) and with $E_c = 400$ kPa, $E_s = 60$ kPa, $\rho_c = 1140$ kg/m^3, $\rho_s = 1060$ kg/m^3. The values of the corresponding cartilage fraction are given in Table 2.1.

Assuming a negligible displacement ζ in comparison to R, one can simplify (4.13) with all terms in ζ/R. Dividing by $R\,dz\,d\theta$, leads to the simplified equation of motion for the elastic airway wall:

$$p + \frac{Eh}{1-\nu_P^2}\frac{\zeta}{R^2} = \rho_{\text{wall}} h \frac{d^2\zeta}{dt^2} \tag{4.15}$$

The set of Eqs. (4.4)–(4.6) and (4.15) form a system of four equations with four unknown parameters.

For a *rigid pipeline* we have

$$\zeta = 2Re^{j\omega(t-\frac{z}{c})} \tag{4.16}$$

introducing this relation in (4.15) and using (4.10) we obtain

$$2R = \frac{A_P}{(\frac{E}{1-\nu_p^2}\frac{h}{R^2} - \rho_{\text{wall}} h\omega^2)} \tag{4.17}$$

such that the movement of the airway wall is given as a function of the pressure

$$\zeta = \frac{A_P}{(\frac{E}{1-\nu_p^2}\frac{h}{R^2} - \rho_{\text{wall}} h\omega^2)} \cdot e^{j\omega(t-\frac{z}{c})} \tag{4.18}$$

The equation for the axial velocity remains the same as in case of a rigid pipeline:

$$w(y) = \frac{M_P}{\omega\rho} M_0(y) e^{j(\omega t - \Phi_P - \pi/2 + \varepsilon_0(y))} \tag{4.19}$$

where

$$M_0(y)e^{j\varepsilon_0(y)} = 1 - \frac{(\delta j^{3/2} y)}{(\delta j^{3/2})} \tag{4.20}$$

Similarly, we define

$$\begin{aligned} M_1 e^{j\varepsilon_1} &= 1 - \frac{2J_1(\delta j^{3/2})}{(J_0(\delta j^{3/2})\delta j^{3/2})} \\ M_2(y) e^{j\varepsilon_2(y)} &= 1 - \frac{2J_1(\delta j^{3/2} y)}{(J_0(\delta j^{3/2})\delta j^{3/2})} \end{aligned} \tag{4.21}$$

denoting the modulus and phase of the Bessel functions of first kind J_i and ith order [1].

For an *elastic pipeline*, the *no-slip* condition is still valid ($w = 0$ for $y = \pm 1$), such that the radial velocity is

$$\begin{aligned} u(y) &= \frac{j\omega R}{2\rho\tilde{c}} \left\{ y - \frac{2J_1(\delta j^{3/2} y)}{J_0(\delta j^{3/2} y)\delta j^{3/2}} \right\} A_P e^{j\omega(t-\frac{z}{\tilde{c}})} \\ &= \frac{Ry}{2\rho\tilde{c}} \left\{ y - \frac{2J_1(\delta j^{3/2} y)}{J_0(\delta j^{3/2})\delta j^{3/2}} \right\} M_P e^{j(\omega t - \Phi_P)} \end{aligned} \tag{4.22}$$

and using (4.21), the equivalent form of (4.22) becomes

$$u(y) = \frac{R}{2\rho\tilde{c}} M_P M_2(y) e^{j(\omega t - \Phi_P + \varepsilon_2(y))} \tag{4.23}$$

The flow is given by

$$Q = \frac{\pi R^2 M_P}{\omega\rho} M_1 e^{j(\omega t - \Phi_P - \pi/2 + \varepsilon_1)} = \frac{\pi R^4 M_P}{\mu\delta^2} M_1 e^{j(\omega t - \Phi_P - \pi/2 + \varepsilon_1)} \tag{4.24}$$

The effective pressure wave has the general form of

$$p(z,t) = A_P e^{j(\omega(t-\frac{z}{\tilde{c}}) - \phi_P)}, \tag{4.25}$$

where ϕ_P can be a phase shift for $z = 0$ at $t = 0$. It follows that

$$-\frac{dp}{dz} = M_P e^{j(\omega t - \Phi_P)} = \frac{A_P\omega}{\tilde{c}} e^{j(\omega(t-\frac{z}{\tilde{c}}) - \phi_P + \pi/2)} \tag{4.26}$$

For $z = 0$, it follows that

$$M_P e^{j(\omega t - \Phi_P)} = \frac{A_P\omega}{\acute{c}_0\sqrt{M_1}} e^{j(\omega t - \phi_P + \pi/2 - \varepsilon_1/2)} \tag{4.27}$$

from which we have

$$M_P = \frac{A_P\omega}{\acute{c}_0\sqrt{M_1}} \tag{4.28}$$

and

$$\Phi_P = \phi_P - \pi/2 + \varepsilon_1/2 \tag{4.29}$$

The pressure gradient is related to the characteristics of the airway duct via the Moens–Korteweg relation for the wave velocity $\acute{c}_0$, with

$$\acute{c}_0 = \sqrt{\frac{Eh}{(2\rho R(1-\nu_P^2))}} \tag{4.30}$$

The model for wave propagation in function of the pressure p (kPa) for axial w (m/s) and radial u (m/s) velocities, for flow Q (l/s) and for the wall deformation ζ (%) at the axial distance $z = 0$ is given by the set of equations:

$$p(t) = A_P e^{j(\omega t - \phi_P)} \tag{4.31}$$

$$u(y,t) = \frac{RA_P\omega}{2\rho\acute{c}_0^2} \cdot \frac{M_2(y)}{M_1} \cos\left(\omega t - \varepsilon_1 - \phi_P + \varepsilon_2(y) + \frac{\pi}{2}\right) \tag{4.32}$$

$$w(y,t) = \frac{R^2 A_P\omega}{\acute{c}_0\mu\sqrt{M_1}} \cdot \frac{M_0(y)}{\delta^2} \sin\left(\omega t - \frac{\varepsilon_1}{2} - \phi_P + \varepsilon_0(y) + \frac{\pi}{2}\right) \tag{4.33}$$

$$Q(t) = \frac{\pi R^4}{\mu} \frac{A_P\omega}{\acute{c}_0\sqrt{M_1}} \frac{M_1}{\delta^2} \sin\left(\omega t + \frac{\varepsilon_1}{2} - \phi_P + \frac{\pi}{2}\right) \tag{4.34}$$

$$\zeta(t) = \frac{A_P}{\frac{hE}{R^2} - \rho_{\text{wall}} h\omega^2} \cos(\omega t - \phi_P) \tag{4.35}$$

with

$$A_P = 2R\left(\frac{E}{1-\nu^2}\frac{h}{R^2} - \rho_{\text{wall}} h\omega^2\right) \tag{4.36}$$

$$\acute{c}_0 = \sqrt{\frac{Eh}{(2\rho R(1-\nu_P^2))}} \tag{4.37}$$

One should note that the model given by (4.31)–(4.35) is a linear hydrodynamic model, adapted from Womersley [168]. This model has been used as basis for further developments by numerous authors [115, 139]. The assumption that air is incompressible and Newtonian has been previously justified and the equations are axi-symmetric for flow in a circular cylinder. The boundary condition linking the wall and pipeline equations (4.31)–(4.35) is the no-slip condition that assumes the fluid particles to be adherent to the inner surface of the airway and hence to the motion of the elastic wall. Due to the fact that the wall elasticity is determined by the cartilage fraction in the tissue, it is possible to consider variations in elasticity with morphology, which in turn varies with pathology.

Generally, it is considered that if the Reynolds number N_{RE} is smaller than 2000, then the airflow is laminar; otherwise it is turbulent [165]. Based on the airway geometry and on an average inspiratory flow rate of 0.5 (l/s) during tidal breathing

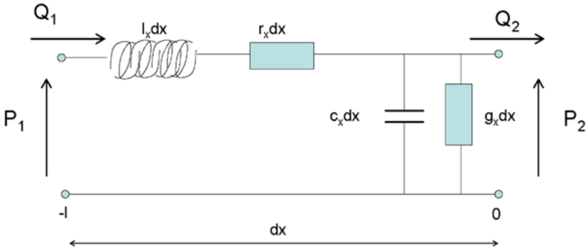

Fig. 4.1 Schematic representation of the infinitesimal distance dx over the transmission line and its parameters

conditions, the Reynolds number can be calculated as

$$N_{\mathrm{RE}} = w \cdot 2R \cdot \frac{\rho}{\mu} \tag{4.38}$$

with $\rho = 1075$ (g/m^3) the air density BTPS (Body Temperature and Pressure, Saturated) and $\mu = 0.018$ (g/m s) the air viscosity BTPS. We have verified the values for the Reynolds number, which indeed indicated laminar flow conditions throughout the respiratory tree, varying from 1757 in the trachea to 0.1 in the alveoli. Hence, the assumption of laminar flow conditions during tidal breathing is correct.

4.2 Electrical Analogy

By analogy to electrical networks, one may consider voltage as the equivalent for respiratory pressure P and current as the equivalent for airflow Q [83]. Electrical resistances R_e may be used to represent respiratory resistance that occur as a result of airflow friction in the airways. Similarly, electrical capacitors C_e may represent volume compliance of the airways which allows them to inflate/deflate. The electrical inductors L_e may represent inertia of air and electrical conductances G_e may represent the viscous losses. These properties are often clinically referred to as mechanical properties: resistance, compliance, inertance, and conductance. The aim of this section is to derive them in function of airway morphology in case of an elastic airway wall (R_e, L_e, C_e) and in the case of a viscoelastic airway wall (R_e, L_e, C_e, G_e).

Suppose the infinitesimal distance dx of a transmission line as depicted in Fig. 4.1. We have the distance-dependent parameters: l_x induction/m; r_x resistance/m; g_x conductance/m; c_x capacity/m. We consider the analogy to voltage as being the pressure $p(x,t)$ and to current as being the airflow $q(x,t)$ and we apply the transmission line theory. We shall make use of the complex notation:

$$\begin{aligned} p(x,t) &= P(x)e^{j(\omega t - \phi_P)} \\ q(x,t) &= Q(x)e^{j(\omega t - \phi_Q)} \end{aligned} \tag{4.39}$$

where x is the longitudinal coordinate (m), t is the time (s), ω is the angular frequency (rad/s), f is the frequency (Hz) and $j = \sqrt{-1}$. The pressure and the flow are harmonics, with the modulus dependent solely on the location within the transmission line (x). ϕ_P and ϕ_Q are the pressure and flow phase angles at $t = 0$. The voltage difference between two points on the transmission line denoted (x) and $(x + dx)$ is due to losses over the resistance and inductance:

$$p(x+dx) - p(x) = -r_x\,dx \cdot q - l_x\,dx\frac{\partial q}{\partial t} \tag{4.40}$$

and the current difference between the same points is due to leakage losses and storage in the capacitor:

$$q(x+dx) - q(x) = -g_x\,dx \cdot p - c_x\,dx\frac{\partial p}{\partial t} \tag{4.41}$$

After division with dx, knowing that in the limit $dx \longrightarrow 0$, and introducing (4.39) in the first and second derivation gives, respectively:

$$\begin{aligned}
\frac{\partial P}{\partial x} &= -(r_x + j\omega l_x)Q = -Z_l Q\\
\frac{\partial Q}{\partial x} &= -(g_x + j\omega c_x)P = -P/Z_t\\
\frac{\partial^2 P}{\partial x^2} &= -(r_x + j\omega l_x)\frac{\partial Q}{\partial x} = -Z_l\frac{\partial Q}{\partial x}\\
\frac{\partial^2 Q}{\partial x^2} &= -(g_x + j\omega c_x)\frac{\partial P}{\partial x} = -\frac{\partial P}{\partial x}\Big/ Z_t
\end{aligned} \tag{4.42}$$

with

$$Z_l = -\frac{\frac{\partial P}{\partial x}}{Q} = r_x + j\omega l_x \tag{4.43}$$

the longitudinal impedance and

$$Z_t = \frac{P}{-\frac{\partial Q}{\partial x}} = \frac{1}{g_x + j\omega c_x} \tag{4.44}$$

the transversal impedance.

From (4.42) we obtain the system equations for $P(x)$ and $Q(x)$:

$$\begin{aligned}
\frac{\partial^2 P}{\partial x^2} - Z_l P/Z_t &= 0\\
\frac{\partial^2 Q}{\partial x^2} - Z_l Q/Z_t &= 0
\end{aligned} \tag{4.45}$$

Introducing the notation

$$\gamma = \sqrt{(r_x + j\omega l_x)(g_x + j\omega c_x)} = \sqrt{\frac{Z_l}{Z_t}} \tag{4.46}$$

it follows that (4.45) can be re-written as

$$\begin{aligned} &\frac{\partial^2 P}{\partial x^2} - \gamma^2 P = 0 \quad \text{and} \\ &\frac{\partial^2 Q}{\partial x^2} - \gamma^2 Q = 0 \end{aligned} \tag{4.47}$$

to which the solution is given by

$$\begin{aligned} &P(x) = Ae^{-\gamma x} + Be^{\gamma x} \quad \text{and} \\ &Q(x) = Ce^{-\gamma x} + De^{\gamma x} \end{aligned} \tag{4.48}$$

with complex coefficients A, B, C, D; using (4.48) in the first two relations from (4.42), the system can be reduced to

$$Q(x) = \frac{1}{Z_0}\left(Ae^{-\gamma x} - Be^{+\gamma x}\right), \quad \text{with} \tag{4.49}$$

$$Z_0 = \sqrt{\frac{r_x + j\omega l_x}{g_x + j\omega c_x}} = \sqrt{Z_l Z_t} \tag{4.50}$$

in which Z_0 is the characteristic impedance of the transmission line cell.

Using the trigonometric relations

$$\begin{aligned} \sinh(\gamma x) &= \frac{e^{\gamma x} - e^{-\gamma x}}{2} \\ \cosh(\gamma x) &= \frac{e^{\gamma x} + e^{-\gamma x}}{2} \end{aligned} \tag{4.51}$$

we can write the relationship between the input $x = -\ell$ and the output $x = 0$ as

$$\begin{vmatrix} P_1 \\ Q_1 \end{vmatrix} \begin{matrix} = \\ = \end{matrix} \begin{vmatrix} \cosh(\gamma\ell) & Z_0 \sinh(\gamma\ell) \\ \frac{1}{Z_0}\sinh(\gamma\ell) & \cosh(\gamma\ell) \end{vmatrix} \begin{vmatrix} P_2 \\ Q_2 \end{vmatrix} \tag{4.52}$$

with

$$Z_0 = \sqrt{\frac{r_x + j\omega l_x}{g_x + j\omega c_x}} = \sqrt{Z_l Z_t} \tag{4.53}$$

the characteristic impedance and

$$Z_l = r_x + j\omega l_x = \gamma Z_0 \tag{4.54}$$

the longitudinal impedance, respectively,

$$Z_t = 1/(g_x + j\omega c_x) = Z_0/\gamma \tag{4.55}$$

the transversal impedance.

The relation for the longitudinal impedance in function of aerodynamic variables is obtained from (4.43), and gives

$$Z_l = \frac{j\omega\rho}{\pi R^2 M_1} e^{-j\varepsilon_1} = \frac{\mu\delta^2}{\pi R^4 M_1} e^{-j(\frac{\pi}{2}-\varepsilon_1)}$$
$$= \frac{\mu\delta^2}{\pi R^4 M_1}\big[\sin(\varepsilon_1) + j\cos(\varepsilon_1)\big] \tag{4.56}$$

respectively, in terms of transmission line parameters, the longitudinal impedance is given by $Z_l = r_x + j\omega l_x$.

By equivalence of the two relations we find that the resistance per unit distance is

$$r_x = \frac{\mu\delta^2}{\pi R^4 M_1}\sin(\varepsilon_1) \tag{4.57}$$

It follows that $\omega l_x = \frac{\mu\delta^2}{\pi R^4 M_1}\cos(\varepsilon_1)$ and recalling that $\delta = R\sqrt{\frac{\omega\rho}{\mu}}$, the inductance per unit distance is

$$l_x = \frac{\rho}{\pi R^2}\frac{\cos(\varepsilon_1)}{M_1} \tag{4.58}$$

4.2.1 Elastic Tube Walls

In case of an *elastic pipeline*, the characteristic impedance is obtained using relations (4.43), (4.44), and (4.50), leading to

$$Z_0 = \frac{\rho}{\pi R^2}\frac{1}{1-\nu_P^2}\sqrt{\frac{Eh}{2\rho R}}\frac{1}{\sqrt{M_1}}e^{-j\frac{\varepsilon_1}{2}} \tag{4.59}$$

and for a lossless line (no air losses trough the airway walls, thus *conductance* g_x *is zero*), the transversal impedance is

$$Z_t = \frac{1}{j\omega c_x} = \frac{Z_0^2}{Z_l} = \frac{Eh}{(j\omega(2\pi R^3(1-\nu_P^2))} \tag{4.60}$$

from where the capacity per unit distance can be extracted:

$$c_x = \frac{2\pi R^3(1-\nu_P^2)}{Eh} \tag{4.61}$$

Thus, from the geometrical (R, h) and mechanical (E, ν_P) characteristics of the airway tube, and from the air properties (μ, ρ) one can express the r_x, l_x and c_x parameters. In this way, the dynamic model can be expressed in an equivalent lossless transmission line by Eqs. (4.57)–(4.61). Notice that the compliance parameter

c_x in (4.61) is independent of the frequency, while both r_x (4.57) and l_x (4.58) are dependent on frequency trough the δ parameter, present also in M_1. Because we are interested only in the input impedance, we can disregard the effects introduced by the reflection coefficient. Hence, for $|\gamma| \ll 1$, one can estimate that over the length ℓ of an airway tube, we have the corresponding properties [73]:

$$R_e = r_x \ell = \ell \frac{\mu \delta^2}{\pi R^4} \frac{\sin(\varepsilon_1)}{M_1} \tag{4.62}$$

$$L_e = l_x \ell = \ell \frac{\rho}{\pi R^2} \frac{\cos(\varepsilon_1)}{M_1} \tag{4.63}$$

$$C_e = c_x \ell = \ell \frac{2\pi R^3 (1 - \nu_P^2)}{Eh} \tag{4.64}$$

4.2.2 *Viscoelastic Tube Walls*

Viscoelasticity is introduced assuming a complex function for the elastic modulus, yielding a real and an imaginary part [8, 23, 143]. This can then be written as a corresponding modulus and phase:

$$E^*(j\omega) = E_S(\omega) + jE_D(\omega) = |E| e^{j\varphi_E} \tag{4.65}$$

The complex definition of elasticity will change the form of the wave velocity from (4.37) into

$$\acute{c}_0 = \sqrt{\frac{|E| h e^{j\varphi_E}}{2\rho R (1 - \nu_P^2)}} = \sqrt{\frac{|E| h}{2\rho R (1 - \nu_P^2)}} e^{j\frac{\varphi_E}{2}} \tag{4.66}$$

The viscoelasticity of the wall is determined by the amount of cartilage fraction in the tissue, as the viscous component (collagen), respectively by the soft tissue fraction in the tissue as the elastic component (elastin) [8]. The equivalent of (4.65) is the ratio between stress and strain of the lung parenchymal tissue. The Young modulus is then defined as the slope of the stress–strain curve. With the model given by the above described equations, it is possible to consider variations in viscoelasticity with morphology and with pathology. This will be discussed in the next chapter.

For a *viscoelastic pipeline*, the characteristic impedance is given by

$$Z_0 = \frac{\rho}{\pi R^2} \frac{1}{1 - \nu_P^2} \sqrt{\frac{|E| h}{2\rho R}} \frac{1}{\sqrt{M_1}} e^{-j\left(\frac{\varepsilon_1}{2} + \frac{\varphi_E}{2}\right)} \tag{4.67}$$

and the transversal impedance is given by

$$Z_t = \frac{1}{g_x + j\omega c_x} = \frac{Z_0^2}{Z_l} = 1 \Big/ \left(\omega \frac{2\pi R^3 (1 - \nu_P^2)^2}{|E| h} e^{j\left(\frac{\pi}{2} - \varphi_E\right)} \right) \tag{4.68}$$

from which the conductance per unit distance can be extracted:

$$g_x = \omega \frac{2\pi R^3(1-\nu_P^2)^2}{|E|h} \sin\varphi_E \tag{4.69}$$

and the capacitance per unit distance is given by

$$c_x = \frac{2\pi R^3(1-\nu_P^2)^2}{|E|h} \cos\varphi_E \tag{4.70}$$

Thus, from the geometrical (R, h) and mechanical (E^*, ν_P) characteristics of the airway tube, and from the air properties (μ, ρ) one can express the r_x, l_x, g_x and c_x parameters. In this way, the dynamic model can be expressed in an equivalent transmission line defined by Eqs. (4.57), (4.58), (4.69), (4.70). Similar to the elastic wall case, we can estimate that, over the length ℓ of an airway tube, we have the corresponding properties:

$$R_e = r_x\ell = \ell \frac{\mu\delta^2}{\pi R^4 M_1} \sin(\varepsilon_1) \tag{4.71}$$

$$L_e = l_x\ell = \ell \frac{\rho}{\pi R^2} \frac{\cos(\varepsilon_1)}{M_1} \tag{4.72}$$

$$G_e = g_x\ell = \ell\omega \frac{2\pi R^3(1-\nu_P^2)^2}{|E|h} \sin\varphi_E \tag{4.73}$$

$$C_e = c_x\ell = \ell \frac{2\pi R^3(1-\nu_P^2)^2}{|E|h} \cos\varphi_E \tag{4.74}$$

4.2.3 Generic Recurrence in the Airways

Variations of the ratios of the mechanical parameters within consecutive airway levels in a branch are given in Fig. 4.2-left. The ratio for the resistance is supra-unitary, hence the resistance increases with the branch. Similarly, a sub-unitary ratio for compliance denotes a decreases in elasticity with each level. Both effects are due to a decrease in the airway cross-section. Figure 4.2-right depicts the same variation, but with the airway level. Due to an increase in the total cross-sectional area from one level to another, the total resistance decreases (sub-unitary ratio), whereas the total compliance increases (supra-unitary ratio). Exponential changes for resistance, inertance and elastance from level 10 onwards show that mechanical properties become important towards the lower ducts (gas exchange).

Notice from Fig. 4.2 that from level 11 onwards, the variations of the ratios are smaller (except the last two bifurcations: 22 and 23). Physiologically, level 11 corresponds to the bronchiole [59, 114]. We can correlate these effects to the variations in the airway radius and in the airway cross-sectional area, respectively. The radius changes from 8 mm to 1.75 mm, whereas the area varies from 254.5 mm^2 to

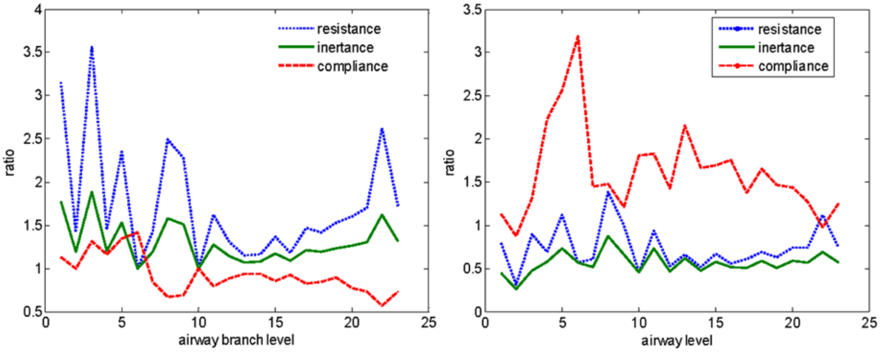

Fig. 4.2 The ratio between two consecutive branches belonging to consecutive levels (*left*) and between two consecutive levels (*right*) in the healthy lung for resistance R_e, inertance L_e, and compliance C_e

2.09 mm^2 from trachea (level 1) to bronchiole (level 11). From level 11 onward, these changes are not so abrupt, thus resulting in lower variance of the mechanical parameters values as well. Functionally, levels up to 11 denote the conductive zone (i.e. they transport air into and out of the lungs) and levels up to 24 denote respiratory zone (i.e. gas exchange takes place here).

4.3 Some Further Thoughts

The set of equations given by (4.31)–(4.35) can be used to investigate the variations in tidal breathing pressure and flow waves caused by pathology in the nominal function of the lung. Due to the fact that we do not seek to obtain a precise/exact value of the pressure and flow components but merely a qualitative evaluation, a more complex formulation may be more realistic, but may serve little to our quest in bringing forward lumped FO parameter models. In the remainder of this chapter, the assumptions and limitations used in the derivation of the electrical analogue are presented.

For typical flow rates during spontaneous breathing ranging 0.5–1 l/s, wall roughness is neglected since it has little effect under laminar flow conditions and for low values of the Womersley parameter. The values of the Womersley parameter δ are always less than 1, varying from 0.0471 in alveoli to 0.785 in the trachea. If one compares these values of δ for the circulatory system, where values become as high as 24, deviations from Poiseuille parabolic flow profile occur as a result [120, 139]. This is not the case for the laminar flow conditions during tidal breathing.

We use a set of simplifying assumptions which emerged from previous studies [41, 102]. The pressure at the boundaries of all parts is the same at all points of the respective boundaries. Three of the boundaries contain gas only on one side: airway opening, alveolar surface, and body surface. Uniform pressure is valid if the gas is in continuity condition and there is no flow. These conditions are fulfilled for the body surface, during panting at the airway opening and the alveoli. The only part which is not in agreement with this hypothesis is the pleural surface, which has tissue on both sides and its pressure distribution cannot be predicted.

To summarize, the results are obtained under the following assumptions:

- laminar flow for typical Reynolds number during quiet breathing less than 2000;
- ducts are long enough (this assumption is not true, thus neglecting the entrance effects);
- the air is homogeneous and Newtonian;
- the axial velocity component is zero at the airway wall;
- linear (visco)elastic, uniform cylindrical duct (valid as approximation);
- for linearization we have assumed the following simplifications:
  - $-\frac{\omega R}{c} \ll \delta$, for in respiration we have values between 3.5904×10^{-5} and 2.1542×10^{-6};
  - the air velocity is small compared to the wave velocity; this is valid for most of the airways; i.e. in trachea there may be velocities as high as 10 m/s, with a wave velocity of 339 m/s;
  - the values for y vary between $0 \longrightarrow \pm 1$ (rigid pipe), although in reality it varies between $0 \longrightarrow \pm(1 + \zeta/R)$ (viscoelastic pipe);
  - the E modulus is dependent on the airway type (cartilage fraction);
- thin-walled ducts; for the healthy respiratory system, the ratio h/R varies between 0.4625 in trachea, to 0.0896 in alveoli. When calculating the value for $\acute{c}_0$, the geometrical characteristics are introduced, modifying it accordingly.

4.4 Summary

In this chapter, the results based on the Womersley theory have been used to determine an electrical equivalent of the respiratory system and capture the mechanical properties in (4.62)–(4.64). For the respiratory system, transmission line models are mostly used within high frequency ranges (above 100 Hz) for sound analysis diagnosis [59]. However, for lower frequencies (0.1–50 Hz) the transmission line theory can be applied in a simplified form, leading to the exact solution for pressure and flow changes in normal breathing conditions. A study of the systemic circulation has been employed in [115], leading to the same formula for the compliance (4.61). Similarity exists between the derivation of the input impedance in the respiratory tree in this study and modeling the smaller systemic arteries, since in both simulations the symmetric structure is employed, along with laminar flow conditions, incompressibility, Newtonian fluid, and the no-slip boundary condition. The input impedance is extended to a more general tree in [115], by adding the equation of crossing a bifurcation based on a law on which the geometry changes over the junction. Nevertheless, we may argue that our choice of choosing to model a completely symmetric tree still reflects its essential behavior, and can be extended with the asymmetry relations adapted from [115].

It is straightforward to apply airway altering/remodeling effects in this simple model representation, but limitations should be taken into account. The major errors which may occur in this study are determined by the heterogeneity of the human lung, i.e. inter-subject variability can affect the values from Table 2.1 and Table 2.2. However, these values are reported in several studies [59, 66, 85, 100, 164] and they had offered a good basis for investigations, originally measured from excised lungs [114, 163] and then in plastic casts [135].

Another further simplification in our reasoning is considering the effects from the branching angles negligible. These angles influence the flow to change direction, may lead to an asymmetrical velocity profile, to develop a secondary flow in the daughter branches and the inner airway walls to be slightly stretched [135]. The change in cross-sectional areas which occurs from parent to daughter branches in a bifurcation causes the fluid to undergo a deceleration and may cause separation of adjoining streamlines. However, this kind of information may be more useful to the study of airflow dynamics in aerosol deposition models.

The model developed in this chapter can be now employed in building an electrical analogue ladder network model preserving the geometry of the respiratory system.

Chapter 5
Ladder Network Models as Origin of Fractional-Order Models

5.1 Fractal Structure and Ladder Network Models

5.1.1 An Elastic Airway Wall

In this section, we make use of the formulas (4.62), (4.63), and (4.64), which are calculated with the morphologic values from Table 2.1. With the resistance, inertance, and capacitance values at hand, one is able to build an electrical network. Suppose we have the electrical network as depicted in Fig. 5.1, which preserves the geometry of the respiratory tree. In this network, Zl_m^* denotes the longitudinal impedance, whereas Zt_m^* denotes the transversal impedance of the airway tubes and m denotes the level in the respiratory tree ($m = 1, \dots, N$).

Assuming that the flow Q is symmetric with respect to each bifurcation (divides equally trough the branches) one can define the equivalent level impedances and admittances as a function of powers 2. Hence, the total resistance per level is given by [108]:

$$R_{em} = R_{em}^*/2^{m-1} \tag{5.1}$$

with R_{em}^* the resistance in a single branch. Similarly, the total inertance per level is given by

$$L_{em} = L_{em}^*/2^{m-1} \tag{5.2}$$

with L_{em}^* the inertance in a single branch; finally, the total capacitance in a level is given by

$$C_{em} = C_{em}^* \cdot 2^{m-1} \tag{5.3}$$

with C_{em}^* the capacitance in a single branch. Using these relations, one can simplify the electrical network from Fig. 5.1 to an equivalent ladder network, schematically depicted in Fig. 5.2. In this ladder network, Zl_m^*, with $m = 1, \dots, N$ denoting the longitudinal impedance, which is defined as $Zl_m^*(s) = R_{em}^* + L_{em}^* s$. Since both resistance and inertance in each level are divided by 2^{m-1}, we can use the equivalent

C.M. Ionescu, *The Human Respiratory System*, Series in BioEngineering,
DOI 10.1007/978-1-4471-5388-7_5,

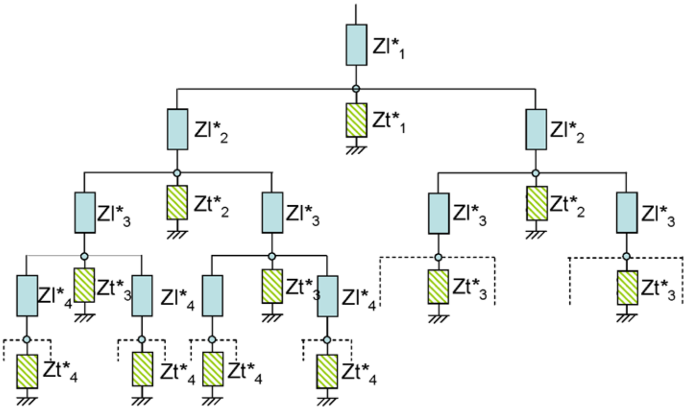

Fig. 5.1 Recursive tree representation of the respiratory tree in its electrical equivalent

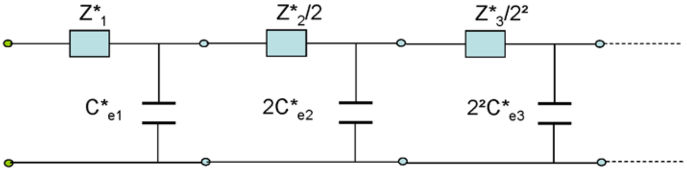

Fig. 5.2 Equivalent ladder network for the symmetric recursive tree

Table 5.1 Ratios of the mechanical parameters between consecutive levels. Values are presented as mean ± standard deviation values for the 1–15 levels, respectively, for the 16–24 levels

Nominal	Levels 1–15	Levels 16–24
λ	0.81 ± 0.32	0.68 ± 0.16
$1/\alpha$	0.56 ± 0.17	0.56 ± 0.08
χ	1.71 ± 0.77	1.55 ± 0.29

representation $Zl_m(s) = Zl_m^*/2^{m-1}$, as in Fig. 5.2. In the same figure, the capacitance is denoted using (5.3).

We introduce the following notations for the ratios between the levels:

$$\frac{R_{em+1}}{R_{em}} = \lambda, \qquad \frac{L_{em+1}}{L_{em}} = \frac{1}{\alpha}, \qquad \frac{C_{em+1}}{C_{em}} = \chi \tag{5.4}$$

with the ratios including both morphological and geometrical properties, as in Fig. 5.2. Hence, using the morphological values from Table 2.1 in (5.1), (5.2), and (5.3), the 'nominal' ratios from (5.4) are calculated and given in Table 5.1.

The total input impedance $Z_N(s)$ of the ladder network from Fig. 5.2 can be written as a continuous fraction expansion [118]. For the sake of mathematical clarity, we shall derive the analysis in terms of the admittance, which is the inverse of the impedance $Y_N(s) = 1/Z_N(s)$.

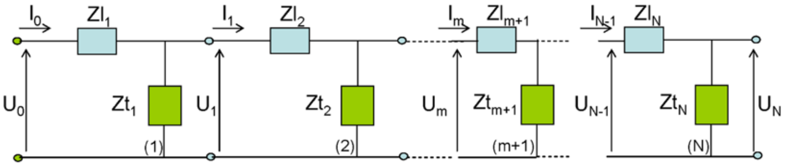

Fig. 5.3 General scheme of a ladder network in gamma-cell configuration; here N denotes the total number of cells

In this chapter we make use of the theoretical basis available in the literature for similar structures, but tailored upon the conditions and the characteristics of the respiratory system.

Consider the generalized case depicted in Fig. 5.3. The longitudinal and transversal impedances can be defined irrespective of their elements, in function of voltage and current:

$$Zl_m(s) = \frac{U_{m-1}(s) - U_m(s)}{I_{m-1}(s)} \tag{5.5}$$

and

$$Zt_m(s) = \frac{U_m(s)}{I_{m-1}(s) - I_m(s)} \tag{5.6}$$

from which we can further write

$$U_m(s) - U_{m+1}(s) = Zl_{m+1}(s) I_m(s) \tag{5.7}$$

or, equivalently,

$$\frac{I_m(s)}{U_m(s)} = \frac{1/Zl_{m+1}(s)}{1 + \frac{U_{m+1}(s)}{I_m(s) Zl_{m+1}(s)}} \tag{5.8}$$

and

$$I_m(s) - I_{m+1}(s) = \frac{U_{m+1}(s)}{Zt_{m+1}(s)} \tag{5.9}$$

or, equivalently

$$\frac{U_{m+1}(s)}{I_m(s)} = \frac{Zt_{m+1}(s)}{1 + Zt_{m+1}(s)\frac{I_{m+1}(s)}{U_{m+1}(s)}} \tag{5.10}$$

From (5.8)–(5.10), the total admittance of the ladder at level $m = 0$ is given by

$$Y_1(s) = \frac{I_0(s)}{U_0(s)} = \frac{1/Zl_1(s)}{1 + \frac{U_1(s)}{I_0(s) Zl_1(s)}} \tag{5.11}$$

or, equivalently, by

$$Y_1(s) = \frac{1/Zl_1(s)}{1 + \frac{Zt_1(s)/Zl_1(s)}{1 + Zt_1(s)\frac{I_1(s)}{U_1(s)}}} \tag{5.12}$$

If we calculate the total admittance until $m = 1$, we have

$$Y_2(s) = \frac{1/Zl_1(s)}{1 + \frac{Zt_1(s)/Zl_1(s)}{1+\frac{Zt_1(s)/Zl_2(s)}{1+\frac{U_2(s)}{I_1(s)Zl_2(s)}}}} \tag{5.13}$$

or, equivalently,

$$Y_2(s) = \frac{1/Zl_1(s)}{1 + \frac{Zt_1(s)/Zl_1(s)}{1+\frac{Zt_1(s)/Zl_2(s)}{1+\frac{Zt_2(s)/Zl_2(s)}{1+Zt_2(s)\frac{I_2(s)}{U_2(s)}}}}} \tag{5.14}$$

From (5.12)–(5.14) one may generalize via recurrence the form of the total admittance with $m = N$ cells, for $N \to \infty$:

$$Y_N(s) = \frac{1/Zl_1(s)}{1 + \frac{Zt_1(s)/Zl_1(s)}{1+\frac{Zt_1(s)/Zl_2(s)}{1+\frac{Zt_2(s)/Zl_2(s)}{\frac{\cdots}{\cdots 1+\frac{Zt_{N-1}(s)/Zl_N(s)}{1+Zt_N(s)/Zl_N(s)}}}}}} \tag{5.15}$$

which is, in fact, a continued fraction expansion [118]. Re-writing (5.15) using the explicit form of the longitudinal and transversal impedances gives

$$Y_N(s) = \frac{1/(R_{e1} + L_{e1}s)}{1 + \frac{1/[C_{e1}s(R_{e1}+L_{e1}s)]}{1+\frac{1/[C_{e1}s(R_{e2}+L_{e2}s)]}{1+\frac{1/[C_{e2}s(R_{e2}+L_{e2}s)]}{1+\frac{1/[C_{e2}s(R_{e3}+L_{e3}s)]}{\frac{\cdots}{\cdots 1+\frac{1/[C_{e(N-1)}s(R_{eN}+L_{eN}s)]}{1+1/[C_{eN}s(R_{eN}+L_{eN}s)]}}}}}}} \tag{5.16}$$

which, in terms of the recursive ratios from (5.4) can be re-written as

$$Y_N(s) = \frac{1/(R_{e1} + L_{e1}s)}{1 + \frac{1/[C_{e1}s(R_{e1}+L_{e1}s)]}{1+\frac{1/[C_{e1}s(\lambda R_{e1}+\frac{L_{e1}s}{\alpha})]}{1+\frac{1/[\chi C_{e1}s(\lambda R_{e1}+\frac{L_{e1}s}{\alpha})]}{1+\frac{1/[\chi C_{e1}s(\lambda^2 R_{e1}+\frac{L_{e1}s}{\alpha^2})]}{\frac{\cdots}{\cdots 1+\frac{1/[\chi^{N-2}C_{e1}s(\lambda^{N-1}R_{e1}+\frac{L_{e1}s}{\alpha^{N-1}})]}{1+1/[\chi^{N-1}C_{e1}s(\lambda^{N-1}R_{e1}+\frac{L_{e1}s}{\alpha^{N-1}})]}}}}}}} \tag{5.17}$$

For the set of conditions:

$$L_{e1} \ll R_{e1} \qquad |s| < \frac{1}{R_{e1} \cdot C_{e1}} \quad \text{and} \quad |s| \ll \frac{R_{e1}}{L_{e1}} \tag{5.18}$$

and

$$\alpha \cdot \chi > 1, \quad \alpha \cdot \lambda > 1, \quad \lambda > 1 \text{ and } \chi > 1, \tag{5.19}$$

we see that in the limit $N \to \infty$, the term $\frac{L_{e1}s}{(\alpha\lambda)^{N-1}}$ from (5.17) becomes very small compared to the term in R_{e1}. Consequently, the continued fraction expansion from (5.17) reduces to

$$Y_N(s) \cong \cfrac{1/R_{e1}}{1 + \cfrac{1/R_{e1}C_{e1}s}{1+\cfrac{1/\lambda R_{e1}C_{e1}s}{1+\cfrac{1/\chi\lambda R_{e1}C_{e1}s}{1+\cfrac{1/\chi\lambda^2 R_{e1}C_{e1}s}{\cdots\cfrac{\cdots}{1+\cfrac{1/\chi^{N-2}\lambda^{N-1}R_{e1}C_{e1}s}{1+1/\chi^{N-1}\lambda^{N-1}R_{e1}C_{e1}s}}}}}}} \tag{5.20}$$

If we introduce the notations

$$W_d(s) = \frac{1}{R_{e1}C_{e1}s}, \qquad W_n(s) = \frac{1}{R_{e1}} \tag{5.21}$$

then (5.20) can be reduced to an analogue representation:

$$Y_N(s) \approx \frac{W_n(s)}{1 + g(W_d(s), \lambda, \chi)} \tag{5.22}$$

in which $g(W_d(s), \lambda, \chi)$ denotes

$$g\big(W_d(s), \lambda, \chi\big) = \cfrac{W_d(s)}{1 + \cfrac{W_d(s)/\lambda}{1+\cfrac{W_d(s)/\lambda\chi}{1+\cfrac{W_d(s)/\lambda^2\chi}{\cdots}}}} \tag{5.23}$$

Since $W_d(s)$ can be taken in front of the expansion and both λ and χ are constants, we can write

$$Y_N(s) \approx \frac{W_n}{K(\lambda, \chi)(W_d(s))^n} \tag{5.24}$$

with the fractional order n given by

$$n = \frac{\log(\lambda)}{\log(\lambda) + \log(\chi)} \tag{5.25}$$

or, in our specific case:

$$Y_N(s) \cong \frac{1/R_{e1}}{K(\lambda, \chi) \cdot (1/R_{e1}C_{e1}s)^n} \tag{5.26}$$

Consequently, the impedance is given by

$$Z_N(s) = \frac{1}{Y_N(s)} \cong \frac{K(\lambda, \chi) \cdot R_{e1}}{(R_{e1}C_{e1}s)^n} \tag{5.27}$$

The values for $K(\lambda, \chi)$ can be determined as described in [118]; since we do not make use of it explicitly, its derivation will not be discussed here. Moreover, our sole purpose was to show that the continuous fraction expansion from (5.16) will lead to a compact form which contains a term in the fractional order n. Hence, relation (5.27) shows the link between the ladder network from Fig. 5.2 and the appearance of a fractional-order term in the form of total input impedance. In the frequency domain, the fractional order will lead to a constant-phase behavior, i.e. a phase-locking in the frequency range given by the convergence conditions [118, 148].

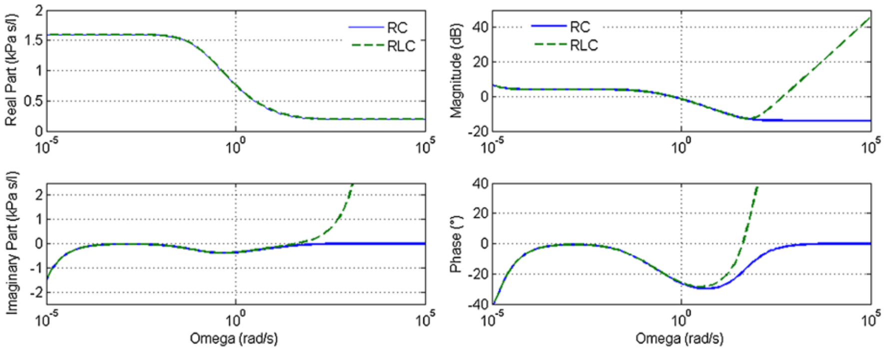

Fig. 5.4 Impedance by means of complex (*left*) and Bode-plot (*right*) representation, for the R–C (*continuous line*) and the R–L–C (*dashed line*) model structures

Depending on the number of cells in the ladder (N), the constant-phase behavior will emerge over a wider range of frequencies. This result is applicable to any kind of ladder network (airways, arteries, etc.). However, the fractional-order value and coefficients will change according to the properties (morphology, geometry) of the system.

In practice, the respiratory tract can be simulated as follows. The relations derived in Chap. 4 for resistance (4.62), inertance (4.63), and compliance (4.64) are used to calculate the total level values as in (5.1), (5.2), and (5.3). Notice that the values in the trachea R_{e1}, L_{e1}, and C_{e1} need to take into account the flow and pressure effects in the upper airways (mouth, nose, larynx, pharynx). Since we do not model the upper airways, we need to take the values from literature [121]: $R_{\mathrm{UA}} = 0.2$ kPa/(l/s), $L_{\mathrm{UA}} = 0.002$ kPa/(l/s^2), and $C_{\mathrm{UA}} = 0.25$ l/kPa. To find the level values, one can make use of the ratios from Table 5.1. The last compartment needs to model the gas compression effect; hence, from literature, we introduce the series impedance consisting of [54] $R_{\mathrm{GC}} = 0.05$ kPa/(l/s), $L_{\mathrm{GC}} = 0.06$ kPa/(l/s^2), and $C_{\mathrm{GC}} = 6$ l/kPa. This last impedance is closing the ladder network, being in parallel with the cell $N = 24$. The total admittance from (5.16) is then calculated. The equivalent total input impedance (including the upper airways and the gas compression compartment) is depicted by means of its real-imaginary parts in Fig. 5.4-left, respectively, by its equivalent Bode-plot representation in Fig. 5.4-right. Notice that, in these figures, we show the impedance in two cases: when the airway tube is modeled by an R–C element, and an R–L–C element, respectively. This comparison allows capturing the effect of the inertance element, while the frequency is increasing.

In the Bode plot, a variation of the phase between 0° and $-26°$ can be observed in the frequency interval $\omega \in [10^{-4}, 10^{2}]$ (rad/s). However, this is not the constant-phase effect as expected from theory, because the fractional-order value n would have to be zero, or 0.3, respectively. If we use the analytical form of (5.25) to calculate this fractional-order value, we obtain $n = 0.59$. This mismatch between simulation and theory is due to the fact that the condition of $\lambda > 1$ is not fulfilled in (5.19). We shall discuss this aspect later on.

Table 5.2 Ratios of the mechanical parameters between consecutive levels. Values are presented as mean ± standard deviation values for the 1–15 levels, respectively, for the 16–24 levels

Nominal	Level 1–15	Level 16–24
λ	0.81 ± 0.32	0.68 ± 0.16
$1/\alpha$	0.56 ± 0.17	0.56 ± 0.08
χ	1.71 ± 0.77	1.55 ± 0.29
o	1.71 ± 0.77	1.55 ± 0.29

It is also worth noticing that the extra parameter L_m has no effect in determining the value of the fractional order, which is then similar to what we expected from theoretical analysis, i.e. relation (5.20) [70]. On the other hand, the effect of this extra term becomes significant with increasing frequencies, namely after the frequency interval where the phase variations are observed ($\omega > 100$ rad/s).

5.1.2 A Viscoelastic Airway Wall

In this section, we shall use the formulas derived in Chap. 4, namely (4.71), (4.72), (4.74), and (4.73), with values from Table 2.1. With these values at hand, one is able to build an electrical network as described in the previous section. The difference from the previous case (elastic) is that now the airway tube is modeled by a R–L–C–G element, as described in Chap. 4. This representation allows us to consider the viscoelastic wall properties, through the elements C–G.

For the special case of the ladder network in which $Zl_m(s) = R_{em} + L_{em}s$ and $1/Zt_m(s) = G_{em} + 1/C_{em}s$, with m denoting a level in the respiratory tree, one can analyze the properties of such a network. Next to the ratios defined in (5.4), we add the ratio for the conductance:

$$\frac{G_{em+1}}{G_{em}} = \frac{1}{o} \tag{5.28}$$

where the ratio is determined similarly as for the other parameters. The nominal ratios are given in Table 5.2. Notice that the ratios for C_e and G_e are similar due to the fact that the forms in (4.74) and (4.73) are the same, except for the sin and cos terms, whose effect are thus very small.

In a similar manner as for the elastic tube case, we can write that the total admittance is given by

$$Y_N(s) = \frac{1/(R_{e1} + L_{e1}s)}{1 + \frac{G_{e1}/[(G_{e1}C_{e1}s+1)(R_{e1}+L_{e1}s)]}{1+\frac{G_{e1}/[(G_{e1}C_{e1}s+1)(R_{e2}+L_{e2}s)]}{1+\frac{G_{e2}/[(G_{e2}C_{e2}s+1)(R_{e2}+L_{e2}s)]}{1+\frac{G_{e2}/[(G_{e2}C_{e2}s+1)(R_{e3}+L_{e3}s)]}{\cdots\frac{\cdots}{1+\frac{G_{e(N-1)}/[(G_{e(N-1)}C_{e(N-1)}s+1)(R_{eN}+L_{eN}s)]}{1+G_{eN}/[(G_{eN}C_{eN}s+1)(R_{eN}+L_{eN}s)]}}}}}}} \tag{5.29}$$

which can be re-written in a convenient form:

$$Y_N(s) = \frac{1/R_{e1}(1 + L_{e1}s/R_{e1})}{1 + \frac{\frac{G_{e1}/G_{e1}C_{e1}s}{(1+1/G_{e1}C_{e1}s)R_{e1}(1+L_{e1}s/R_{e1})}}{1+\frac{\frac{G_{e1}/G_{e1}C_{e1}s}{(1+1/G_{e1}C_{e1}s)R_{e2}(1+L_{e2}s/R_{e2})}}{1+\frac{\frac{G_{e2}/G_{e2}C_{e2}s}{(1+1/G_{e2}C_{e2}s)R_{e2}(1+L_{e2}s/R_{e2})}}{1+\frac{\frac{G_{e2}/G_{e2}C_{e2}s}{(1+1/G_{e2}C_{e2}s)R_{e3}(1+L_{e3}s/R_{e3})}}{\cdots\frac{\cdots}{1+\frac{\frac{G_{e(N-1)}/G_{e(N-1)}C_{e(N-1)}s}{(1+1/G_{e(N-1)}C_{e(N-1)}s)R_{eN}(1+L_{eN}s/R_{eN})}}{1+\frac{G_{eN}/G_{eN}C_{eN}s}{(1+1/G_{eN}C_{eN}s)R_{eN}(1+L_{eN}s/R_{eN})}}}}}}}} \tag{5.30}$$

We introduce the notation

$$W_d(s) = \frac{1}{R_{e1}C_{e1}s}, \qquad W_0(s) = \frac{1}{G_{e1}C_{e1}s} \quad \text{and} \quad W_1(s) = \frac{L_{e1}s}{R_{e1}} \tag{5.31}$$

and replace the ratios in (5.30) and we obtain

$$Y_N(s) = \frac{1/R_{e1}(1 + W_1(s))}{1 + \frac{\frac{W_d(s)/(W_0(s)+1)}{(1+W_1(s))}}{1+\frac{\frac{W_d(s)/\lambda(W_0(s)+1)}{(1+W_1(s)/\alpha\lambda)}}{1+\frac{\frac{W_d(s)/\lambda\chi(oW_0(s)/\chi+1)}{(1+W_1(s)/\alpha\lambda)}}{1+\frac{\frac{W_d(s)/\lambda^2\chi(oW_0(s)/\chi+1)}{(1+W_1(s)/\alpha^2\lambda^2)}}{\cdots\frac{\cdots}{1+\frac{\frac{W_d(s)/\lambda^{N-1}\chi^{N-2}(o^{N-2}W_0(s)/\chi^{N-2}+1)}{(1+W_1(s)/\alpha^{N-1}\lambda^{N-1})}}{1+\frac{W_d(s)/\lambda^{N-1}\chi^{N-1}(o^{N-1}W_0(s)/\chi^{N-1}+1)}{(1+W_1(s)/\alpha^{N-1}\lambda^{N-1})}}}}}}}} \tag{5.32}$$

For the set of conditions from (5.18) and for

$$\alpha \cdot \chi > 1, \quad \alpha \cdot \lambda > 1, \quad \lambda > 1 \text{ and } \chi \geq o, o > 1, \tag{5.33}$$

we find that the term $\frac{o^{N-1}}{(G_{e1}C_{e1}s)\chi^{N-1}}$ from (5.32) goes to zero as frequency increases. In this case, the limit $N \to \infty$ does not play any role, since $\chi = o$; however, if $1/(G_{e1}C_{e1}s) \ll 1$ then we can then re-write (5.32) as

$$Y_N(s) \cong \frac{1/R_{e1}(1 + W_1(s))}{1 + \frac{W_d}{1+\frac{W_d/\lambda}{1+\frac{W_d/\chi\lambda}{1+\frac{W_d/\chi\lambda^2}{\cdots\frac{\cdots}{1+\frac{W_d/\chi^{N-2}\lambda^{N-1}}{1+W_d/\chi^{N-1}\lambda^{N-1}}}}}}}} \tag{5.34}$$

which is similar in form to (5.22)

$$Y_N(s) \approx \frac{1/R_{e1}(1 + W_1(s)))}{1 + g(W_d(s), \lambda, \chi)} \tag{5.35}$$

in which

$$g\big(W_d(s), \lambda, \chi\big) = \frac{W_d(s)}{1 + \frac{W_d(s)/\lambda}{1+\frac{W_d(s)/\lambda\chi}{1+\frac{W_d(s)\lambda^2\chi}{\cdots}}}} \tag{5.36}$$

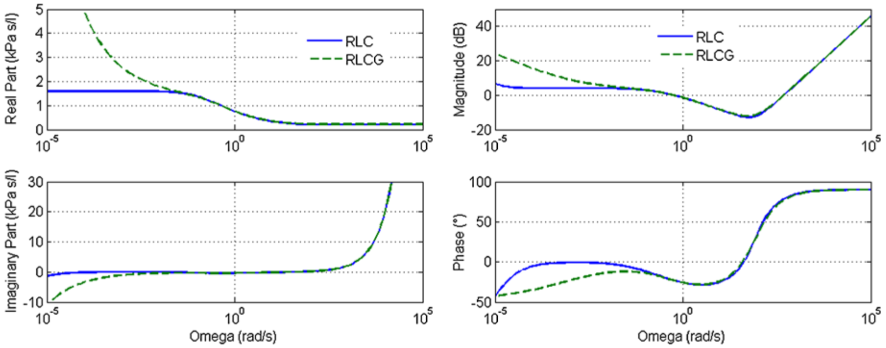

Fig. 5.5 Impedance by means of complex (*left*) and Bode-plot (*right*) representation, for the R–L–C (*continuous line*) and the R–L–C–G (*dashed line*) model structures

which can be re-written as

$$Y_N(s) \approx \frac{1/(R_{e1} + L_{e1}s)}{K(\lambda, \chi)(W_d(s))^n} \tag{5.37}$$

with the fractional order n given by

$$n = \frac{\log(\lambda)}{\log(\lambda) + \log(\chi)} \tag{5.38}$$

In our specific case we have

$$Y_N(s) \cong \frac{1/(R_{e1} + L_{e1}s)}{K(\lambda, \chi) \cdot (1/R_{e1}C_{e1}s)^n} \tag{5.39}$$

Consequently, the impedance is given by

$$Z_N(s) = \frac{1}{Y_N(s)} \cong \frac{K(\lambda, \chi) \cdot (R_{e1} + L_{e1}s)}{(R_{e1}C_{e1}s)^n} \tag{5.40}$$

The respiratory tract is simulated in a similar manner as explained in the previous section, with the same values for the upper airways and the gas compression impedance. There is no information upon the upper airway values for G_{UA}, thus we take arbitrary values for $G_{\mathrm{UA}} = 1/[R_{\mathrm{UA}} \cdot 200]$. The total impedance from (5.29) is then calculated and depicted by means of its real-imaginary parts in Fig. 5.5-left, respectively, by its equivalent Bode-plot representation in Fig. 5.5-right. Notice that in these figures, we show the impedance in two cases: when the airway tube is modeled by the R–L–C element, and by the R–L–C–G element, respectively. This comparison allows capturing the effect of the conductance element at frequencies below 0.1 rad/s.

A similar FO behavior can be observed as in Fig. 5.4. This is again in accordance to the theoretical result from relations (5.34) and (5.38), which shows that only the ratios for R_{m+1}/R_m and C_{m+1}/C_m play a role in determining the value for the fractional order at low frequencies.

5.2 Effects of Structural Asymmetry

In his recent publication, Weibel discusses the reduction of diameter and length by a constant factor for both blood vessels and airways [164]. He recognizes the theoretical contributions of Murray [107], i.e. that the dissipation of energy due to flow of blood or air in a branched tube system can be minimized if the diameter of the two daughter-branches are related to the diameter of the parent as in $d_{\text{parent}}^3 = d_1^3 + d_2^3$. In the context of fractal geometry, the reduction factor depends on the fractal dimension FD of the branching tree such that the correct formula is $d_1 = d_{\text{parent}} \cdot 2^{-1/FD}$. In the case of Hess–Murray law, $FD = 3$ because the tree is considered to be space-filling [34]. In his investigations, Weibel found that the slope of the conducting airway diameters against the generations was given by $d(m) = d_0 \cdot 2^{-m/3}$, with d_0 the tracheal diameter and m the airway generation. He then concludes that the conducting airways of the human lung are designed as a self-similar and space-filling fractal tree, with a homothety factor of $2^{-1/3} = 0.79$ (similitude ratio). However, as discussed in Chap. 3 and in the beginning of Chap. 4, this average has a significant variance in the first generations. Hence, the average value changes in the diffusion zone (airways from 16th generation onward). These observations and the fact that Weibel himself discusses that a small change in the homothety factor results in a dramatic increase in peripheral bronchiolar resistance imply that the lung must be capable to adjust itself to the optimality conditions. Indeed, a closer analysis reveals that the homothety factor is about 0.79 in the sixth generation, but it increases slowly to about 0.9 in the 16th generation, with an average of 0.85 for the small airways [164]. The physiological implications of this observation are:

- the flow resistance decreases in the small airways and
- a small reduction in the homothety factor does not affect significantly the lung function.

In the context of the above observations, one may explore the possibility of the respiratory system as a multi-fractal structure. A self-similar multi-fractal spatial distribution forms the basis for breaking the symmetry of bifurcation design within a tree. In [167], the author discusses the implications of self-affine scaling. It turns out that the fractal dimension changes when calculated from different reference points. Therefore, the slope determining the homothety factor changes when viewed at a fine or coarse grained diameter scale. This latter observation is of interest in the context of this book, since it supports the idea of a multi-fractal structure. For example, the average of the radius ratio changes from $2^{-0.17} = 0.88$ to 0.89 when only the first 16 generations are taken into account, respectively, to 0.87 for the alveoli (generations 17–24). This implies that the homothety factor changes, depending on the spatial location within the tree. On the other hand, if we analyze the radius ratio from generations 1 to 24 in steps of 4, we obtain an average of 0.85, whereas if we use steps of 2, we obtain an average homothety factor of 0.86. These changes might not seem significant, but one should recall that they originate by the symmetric geometry of the respiratory tree. However, when asymmetry is considered, one deals with several homothety factors, i.e. as schematically drawn in Fig. 5.6.

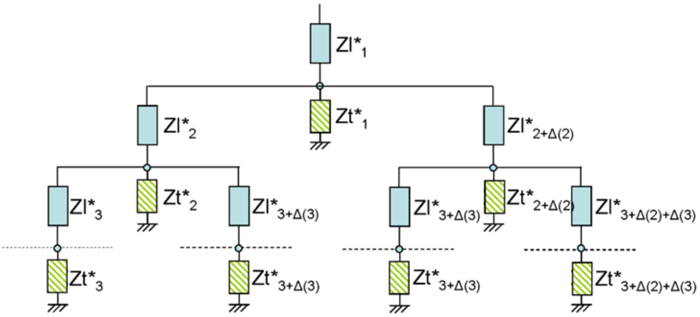

Fig. 5.6 Asymmetric representation for the first four generations, in its electrical equivalent

Fig. 5.7 Number of branches for each generation, in the asymmetric (*top*) and symmetric (*bottom*) generation. Notice that the Y-axis is logarithmic

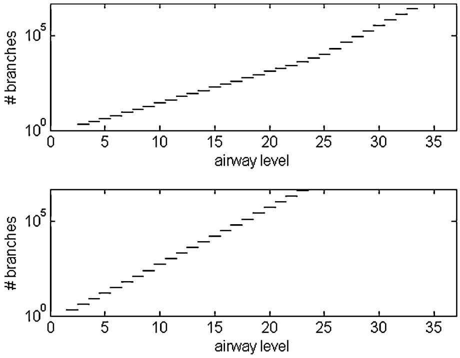

It has been demonstrated by a systematic analysis that the airway tree in different species shows a common fractal structure, in spite of some gross differences in airway morphology [164]. Nevertheless, let us investigate the case of asymmetric branching in the human lungs. The Horsfield representation will be used, as from [65], with the values listed in Table 2.2. In this scenario, an airway of level m bifurcates into two daughters: one of order $m+1$ and one of order $m+1+\Delta$, with Δ the asymmetry index. As a result of the asymmetry, the electrical network becomes as in Fig. 5.6. Figure 5.7 shows the number of branches that are in one generation, for the symmetric and asymmetric lung structure. Notice the different slope which characterizes the space-filling distribution; the top figure shows that the slope is lower in the asymmetric tree section than in the symmetric tree section.

Since the symmetry is lost, one cannot simplify the electrical network to its ladder network equivalence as in Fig. 5.2. Therefore, one must calculate explicitly the impedance from level 36 to level 1. To avoid complex numerical formulations, the impedance along the longest path was calculated, as in [54]. One should notice that from level 26 onward, the asymmetry index is zero, therefore symmetric bifurcation occurs (recall here Table 2.2). The effect of this change in the asymmetry index is visible in Fig. 5.7, i.e. a change in the slope. The initial values in the trachea are imposed similarly as in the symmetric case [121]. Figure 5.8 shows the total impedance by means of its complex representation (left) and its Bode plot (right),

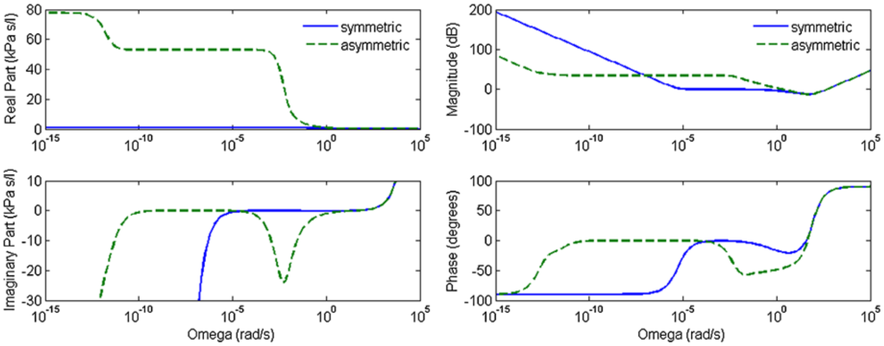

Fig. 5.8 Impedance by means of complex (*left*) and Bode-plot (*right*) representation, for the symmetric (*continuous line*) and the asymmetric (*dashed line*) tree

Fig. 5.9 Detailed view of the impedance by means of the Bode-plot representation, for the symmetric (*continuous line*) and the asymmetric (*dashed line*) tree

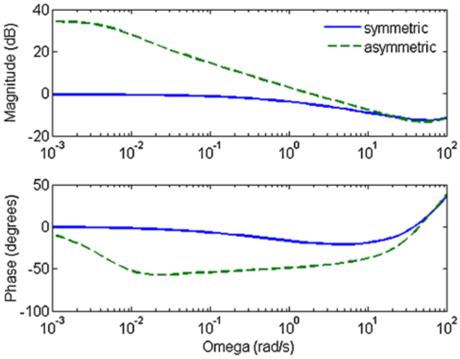

for the symmetric and the asymmetric tree, whereas the airway tubes are modeled by an R–L–C element in both representations.

It is significant to observe that in the frequency interval of clinical interest, $\omega \in [25, 300]$ rad/s, the two impedances tend to behave similarly. A detail of Fig. 5.8 can be viewed in Fig. 5.9. For the asymmetric case, we have a decrease of about -10 dB/dec and a phase of approximately $-50°$, resulting in a fractional order of $n \cong 0.5$. The constant-phase behavior is emphasized at frequencies below those evaluated standardly in clinical practice, i.e. below 5 Hz. However, in the standard clinical range of frequencies for the forced oscillation technique, namely 4–48 Hz, both models give similar results, as depicted in Figs. 5.10 and 5.11.

5.3 Relation Between Model Parameters and Physiology

5.3.1 A Simulation Study

For the simulations in this study, the admittance from (5.17) will be used, with ratios calculated with (5.4) using morphological values from Table 2.1. The respiratory

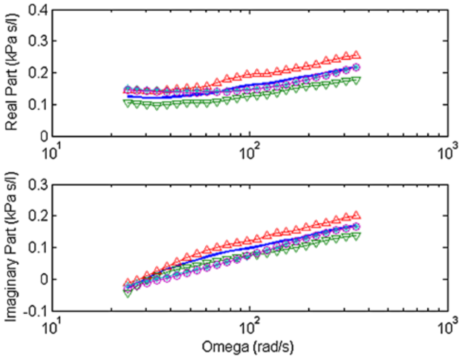

Fig. 5.10 The estimated impedance within the measured frequency range for the symmetric (*) and the asymmetric (o) case, against averaged data from healthy subjects

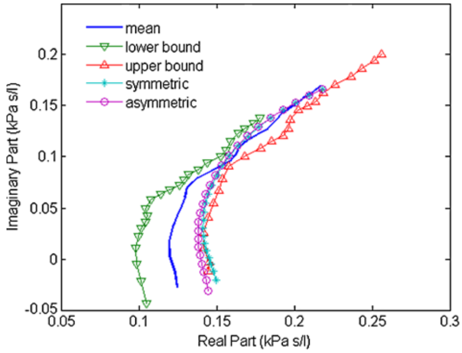

Fig. 5.11 Equivalent polar plot representation of Fig. 5.10

tract is simulated by approximating each level m as one cell in the ladder network, thus $N = 24$. The system given by (5.17) has been simulated starting from initial conditions given by the upper airway tract (mouth–trachea) as from [121]:

$$\begin{aligned} &R_{UA} = 0.047\ (\text{kPa}\,\text{s/l}), \qquad L_{UA} = 0.0008\ \left(\text{kPa}\,\text{s}^2/\text{l}\right) \quad \text{and} \\ &C_{UA} = 0.01341\ (\text{l/kPa}) \end{aligned} \tag{5.41}$$

Notice that these values are only averaged values and they do not represent the exact upper airway tract impedance for each individual person. Taking into account the effect of the upper airways is done by putting the upper airway impedance in series to that of the recurrent tree modeled by (5.17), in order to obtain the total estimated input impedance.

To validate the theoretical developments, we investigate three simulated cases: the nominal, the pathologic and the extended case.

In the *nominal case*, the total impedance from (5.17) is calculated with initial values from (5.41) and the ratios:

$$\begin{aligned} &\lambda = 0.818, \quad \chi = 1.715, \quad \alpha = 1.764, \quad \text{for } m = 1, \ldots, 13 \\ &\lambda = 0.686, \quad \chi = 1.556, \quad \alpha = 1.783, \quad \text{for } m = 14, \ldots, 24 \end{aligned} \tag{5.42}$$

Notice that the convergence of (5.17) to the form in (5.24) and the term in (5.25) is not guaranteed, since the condition $\lambda > 1$ is not fulfilled. It is also interesting

Fig. 5.12 Impedance by means of Bode-plot representation, for the nominal and the pathologic scenario

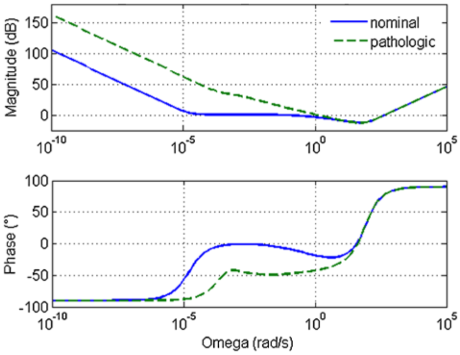

Fig. 5.13 For the pathologic case, but with increasing number of cells in the ladder network (the extended scenario)

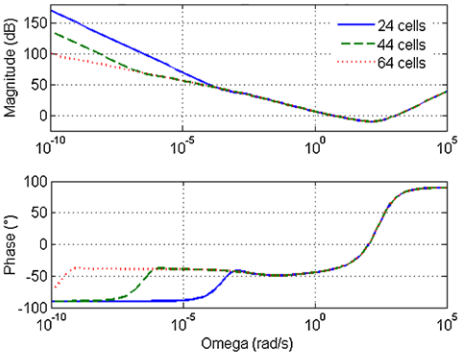

to note that these ratios have a significantly different mean in the first part of the respiratory tree (conductive zone) from that in the second part of it (respiratory zone), hence we considered it necessary to vary them accordingly in the model.

In the *pathologic case*, due to the fact that airway morphology is affected by disease, changes occur in the mechanical parameters such that the overall resistance increases and the compliance decreases (e.g. in chronic obstructive pulmonary disease) [72]. This results in the following ratios:

$$\begin{aligned} &\lambda = 1.127, \quad \chi = 1.220, \quad \alpha = 1.846, \quad \text{for } m = 1, \dots, 13 \\ &\lambda = 1.167, \quad \chi = 1.226, \quad \alpha = 1.535, \quad \text{for } m = 14, \dots, 24 \end{aligned} \tag{5.43}$$

It is clear that the condition on $\lambda > 1$ is fulfilled in the pathologic case. All other conditions imposed as $\alpha\chi > 1, \alpha\lambda > 1$, and $\chi > 1$ are also fulfilled. The *extended case* consists of increasing the number of cells in the ladder network, while maintaining the ratios from (5.43).

The simulated total input impedance is depicted by means of its equivalent Bode-plot representation in Fig. 5.12 in the nominal case, in the pathologic case and in Fig. 5.13 the extended case (varying the number of cells in the ladder network). From the Bode plot, it is clear that the fractional-order behavior (phase locking) depends on the ratios between the ladder network parameters, since its value varies from one scenario to the other.

For the *simulated nominal case* observed in Fig. 5.12, with averaged ratios from (5.42), the calculated fractional-order value is $n = 0.59$, corresponding in the impedance plots to a phase constancy of about -53°. This value does not correspond to our simulation results, due to the fact that the values for λ are sub-unitary, therefore not fulfilling the condition for convergence. Since the formula for n is valid only for positive values of the logarithm, for $\lambda < 1$ the formula (5.25) will be inaccurate.

In the *simulated pathologic case*, one may observe in Fig. 5.12 that in the frequency interval $\omega \in [10^{-4}, 10^{-1}]$ (rad/s) the constant-phase effect is visible. The magnitude decreases with 45 dB over four decades, which results in a change of about -11 dB/dec. The phase exhibits a phase-locking within this frequency range, around the value of -48°. From $-n \cdot 20$ dB/dec $= -11$ we have $n \approx 0.55$, and from $-n \cdot 90^\circ = -48^\circ$, it follows that $n \approx 0.53$. If one calculates the fractional-order value from (5.25) with averaged ratio values from (5.43), one comes up with $n = 0.59$ for the admittance in (5.26), which corresponds closely to the value observed in Fig. 5.12. This result proves that the formula (5.25) for calculating n is valid in the limit if and only if all convergence conditions are fulfilled.

In the *simulated extended case*, Fig. 5.13 shows the effect of increasing the number of cells, while keeping the same ratios as in (5.43). Increasing the number of cells will help convergence in the limit; recall here that the formula (5.25) was derived from (5.17) assuming $N \to \infty$. Increasing the number of cells in the ladder network leads indeed to a constant-phase behavior corresponding to a similar phase value as in the pathologic case, but its effect will be visible over a broader frequency band. It is worth to notice that the frequency band is linearly dependent with the increasing in the number of cells.

Our findings justify the use of a FO parametric model to characterize the respiratory input impedance [69]. Hence, we established that the origins of the FO behavior are not only the viscoelastic properties of the lung tissue, typically visible at low frequencies, but also the fractal structure of the respiratory tree. It is interesting to note that both viscoelasticity and diffusion appear at low frequencies; the diffusion is not tackled in this book. The proposed model allows variations in the parameters by altering the elastic modulus E and cartilage fraction κ, as well as variations in the airway geometry by altering the airway radius R, length ℓ, and thickness h. Although preserving its fractal structure, these alterations can be correlated to airway remodeling in pathology, leading to different values in the ratios, e.g. those given in (5.43). The results depicted in Figs. 5.12 and 5.13 indicate that viscoelastic and diffusion phenomena are not the only origin of the phase constancy (non-integer order) models for the lungs, but also the intrinsic recurrent geometry has a similar contribution. Although simple, the nominal case of this model proves to be reasonably close to the data measured from the healthy subjects, showing that it is able to capture the intrinsic properties of the respiratory tree.

Table 5.3 Biometric parameters of the investigated subjects in the mid-frequency range (4–48 Hz) and in the low frequency range (0.9–5.3 Hz); values are presented as mean ± standard deviation

	4–48 Hz		0.9–5.3 Hz	
	male (15)	female (8)	male (8)	female (2)
Age (yrs)	23 ± 0.7	23 ± 1.3	27.2 ± 2.1	28.5 ± 2.1
Height (m)	1.76 ± 0.06	1.68 ± 0.03	1.75 ± 0.07	1.72 ± 0.02
Weight (kg)	73 ± 5.1	63 ± 2.8	71.1 ± 7.11	66.5 ± 10.6

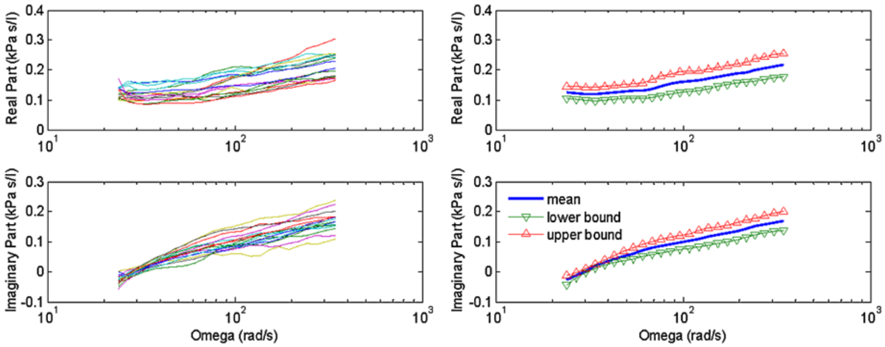

Fig. 5.14 Measured impedance values from healthy subjects (*left*) and the corresponding mean with standard deviation values (*right*)

5.3.2 A Study on Measured Respiratory Impedance

In order to validate this ladder network model, respiratory impedance has been estimated using non-parametric methods described in Chap. 2 and in (3.8) in two different frequency intervals: (i) mid-range frequencies between 4–50 Hz and (ii) low-range frequencies between 0.9–5.3 Hz. The impedance over the mid-frequency range interval has been acquired using the standard FOT device described previously. Since a loudspeaker has limitations at low frequencies, a prototype mechanical device has been used to measure impedance over the low frequency range.

The measured frequency interval used in standard clinical tests is 4–48 Hz, respectively, 25–300 rad/s. Previously available records from 23 healthy volunteers have been used to support the validity of the model with morphological values [72], and their biometric values are given in Table 5.3. An additional set of 10 healthy volunteers whose biometric values are given in the same table are measured with low frequency FOT, for the 0.9–5.3 Hz frequency interval. The impedance data from the healthy subjects with the corresponding mean and standard deviation values is given in Fig. 5.14.

From the measured healthy subjects, we obtain the averaged impedance and the standard deviation values which offer a lower and upper bound, as depicted in Fig. 5.14. The RLC-ladder model for the respiratory tree calculated with parameters from Table 2.1 and (4.62)–(4.64) neglects the impedance introduced by the upper airways segment. In order to make the comparison with the measured data,

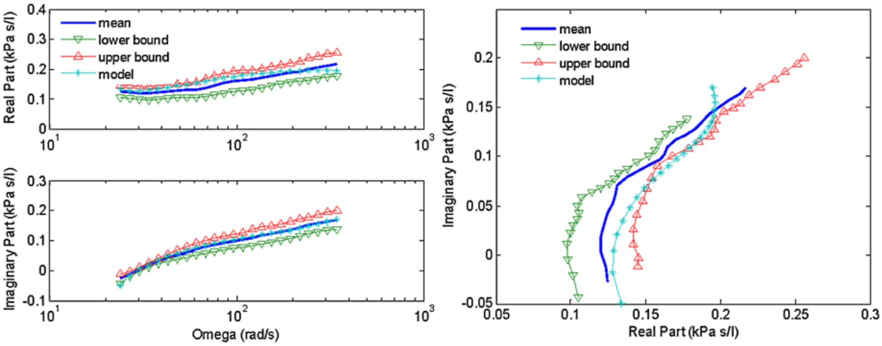

Fig. 5.15 Comparison of the RLC-ladder model performance, within the measured frequency range, against data from healthy subjects (*left*) and equivalent polar plot representation (*right*)

one has to add this extra impedance to obtain the total estimated input impedance. By adding the values of upper airway impedance parameters: $R_{\mathrm{UA}} = 0.35$ kPa/(l/s), $L_{\mathrm{UA}} = 0.00045$ kPa/(l/s^2), $C_{\mathrm{UA}} = 0.85$ l/kPa, one obtains satisfactory values in the clinical range of frequencies, as depicted in Fig. 5.15. One should keep in mind that no study has been reported in the literature upon the variations and confidence intervals of the upper airway parameters values. These values represent a tuning parameter of our ladder network model, and in this particular case they have been tuned for the averaged values of impedance given in Fig. 5.15.

Since Fig. 5.5 shows the same result in the 25–300 rad/s frequency range for both elastic and viscoelastic airway wall models, it is clear that the same result is obtained for the R–L–C–G ladder network model as in Fig. 5.15.

The impedance data collected in 10 volunteers at frequencies below 6 Hz is given in Fig. 5.16 by means of the complex impedance values, respectively, in Fig. 5.17 by means of its equivalent Bode plot. Both figures show the statistical significance of each measured frequency point, by means of its mean value, value distribution within the group, and confidence intervals. These figures may suggest that the lower the frequency, the lower the signal-to-noise ratio, due to interference with the harmonics from the breathing frequency (about 0.25 Hz).

The values identified from the 10 volunteers tested for this study in our laboratory are also summarized in Table 5.4, with the identification method from Chap. 3 and error formula from (3.12). A further comparison of this ladder network model with two papers from literature discussing low frequency impedance values is provided in [4, 76, 121].

It can be observed in the results summarized in Table 5.4 that the fifth subject had a high initial resistance values due to inflammation of the respiratory tract (i.e. flu). The results also show that smoking did not affect significantly the model values, suggesting that the proposed model may not be sensitive to the specific small changes in the airways. The outlier subject indicates that age plays an important role in determining the properties of the respiratory tree, namely an increased resistance value, which correlates with the clinical expertise [53]. Minor differences can be

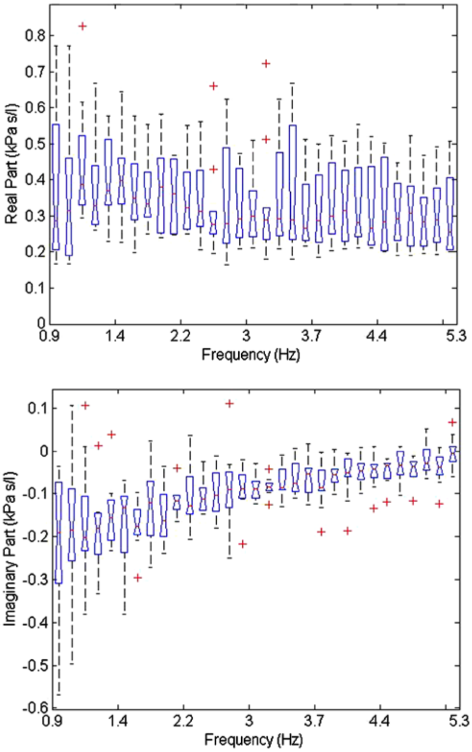

Fig. 5.16 The complex impedance by means of its real (*top*) and imaginary (*bottom*) parts measured from the 10 volunteers at low frequencies. Each frequency point is depicted by its mean value, distribution, and confidence intervals. Crosses denote outliers defined as 1.5 times further than the mean value

observed also in the slim (s) and the tall (t) subjects, but in order to quantify the relation of the ladder network structure with weight and height, more measurements are necessary. When validating with external data and population data, it is important to notice that the phase-locking effect takes place in frequencies lower than the standard clinical range of tested frequencies.

The results of the identification are plotted in Figs. 5.18, 5.19, 5.20, 5.21 and 5.22. The good results support the claim that when modeling the respiratory system with lumped parametric models, the use of FO terms is justified by the intrinsic structure of the respiratory tree. The fact that this augmented ladder network model comprising the full recurrent ladder network was able to capture the impedance is an indication that FO models are therefore natural solutions for a parsimonious modeling approach.

5.4 Summarizing Thoughts

Based on the results presented in this chapter, one may speculate that the proposed model can be successfully used for characterization of the intrinsic fractal geometry and its implicit properties: self-similarity and recurrence.

For the symmetric tree representation, we have established the following:

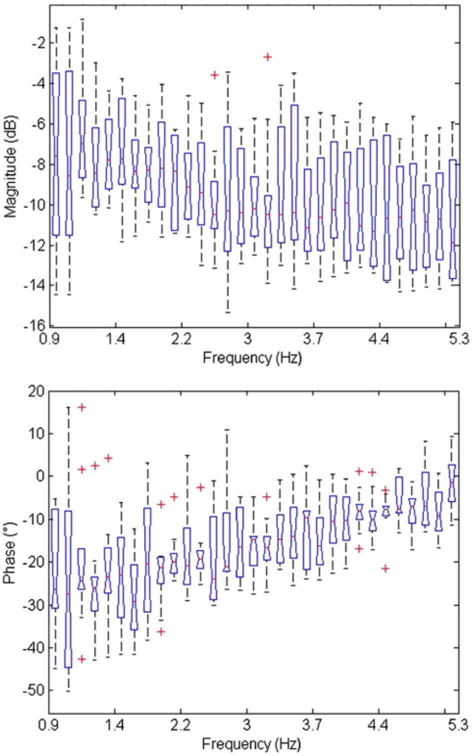

Fig. 5.17 The impedance by means of its magnitude (*top*) and phase (*bottom*) measured from the 10 volunteers at low frequencies. Each frequency point is depicted by its mean value, distribution, and confidence intervals. Crosses denote outliers defined as 1.5 times further than the mean value

Table 5.4 Identified values for the ladder network from data in 10 healthy subjects at low frequencies (0.5–5.7 Hz). See text for symbol explanations

	R_{UA}	L_{UA}	C_{UA}	R_{e1}	L_{e1}	C_{e1}	2λ	$2/\alpha$	$\chi/2$	E_T
1	0.428	0.005	0.451	0.009	0.001	0.001	2.40	0.12	0.55	0.06
2	0.353	0.006	0.648	0.007	0.001	0.001	2.34	0.29	0.56	0.05
3	1.015	0.066	0.150	0.017	0.005	0.001	2.19	0.53	0.57	0.09
4[a]	0.342	0.010	0.457	0.012	0.001	0.001	2.08	0.47	0.57	0.07
5[a]	0.389	0.004	0.534	0.009	0.001	0.001	2.23	0.54	0.56	0.06
6s	0.854	0.015	1.434	0.027	0.005	0.001	2.17	0.51	0.57	0.09
7	0.365	0.080	0.286	0.004	0.002	0.001	2.25	0.49	0.60	0.03
8t	1.221	0.535	0.028	0.003	0.002	0.001	2.31	0.58	0.61	0.05
9[a]	0.731	0.047	0.204	0.006	0.003	0.001	2.29	0.50	0.58	0.05
10[b]	0.717	0.074	0.156	0.014	0.004	0.001	2.21	0.46	0.58	0.12

[a] denotes occasional smoker

[b] denotes outlier data: male, 59 years, 80 kg, 1.75 m; s denotes slim (53 kg); t denotes tall (1.90)

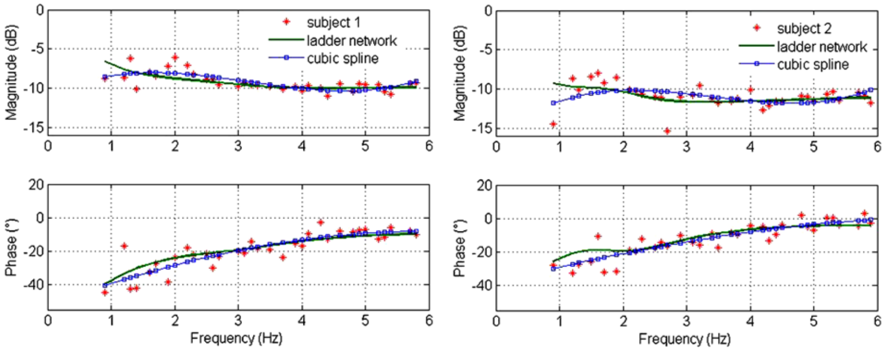

Fig. 5.18 Result of the identification for subject 1 (*left*) and subject 2 (*right*)

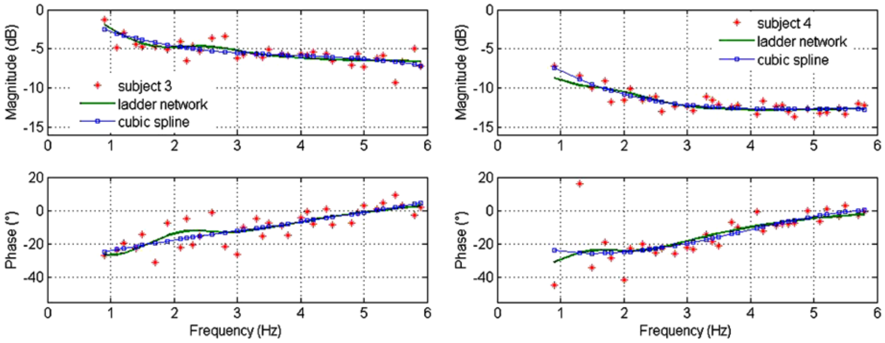

Fig. 5.19 Result of the identification for subject 3 (*left*) and subject 4 (*right*)

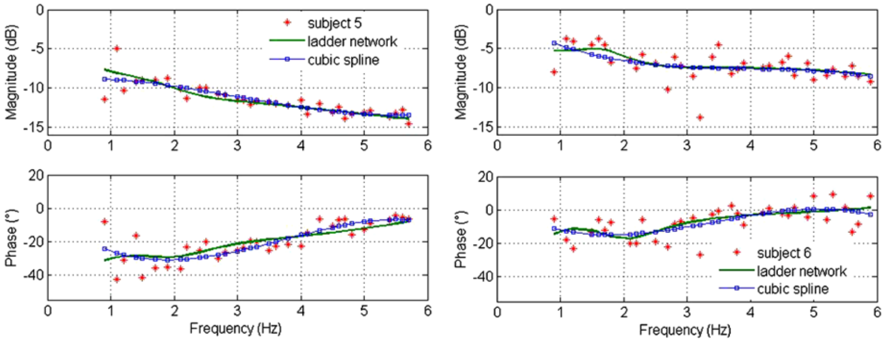

Fig. 5.20 Result of the identification for subject 5 (*left*) and subject 6 (*right*)

- a recurrent relation can be obtained between the model parameters of each airway generation;
- the recurrence leads to a homothety factor, which is different for the conductive zone (levels 1–15) and respiratory zone (levels 16–24);

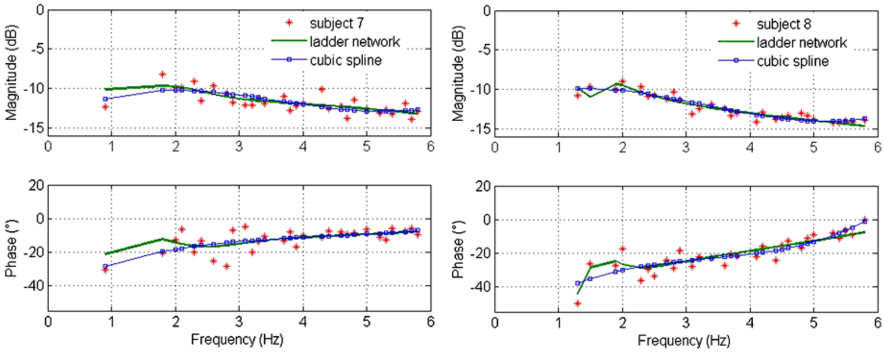

Fig. 5.21 Result of the identification for subject 7 (*left*) and subject 8 (*right*)

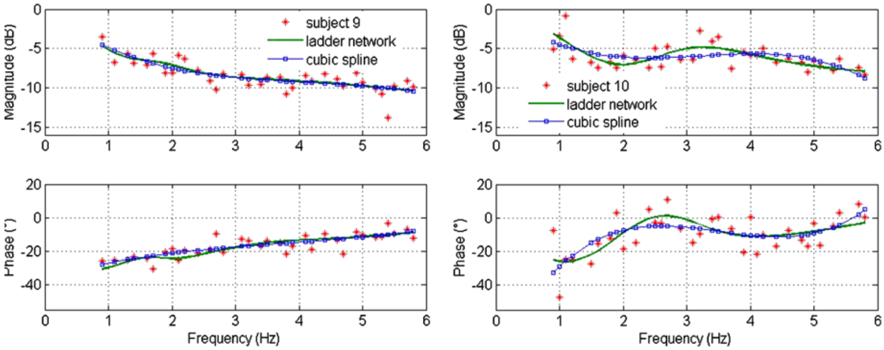

Fig. 5.22 Result of the identification for subject 9 (*left*) and subject 10 (*right*)

- if symmetry exists, then the total input impedance can be calculated in a simplified, recurrent manner;
- the impedance exhibits a fractional-order behavior leading to a fractional-order value for the symmetric case, if the convergence conditions are fulfilled; otherwise the constant-phase behavior is missing;
- the ratios for inertance $1/\alpha$ and for the conductance o elements do not play a role in determining the value of the fractional order, the latter being determined solely by the ratios of the resistance λ and of the capacitance χ elements.

For the asymmetric tree representation, the following remarks can be summarized:

- the impedance exhibits a fractional-order behavior in the nominal case, without fulfilling the theoretical conditions for convergence; in this case it is difficult to calculate analytically the value of the fractional order;
- the fractional-order behavior is still present, although the fractal structure and dimension is not uniquely characterized;
- the fractional-order value is changing if the degree of asymmetry is changed (this observation is significant for the case of diseased lungs).

Chapter 6
Modeling the Respiratory Tree by Means of Mechanical Analogy

6.1 Basic Elements

When a force F is applied to an object with initial length ℓ and cross-sectional area A, a mechanical stress σ results. Consequently, a deformation occurs $\Delta\ell$, which leads us to define the strain ε:

$$\sigma = \frac{F}{A}; \qquad \varepsilon = \frac{\Delta\ell}{\ell} \tag{6.1}$$

The following relations can be defined between the stress and the strain, in which E is the elasticity modulus and η the viscosity coefficient [23].

For a spring:

$$\sigma(t) = E \cdot \varepsilon(t) \tag{6.2}$$

denoting Hooke's Law and the linear elastic behavior of materials. Supposing a sinusoidal strain applied to the material: $\varepsilon(t) = \varepsilon_0 \cdot \sin(\omega t)$, then the stress is in phase with the strain and its amplitude is given by $E \cdot \varepsilon_0$. Observing the corresponding stress–strain curve from Fig. 6.1-left, the load and unload are following the same path; therefore no loss of energy occurs. Hence, we conclude that elastic materials do not show energy-dissipation phenomena.

For a damper:

$$\sigma(t) = \mu \cdot \frac{d}{dt}\varepsilon(t) \tag{6.3}$$

denoting Newton's Law and describing the viscous behavior of a linear flow. Applying a similar strain as above, the stress will lead the strain by 90° with an amplitude equal to $\mu \cdot \omega \cdot \varepsilon_0$. The amplitude is therefore frequency dependent. When both signals are opposite in phase, as depicted in Fig. 6.1-right, we see that all the energy is used (equal hysteresis on both sides). Therefore, we conclude that viscous materials show energy-dissipation phenomena.

Emerging theories of fractional calculus allowed the appearance of a novel term, i.e. a *spring-pot* of order n (with $0 \le n \le 1$), characterized by the following relation:

$$\sigma(t) = \eta \cdot \frac{d^n}{dt^n}\varepsilon(t) \tag{6.4}$$

C.M. Ionescu, *The Human Respiratory System*, Series in BioEngineering,
DOI 10.1007/978-1-4471-5388-7_6,

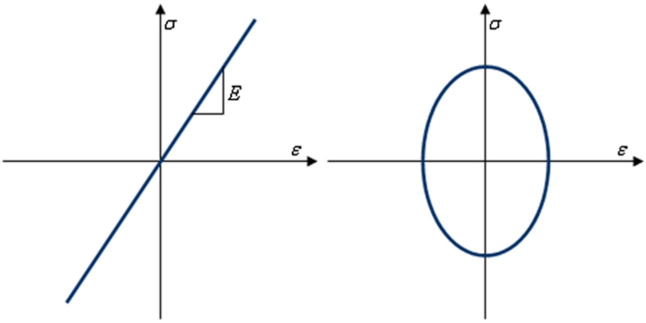

Fig. 6.1 The stress–strain curves for a spring (*left*) and for a damper (*right*)

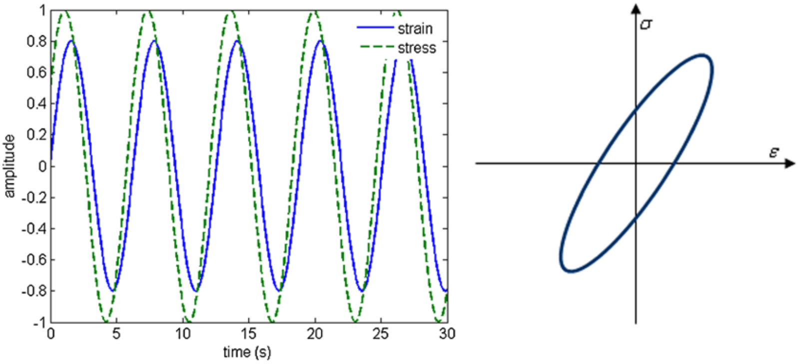

Fig. 6.2 The stress–strain curve of a viscoelastic material

which denotes an element characterizing the combined effect of elastic and viscous behavior in a material. Notice that for $n = 0$ we have a pure elastic element (spring), whereas for $n = 1$ we have a pure viscous element (dashpot).

When the material undergoes a dynamical excitation, the stress will lead the strain in phase with an angle φ between 0 en $\pi/2$ radians. The amplitude of the stress is $E_d \cdot \varepsilon$, from

$$\sigma(t) = E_d(\omega) \cdot \varepsilon \cdot \sin\bigl(\omega t + \varphi(\omega)\bigr) \tag{6.5}$$

The plot of the stress and strain below shows that part of the energy is stored and part is dissipated, resulting in hysteresis.

The most simple combination of the basic elements presented above is a series spring-dashpot, referred to as the *Maxwell element* and depicted in Fig. 6.3.

For a constant strain variation (i.e. step inputs) we have

$$\sigma(t) = E \cdot \varepsilon \cdot e^{(-\frac{t}{\tau})} \tag{6.6}$$

with $\tau = \frac{\eta}{E}$, the relaxation time, as from (6.4). At time $t = 0$ the spring will be fully taut, whereas the damper will remain unchanged. Within some time, the damper will

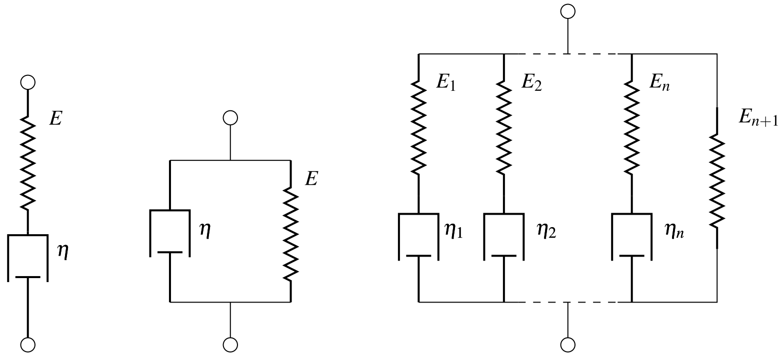

Fig. 6.3 From left to right: the Maxwell and the Kelvin–Voigt element, followed by a combination of the two

start to take over the stress from the spring and relax it. Hence, the Maxwell element can characterize stress relaxation.

For a constant stress variation (i.e. step inputs) we have

$$\varepsilon(t) = \sigma\left(\frac{1}{E} + \frac{t}{\eta}\right) \tag{6.7}$$

which shows a spontaneous elastic strain with the stress. When the stress variation stops, the spring returns to its initial position, while the damper remains in an irreversible state.

A second possible combination is the parallel spring-dashpot, referred to as the *Kelvin–Voigt* element (see Fig. 6.3). In this model, we cannot account for a constant strain, given the force on the damper must be infinitely big; hence, this model does not show stress-relaxation properties.

Assuming a constant stress input, we have

$$\varepsilon(t) = \frac{\sigma}{E}\left(1 - e^{(-\frac{t}{\tau})}\right) \tag{6.8}$$

with $\tau = \frac{\eta}{E}$, the relaxation time. At the time instant $t = 0$, the damper begins to change slowly, while the spring reached asymptotically its taut value. Hence, the Kelvin–Voigt element describes the creep phenomena in viscoelastic materials well.

Finally, both the Maxwell element and the Kelvin–Voigt element do not fully characterize the true viscoelastic behavior. Hence, combining both elements seems to be a good solution to overcome their individual limitation: N parallel Maxwell-elements, all in parallel with an extra spring, as shown in Fig. 6.3.

6.2 Mechanical Analogue and Ladder Network Models

In this chapter we treat the *symmetric* structure of the respiratory tree [97, 135, 163, 164], with morphological values given as in Table 2.1. For the purpose of this

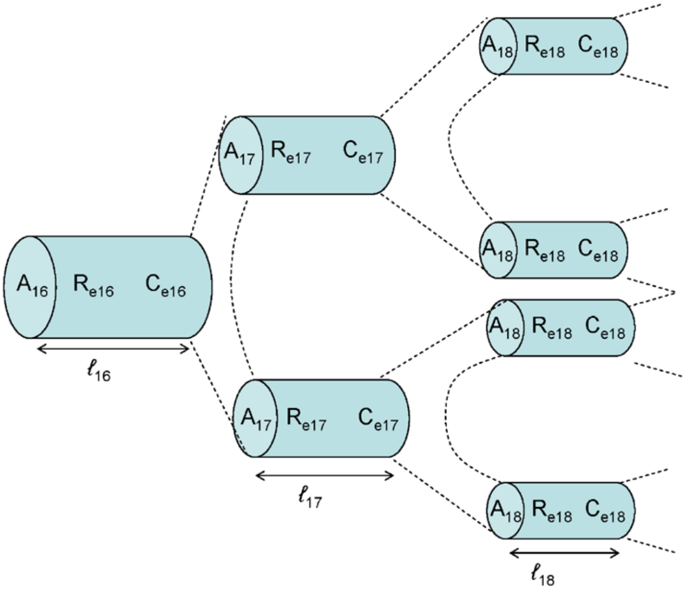

Fig. 6.4 A schematic representation of the electrical model for the lung parenchymal tissue as an interconnected system (starting from level 16)

study, we investigate the airways within the respiratory zone, corresponding to levels 16–24, as schematically depicted in Fig. 6.4 [66, 164]. In this figure, A_m denotes the cross-sectional area, ℓ_m denotes the length, R_{em} the resistance, and C_{em} the capacitance of one airway tube from level m, respectively.

In the respiratory zone, the oxygen and carbon dioxide exchange takes place between the air in the lung and the blood in the small-diameter blood vessels that surround the alveoli. The gas compression impedance is modeled by a $R_{\mathrm{GC}} - L_{\mathrm{GC}} - C_{\mathrm{GC}}$ series impedance, as described in Chap. 5.

For the case of elastic tube walls, we have no viscous losses, thus no conductance G_e element, as defined in Sect. 4.2.1. Using (4.62)–(4.64), the equations for the electrical model are given by

$$\begin{aligned} e_0 &= R_{e1} i_1 + e_1; \quad & e_1 &= \frac{R_{e2}}{2} i_2 + e_2 \\ i_1 &= i_2 + C_{e1} \dot{e}_1; \quad & i_2 &= 2 C_{e2} \dot{e}_2 \end{aligned} \tag{6.9}$$

with e the voltage and i the current represented as in Fig. 6.5. The electro-mechanical analogy is given in Table 6.1.

Using the electro-mechanical analogy from Table 6.1, we can derive an equivalent mechanical model. This can be done starting from the electrical model equations (6.9). The electrical element ($R_e C_e$ series) corresponds to the mechanical Kelvin–Voigt element (spring in parallel with dashpot):

$$\begin{aligned} F_0 &= B_1 v_1 + F_1; \quad F_1 = \frac{B_2}{2} v_2 + F_2 \\ v_1 &= v_2 + \frac{1}{K_1}\dot{F}_1; \quad v_2 = \frac{2}{K_2}\dot{F}_2 \end{aligned} \tag{6.10}$$

The values of resistors and capacitors are calculated with the model from Fig. 6.5 and relations (4.62)–(4.64): $R_{e16} = 1.57$ kPa/(l/s) and $C_{e16} = 3.06 \cdot 10^{-6}$ l/kPa. From these values one can calculate the equivalent B_m^* and K_m^* values, taking into account that $R_{em} = R_{em}^*/2^{m-1}$ and $C_{em} = 2^{m-1}C_{em}^*$, respectively, from (5.1) and (5.3). The superscript $*$ denotes a single branch in the respiratory level represented by the subscript m:

$$\begin{aligned} B_m^* &= \frac{F_m}{v_m} = \frac{P_m}{Q_m}A_m^2 = R_{em}^* A_m^2 \\ K_m^* &= \frac{F_m}{x_m} = \frac{P_m}{V_m}A_m^2 = \frac{A_m^2}{C_{em}^*} \end{aligned} \tag{6.11}$$

with P the pressure, Q the flow, V the volume, $A_m = \pi R_m^2$ the area, R_m the radius of a tube at level m, and x the axial displacement.

Figure 6.6-left depicts the evolution of the parameters in a single tube at a certain level m, whereas Fig. 6.6-right depicts their evolution in the entire level. One

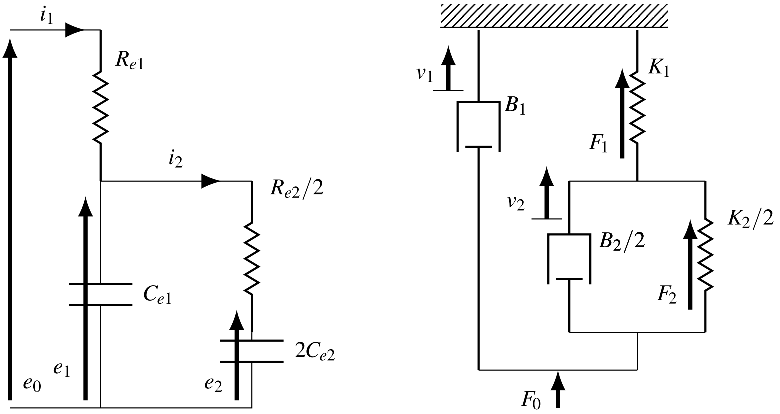

Fig. 6.5 An illustrating example of the first two levels in the electrical and the mechanical networks

Table 6.1 The electro-mechanical analogy

Electrical	Mechanical
Voltage e [V]	Force F [N]
Current i [A]	Velocity v [m/s]
Resistance R_e [Ω]	Damping constant B [N s/m]
Capacitance C_e [F]	Spring constant $1/K$ [m/N]
Inductance L_e [H]	Mass M [kg]

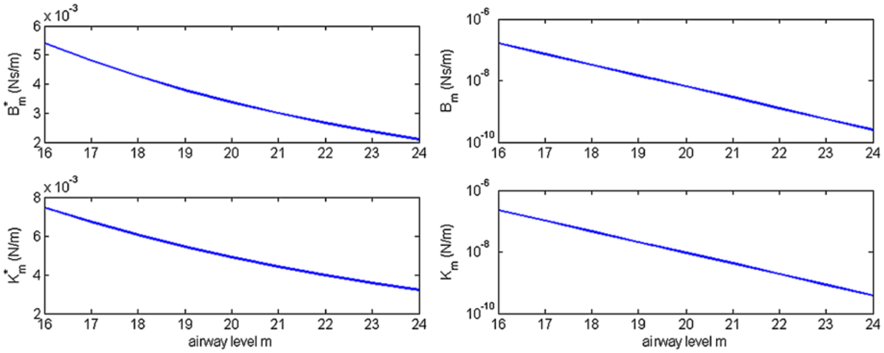

Fig. 6.6 Parameter evolution in singular tubes (*left*) and in the entire level (*right*), for levels 16–24

may observe that the evolution in a single tube, in consecutive levels is quasi-linear for both parameters (Fig. 6.6-left). However, since the total parameter values from Fig. 6.6-right depend on the total number of tubes within each level, they change as an exponential decaying function. When represented on a logarithmic scale, one can observe a quasi-linear behavior, as in Fig. 6.6-right.

In a similar manner as the electrical impedance, one may obtain $H(s)$, which defines the relation from velocity (input) to force (output) $F(s)/v(s)$, with s the Laplace operator. The transfer function of a cell in the ladder network consisting of one damper and one spring, is

$$H(s) = B + \frac{K}{s} \tag{6.12}$$

which can be evaluated over a range of frequencies, e.g. $\omega \in [10^{-5}, 10^{5}]$, with the result depicted in Fig. 6.7. In this figure '24' denotes that the $H(s)$ is calculated at level 24; '23' denotes that $H(s)$ is calculated at level 23, etc.

Due to the fact that the network is dichotomous and symmetric, we can obtain the total mechanical impedance using the network structure as in Fig. 6.5, with B_m and K_m calculated with (6.11). Since the Kelvin–Voigt elements corresponding to one level are in parallel, their transfer function H_m will be in series with the spring in the level $m-1$. The next corresponding transfer function is in parallel with the damper in the level $m-1$, as depicted schematically by Fig. 6.9. In this manner, the total transfer function $H(s)$ can be determined, starting at level 24 [26].

The lung parenchyma consists of interwoven collagen (infinitely stiff) and elastin (elastic) fibers. Each level in the respiratory tree has a specific balance between these two components. In our model we take this balance into account in (4.14), in function of the cartilage percent (Table 2.1). Following this reasoning, a similar representation of the mechanical model is given in Fig. 6.8. Here, the cylinders represent the collagen fibers within one level, which are interconnected with elastin fibers, represented by inextensible unstressed strings. This representation varies from that of Bates in that it represents the total collagen–elastin distribution in a level and not

Fig. 6.7 The corresponding frequency response of the transfer function for the network of spring-dashpot elements in levels 16–24

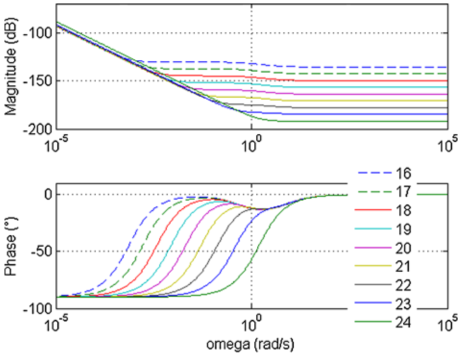

Fig. 6.8 A schematic representation of the mechanical model for the lung parenchymal tissue (levels 16–24)

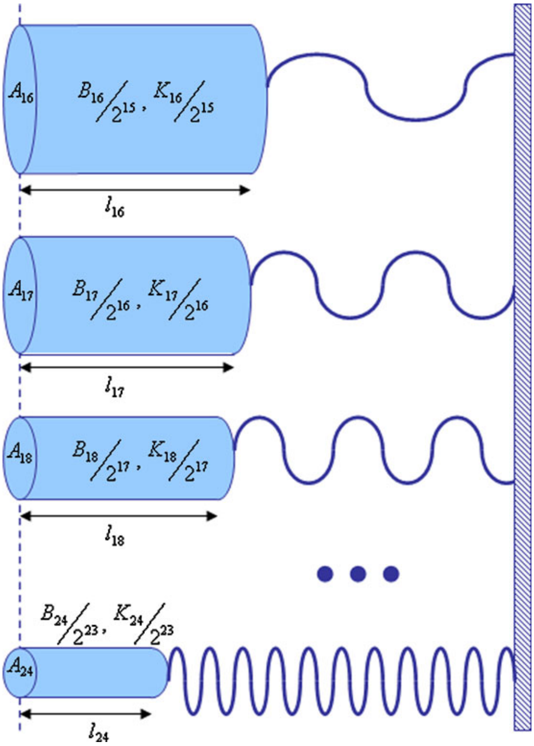

in a single tissue strip [8]. In his book, Bates shows the clinical implication of viscoelastic (mechanical) models and their bearing to the origin of FO lumped models. A more medical-oriented comprehensive book is therefore referred in [9].

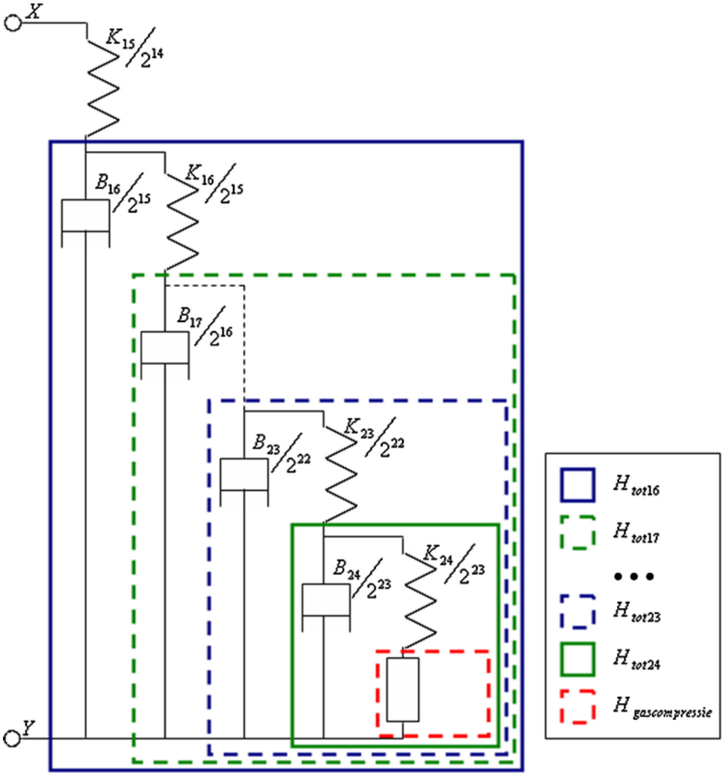

Fig. 6.9 A schematic representation of how the mechanical impedance $H(s)$ is calculated from level 24 by adding levels up to level 16 [26]

6.3 Stress–Strain Curves

6.3.1 Stepwise Variations of Strain

The elastic modulus is defined as the ratio between stress and strain properties. The Kelvin–Voigt body is the simplest viscoelastic model that can store and dissipate energy, consisting of a perfectly elastic element (i.e. spring) arranged in parallel with a purely viscous element (i.e. dashpot). Connecting the notions introduced in the previous sections of this chapter, we obtain the link between stress–strain properties and morphology of the lungs. The corresponding equation is given by

$$\sigma(t) = \frac{K\ell}{A}\varepsilon(t) + \frac{B\ell}{A}\frac{d\varepsilon(t)}{dt} \tag{6.13}$$

with σ the stress, ε the strain, ℓ the length, A the area and K, B the constants of the spring and dashpot, respectively [23]. The stress can be defined as pressure, whereas the latter is given by force distribution over the area. The strain ε is defined as the ratio of the change in length over the initial length: $\Delta\ell/\ell$. Starting with an unstressed tissue, we apply a strain that increases in steps of 10 % until it reaches 100 %. The new length can be calculated as

$$\ell_{\text{new}} = (1 + \varepsilon)\ell_{\text{old}} \tag{6.14}$$

with the subscript *old* denoting the characteristics before applying the strain step. Assuming a constant tissue volume V_t, the radius will decrease:

$$R_{\text{new}} = \frac{V_t}{2\pi \ell_{\text{new}} h} = \frac{R_{\text{old}} \cdot \ell_{\text{old}}}{\ell_{\text{new}}} \tag{6.15}$$

with R_{new} and R_{old} the new and old airway radius, respectively. We neglect the changes in the thickness h of the tube wall with changes in the strain. Applying a typical value for the oscillatory flow $Q = 0.5$ l/s at the oscillatory frequency of 5 Hz, the velocity v can be calculated as

$$v_{\text{new}} = \frac{5 \cdot 10^{-4}}{A_{\text{new}}} \tag{6.16}$$

Since the B's and K's are time-invariant material properties, the transfer function $H(s)$ from (6.12) will be independent of the strain. The elongation $\Delta\ell$ of the airway tube will have an effect on the pipeline equation (4.13) which can be expressed as

$$p + \frac{h}{R(1 - \nu_p^2)} \left(\frac{K\ell}{A} \varepsilon + \frac{B\ell}{A} \frac{d\varepsilon}{dt} \right) = 0 \tag{6.17}$$

with ν_p the Poisson coefficient. The new values for the pressure and the stress are given by

$$P_{\text{new}} = \frac{F_{\text{new}}}{A_{\text{new}}} = \frac{v_{\text{new}} H}{\pi R_{\text{new}}^2} \tag{6.18}$$

$$\sigma_{\text{new}} = -P_{\text{new}} \frac{R_{\text{new}}(1 - \nu_p^2)}{h} \tag{6.19}$$

Hence, in this representation, the stress and strain properties can be evaluated using (6.14)–(6.19), leading to the stress–strain curves depicted in Fig. 6.10. The strain is increased in steps of 10 % from 10 to 100 %. Starting from level 24, one can then calculate the stress–strain curve at the input of each level. This then will give rheological information in the context that all parenchymal levels are interconnected.

As expected, the stress increases with the degree of elongation applied to the entire structure. The more levels we have in our structure, the higher the values of the stress–strain curve, due to higher amount of cartilage tissue (collagen). The latter observation has been illustrated in Fig. 6.8. The obtained results are qualitatively similar to those reported in literature [18, 96, 143]. Quantitatively, it is not possible to make an evaluation of our model, since the values reported hitherto in the literature are based on excised tissue strips.

Fig. 6.10 The stress–strain curves for a ladder network model of the level 24, building up additional cells, until level 16

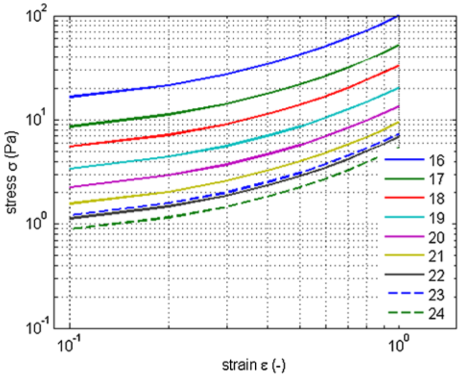

Fig. 6.11 Example of stress and strain as a function of time with normalized units. Observe the phase shift

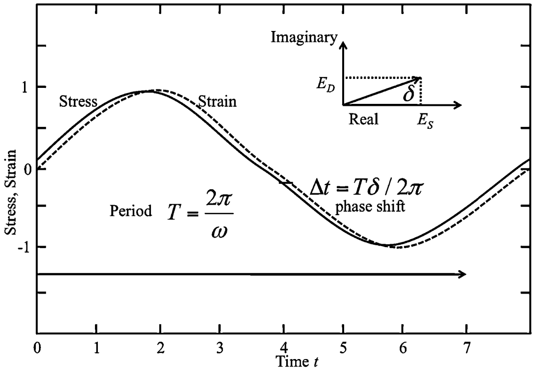

6.3.2 Sinusoidal Variations of Strain

In the previous section, a stepwise strain excitation was applied in steps of 10 % until 100 %. Similarly to the calculus presented previously, the new fractal-mechanical model can be excited by a dynamic strain excitation; i.e. a sinusoidal excitation, which is closer to the breathing phenomenon. It is noteworthy to realize that since our model consists of a combination of springs and dampers, the stress–strain curve will be a result of the two individual curves from Fig. 6.1. Moreover, since we only characterize the respiratory zone by the viscoelastic lung parenchyma, we also expect a stress–strain curve as in Fig. 6.2.

Oscillatory stress and strain histories are represented by sinusoid functions. Suppose we have $\sigma(\omega t) = \sigma_0 \sin \pi t$, in which t denotes time, σ_0 denotes the amplitude, and ω is the angular frequency. The sine function repeats every 2π radians. So $\sigma(\omega t + 2\pi) = \sigma(\omega t)$. The time T required for the sine function to complete one cycle is obtained from $\omega T = 2\pi$, or $T = 2\pi/\omega$. In a viscoelastic material, stress and strain sinusoids are out of phase. To represent the phase shift consider two sinusoids, $\sin \omega t$ and $\sin(\omega t + \delta)$. The quantity δ is called the phase angle. In a plot of the two waveforms, the sinusoids are shifted with respect to each other on the time axis as in Fig. 6.11. Recall that the cosine function is $\pi/2$ radians out of phase with the sine function. Sinusoidal functions that represent oscillatory quantities in which phase is important are commonly written in complex exponential notation.

Applying a sinusoidal strain on the lung model with amplitude ε_0 and frequency $\omega = 2\pi f$ it follows that

$$\varepsilon(t) = \varepsilon_0 \cdot \sin(\omega t) \tag{6.20}$$

which results in a sinusoidal stress response, as in (6.5).

Using $\sin(a+b) = \cos(a)\sin(b) + \sin(a)\cos(b)$ yields

$$\begin{aligned}\sigma(t) &= E_d \cdot \varepsilon_0 \cdot \sin(\omega t + \varphi_d)\\ &= \varepsilon_0 \cdot \left[E_d \cos(\varphi_d)\sin(\omega t) + E_d \sin(\varphi_d)\cos(\omega t)\right]\end{aligned} \tag{6.21}$$

with E_d the dynamic modulus and φ_d the corresponding angle. Introducing the storage modulus $E_S = E_d \cos(\varphi_d)$ and the loss modulus $E_D = E_d \sin(\varphi_d)$, one may calculate the dissipated energy W in one cycle:

$$\begin{aligned}W &= \int \sigma \, d\varepsilon\\ &= \int_0^T \varepsilon_0 \cdot \left[E_d \cos(\varphi_d)\sin(\omega t) + E_d \sin(\varphi_d)\cos(\omega t)\right]\varepsilon_0 \sin(\omega t)\, dt\\ &= \pi \varepsilon_0^2 E_d \sin(\varphi_d)\end{aligned} \tag{6.22}$$

with $T = 1/f$ the corresponding period and f the frequency in Hz. The used energy is therefore directly proportional to the loss modulus. The storage modulus is a measure for the necessary power to overcome elastic forces and to release them when the excitation ceases.

Viscoelastic properties can be analyzed by means of a frequency-dependent complex elastic modulus E^* [23]:

$$E^*(j\omega) = \frac{\sigma(j\omega)}{\varepsilon(j\omega)} = E_S(\omega) + jE_D(\omega) \tag{6.23}$$

whereas the parameters are related to the viscous behavior of the material.

In the Kelvin–Voigt model, the relation between stress and strain is given by

$$\sigma(t) = E\varepsilon(t) + \eta \frac{d\varepsilon(t)}{dt} \tag{6.24}$$

Applying the Fourier transform leads to

$$E^*(j\omega) = E + \eta(j\omega) \tag{6.25}$$

For a viscoelastic material the mechanical impedance $H(s)$ of this material is given by

$$H(s) = \frac{K}{s} + B \tag{6.26}$$

which leads to the following relation for the complex modulus:

$$E^*(s) = \frac{\ell}{A} \cdot s \cdot H(s) \tag{6.27}$$

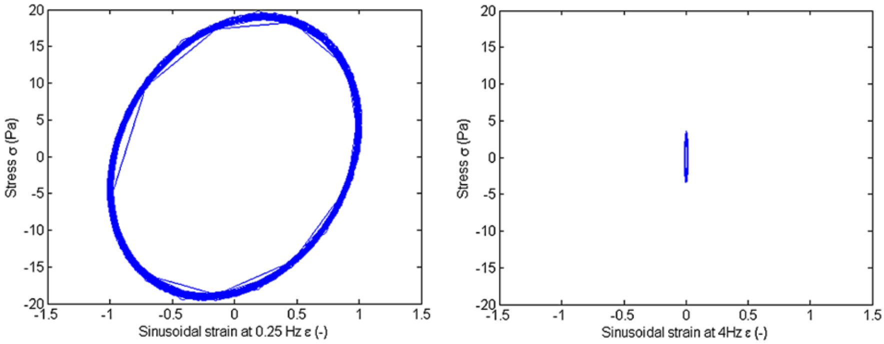

Fig. 6.12 The stress–strain curve for sinusoidal strain at $\varepsilon(t) = \varepsilon_0 \cdot \sin(2\pi 0.25t)$ and at $\varepsilon(t) = \varepsilon_0 \cdot \sin(2\pi 4t)$

Applying the Laplace transform on the sinusoidal strain $\varepsilon(t) = \varepsilon_0 \cdot \sin(\omega t)$ we have

$$\varepsilon(s) = \varepsilon_0 \frac{\omega}{s^2 + \omega^2} \tag{6.28}$$

and the stress can be calculated as

$$\begin{aligned} \sigma(s) &= E^*(s)\varepsilon(s) \\ \sigma(t) &= L^{-1}\{\sigma(s)\} \end{aligned} \tag{6.29}$$

The results for a sinusoidal strain of $\omega = 2\pi 0.25$ (rad/s) and of $\omega = 2\pi 4$ (rad/s) are given in Fig. 6.12.

As expected, the energy is dissipated and the ellipse curve is deformed to a hysteresis curve [62]. There is also a slope on this hysteresis loop, which points to the fact that both energy storage and dissipation occurs during the test. As the frequency increases, the loop becomes closer to the ellipse form, suggesting that viscous behavior becomes negligible.

The evolution with frequency of the complex modulus from (6.27) is depicted in Fig. 6.13. It is clear that the real part varies with frequency, hence if one would identify a lumped model in a limited frequency range, would need a fractional-order model [67], as explained by means of (3.11). Notice that in our model representation, the ladder network leads to a similar effect of constant-phase behavior as that of the electrical ladder network in the previous chapter. This effect is visible in Fig. 6.13-right, below the $\omega < 10^{0.3}$ (rad/s) frequency range.

In a similar study, Craiem acknowledged the necessity of a fractional order to characterize viscoelasticity in the arterial wall of the circulatory system in a sheep [23]. Compared to the values in literature, one may say that our results are within reasonable values. For example, in [162] the authors obtain values of 2–8 kPa for the storage modulus, respectively values of 0.2–1 kPa for the loss modulus in guinea pigs lung tissue strips. It is difficult to compare our results to those from [162], because they come from animal studies and in general, most of the authors provide values from tissue strips instead of an interconnected system of lung parenchymal airways.

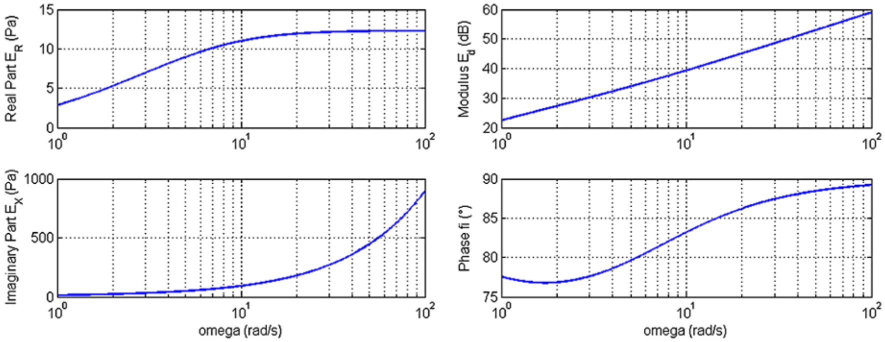

Fig. 6.13 The frequency response of the elastic modulus in its complex representation (*left*) and in its equivalent Bode plot (*right*)

6.4 Relation Between Lumped FO Model Parameters and Viscoelasticity

A typical feature of FO models is that of characterizing history-dependent systems [169]. Viscoelastic materials, such as polymers, i.e. materials very close in their dynamics to lung parenchymal tissue, are history dependent [9]. The following simple, nonlinear relation allows for prediction of history dependence, called nonlinear superposition, which allows the relaxation function to depend on strain level:

$$\sigma(t) = \int_0^t E\big(t-\tau, \varepsilon(\tau)\big)\frac{d\varepsilon}{d\tau}\,d\tau \tag{6.30}$$

A similar equation may be written for stress-dependent creep in the compliance formulation.

$$\varepsilon(t) = \int_0^t J\big(t-\tau, \sigma(\tau)\big)\frac{d\sigma}{d\tau}\,d\tau \tag{6.31}$$

If a series of relaxation tests is done at different strain levels, relaxation will be observed, but the functional form of the relaxation curves will depend on the strain level.

However, nonlinearly viscoelastic materials cannot be analyzed via Laplace transforms because the Laplace transform is a linear operator. The interrelation between creep and relaxation is developed here by direct construction. Look at Fig. 6.14 and start by writing the time-dependent strain due to a constant stress σ_c as a sum of immediate and delayed Heaviside step functions in time $H(t)$,

$$\varepsilon(t) = \varepsilon(0)H(t) + \sum_{i=0}^{N}\Delta\varepsilon_i H(t-t_i) \tag{6.32}$$

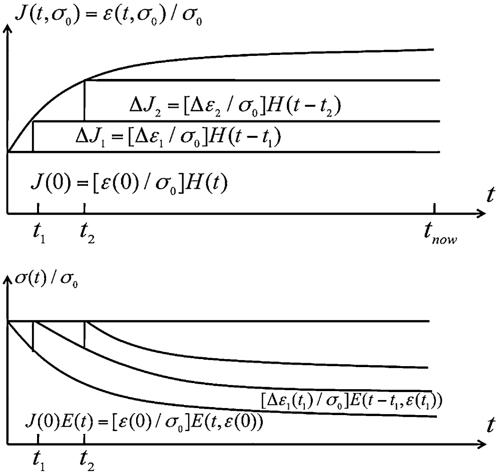

Fig. 6.14 Example of history-dependent strain as a function of constant stress divided into Heaviside step functions

Based on the definition of the relaxation function each step strain in the summation gives rise to a relaxing component of stress. Assuming there is no effect from the interaction between the step components, we have

$$\sigma_c = \varepsilon(0)E(t,\varepsilon) + \sum_{i=0}^{N} \Delta\varepsilon_i E(t-t_i,\varepsilon) \tag{6.33}$$

Divide by σ_c, and use the definition of the creep compliance from (6.4),

$$1 = J(0)E(t,\varepsilon) + \sum_{i=0}^{N} \Delta J_i E\big(t-t_i,\varepsilon(t_i)\big) \tag{6.34}$$

If we consider in the limit that we have infinitely many fine step components (i.e. similar rationale to the decomposition of the recurrent ladder network elements), we obtain a Stieltjes integral, with τ as a time variable of integration:

$$1 = J(0)E(t,\varepsilon) + \int_0^t E\big(t-\tau,\varepsilon(\tau)\big)\frac{dJ(\tau,\sigma_c)}{d\tau}\,d\tau \tag{6.35}$$

This relationship is implicit and is analogous to the one for the linear case. In order to develop an explicit form, one needs to assume a specific form for the creep behavior. First, assume the creep function to be separable into a stress-dependent portion and a power law in time. Such a form, called quasi-linear viscoelasticity has been used widely in biomechanics [49]:

$$J(t,\sigma) = g(\sigma)t^n = \left[g_1 + g_2\sigma + g_3\sigma^2 + \cdots\right]t^n \tag{6.36}$$

where g_1, g_2, g_3 are constants. Consider the following relaxation function, with f_1, f_2, f_3 constants, as a trial solution. A separable form does not give rise to a solution:

$$E(t,\sigma) = f_1 t^{-n} + f_2\varepsilon(t)t^{-2n} + f_3\varepsilon(t)^2 t^{-3n} + \cdots \tag{6.37}$$

The creep strain is $\varepsilon(t) = J(t)\sigma_c = \varepsilon_0 t^n$, with ε_0 as the strain amplitude. Substitution leads to

$$1 = \int_0^t \left[f_1(t-\tau)^{-n} + f_2\varepsilon_0(t-\tau)^n(t-\tau)^{-2n} + f_3\varepsilon_0^2(t-\tau)^{2n}(t-\tau)^{-3n} + \cdots\right] \times \left[g_1 + g_2\sigma + g_3\sigma^2 + \cdots\right] n\tau^{n-1}\,d\tau \tag{6.38}$$

Factorization of the stress-dependent and the time-dependent parts delivers:

$$1 = \left[g_1 + g_2\sigma + g_3\sigma^2 + \cdots\right]\left[f_1 + f_2\varepsilon_0 + f_3\varepsilon_0^2 + \cdots\right] \int_0^t n(t-\tau)^{-n}\tau^{n-1}\,d\tau \tag{6.39}$$

The integral part gives results ($\frac{1}{n\pi}\sin n\pi$) identical to the linear case by Laplace transformation of the integral and an identity involving the gamma function. This is in fact quite similar to the definitions of fractional derivative as from fractional calculus (see the Appendix for detailed information). Again, we stumble on the obvious origin of genesis of lumped fractional-order models characterizing viscoelastic properties in the lungs. However, we need to make an explicit link between the constitutive equations of viscoelastic behavior and the fractional-order terms in FO models.

Before proceeding further with our theoretical development, it is necessary to discuss the implications of stress–strain response in relation to history dependence. Consider a stress history that is triangular in time (i.e. quite close to the actual breathing patterns in some patients):

$$\begin{aligned}
&\sigma(t) = 0 \quad \text{for } t < 0,\\
&\sigma(t) = (\sigma_0/t_1)t, \quad \text{for } 0 < t < t_1,\\
&\sigma(t) = 2\sigma_0 - (\sigma_0/t1)t, \quad \text{for } t_1 < t < 2t_1, \quad \text{and}\\
&\sigma(t) = 0 \quad \text{for } 2t_1 < t < \infty
\end{aligned} \tag{6.40}$$

Use the Boltzmann integral and consider that slopes are piecewise constant:

$$\begin{aligned}
&\varepsilon(t) = 0 \quad \text{for } t < 0,\\
&\varepsilon(t) = \frac{\sigma_0}{t_1}\int_0^t J(t-\tau)\,d\tau, \quad \text{for } 0 < t < t_1\\
&\varepsilon(t) = \frac{\sigma_0}{t_1}\left[\int_0^{t_1} J(t-\tau)\,d\tau - \int_{t_1}^{t} J(t-\tau)\,d\tau\right], \quad \text{for } t_1 < t < 2t_1, \quad \text{and}\\
&\varepsilon(t) = \frac{\sigma_0}{t_1}\left[\int_0^{t_1} J(t-\tau)\,d\tau - \int_{t_1}^{2t_1} J(t-\tau)\,d\tau\right], \quad \text{for } 2t_1 < t < \infty
\end{aligned} \tag{6.41}$$

Substitute the given creep function and decompose the exponential as follows:

$$\int_a^b \left[1 - \exp\left(-\frac{t-\tau}{\tau_c}\right)\right] d\tau = b - a - \tau_c\left[e^{-\frac{t-b}{\tau_c}} - e^{-\frac{t-a}{\tau_c}}\right] \tag{6.42}$$

A more meaningful approach to theoretical basis of viscoelasticity is to look at the response of viscoelastic materials to sinusoidal load, referred to as *dynamic behavior*. Notice, however, that the term dynamic in this context has no connection with inertial terms or resonance and should not be confounded with other linear terminology. The dynamic behavior is of special interest because viscoelastic materials are used in situations in which the damping of vibration or the absorption of sound is necessary. At first sight, this may not be an obvious relation to the lungs, but bear in mind that lung parenchyma is very similar to polymers, used for such purposes.

The frequency of the sinusoidal load applied to an object or structure may be so slow that inertial terms do not appear (i.e. the subresonant regime). For respiratory impedance, these frequencies are below 1 Hz. By contrast, the frequency of the sinusoidal load may be high enough such that resonance occurs. For respiratory system, these resonant frequencies alternate starting from about 10 Hz. A separate study of these will be done in the next chapter. However, at a sufficiently high frequency, dynamic behavior is manifested as wave motion. This distinction between ranges of frequency does not appear in the classical continuum description of a homogeneous material, because the continuum view deals with differential elements of material. The lungs are non-homogeneous materials, and the degree of heterogeneity is an important classification index for correlating the impedance to structural changes in pathology [145].

The stress–strain plot for a linearly viscoelastic material under sinusoidal load is elliptical, as demonstrated in previous sections of this chapter, and the shape of the ellipse is independent of stress. By contrast, an elastic–plastic material exhibits a threshold. Below the threshold yield stress, the material is elastic, and its stress–strain plot is a straight line. Above the yield stress, irreversible deformation occurs in the elastic-plastic material.

Let the history of strain to be purely sinusoidal. In complex exponential form, $\varepsilon(t) = \varepsilon_0 e^{i\omega t}$, with ω the angular frequency in radians per second. We make use of the Boltzmann superposition integral, with the lower limit taken as $-\infty$ since in strict mathematical terms a sinusoid has no starting point:

$$\sigma(t) = \int_{-\infty}^{t} E(t-\tau)\frac{d\varepsilon}{d\tau}\,d\tau \tag{6.43}$$

To achieve explicit convergence of the integral, we must decompose the relaxation function into the sum $E(t) \cong \hat{E}(t) + E_e$ with $E_e = \lim_{t-\infty} E(t) = E(\infty)$ called the *equilibrium modulus* (in the context of polymers) and substitute the strain history in (6.43). Recalling that $E_e > 0$ for solids and $E_e = 0$ for liquids, it follows that

$$\sigma(t) = E_e\varepsilon_0 e^{i\omega t} + i\omega\varepsilon_0 \int_{-\infty}^{t} \hat{E}(t-\tau)e^{i\tau\omega}\,d\tau \tag{6.44}$$

Make the substitution of a new time variable $t' = t - \tau$, and obtain

$$\sigma(t) = \varepsilon_0 e^{i\omega t}\left[E_e + \omega\int_0^{\infty} \hat{E}(t')\sin\omega t'\,dt' + i\omega\int_0^{\infty} \hat{E}(t')\cos\omega t'\,dt'\right] \tag{6.45}$$

If the strain is sinusoidal in time, so is the stress, but they are no longer in phase. The stress–strain relation becomes

$$\sigma(t) = E^*(\omega)\varepsilon(t) = (E_S + jE_D)\varepsilon(t) \tag{6.46}$$

in which, with $\hat{E}(t) = E(t) - E(\infty)$,

$$E_S(\omega) \cong E_e^+ \omega \int_0^\infty \hat{E}\left(t'\right) \sin \omega t' \, dt' \tag{6.47}$$

is called the *storage modulus*,

$$E_D(\omega) \cong \omega \int_0^\infty \hat{E}\left(t'\right) \cos \omega t' \, dt' \tag{6.48}$$

is called the *loss modulus*, and the *loss tangent* (dimensionless) is given by

$$\tan \delta(\omega) \cong \frac{E_D(\omega)}{E_S(\omega)} \tag{6.49}$$

The above equations give the dynamic, frequency-dependent mechanical properties in terms of the relaxation modulus. E_S is the component of the stress–strain ratio in phase with the applied strain, while E_D is the component 90 degrees out of phase. These relations may be inverted in order to obtain

$$E(t) = E_e + \frac{2}{\pi} \int_0^\infty \frac{(E_S - E_e)}{\omega} \sin \omega t \, d\omega \tag{6.50}$$

$$E(t) = E_e + \frac{2}{\pi} \int_0^\infty \frac{E_D}{\omega} \cos \omega t \, d\omega \tag{6.51}$$

Physically, the quantity δ represents the phase angle between the stress and strain sinusoids. The dynamic stress–strain relation can be expressed as

$$\sigma(t) = \left|E^*(\omega)\right| \varepsilon_0 e^{j(\omega t + \delta)} \tag{6.52}$$

with $E^* = E_S + jE_D$.

One can also consider the dynamic behavior in the compliance formulation. In the modulus formulation, $\sigma(t) = E^*(\omega)\varepsilon(t)$ is an algebraic equation for sinusoidal loading, hence the strain is

$$\varepsilon(t) = \frac{1}{E^*(\omega)} \sigma(t) \tag{6.53}$$

However, the complex compliance J^* is defined by the equation

$$\varepsilon(t) = J^*(\omega)\sigma(t), \tag{6.54}$$

with $J^* = J_S - jJ_D$. Hence, the relationship between the dynamic compliance and the dynamic modulus is

$$J^*(\omega) = \frac{1}{E^*(\omega)} \tag{6.55}$$

This is considerably simpler than the corresponding relation for the transient creep and relaxation properties. Notice that $\tan \delta(\omega) = J_D(\omega)/J_S(\omega)$.

Plots of dynamic viscoelastic functions may assume a variety of forms. For instance, one may plot the dynamic properties versus frequency, with the frequency scale given logarithmically. Alternatively, one may plot the imaginary part versus the real part: E_D versus E_S or J_D versus J_S. Such a plot is often used in dielectric

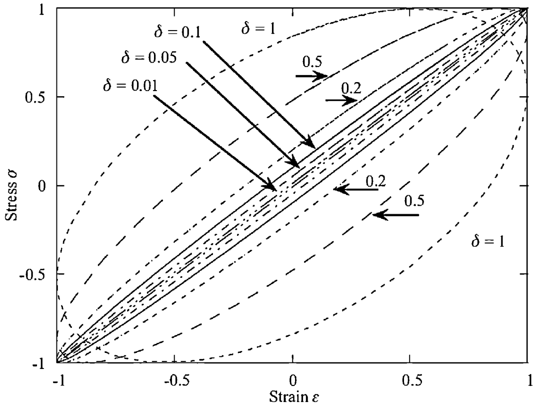

Fig. 6.15 Example of stress–strain curves with slopes and intercepts for a linear viscoelastic material under oscillatory load, e.g. viscoelastic rubber

relaxation studies and is referred to as a Cole–Cole plot [80]. A single relaxation-time process gives a semicircle in a Cole–Cole plot. Another usual graphical representation is that of stiffness versus loss: $|E^*|$ versus $\tan\delta$, i.e. a stiffness–loss map.

In the remainder of this section, we shall focus our attention on the loss tangent and its relation to hysteresis loops. Consider again the relation between stress and strain in dynamic loading of a linearly viscoelastic material. First, the shape of the stress–strain curve is determined, and a relation for the loss tangent is developed. Hitherto, we have considered stress and strain as they depend on time. Suppose we have

$$\varepsilon = B\sin\omega t \tag{6.56}$$

and

$$\sigma = D\sin(\omega t + \delta) \tag{6.57}$$

which determine an elliptic Lissajous as given in Fig. 6.15, the direct consequence of linearly viscoelastic behavior. For some materials, the curve of stress versus strain in dynamic loading is not elliptical, but has pointed ends; this behavior is a manifestation of material nonlinearity. The loop is called a hysteresis loop. Hysteresis, in general, refers to a lag between cause and effect. In some contexts, such as the study of polymers, a specific view of hysteresis is taken; it then represents a frequency-independent damping, as discussed in the next chapter. To interpret the dimensions and intercepts of the figure, first let the intersection with the axis be called A, assumed to occur at time t_1. Then, consider $A = B\sin\omega t_1$ and

$$0 = D\sin(\omega t_1 + \delta) = D\sin(\omega t_1)\cos\delta + D\cos\omega t_1\sin\delta \tag{6.58}$$

Substituting $\sin\omega t_1 = \frac{A}{B}$ and $\cos\omega t_1 = \frac{1}{B}\sqrt{B^2 - A^2}$ into the last expression, we obtain

$$0 = D\frac{A}{B}\cos\delta + \frac{D}{B}\sqrt{B^2 - A^2}\sin\delta \tag{6.59}$$

Squaring the last expression leads to $A^2\cos^2\delta = B^2\sin^2\delta - A^2\sin^2\delta$, hence $A^2(\cos^2\delta + \sin^2\delta) = B^2\sin^2\delta$. This implies that $\sin\delta = \frac{A}{B}$. If $\omega t = -\delta$, then $\sigma = 0$.

Consequently, $\varepsilon_A = B\sin(-\delta)$ at the intersection. However, the ellipse is symmetric, so $A = B\sin\delta$.

Now, with the aim of obtaining a different relation between δ and the parameters of the ellipse, consider the point of maximum stress, which occurs when $\sin(\omega t + \delta) = 1$. Then $\omega t + \delta = \frac{\pi}{2}$, and referring to Fig. 6.15, we have

$$C = \varepsilon(\sigma_{\max}) = B\sin\left(\frac{\pi}{2} - \delta\right) = B\left[\sin\frac{\pi}{2}\cos(-\delta) + \cos\frac{\pi}{2}\sin(-\delta)\right] \tag{6.60}$$

thus

$$\varepsilon(\sigma_{\max}) = B\cos\delta \tag{6.61}$$

Since $A = B\sin\delta$, then $\tan\delta = A/C$, it follows that the width of the elliptic Lissajous figure is a measure of the loss angle δ of a linearly viscoelastic material.

To obtain a relation for the *storage modulus* E_S in connection with the elliptic stress–strain curve, suppose $\varepsilon = \varepsilon_{\max}\sin\omega t$. Then, the stress σ at the maximum strain is $\sigma = E_S\varepsilon_{\max}\sin\omega t + E_D\varepsilon_{\max}\cos\omega t$. For $\varepsilon_{\max}, \omega t = \pi/2$, then $\sigma = E_S\varepsilon_{\max}$ so the slope of the line from the origin to the point of maximum strain is E_S, as shown in Fig. 6.15.

To obtain a relation for the *storage compliance* J_S in connection with the elliptic stress–strain curve, suppose $\sigma = \sigma_{\max}\sin\omega t$. Then, the strain at the maximum stress is, by the definition of $|J^*|$, $\varepsilon = (J_S - jJ_D)\sigma_{\max}$. Hence $\varepsilon = J_S\sigma_{\max}\sin\omega t - J_D\sigma_{\max}\cos\omega t$, because $j = \sqrt{-1}$ implies a 90-degree phase shift. For $\sigma_{\max}, \omega t = \pi/2$, then $\varepsilon = J_S\sigma_{\max}$ or $\sigma_{\max} = \varepsilon/J_S$. Therefore, the slope of the line from the origin to the point of maximum stress is $1/J_S$, as shown in Fig. 6.15. Observe that $1/J_S \geq E_S$ equality occurs if the material is elastic (i.e. $\delta = 0$).

Consider now the time $t = 0$, and $\varepsilon = 0$. It follows that $\sigma(t) = D\sin\delta$, with $\sigma(t) = \varepsilon_{\max}[E_S\sin\omega t + E_D\cos\omega t]$. For $t = 0$, $\sigma_0 = \varepsilon_{\max}E_D$, which is marked as an intercept on the ordinate in Fig. 6.15.

Also observe that $\sigma_{\max} = |E_*|\varepsilon_{\max}$, so, again referring to Fig. 6.15, this modulus corresponds to a line of intermediate slope between that for E_S and that for $1/J_S$.

To conclude this line of thoughts, the loss angle δ, or the loss tangent $\tan\delta$, may be considered as the fundamental measure of damping in a linear material.

However, the above derivation is not limited to linear viscoelastic properties. Also nonlinear viscoelastic materials can be excited by sinusoidal loads. The simplest dynamic example of the effect of nonlinearity is nonlinear elasticity in one dimension. Suppose that

$$\sigma = f(\varepsilon) \tag{6.62}$$

If we write $f(\varepsilon)$ as a power series we obtain

$$\sigma = a_1\varepsilon^1 + a_2\varepsilon^2 + a_3\varepsilon^3 + \cdots \tag{6.63}$$

and if the strain is sinusoidal, say $\varepsilon = \cos\omega t$ and using trigonometric identities, for example,

$$\cos^2\omega t = \frac{1}{2}(1 + \cos 2\omega t) \tag{6.64}$$

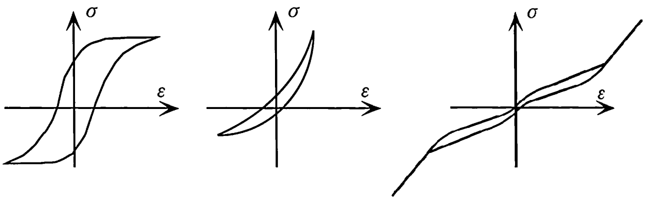

Fig. 6.16 Several example of the response from nonlinear materials under cyclic load. Observe that the loop is no longer elliptical. Such response is very similar to pressure–volume loops in diagnosed patients

and

$$\cos^3 \omega t = \frac{1}{4}\cos 3\omega t + \frac{3}{4}\cos \omega t \tag{6.65}$$

then we can express the stress as a sum of sinusoids:

$$\sigma(t) = \sum_{n=1}^{N} a_n \sin n\omega_n t + \phi_n \tag{6.66}$$

Consequently, the effect of the nonlinearity is to generate higher harmonics (integer multiples) of the driving frequency. If the driving signal contains several frequencies, the material responds at new frequencies corresponding to sums and differences of the drive frequencies.

As for a viscoelastic material obeying nonlinear superposition, analysis shows that higher harmonics are generated as well. In the electrical engineering community, this sort of response is called harmonic distortion. Response of a nonlinear material to cyclic load may also be visualized via a plot of stress versus strain, as shown schematically in Fig. 6.16. In a nonlinear material, the plot is no longer elliptical in shape, as it is in a linear material, because harmonic distortion generates a non-elliptic plot. Many types of curves are observed in healthy and pathologic lung function pressure–volume loops. The area within the closed curve, as in the case of linear materials, represents the energy per volume dissipated per cycle, also known as *work of breathing*.

6.5 Implications in Pathology

Materials can be time dependent in ways other than viscoelastic response. For example, a structural member, such as an alveolar wall, can gradually become stiffer and stronger if additional substance is added in response to heavy loading [7, 43]. By contrast, it can become less dense and weaker if material is removed in response to minimal loading. Biological materials intrinsically behave in this way, performing an *adaptation* to maintain functionality of the system. For instance, a change in stiffness of the lung parenchyma can be assumed to depend on its porosity [86]:

$$\sigma_{ij} = (\xi_0 + e)C_{ijkl}(e)\varepsilon_{kl} \tag{6.67}$$

Specifically, a change e in the solid volume fraction of a porous material with respect to a reference volume fraction drives the adaptation process:

$$\frac{de}{dt} = a(e) + A_{ij}(\varepsilon_{ij}) \tag{6.68}$$

Here, a and A are coefficients that depend on the type of structure, e.g. airway walls, alveolar walls, etc. Almost all biologic materials are adaptive, i.e. *smart*, and pose specific characteristics as self-repair, adaptability to various environmental conditions, self-assembly, homeostasis, and the capacity for regeneration.

Recoil pressures at same lung volumes are always less during deflation than inflation (hysteresis), hence the mechanical energy (work of breathing) follows the same property. The area within the pressure–volume loops represents the lost energy per breathing cycle. During quiet breathing, this area is nearly independent of frequency. Thus, under constant amplitude cycling, energy dissipation is nearly independent of frequency. However, the dissipation is proportional to the product of resistance and frequency, hence, implying that the resistance is inversely proportional to the frequency.

The constant-phase model from [57], i.e. (3.9), describing the viscoelastic properties of lung tissues, has been considered superior to the classic spring and dashpot representation, since it contains a combined element. Although the electrical analogue of viscoelastic processes as well as the phenomenological and mechanical approaches yield good quantitative correspondence with data, they lack anatomic and mechanistic specificity.

Later models tried to deal with dynamic tissue behavior on a mechanistic basis. Some mechanisms have been proposed as contributors to the constant-phase tissue viscoelasticity, such as the structural disposition of fibers and their instantaneous configuration during motion, since elastic fibers dissipate energy as they slip with respect to each other. Additionally, lung tissue might exhibit molecular mechanisms similar to those proposed for polymer rheology. Maksym [96] suggested a role for the relative stress-bearing contributions of collagen and elastin fibers based on the differential elastic properties of these two types of fibers, in which collagen fibers were progressively recruited with strain. Bates [8] also proposed that the nonlinear elastic properties and linear elastic behavior of lung tissues arise from different physical processes, whereas elastic recoil is linked to geometry as fibers rearrange themselves; stress adaptation would reflect a process of diffusion due to the thermal motion of the fibers with respect to each other and to the ground substance.

6.6 Summary

Based on the concept laid down in previous chapters, the analogy to mechanical parametric models has been made. This analogy has been used as a theoretical basis for analyzing viscoelastic properties in the lung tissue. The relation between the lumped fractional-order model parameters and viscoelasticity has been developed and the implications in pathology are discussed.

It is obvious to see that changes in mechanical structure, parameters, and geometry can be applied to evaluate their effect on the total properties of the tissues and airways in the lungs. So far, we have established both an electrical and a mechanical analogue to perform such evaluations.

In the next chapters, we shall apply the concepts and models learned so far on real impedance data and signals measured from volunteers.

Chapter 7
Frequency Domain: Parametric Model Selection and Evaluation

7.1 Overview of Available Models for Evaluating the Respiratory Impedance

Hitherto in this book, we have discussed available models from literature in Chap. 3, and we have established an anatomical and morphological basis for the appearance of recurrent ladder networks in Chap. 4. The next step was to provide analogy between the respiratory airways and the electrical, respectively mechanical elements. In Chap. 5 was also established the convergence of such ladder networks to a lumped parametric model of fractional order, where clearly changes in the airways structure lead to changes in the fractional-order values. Similarly, in Chap. 6 we discussed the relation of such ladder networks to viscoelastic properties of lung parenchyma, in a mechanical context.

Such ladder network models are useful to characterize broad ranges of frequencies, since they allow (more) significant variations of model parameters with frequency. However, certain variability in the fractional-order value is not captured, making these models unsuitable for multi-fractal systems. Of course, multiple ladder networks will lead to multiple fractional-order lumped parametric models. It is also meaningful to observe that the recurrent values in the airways are different for conductive zone (i.e. nose, pharynx, larynx, trachea, bronchi, bronchioles, and terminal bronchioles) than for the respiratory zone (i.e. below terminal bronchioles, where gas exchange takes place). This already suggests that the complexity of the respiratory system naturally requires a multi-fractal parametric model [63].

It has already been acknowledged in the research community that multi-fractal lumped parametric models are indeed good candidates for characterizing the respiratory impedance, but the genesis of such models is not fully understood. Such complexity in both structure and function has gathered the attention of many biologists, physiologists, anesthesiologists, and engineers [63]. As the emerging tools from fractional calculus and chaos theory are rather new in biological applications, we must recognize the need for a well-defined terminology and standardized analysis.

C.M. Ionescu, *The Human Respiratory System*, Series in BioEngineering,
DOI 10.1007/978-1-4471-5388-7_7,

This chapter will guide the reader in choosing the suitable model for the frequency range where respiratory input impedance needs to be analyzed.

7.2 FO Model Selection in Relation to Various Frequency Intervals

It is important to understand the limitations of lumped FO parametric models over various frequency intervals. There exists no generally valid model, since the variations of the impedance values with frequency are significant, as we will see later in this chapter. To begin with, we discuss the available FO models in order of complexity.

The first model, from here-on referred to as FO1, is defined as

$$Z_{\mathrm{FO1}}(s) = R_r + \frac{1}{C_r s^{\beta_r}} \tag{7.1}$$

with R_r the resistance (kPa/(l/s)), C_r the capacitance (l/kPa) and $0 \leq \beta_r \leq 1$. This model was initially developed for frequencies below 5 Hz, whereas the effect of the inductance is negligible [57]. Therefore, when evaluating such model in the 4–48 Hz frequency interval, one may expect poor performance results.

The second model included in our discussion, referred to as FO2, is obtained from (7.1) by adding the inductance term [58]:

$$Z_{\mathrm{FO2}}(s) = R_r + L_r s + \frac{1}{C_r s^{\beta_r}} \tag{7.2}$$

As described in Chap. 3, experimental results show that in several patients, the real part of the complex impedance may increase with frequency. Splitting (7.2) in its real and imaginary parts yields

$$Z_r(j\omega) = R_r + \frac{1}{C_r \omega^{\beta_r}} \cos\left(\frac{\beta_r \pi}{2}\right) + j \cdot \left[L_r \omega \sin\left(\frac{\pi}{2}\right) - \frac{1}{C_r \omega^{\beta_r}} \sin\left(\frac{\beta_r \pi}{2}\right)\right] \tag{7.3}$$

Hence, it can be observed that when frequency increases, the real part of the term in C_r decreases, therefore unable to characterize correctly the impedance. However, if the model is evaluated in a frequency range in which the real part of the impedance is decreasing with frequency, the model performs well.

The third model (FO3) introduced in the discussion contains an extra FO term in the inductance:

$$Z_{\mathrm{FO3}}(s) = R_r + L_r s^{\alpha_r} + \frac{1}{C_r s^{\beta_r}} \tag{7.4}$$

which is in fact (3.10). This model is able to counteract the limitation of FO2 and captures both increasing, as well as decreasing variations with frequency in the real part of the impedance.

The last model (FO4) proposed for evaluation in this chapter is based on FO3, but takes into account the ability of fractional-order terms to model constant elements in the gain of the term. This results in a simplification of the FO3 model to

$$Z_{\mathrm{FO4}}(s) = L_r s^{\alpha_r} + \frac{1}{C_r s^{\beta_r}} \tag{7.5}$$

which does not contain the resistance term R_r. Indeed, the theory of fractional-order appearance in ladder networks shows that the effects of R_r are indirectly captured in the values of the FO terms and FO coefficients [76, 118]. Hence, if it turns out that the R_r term in FO3 will not give significant values, then FO4 will have less model parameters to be interpreted by the clinicians.

In order to illustrate the above rationale, two groups of respiratory impedance data will be employed in an example. The remainder of this section presents the results of these models and makes a discussion on the model parameter values.

7.2.1 Relation Between Model Parameters and Physiology

Recalling here the identification procedure described in Sect. 3.1 using (3.8), one obtains the complex impedance by means of its real and imaginary parts as a function of frequency. From the real and imaginary parts of the complex impedance, the model parameters of (7.5) were identified. The modeling errors were calculated with (3.12).

From the identified model parameters one can derive the tissue damping G_r and elastance H_r, defined as [57, 58]

$$\begin{aligned} G_r &= \frac{1}{C_r \omega^{\beta_r}} \cos\left(\beta_r \frac{\pi}{2}\right) \\ H_r &= \frac{1}{C_r \omega^{\beta_r}} \sin\left(\beta_r \frac{\pi}{2}\right) \end{aligned} \tag{7.6}$$

both in (l/kPa). The hysteresivity coefficient η_r (dimensionless) is defined as [42]

$$\eta_r = \frac{G_r}{H_r} \tag{7.7}$$

This parameter characterizes the heterogeneity of the lung tissue and has been shown to vary significantly with pathology. Since all these parameters from (7.6) and (7.7) are frequency dependent, the lumped identified values will in fact represent an averaged value over the 4–48 Hz frequency range.

Apart from the identified model parameters, some additional parameters are introduced in this analysis. The real part of the complex impedance at 6 Hz ($R6$) can be used to characterize the total resistance at this frequency, a parameter often encountered in clinical studies. The resonant frequency (*Frez*) could also be used as a classifying parameter, since it has been shown that the balance between elastic and inertial properties change with pathology.

We also introduce two dimensionless indices, namely the quality factor at 6 Hz ($QF6$), denoted by the ratio of the reactive power to the real power:

$$QF6 = \frac{\mathrm{Im}_6}{\mathrm{Re}_6} = \tan\phi_z \tag{7.8}$$

where Re_6 and Im_6 denote the real and imaginary parts of the complex impedance evaluated at 6 Hz and ϕ_z denotes the phase angle at 6 Hz. From (7.8), one can calculate the corresponding power factor $PF6$:

$$PF6 = \sqrt{\frac{1}{QF6^2+1}} = \sqrt{\frac{\mathrm{Re}_6^2}{(\mathrm{Re}_6^2+\mathrm{Im}_6^2)^2}} = \frac{\mathrm{Re}_6}{\mathrm{Re}_6^2+\mathrm{Im}_6^2} = \cos\phi_z \tag{7.9}$$

In engineering, the quality factor QF compares the time constant for decay of an oscillating physical system's amplitude with respect to its oscillation period. In other words, it compares the frequency at which a system oscillates to the rate at which it dissipates its energy, also known as the damping factor. For a second order linear time invariant system, a system is said to be over-damped if $QF < 0.5$, under-damped for $QF > 0.5$ and critically damped for $QF = 0.5$. In other words, a low QF denotes a high energy loss, while a high QF denotes a low energy loss. For the power factor PF, we find that for $PF = 0$ the energy flow is entirely reactive (hence the stored energy in the load returns to the source with each cycle), and if $PF = 1$, all the energy supplied by the source is consumed by the load.

Because FO are natural solutions in dielectric materials [80, 131], it is interesting to look at the permittivity property of respiratory tissues. In electric engineering, it is common to relate permittivity to a material's ability to transmit (or *permit*) an electric field. By electrical analogy, changes in trans-respiratory pressure relate to voltage difference, and changes in air flow relate to electrical current flows. When analyzing the permittivity index, one may refer to an increased permittivity when the same amount of air-displacement is achieved with smaller pressure difference. The complex permittivity has a real part, related to the stored energy within the medium and an imaginary part related to the dissipation (or loss) of energy within the medium. The imaginary part of permittivity corresponds to

$$\varepsilon_r = L_r \sin\left(\frac{\pi}{2}\alpha_r\right) \tag{7.10}$$

7.2.2 Subjects

The first group evaluated here consists of male volunteers without a history of respiratory disease, whose lung function tests were performed in the laboratory of Ghent University, Department of Electrical energy, Systems and Automation. Table 7.1 presents their biometric parameters, whereas a detailed analysis on their respiratory impedance parameters will be discussed later in this chapter.

A second group consists of former coal miners from the Petrosani area, tested periodically for their lung function at the 'Leon Danielo' Hospital in Cluj-Napoca,

Table 7.1 Biometric and spirometric parameters of the investigated subjects. Values are presented as mean ± standard deviations; % pred: predicted according to the asymptomatic males of the study; *VC*: vital capacity; FEV_1: forced expiratory volume in one second

	Healthy (17)	COPD (17)
Age (yrs)	26 ± 3	51 ± 11
Height (m)	1.67 ± 0.04	1.74 ± 0.09
Weight (kg)	64 ± 3.7	76 ± 8
VC % pred	–	89 ± 7
FEV_1 % pred	–	44 ± 6

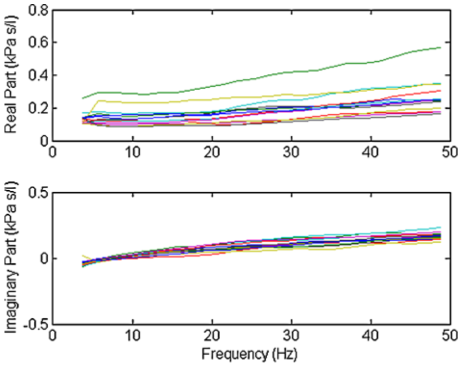

Fig. 7.1 Impedance plots for the healthy group

Romania, and diagnosed with COPD (Chronic Obstructive Pulmonary Disease). Table 7.1 presents the corresponding biometric and spirometric parameters.

The measurements of the input impedance values for these two groups of volunteers have been performed according to the forced oscillation lung function test described in Sect. 3.1 and the model from (3.8). The modeling errors have been calculated according to (3.12).

7.2.3 Results

The complex impedance values for the healthy and COPD patients have been obtained using (3.8) and they are depicted in Figs. 7.1 and 7.2. It can be observed that the healthy group has a resonant frequency (zero crossing in the imaginary part) around 8 Hz, whereas the COPD group around 16 Hz. The real part denotes mainly the mechanical resistance of the lung tissue, which is generally increased in the COPD group, resulting in higher work of breathing. Also, the resistance at low frequencies is much increased in the COPD group, suggesting increased damping of the lung parenchyma [64].

Next, the models from (7.1)–(7.5) are fitted to these complex impedance values. Identification is performed using the System Identification Toolbox within the MatLab platform, i.e. the `lsqnonlin` optimization function (a nonlinear least squares

Fig. 7.2 Impedance plots for the COPD group

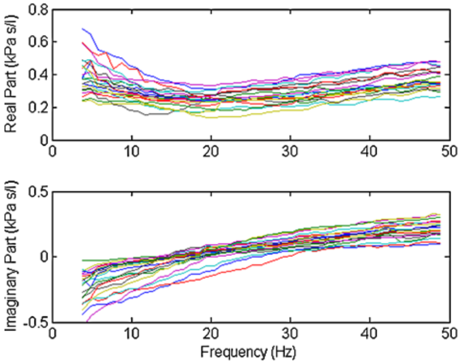

algorithm). The estimated parameter values along with the modeling error values are given in Table 7.2 for the healthy subjects, respectively in Table 7.3 for the COPD patients.

Independent Student's t tests with unequal sample size were used to compute the confidence intervals. The classification results were considered significant if $p \leq 0.05$ (i.e. within 95 % confidence interval).

The model parameters were compared between groups using `boxplots`. The lower and upper lines of the boxplot are the 25th and 75th percentiles of the sample group. The distance between the top and bottom of the box is the interquartile range. The line in the middle of the box is the sample group median value. If the median is not centered in the box, it is an indication of skewness. The whiskers are lines extending below and above the box. They show the extent of the rest of the sample group (unless there are outliers). Assuming no outliers, the maximum of the sample is the top of the upper whisker, respectively, the minimum is the bottom of the lower whisker. An outlier is a value more than 1.5 times the interquartile range away from the top or bottom of the box, and they are denoted by plus signs. A side by side comparison of two or more boxplots provides a graphical way to determine which groups have significantly different medians (typical measure in classification studies).

From the model parameters, one can calculate the tissue damping $G_r = \frac{1}{C_r}\cos(\frac{\pi}{2}\beta_r)$ and tissue elastance $H_r = \frac{1}{C_r}\sin(\frac{\pi}{2}\beta_r)$ [57] and tissue hysteresivity $\eta_r = G_r/H_r$ [42]. The relationship with (7.2) is found if the terms in C_r are rewritten as:

$$\frac{1}{C_r\omega_r^{\beta}}\cos\left(\frac{\pi}{2}\beta_r\right) - j\frac{1}{C_r\omega_r^{\beta}}\sin\left(\frac{\pi}{2}\beta_r\right) = \frac{G_r - jH_r}{\omega_r^{\beta}} \tag{7.11}$$

From Tables 7.2 and 7.3 one may observe that the model FO4 gives the smallest total error. This is due to the fact that two FO terms are present in their model structure, allowing both a decrease and increase in the real part of the impedance values. The FO2 model is the most commonly employed in clinical studies, with similar errors for the imaginary part, but higher error in the real part of the impedance than the FO4 model. The underlying reason is that the model can only capture a decrease

Table 7.2 Estimated model parameters and modeling errors for the healthy group in all candidate FO models

Healthy	FO1	FO2	FO3	FO4
R_r	0.22 ± 0.09	0.22 ± 0.09	0.01 ± 0.01	–
L_r	–	$0.7 \times 10^{-3} \pm 0.1 \times 10^{-3}$	$19.3 \times 10^{-3} \pm 3.02 \times 10^{-3}$	$3.74 \times 10^{-3} \pm 3.11 \times 10^{-3}$
α_r	–	–	0.46 ± 0.07	0.43 ± 0.10
$1/C_r$	0	1.36 ± 0.98	0.99 ± 0.03	2.02 ± 1.47
β_r	0.99 ± 0.00	0.99 ± 0.01	0.72 ± 0.08	0.79 ± 0.16
E_R	0.05 ± 0.02	0.05 ± 0.02	0.02 ± 0.01	0.02 ± 0.01
E_X	0.12 ± 0.02	0.01 ± 0.00	0.01 ± 0.00	0.01 ± 0.00
E_T	0.13 ± 0.03	0.05 ± 0.02	0.02 ± 0.01	0.02 ± 0.01

Table 7.3 Estimated model parameters and modeling errors for the COPD group in all candidate FO models

COPD	FO1	FO2	FO3	FO4
R_r	0.18 ± 0.08	0.26 ± 0.08	0.006 ± 0.01	–
L_r	–	$0.9 \times 10^{-3} \pm 0.1 \times 10^{-3}$	$7.7 \times 10^{-3} \pm 2.7 \times 10^{-3}$	$15.1 \times 10^{-3} \pm 8.1 \times 10^{-3}$
α_r	–	–	0.56 ± 0.06	0.59 ± 0.09
$1/C_r$	1.73 ± 3.32	5.20 ± 2.49	3.37 ± 1.73	2.94 ± 1.54
β_r	0.18 ± 0.36	0.83 ± 0.16	0.51 ± 0.08	0.52 ± 0.11
E_R	0.05 ± 0.01	0.04 ± 0.01	0.03 ± 0.01	0.03 ± 0.01
E_X	0.14 ± 0.02	0.02 ± 0.00	0.03 ± 0.01	0.02 ± 0.00
E_T	0.15 ± 0.02	0.05 ± 0.01	0.04 ± 0.02	0.04 ± 0.01

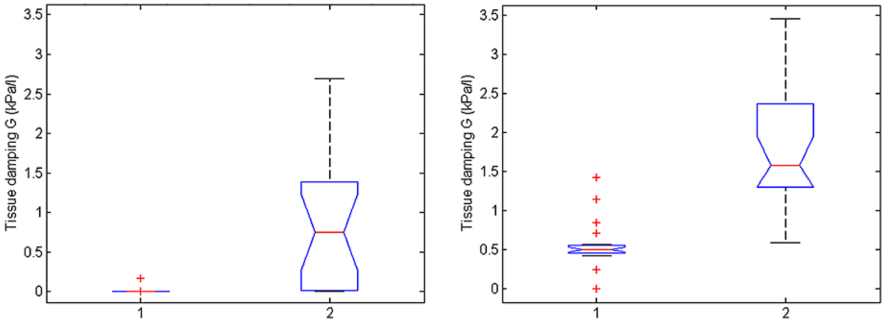

Fig. 7.3 Tissue damping G_r (kPa/l) with FO2, $p < 3e^{-5}$ (*left*) and with FO4, $p < 10^{e-8}$ (*right*); *1*: Healthy subjects and *2*: COPD patients

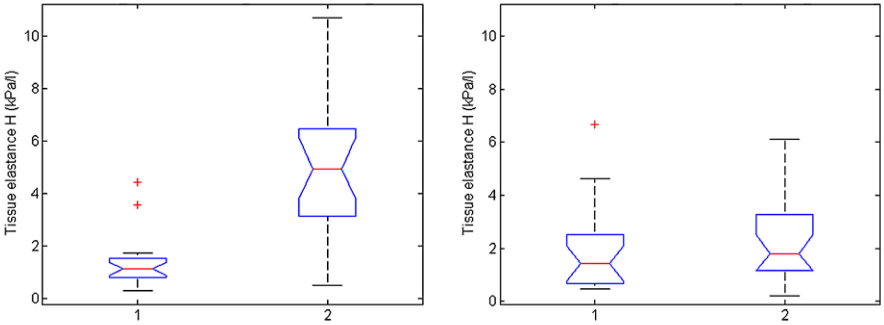

Fig. 7.4 Tissue elastance H_r (kPa/l) with FO2, $p < 0.0012$ (*left*) and with FO4, $p < 0.0004$ (*right*); *1*: Healthy subjects and *2*: COPD patients

in real part values of the impedance with frequency, whereas some patients may present an increase.

Figures 7.3, 7.4 and 7.5 depict the boxplots for the FO2 and FO4 for the tissue damping G_r, tissue elastance H_r and hysteresivity η_r. Due to the fact that FO2 has higher errors in fitting the impedance values, the results are no further discussed. Although a similarity exists between the values given by the two models, the discussion will be focused on the results obtained using FO4 in the 4–48 Hz frequency range.

The damping factor is a material parameter reflecting the capacity for energy absorption. In materials similar to polymers, as lung tissue properties are very much alike polymers, damping is mostly caused by viscoelasticity, i.e. the strain response lagging behind the applied stresses [142, 143, 145]. In both FO models, the exponent β_r governs the degree of the frequency dependence of tissue resistance and tissue elastance. The increased lung elastance $1/C_r$ (stiffness) in COPD results in higher values of tissue damping and tissue elastance, as observed in Figs. 7.3 and 7.4. The loss of lung parenchyma (empty spaced lung), consisting of collagen and elastin, both of which are responsible for characterizing lung elasticity, is the leading cause

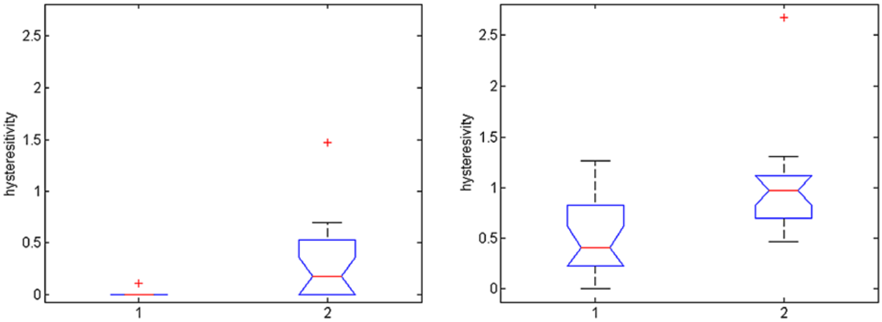

Fig. 7.5 Tissue hysteresivity η_r with FO2, $p < 0.0012$ (*left*) and with FO4, $p < 0.0004$ (*right*); *1*: Healthy subjects and *2*: COPD patients

of increased elastance in COPD. The hysteresivity coefficient η_r introduced in [42] is G_r/H_r in this model representation. Given the results observed in Fig. 7.5, it is possible to distinguish between tissue changes from healthy to COPD case. Since pathology of COPD involves significant variations between inspiratory and expiratory air flow, an increase in the hysteresivity coefficient η_r reflects increased inhomogeneities and structural changes in the lungs. In other words, the hysteresivity coefficient incorporates this property for the capacitor, that is, the COPD group has an increased capacitance, justified by the pathology of the disease. Many alveolar walls are lost by emphysematous lung destruction, the lungs become so loose and floppy that a small change in pressure is enough to maintain a large volume, thus the lungs in COPD are highly compliant (elastic) [6, 64, 71].

Another interesting aspect to note is that in the normal lung, the airways and lung parenchyma are interdependent, with airway caliber monotonically increasing with lung volume. In emphysematous lung, the caliber of small airways changes less than in the normal lung (defining compliant properties) and peripheral airway resistance may increase with increasing lung volume. At this point, the notion of space competition has been introduced [64], hypothesizing that enlarged emphysematous air spaces would compress the adjacent small airways, according to a nonlinear behavior. Therefore, the compression would be significantly higher at higher volumes rather than at low volumes, resulting in blunting or even reversing the airway caliber changes during lung inflation. This mechanism would therefore explain the significantly marked changes in model parameters in tissue hysteresivity depicted in Fig. 7.5. It would be interesting to notice that since small airway walls are collapsing, resulting in limited peripheral flow, it also leads to a reduction of airway depths. A correlation between such airway depths reduction in the diseased lung and model's non-integer orders might give insight on the progress of the disease in the lung.

In COPD, due to the sparseness of the lung tissue, the air flow in the alveoli is low, thus a low level of energy absorption is observed in Fig. 7.6. In healthy subjects, due to increased alveolar surface, higher levels of energy absorption are present, thus increased permittivity.

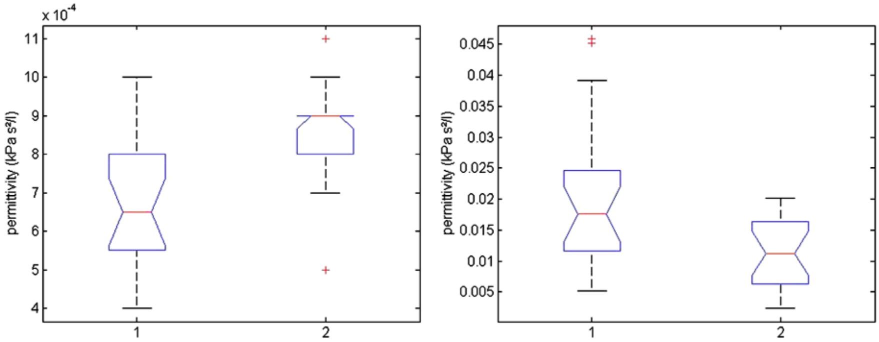

Fig. 7.6 Boxplots for the computed permittivity index ε_r in the FO2, $p < 0.0081$ (*left*) and in FO4, $p < 0.0002$ (*right*), in the two groups; *1*: Healthy subjects and *2*: COPD patients

The concluding observation for this section is that in general, FO4 identified more statistically significant model parameter values than FO2. In Figs. 7.3–7.5 FO4 parameters had identified similar variations between healthy and COPD groups. However, in Fig. 7.6, one can observe that FO4 identified a more realistic variation between healthy and COPD groups, i.e. a decreased permittivity index in COPD than in healthy.

7.3 Implications in Pathology

In the remainder of this chapter, the term *subjects* will refer to healthy volunteers, whereas the term *patients* will refer to diagnosed volunteers. The forced oscillations lung function test (FOT) was employed to perform measurements of the input respiratory impedance, as described in Sect. 3.1. The measurement was performed in the $f \in [4, 48]$ (Hz) frequency interval, respectively $\omega \in [25, 300]$ (rad/s).

Drop-out criteria were: (i) technically biased measurements (swallowing, coughing, glottis closure); (ii) fatigue and therefore reduced ability to breath spontaneously; and (iii) irregular breathing period. All subjects and patients were in stable physical conditions at the time of the evaluation.

Written and/or oral consent was obtained from all participants, and in case of children, from both children and their parents. Further selection of the participants was performed by oral/written questionnaire ruling out any other respiratory disease than the one envisaged for the study at the time of measurement or in the past 4 weeks. The remainder of this section presents the data for the participants to whom these inclusion criteria applied.

7.3.1 FOT Measurements on Adults

The *healthy adult group* evaluated in this study consists of 80 Caucasian volunteers (students) without a history of respiratory disease, whose lung function tests were

Table 7.4 Biometric parameters of the healthy subjects. Values are presented as mean ± standard deviation

	Healthy (80)
Female/male	31/49
Age (yrs)	27 ± 5
Height (m)	1.73 ± 0.17
Weight (kg)	69 ± 9.6

performed in our laboratory, and Table 7.4 presents their biometric parameters. The measurements were performed over the 2005–2009 time interval.

According to Pasker, the real (Re) and imaginary (Im) parts of the impedance can be predicted from their biometric data as given below [119]:

$$
\begin{aligned}
&\textbf{Female}\\
&\mathrm{Re}_0 = -0.4300 \cdot \underline{h} + 0.00165 \cdot \underline{w} - 0.00070 \cdot \underline{a} + 0.9312\\
&(RSD = 0.0619)\\
&\mathrm{Re}_1 = 0.01176 \cdot \underline{h} - 0.000106 \cdot \underline{w} - 0.000045 \cdot \underline{a} - 0.00817\\
&(RSD = 0.00256)\\
&\mathrm{Im}_0 = 0.2487 \cdot \underline{h} - 0.001700 \cdot \underline{w} - 0.00053 \cdot \underline{a} - 0.2158\\
&(RSD = 0.0406)\\
&\textbf{Male}\\
&\mathrm{Re}_0 = -0.2454 \cdot \underline{h} + 0.001564 \cdot \underline{w} - 0.00055 \cdot \underline{a} + 0.5919\\
&(RSD = 0.0493)\\
&\mathrm{Re}_1 = 0.01176 \cdot \underline{h} - 0.000106 \cdot \underline{w} - 0.000045 \cdot \underline{a} - 0.00817\\
&(RSD = 0.00197)\\
&\mathrm{Im}_0 = 0.2487 \cdot \underline{h} - 0.001700 \cdot \underline{w} - 0.00053 \cdot \underline{a} - 0.2158\\
&(RSD = 0.0306)
\end{aligned}
\tag{7.12}
$$

where $\underline{h}$ denotes height in (m), $\underline{w}$ denotes weight in (kg), $\underline{a}$ denotes age in (yrs) and *RSD* is the residual standard deviation. The real and imaginary parts of the impedance are fitted by the polynomial:

$$R_{rs} = \underline{D} f + \underline{E} \tag{7.13}$$

where f is the frequency. The coefficients calculated with (7.12) from their biometric parameters are then validated with the $\underline{E}$ and $\underline{D}$ coefficients resulting from the curve fitting. For the real part of the impedance, the coefficient $\underline{E}$ is validated with the coefficient Re_0, respectively the coefficient $\underline{D}$ is validated with the coefficient Re_1. For the imaginary part of the impedance, the coefficient $\underline{E}$ is validated with the coefficient Im_0. Since the volunteers were presumed healthy (but not guaranteed), the predicted values for terms in (7.13) were verified with the reference values from [119, 121]. Only in 56 (from the initial 80) subjects, the identified values from (7.13) remained close to the predicted values of Re_0, Re_1 and Im_0, within the 95 % confidence interval.

Table 7.5 Biometric and spirometric parameters of the COPD patients. Values are presented as mean ± standard deviation; % pred: predicted according to the asymptomatic males of the present study; VC: vital capacity; FEV_1: forced expiratory volume in one second

	COPD (47)
Female/male	0/47
Age (yrs)	64 ± 13
Height (m)	1.74 ± 0.12
Weight (kg)	79 ± 12
VC % pred	84 ± 12
FEV_1 % pred	38 ± 8

The second adult group was diagnosed with *chronic obstructive pulmonary disease (COPD)*. COPD is a generic name for any disorder that persistently obstructs the bronchial air flow [6, 64]. However, it mainly involves two related diseases—chronic bronchitis and emphysema. Both cause chronic obstruction of air flowing through the airways and in and out of the lungs. The obstruction is irreversible and progresses (becomes worse) over the time. Most cases of COPD develop after long-term exposure to lung irritants that damage the lungs and the airways (e.g. miners, smoke). Second-hand smoke (i.e. smoke in the air from other people smoking) can also irritate the lungs and contribute to COPD. Breathing in air pollution and chemical fumes or dust from the environment or workplace also can contribute to COPD.

The COPD group under study consisted of 47 Caucasian patients, diagnosed and under observation at the "Leon Danielo" Hospital in Cluj-Napoca, Romania. The patients were former coal miners from the Petrosani area in Romania. Their biometric and spirometric parameters are given in Table 7.5. The measurements were performed in January 2006, Cluj Napoca, Romania.

The third and last group of adult patients was diagnosed with *kyphoscoliosis*. Kyphoscoliosis is a disease of the spine and its articulations, mostly beginning in childhood [103]. The deformation of the spine characteristically consists of a lateral displacement or curvature (scoliosis) or an antero–posterior angulation (kyphosis) or both (kyphoscoliosis). The angle of the spinal curvature called *the angle of Cobb* determines the degree of the deformity and consequently the severity of the restriction. Severe kyphoscoliosis may lead to respiratory failure, which often needs to be treated with non-invasive nocturnal ventilation.

This study was approved by the local Ethics Committee of the University Hospital Gent (UZGent) and informed consent was obtained from all volunteers before inclusion in the study. The study involved nine adults diagnosed with kyphoscoliosis and their corresponding biometric and spirometric values are given in Table 7.6. The measurements were performed during the June 2009–August 2009 time interval.

7.3.2 Healthy vs. COPD

The complex impedance values for the healthy and COPD patients obtained with (3.8) are similar to those presented in Sect. 6.1; the equivalent Bode plots are given

Table 7.6 Biometric and spirometric parameters of the adults diagnosed with kyphoscoliosis. Values are presented as mean±standard deviation values; % pred: predicted values; VC: vital capacity; FEV1: forced expiratory volume in one second; FVC: forced vital capacity; Cobb angle: the angle of spinal deformity (one patient was excluded for it has outlier value for Cobb angle, i.e. 178°; C_{cw}: chest wall compliance; pred*: denotes values predicted from the Cobb angle, according to [103]; R_{aw}: airway resistance from bodybox lung function test. All patients were on nocturnal ventilation

	Kyphoscoliosis (9)
Female/male	3/6
Age (yrs)	62.25 ± 10.12
Height (m)	1.55 ± 0.08
Weight (kg)	63.25 ± 15.62
VC % pred	33.25 ± 14.15
FEV_1 % pred	31.62 ± 11.30
FVC % pred	34.62 ± 12.12
Cobb angle (°)	75 ± 19.63
R_{aw} (kPa/l/s)	0.51 ± 0.12
C_{cw} pred* (l/kPa)	0.98 ± 0.29
VC % pred*	65.06 ± 10.48

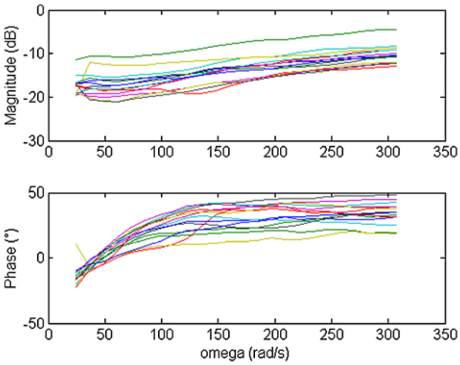

Fig. 7.7 Bode plots for the healthy group

in Figs. 7.7 and 7.8. The real part denotes mainly the mechanical resistance of the lung tissue, which is generally increased in the COPD group, resulting in a higher work of breathing. Also, the resistance at low frequencies is much increased in the COPD group, suggesting increased damping of the lung parenchyma (viscoelasticity is mainly analyzed at low frequencies).

The estimated and derived model parameter values along with the real, imaginary, and total error values are given in Table 7.7 for the healthy subjects and for the COPD patients.

Tissue destruction (emphysema, COPD) and changes in air-space size and tissue elasticity are matched with changes in model parameters when compared to

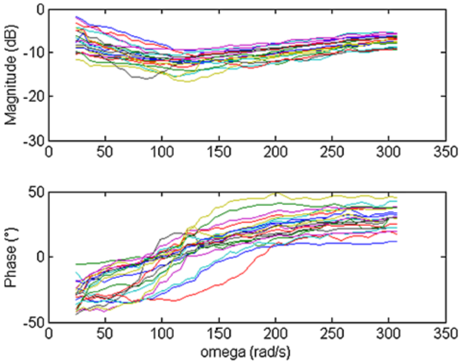

Fig. 7.8 Bode plots for the COPD group

Table 7.7 Estimated and derived model parameters and modeling errors for the healthy and COPD groups. Values are given as mean ± standard deviation; values in brackets indicate the corresponding 95 % confidence intervals

	Healthy	COPD
L_r	0.032 ± 0.029 (0.019, 0.045)	0.016 ± 0.007 (0.013, 0.019)
$1/C_r$	1.59 ± 1.10 (1.09, 2.08)	2.81 ± 1.45 (2.15, 3.47)
α_r	0.42 ± 0.08 (0.38, 0.47)	0.56 ± 0.07 (0.53, 0.60)
β_r	0.75 ± 0.11 (0.70, 0.80)	0.52 ± 0.10 (0.47, 0.56)
G_r	0.44 ± 0.15 (0.37, 0.50)	1.77 ± 0.73 (1.43, 2.10)
H_r	1.49 ± 1.14 (0.98, 2.00)	2.15 ± 1.30 (1.55, 2.74)
η_r	0.41 ± 0.21 (0.32, 0.51)	0.99 ± 0.41 (0.80, 1.18)
$R6$	0.13 ± 0.05 (0.11, 0.16)	0.33 ± 0.07 (0.29, 0.36)
$Frez$	10.48 ± 3.56 (8.75, 13.87)	20.58 ± 8.98 (11.89, 30.27)
$QF6$	0.09 ± 0.09 (0.02, 0.17)	0.55 ± 0.24 (0.44, 0.66)
$PF6$	0.99 ± 0.01 (0.98, 0.99)	0.86 ± 0.08 (0.82, 0.90)
E_R	0.02 ± 0.01	0.03 ± 0.01
E_X	0.013 ± 0.006	0.02 ± 0.006
E_T	0.02 ± 0.01	0.04 ± 0.01

the healthy group. The physiological effects of chronic emphysema are extremely varied, depending on the severity of the disease and on the relative degree of bronchiolar obstruction versus lung parenchymal destruction [6]. Firstly, the bronchiolar obstruction greatly increases airway resistance and results in increased work of breathing. It is especially difficult for the person to move air through the bronchioles during expiration because the compressive force on the outside of the lung not only compresses the alveoli but also compresses the bronchioles, which further increase their resistance to expiration. This might explain the decreased values for inertance (air mass acceleration), captured by the values of L_r.

Secondly, the marked loss of lung parenchyma greatly decreases the elastin cross-links, resulting in loss of attachments [64]. The latter can be directly related to

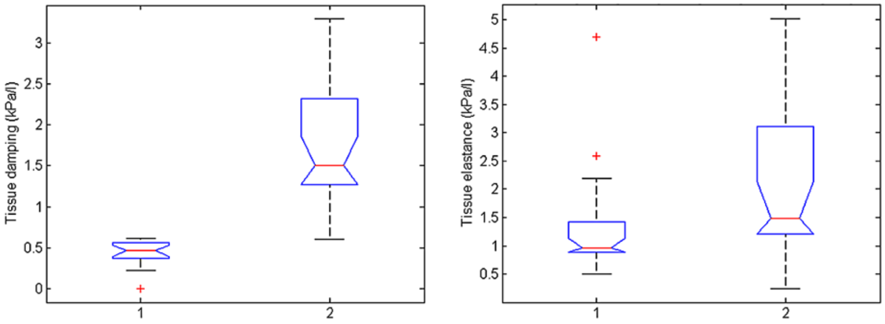

Fig. 7.9 Tissue damping G_r (*left*) and tissue elastance H_r (*right*) in *1*: Healthy subjects and *2*: COPD patients

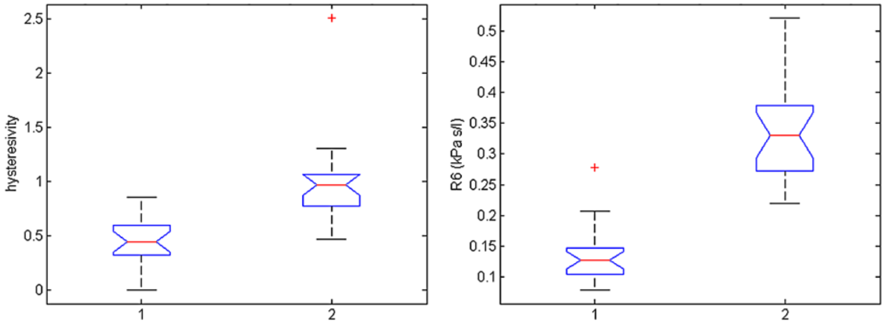

Fig. 7.10 Tissue hysteresivity η_r (*left*) and real part of impedance $R6$ evaluated at 6 Hz (*right*) in *1*: Healthy subjects and *2*: COPD patients

the fractional order of compliance, which generally expresses the capability of a medium to propagate mechanical properties [143]. The damping factor is a material parameter reflecting the capacity for energy absorption. In materials similar to polymers, as lung tissue properties are very much alike polymers, damping is mostly caused by viscoelasticity, i.e. the strain response lagging behind the applied stresses [142, 143]. In the FO model, the exponent β_r governs the degree of the frequency dependence of tissue resistance and tissue elastance. The increased lung elastance $1/C_r$ (elasticity) in COPD results in higher values of tissue damping and tissue elastance, as observed in Fig. 7.9. The loss of lung parenchyma (empty spaced lung), consisting of collagen and elastin, both of which are responsible for characterizing lung elasticity, is the leading cause of increased elastance in COPD. Given the results observed in Fig. 7.10, it is possible to distinguish between tissue changes from healthy to COPD case from the variations in the hysteresivity index η_r ($p \ll 0.01$). Since pathology of COPD involves significant variations between inspiratory and expiratory air flow, an increase in the hysteresivity coefficient η_r reflects increased inhomogeneities and structural changes in the lungs.

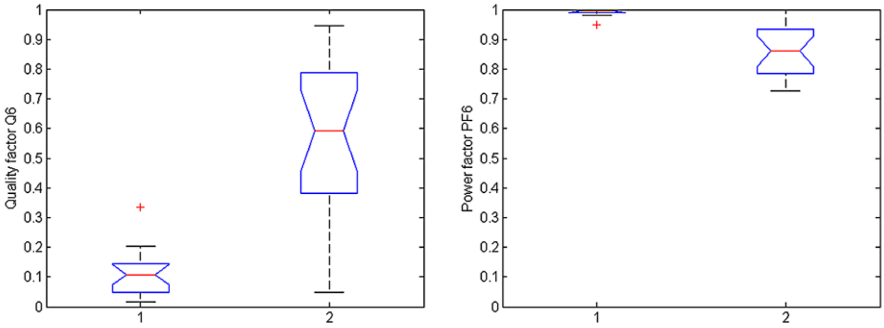

Fig. 7.11 Quality factor $QF6$ (*left*) and power factor $PF6$ (*right*) in *1*: Healthy subjects and *2*: COPD patients

Figures 7.9, 7.10 depict the boxplots for the tissue damping G_r ($p \ll 0.01$), tissue elastance H_r ($p \ll 0.01$), tissue hysteresivity η_r ($p \ll 0.01$) and resistance at 6 Hz $R6$ ($p \ll 0.01$) calculated with the parameters from Table 7.7. In emphysematous lung, the caliber of small airways changes less than in the normal lung (defining compliant properties) and peripheral airway resistance may increase with increasing lung volume. At this point, the notion of space competition has been introduced [64], hypothesizing that enlarged emphysematous air spaces would compress the adjacent small airways, according to a nonlinear behavior. Therefore, the compression would be significantly higher at higher volumes rather than at low volumes, resulting in blunting or even reversing the airway caliber changes during lung inflation. This mechanism would therefore explain the significantly marked changes in model parameters in tissue hysteresivity depicted in Fig. 7.10.

Many alveolar walls are lost by emphysematous lung destruction, the lungs become so loose and floppy that a small change in pressure is enough to maintain a large volume, thus the lungs in COPD are highly compliant (elastic) [6, 64, 71]. This is observed in the high values identified for $1/C_r$.

The quality factor $QF6$ is close to 0.5 in COPD in Fig. 7.11, suggesting a critically damped tissue characteristic. As expected, the quality factor remained low in healthy, denoting the under-damped character of lung parenchyma. This will then result in a high power factor for healthy and decreased power factor in COPD, hence increased work of breathing in COPD.

7.3.3 Healthy vs. Kyphoscoliosis

The complex impedance values for the kyphoscoliosis patients obtained using (3.8) are depicted in Fig. 7.12 and the equivalent Bode plots are given in Fig. 7.13. The healthy volunteers are the same as in the previous section.

Table 7.8 presents the results obtained from the identification of model parameters (3.10). There were significant variances between the groups for tissue damping G_r ($p \ll 0.01$), but not for tissue elastance H_r ($p < 0.75$), as observed from

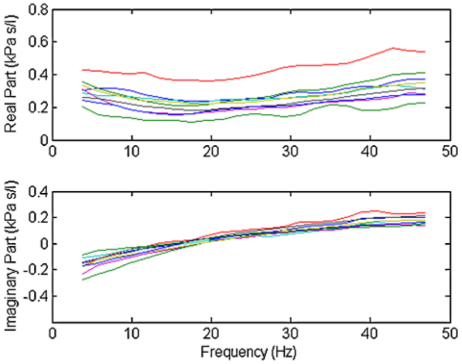

Fig. 7.12 Impedance plots for the kyphoscoliosis group

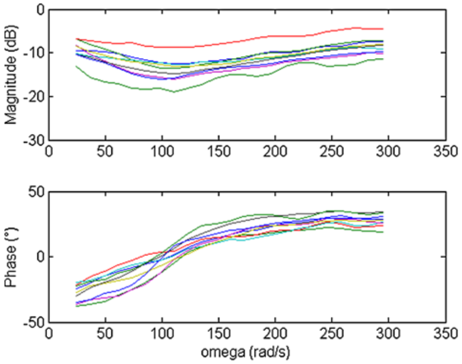

Fig. 7.13 Bode plots for the kyphoscoliosis group

Table 7.8 Estimated and derived model parameters and modeling errors for the healthy and kyphoscoliosis groups. Values are given as mean ± standard deviation; values in brackets indicate the 95 % confidence intervals

	Healthy	Kyphoscoliosis
L_r	0.032 ± 0.029 (0.019, 0.045)	0.0173 ± 0.012 (0.007, 0.02)
$1/C_r$	1.59 ± 1.10 (1.09, 2.08)	2.47 ± 0.76 (1.85, 3.10)
α_r	0.42 ± 0.08 (0.38, 0.47)	0.54 ± 0.05 (0.49, 0.58)
β_r	0.75 ± 0.11 (0.70, 0.80)	0.55 ± 0.05 (0.50, 0.59)
G_r	0.44 ± 0.15 (0.37, 0.50)	1.55 ± 0.39 (1.25, 1.86)
H_r	1.49 ± 1.14 (0.98, 2.00)	1.91 ± 0.73 (1.34, 2.48)
η_r	0.41 ± 0.21 (0.32, 0.51)	0.85 ± 0.16 (0.72, 0.98)
$R6$	0.13 ± 0.05 (0.11, 0.16)	0.28 ± 0.06 (0.23, 0.33)
$Frez$	10.48 ± 3.56 (8.75, 13.87)	15.01 ± 2.08 (12.80, 18.02)
$QF6$	0.09 ± 0.09 (0.02, 0.17)	0.58 ± 0.15 (0.46, 0.71)
$PF6$	0.99 ± 0.01 (0.98, 0.99)	0.85 ± 0.05 (0.81, 0.90)
E_R	0.02 ± 0.01	0.03 ± 0.008
E_X	0.013 ± 0.006	0.01 ± 0.005
E_T	0.02 ± 0.01	0.03 ± 0.008

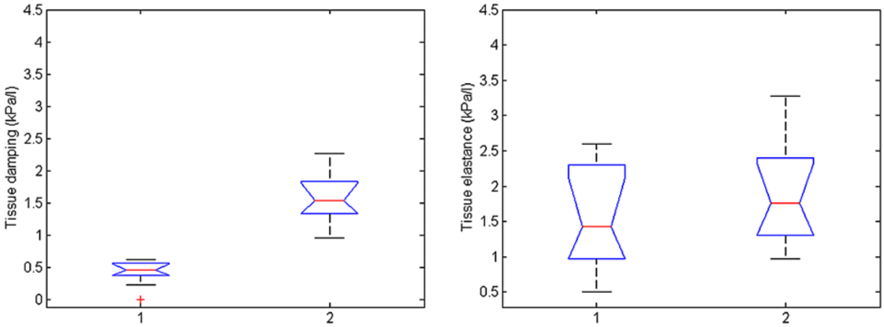

Fig. 7.14 Tissue damping G_r (*left*) and tissue elastance H_r (*right*) in *1*: healthy and *2*: kyphoscoliosis. See corresponding p-values discussed in text

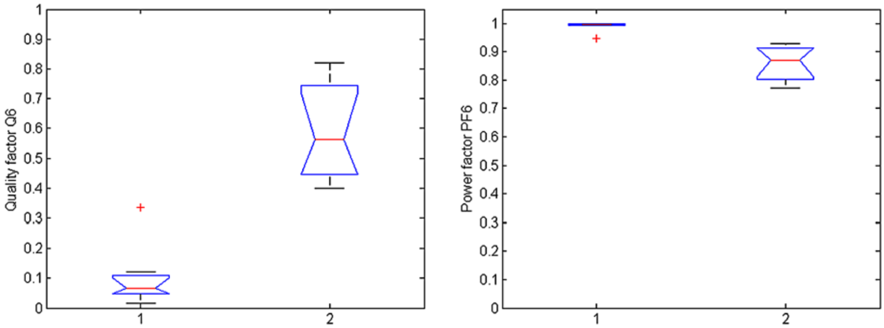

Fig. 7.15 Quality factors $QF6$ (*left*) and power factors $PF6$ (*right*) evaluated at 6 Hz in *1*: healthy and *2*: kyphoscoliosis. See corresponding p-values discussed in text

Fig. 7.14. The boxplots for the quality factor $QF6$ and the power factor $PF6$ are given in Fig. 7.15, which were significantly different between the groups ($p \ll 0.01$). Finally, the boxplot for the real part of impedance at 6 Hz, $R6$ ($p \ll 0.01$), and for tissue hysteresivity η_r ($p \ll 0.01$) are given in Fig. 7.16.

The total lung capacity can be markedly reduced in kyphoscoliosis, with a relative preservation of residual volume. Hence, the reduction in volume capacity (VC) is consequent. The fact that the predicted values in VC from the Cobb angle values were higher than measured, can be attributed to the fact that these patients may have secondary kyphoscoliosis, whereas the predicted values correlate better with idiopatic scoliosis [103]. Similarly, a stiff chest wall (low C_{cw} values from Cobb angle) will diminish the resting position of the chest wall, which in turn, reduces the functional residual capacity. Stiffening of the chest wall leads as well to an overall reduction in the lung compliance (increased damping). One must keep in mind that these changes are not resulted from a diseased parenchyma, but a consequence of the relatively immobile chest wall.

The restrictive nature of the disease (from reduced lung volume) was confirmed by a significantly increased tissue damping G_r, airway resistance $R6$, and quality

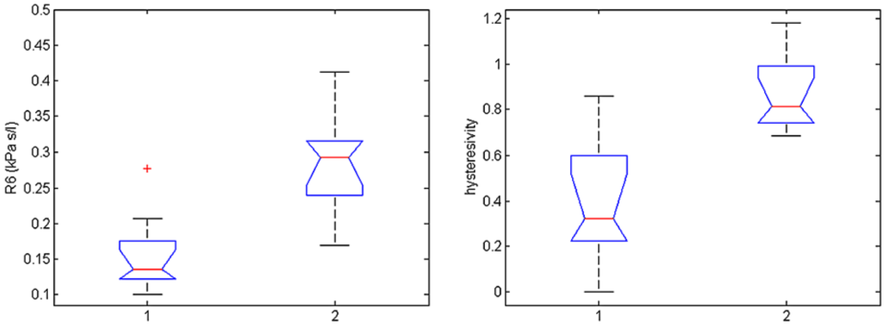

Fig. 7.16 Real part of impedance $R6$ evaluated at 6 Hz (*left*) and the tissue hysteresivity η_r in *1*: healthy and *2*: kyphoscoliosis. See corresponding p-values discussed in text

Table 7.9 Biometric parameters of the healthy children. Values are presented as mean ± standard deviation values

	Healthy (16)
Female/male	13/3
Age (yrs)	9.66 ± 0.47
Height (m)	1.39 ± 0.07
Weight (kg)	32.3 ± 6.34

factor $QF6$. The latter suggested an over-damped dynamical system. The reduced lung and chest wall compliances increase the elastic load on the respiratory muscles and therefore increase the inspiratory pressure needed to inhale a given air volume. Consequently, the work of breathing is increased, reflected in the lower values for the power factor $PF6$.

Tissue elastance was not significantly different between the groups, but the tissue hysteresivity η_r provided a significantly increased heterogeneity in the lungs of the kyphoscoliosis group. Indeed, this result reflects the modified structure of the lungs as originated by the spinal deformity. For example, airway obstruction can occur in some cases as a consequence of changes in the geometry of the airways, or as a result of the aorta impinging on the tracheal wall.

7.3.4 FOT Measurements on Children

The measurements on children included also a *healthy children group*. This study was approved by the local Ethics Committee of the University Hospital in Antwerp (UZA) and informed consent was obtained from all volunteers before inclusion in the study. The study involved 16 healthy children and their corresponding biometric values are given in Table 7.9. The measurements were performed in May 2009, at the St. Vincentius Basis School in Zwijnaarde, Belgium.

Table 7.10 Biometric and spirometric parameters of the asthmatic children and the healthy children used for comparison. Values are presented as mean ± standard deviation values; % pred: predicted values; VC: vital capacity; FEV1: forced expiratory volume in one second; FEF: forced expiratory flow; MEF75/25: mean expiratory flow at 75 %, respectively at 25 % capacity; NA: data not available

	Asthma (19)	Healthy (16)
Female/male	3/16	13/3
Age (yrs)	11.05 ± 4.7	9.66 ± 0.47
Height (m)	1.40 ± 0.17	1.39 ± 0.07
Weight (kg)	36.25 ± 15.58	32.3 ± 6.34
FEF/VC % pred	85.31 ± 31.15	NA
FEV_1/VC % pred	97.75 ± 12.83	NA
$MEF75/25$ (l)	2.12 ± 0.95	NA

The healthy children had no history of pulmonary disease, and were selected using a specific questionnaire. The questionnaire verified the absence of dyspnoea, chronic cough, wheeze in the chest, etc.

In order to validate the measurements in healthy children, the real part of the complex impedance evaluated at 6 Hz ($R6$) was predicted from

$$R6 = 0.0017 \cdot \underline{h}^2 - 0.5407 \cdot \underline{h} + 47.7323 \qquad (7.14)$$

with $\underline{h}$ the height in (cm) [33]. All subjects were within the 95 % confidence interval values.

The second children group was diagnosed with *asthma*. Asthma denotes a pulmonary disease in which there is obstruction to the flow of air out of the lungs, but the obstruction is usually reversible and between attacks of asthma the flow of air through the airways is usually good [17, 19, 161]. Asthma is caused by chronic (ongoing, long-term) inflammation of the airways, making them highly sensitive to various triggers. Such triggers are usually: indoor and outdoor allergens, indoor and outdoor dust, exercise. In an asthma attack, the muscles in the airways contract (bronchospasm), causing narrowing of the airway walls. With proper treatment, people with asthma can have fewer and less severe attacks; while without treatment, they will have more frequent and more severe asthma attacks and can even die. Asthma can be controlled using specific medication (inhaled steroids).

This study was approved by the local Ethics Committee of the University Hospital Antwerp (UZA) and informed consent was obtained from all volunteers before inclusion in the study. The study involved 19 asthmatic children and their corresponding biometric and spirometric values are given in Table 7.10. The measurements were performed during the December 2008–March 2009 time interval.

The protocol in this clinical trial was as follows: initial measurements of FOT and spirometry were performed, followed by a bronchodilatator test. Typically, the spontaneous improvement of the symptoms mentioned above, after the bronchodilatator use, is also an indicative of asthma (>12 % improvement of forced expira-

Table 7.11 Number of the asthmatic children related to various asthma parameters: ICS: inhaled corticosteroid; LABA: long acting beta agonist; LRA: leukotriene receptor antagonist; PC: partially controlled; C: controlled

Medication	ICS: 12	LABA: 15	LRA: 8
Level of asthma control	PC: 6	C: 8	none: 5
Time of diagnose (years)	<1: 9	<2: 3	<5: 7
Allergic asthma	Yes: 17	No: 2	–

tory volume for the 1 second (FEV1) predicted baseline after inhalation). For the bronchodilatation test, Ventolin 100 (4 × Salbutamol 100 mg) was administered. The patient has to breath in and breath out in a nebulizer 4 times the administered medication. A time interval of 12 minutes was allowed to pass after the inhalation, such that the airways have time to respond to the bronchodilatator. Repeated measurements of FOT and spirometry evaluated the patients after the bronchodilatation test.

As additional information, allergy was determined based on specific positive reaction to inhaled allergen (house dust mite, birch tree, grass pollen, weed, dog/cat dander), and further details are given in Table 7.11.

The third group included children diagnosed with *cystic fibrosis*. This is one of the most common severe genetic diseases, characterized by the production of abnormal secretions, leading to mucous build-up, and persistent infections and inflammation in a variety of organs [15, 132]. Inflammation and infection also cause injury and structural changes to the lungs, leading to a variety of symptoms and eventually to respiratory failure. Without treatment, CF results in death for 95 % of affected children before the age of 5, hence early diagnosis is critical.

This study was approved by the local Ethics Committee of the University Hospital Antwerp (UZA) and informed consent was obtained from all volunteers before inclusion in the study. The study involved 10 children diagnosed with cystic fibrosis and their corresponding biometric and spirometric values are given in Table 7.12. The measurements were performed during the December 2008–March 2009 time interval.

The patients were clinically diagnosed and hospitalized at the time of measurement. Diagnosis was based on a sweat test and detection of a minimum of 1 gene mutation responsible for cystic fibrosis.

7.3.5 Healthy vs. Asthma in Children

Using a closed circuit spirometer (JAEGER MasterLab, Germany) measurements for forced vital capacity (FVC), forced expiratory volume in one second (FEV1), the ratio FEV1/FVC and the ratio of forced expiratory flow (FEF) between 25 % and 75 % of FVC to FVC (FEF/FVC) were obtained for the asthmatic patients in a sitting position. These parameters were presented as raw data and percentile of the

Table 7.12 Biometric and spirometric parameters of the children diagnosed with cystic fibrosis and the healthy children used for comparison. Values are presented as mean ± standard deviation values; % pred: predicted values; VC: vital capacity; FEV1: forced expiratory volume in one second; FEF: forced expiratory flow; MEF75/25: mean expiratory flow at 75 %, respectively at 25 % capacity; NA: data not available

	Cystic fibrosis (10)	Healthy (16)
Female/male	4/6	13/3
Age (yrs)	14.44 ± 6.21	9.66 ± 0.47
Height (m)	1.49 ± 0.15	1.39 ± 0.07
Weight (kg)	39.89 ± 11.67	32.3 ± 6.34
FEF/VC % pred	86.51 ± 36.12	NA
FEV_1/VC % pred	95.71 ± 9.42	NA
$MEF75/25$ (l)	2.08 ± 1.13	NA

predicted values (% pred) in a healthy subject with the same biometric details. Quality control of spirometry is given by the ATS criteria (American Thoracic Society), with the software allowing detection of non-acceptable manoeuvres. From the 19 patients with clinical diagnosis of asthma, 16 presented normal respiratory response by spirometry, and will be further referred to as normal-to-the exam (NE) patients. The underlying reason for this was that the patients had a *controlled asthma*.

The predicted values in $R6$ are very close to the measured values, in both healthy and asthmatic children, as depicted by Fig. 7.17. This then supports the spirometric data from Table 7.10, which shows values close to 100 % of the predicted values in all subjects, thus denoting the NE patients. The high standard deviation values in Table 7.10 for the spirometric indices are due to the few asthmatic patients which were not normal to the exam, also visible in Fig. 7.17 with $R6$ values higher than the rest of the group. As observed from Fig. 7.18, there was a linear dependence between the $FEV1/VC\%$ index and height in asthmatic children, in agreement with similar studies from literature [33, 121].

The complex impedance values for the healthy and asthmatic children obtained using (3.8) are depicted in Figs. 7.19 and 7.20. The equivalent Bode plots are given in Figs. 7.21 and 7.22. Table 7.13 presents the results obtained from the identification of model parameters.

It can be observed that for the inductance L_r and its corresponding fractional-order parameter α_r, the confidence intervals are overlapping; hence, there are no significant differences from these parameters between the three groups. The elastance $1/C_r$ and its corresponding fractional-order parameter β_r were significantly different between the groups, leading to significantly different values for the tissue damping G_r ($p \ll 0.01$) and tissue elastance H_r ($p \ll 0.01$), as observed in Fig. 7.23. The corresponding boxplots for tissue damping G_r and tissue elastance H_r in the three groups: healthy, asthma before bronchial challenge, and asthma after bronchial challenge test are given in Fig. 7.23. The boxplots for the quality factor

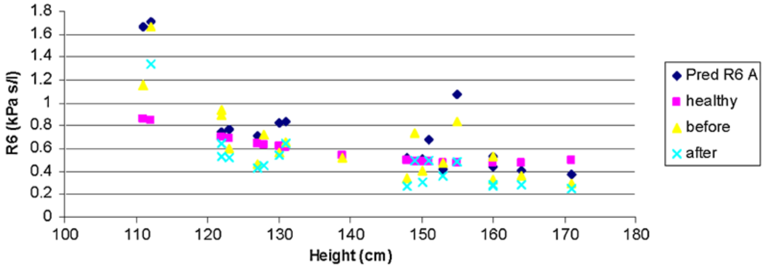

Fig. 7.17 The real part of impedance $R6$ evaluated at 6 Hz against the height in healthy (*square*), asthma before bronchial challenge (*triangle*) and asthma after bronchial challenge (*crosses*). Predicted values for $R6$ from [33] (*diamond*)

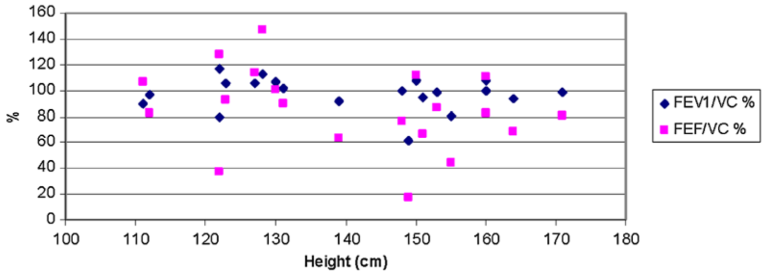

Fig. 7.18 The percent ratios $FEV1/VC\%$ (*diamond*) and $FEF/VC\%$ (*square*) against height

Fig. 7.19 Impedance plots for the healthy children group

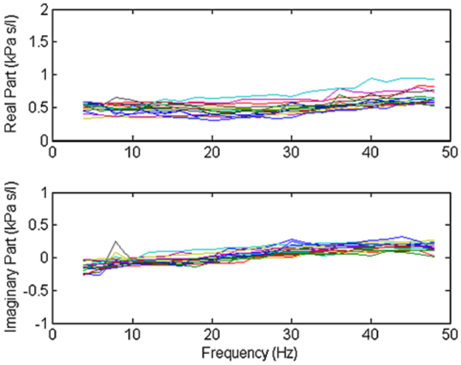

$QF6$ and the power factor $PF6$ are given in Fig. 7.24. Finally, the boxplots for the real part of impedance $R6$ and resonant frequency η_r are given in Fig. 7.25.

There were no significantly different values obtained between the groups for the hysteresivity η_r ($p < 0.41$), perhaps due to prior medication of the asthmatic group. Indeed, in lung tissues, the frictional stress is almost invariably between 0.1 and 0.2 of the elastic stress, a fraction known as hysteresivity. This means that for each unit of peak elastic strain energy that is stored during a cyclic deformation, 10 to 20 % of that energy is lost irreversibly to heat. This fixed relationship holds at the level of

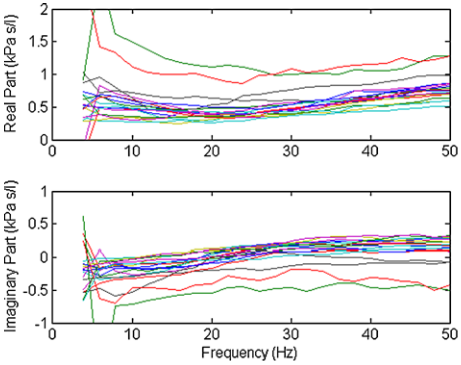

Fig. 7.20 Impedance plots for the children with asthma

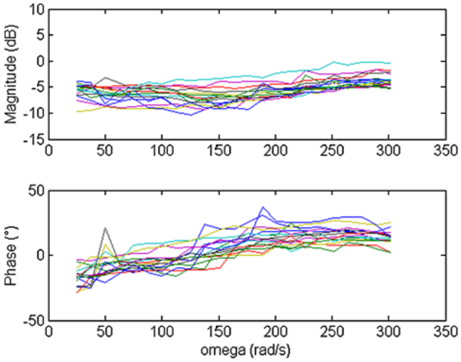

Fig. 7.21 Bode plots for the healthy children group

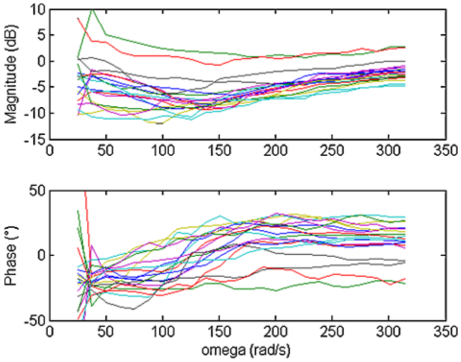

Fig. 7.22 Bode plots for the children with asthma

the whole lung, isolated lung parenchymal tissue strips [143], and isolated smooth muscle strips [162]. The fact that in our case we do not have variations in hysteresivity with bronchial challenge is explained by the fact that in all asthma patients, a spontaneous improvement higher than 12 % was absent, due to prior medication intake (see Table 7.11). Nevertheless, the tissue damping and tissue elastance coefficients were sensitive to detect variations between the groups when evaluated inde-

Table 7.13 The identified model parameters in the three groups; values are given as mean ± standard deviation; (*bc*) denotes values after bronchial challenge; values in brackets denote the 95 % confidence intervals

	Healthy	Asthma	Asthma (bc)
L_r	0.11 ± 0.08 (0.06, 0.15)	0.13 ± 0.17 (0.03, 0.23)	0.08 ± 0.04 (0.06, 0.11)
$1/C_r$	4.73 ± 2.73 (3.2, 6.2)	7.96 ± 3.16 (6.21, 9.7)	7.95 ± 3.31 (6.13, 9.78)
α_r	0.32 ± 0.11 (0.26, 0.38)	0.32 ± 0.09 (0.27, 0.38)	0.34 ± 0.10 (0.28, 0.40)
β_r	0.63 ± 0.16 (0.54, 0.72)	0.70 ± 0.13 (0.62, 0.77)	0.76 ± 0.15 (0.67, 0.85)
G_r	1.91 ± 0.68 (1.53, 2.29)	3.21 ± 1.75 (2.25, 4.18)	2.33 ± 0.90 (1.84, 2.82)
H_r	4.10 ± 3.01 (2.44, 5.76)	7.06 ± 3.18 (5.3, 8.81)	7.47 ± 3.61 (5.34, 9.39)
η_r	0.70 ± 0.38 (0.49, 0.91)	0.53 ± 0.29 (0.37, 0.70)	0.48 ± 0.66 (0.13, 0.84)
$QF6$	0.41 ± 0.11 (0.35, 0.48)	0.60 ± 0.17 (0.52, 0.69)	0.61 ± 0.16 (0.52, 0.7)
$PF6$	0.91 ± 0.03 (0.89, 0.93)	0.85 ± 0.06 (0.82, 0.88)	0.85 ± 0.06 (0.81, 0.88)
$R6$	0.49 ± 0.06 (0.46, 0.53)	0.61 ± 0.37 (0.42, 0.8)	0.44 ± 0.24 (0.31, 0.56)
$Frez$	21 ± 5.9 (17.81, 24.18)	22.94 ± 12.29 (17.01, 28.87)	16.66 ± 9.4 (11.98, 21.34)
E_R	0.05 ± 0.01	0.09 ± 0.03	0.08 ± 0.02
E_X	0.04 ± 0.01	0.06 ± 0.04	0.04 ± 0.01
E_T	0.06 ± 0.02	0.12 ± 0.05	0.09 ± 0.03

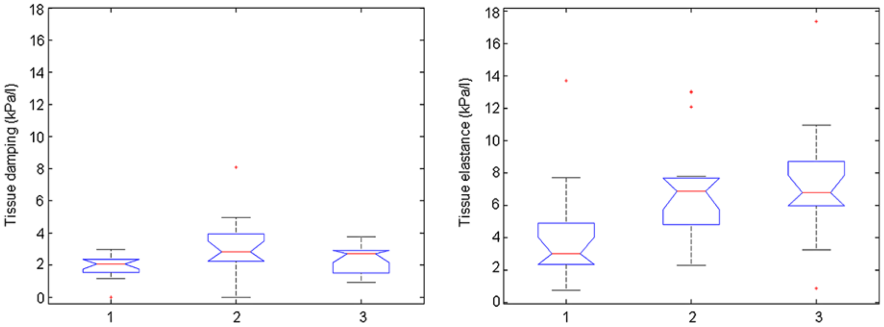

Fig. 7.23 Tissue damping G_r (*left*) and tissue elastance H_r (*right*) in *1*: healthy; *2*: asthma; and *3*: asthma after bronchial challenge. See corresponding p-values discussed in text

pendently. Tissue damping was higher in asthma and became lower after bronchial challenge. Tissue elastance increased in asthma after bronchial challenge.

Lower $QF6$ values were obtained in the healthy group in Fig. 7.24 ($p \ll 0.01$), denoting that higher amount of air circulates in the lungs than in asthma. A slight decrease in $QF6$ values suggests an improvement in the air flow after bronchial challenge in asthma groups (decreased overall damping factor). The corresponding values for the $PF6$ show that in healthy lungs, the overall system is more efficient to use the available energy than in asthmatic lungs ($p \ll 0.01$), hence increased work of breathing in asthma.

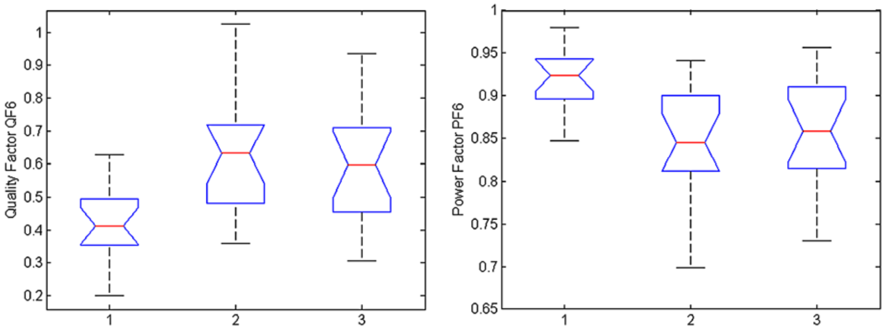

Fig. 7.24 Quality factors $QF6$ (*left*) and power factors $PF6$ (*right*) evaluated at 6 Hz in *1*: healthy; *2*: asthma; and *3*: asthma after bronchial challenge. See corresponding p-values discussed in text

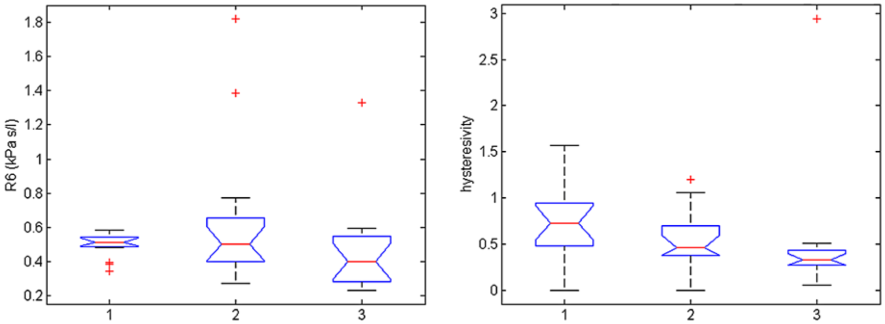

Fig. 7.25 Real part of impedance $R6$ evaluated at 6 Hz (*left*) and tissue hysteresivity η_r (*right*) in *1*: healthy; *2*: asthma; and *3*: asthma after bronchial challenge. See corresponding p-values discussed in text

The real values of impedance $R6$ ($p < 0.22$) and the tissue hysteresivity η_r ($p < 0.29$) were not significantly different between the groups. These findings are in agreement with similar studies in asthma groups, using forced oscillation lung function test [19]. The authors also report no statistical significant differences between the control and NE groups in mean reactance, mean resistance and resonant frequency.

7.3.6 *Healthy vs. Cystic Fibrosis in Children*

The complex impedance values for the cystic fibrosis (CF) children obtained using (3.8) are depicted in Fig. 7.26 and the equivalent Bode plots are given in Fig. 7.27. The healthy children are the same as in the previous section.

Table 7.14 presents the results obtained from the identification of model parameters. There were no significant variances between the groups for tissue damping

Fig. 7.26 Impedance plots for the children with cystic fibrosis

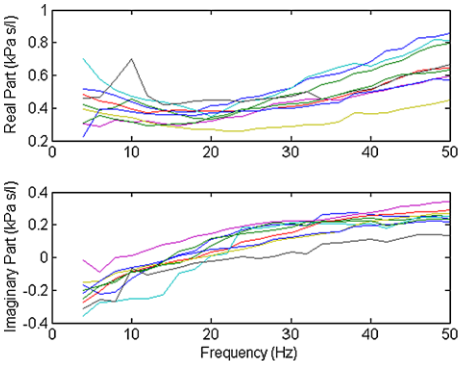

Fig. 7.27 Bode plots for the children with cystic fibrosis

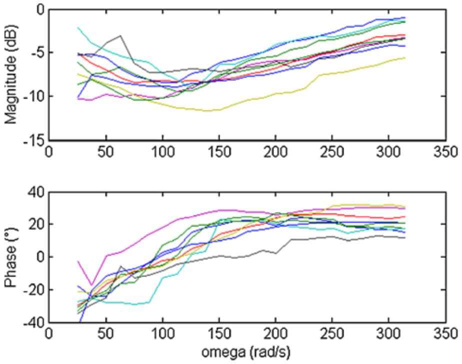

Table 7.14 The identified model parameters in the two groups; values are given as mean ± standard deviations; values in brackets denote the 95 % confidence intervals

	Healthy	Cystic fibrosis
L_r	0.11 ± 0.08 (0.06, 0.15)	0.07 ± 0.03 (0.05, 0.10)
$1/C_r$	4.73 ± 2.73 (3.2, 6.2)	8.67 ± 4.63 (5.11, 12.23)
α_r	0.32 ± 0.11 (0.26, 0.38)	0.38 ± 0.08 (0.31, 0.44)
β_r	0.63 ± 0.16 (0.54, 0.72)	0.77 ± 0.15 (0.66, 0.89)
G_r	1.91 ± 0.68 (1.53, 2.29)	2.07 ± 0.85 (1.41, 2.73)
H_r	4.10 ± 3.01 (2.44, 5.76)	8.26 ± 4.86 (4.52, 12.00)
η_r	0.70 ± 0.38 (0.49, 0.91)	0.38 ± 0.29 (0.15, 0.61)
$R6$	0.49 ± 0.06 (0.46, 0.53)	0.38 ± 0.08 (0.32, 0.45)
$Frez$	21 ± 5.9 (17.81, 24.18)	15.75 ± 4.71 (11.80, 19.69)
$QF6$	0.41 ± 0.11 (0.35, 0.48)	0.67 ± 0.18 (0.52, 0.81)
$PF6$	0.91 ± 0.03 (0.89, 0.93)	0.82 ± 0.06 (0.77, 0.88)
E_R	0.05 ± 0.01	0.07 ± 0.03
E_X	0.04 ± 0.01	0.05 ± 0.04
E_T	0.06 ± 0.02	0.10 ± 0.05

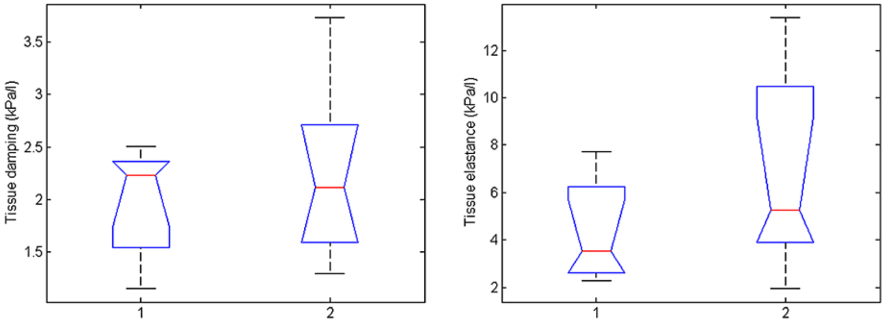

Fig. 7.28 Tissue damping G_r (*left*) and tissue elastance H_r (*right*) in *1*: healthy and *2*: cystic fibrosis. See corresponding p-values discussed in text

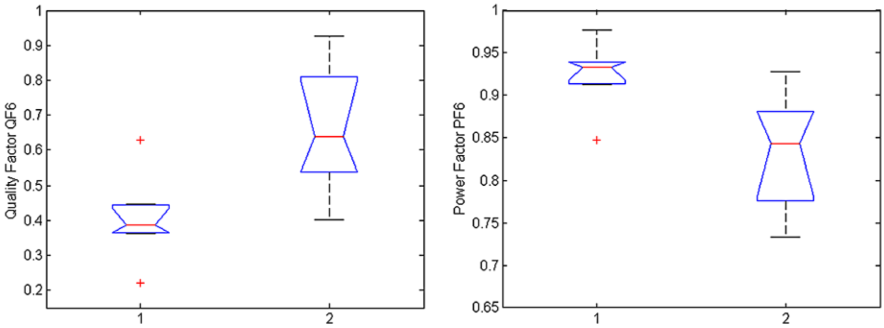

Fig. 7.29 Quality factors $QF6$ (*left*) and power factors $PF6$ (*right*) evaluated at 6 Hz in *1*: healthy and *2*: cystic fibrosis. See corresponding p-values discussed in text

G_r ($p < 0.46$) and tissue elastance H_r ($p < 0.17$), as observed from Fig. 7.28. The boxplots for the quality factor $QF6$ and the power factor $PF6$ are given in Fig. 7.29, which were significantly different between the groups ($p \ll 0.01$). Finally, the boxplot for the real part of impedance at 6 Hz, $R6$ ($p \ll 0.01$), and for tissue hysteresivity η_r ($p < 0.23$) are given in Fig. 7.30.

Lung disease in CF begins in the distal airways and should be therefore reflected in abnormalities of the intra-parenchymal airways and parenchymal mechanics. By its intrinsic nature, the identified FO4 model should be able to determine such changes. However, in order to partition the airway and parenchymal mechanics, one needs to measure at low frequencies, i.e. a decade lower than 5 Hz. Since in our study we are not envisaging such frequency range, it is not surprising that no statistical significant differences in tissue damping, elastance, and hysteresivity were obtained. In a study over the 0.5–20 Hz frequency range using the model structure from (7.2), there was also no significant difference between the measures of lung function (airway or parenchymal) in infected or uninfected children with respiratory pathogen [15]. In [15] it was shown that the FO2 model can provide separate

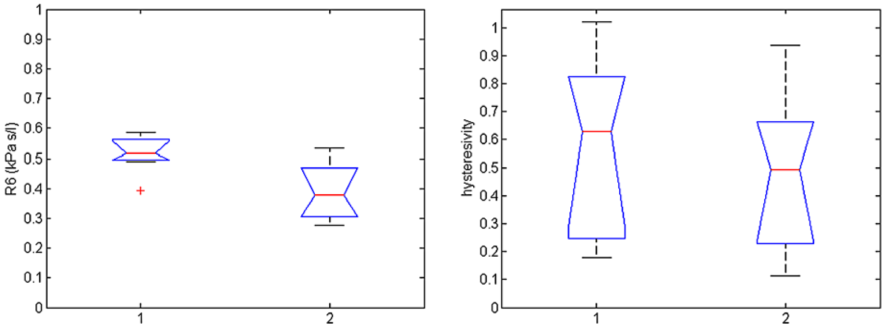

Fig. 7.30 Real part of impedance $R6$ evaluated at 6 Hz (*left*) and the tissue hysteresivity η_r (*right*) in *1*: healthy and *2*: cystic fibrosis. See corresponding p-values discussed in text

estimates of the mechanical properties of the airways and pulmonary parenchyma in CF, but in a lower frequency decade than in this present study.

In the 4–48 Hz frequency range, the only parameters able to classify between healthy and CF children were those derived from the identified impedance at 6 Hz: $R6$, $QF6$, and $PF6$. One should recall that the quality factor $QF6$ is related to the overall damping factor of the respiratory system, hence indirectly related to G_r. $QF6$ was significantly higher in CF than in healthy, denoting an over-damped tissue property. Consequently, the power factor $PF6$ was below that of healthy children, suggesting lower efficiency in breathing, thus requiring higher work of breathing.

Although one might expect increased airway resistance in CF than in healthy, the values for $R6$ were significantly lower in CF than in healthy. One of the reasons for this result might be that prior to the lung function exam, the CF patients undergone removal of retained secretions using specific physiotherapy which resulted in decreased airway obstruction and overall resistance [132].

The lung function measured by spirometry is insensitive to changes in airway structure, therefore it is not sufficient for early diagnosis of CF. We expect that the FO4 model is able to capture such changes, but in a lower frequency range.

7.4 Parametric Models for Multiple Resonant Frequencies

7.4.1 High Frequency Range of Respiratory Impedance

Lumped parameter models for the input impedance have been developed for both low frequency range (0.1–5 Hz) [31], as well as in the high frequency range (8–256 Hz) [39], with constant-phase model elements used to model the respiratory impedance for frequencies below 50 Hz [56–58].

There is not much information in the literature upon respiratory impedance evaluated at frequencies higher than 50 Hz. A possible underlying reason is that viscoelastic properties become important at low frequencies and their characteristics are changing with the evolution of the respiratory diseases. By contrast, the structure and morphology of the lungs influences the mechanical properties at higher frequencies, given the coupling between the various respiratory compartments [9]. Studies have shown that the respiratory impedance poses several resonance (minima)–anti-resonance (maxima) frequency intervals. It is thought that the first anti-resonance peak (around 50–150 Hz) reflects the interaction between lung tissue and air volume and changes with respiratory disease. The second peak (between 150–600 Hz) depends on airway walls compliance and respiratory gas properties [44–46, 133] and has not been yet related to changes in respiratory mechanics with disease.

The work presented in this section is based on the previous chapters where it was shown that equivalent ladder network models preserving the human lung morphology and structure are in good qualitative agreement with general impedance values. We employ here two parametric models for characterizing the impedance over a long range in the frequency domain. The first model is the recurrent ladder network model from (5.17) and re-visited to accommodate for the upper airway shunt and the second model has been recently published in [78, 79]. The primary objective is to evaluate the performance of these models in a group of 31 healthy patients. The secondary objective is to determine from the recurrent ladder network the fractional-order value which characterizes the specific feature of the respiratory mechanics at high frequencies.

The measurements of the signals analyzed in this section have been performed using the device described in Chap. 3 able to assess the respiratory mechanics in the range 7–250 Hz. On the non-parametric estimation of the respiratory impedance using (3.8), we fit the recurrent ladder network described in Chap. 5.

For comparison purposes, we employ the parametric model given in [78] is

$$Z_{\mathrm{PAR}} = R_p + \frac{Z_m Z_g Z_{ts} + Z_m Z_{aw} Z_g + Z_m Z_{aw} Z_{ts}}{Z_g Z_m + Z_{ts} Z_m + Z_g Z_{ts} + Z_{aw} Z_g + Z_{aw} Z_{ts}} \tag{7.15}$$

with R_p the peripheral resistance, Z_m the impedance of the upper airway compliance C_m; Z_{aw} the impedance of the series connection of airway resistance R_{aw} and inertance L_{aw}; Z_g the impedance of the alveolar gas compliance C_g and Z_{ts} the impedance of the series connection of lung tissue and chest wall resistance R_{ts}, inertance L_{ts} and compliance C_{ts}. This model has been shown to be in good agreement with frequency response values in the 4–500 Hz interval [78]. To our knowledge, this is the most complete model developed for analysis of the respiratory mechanics in the high frequency range.

The first segment in the respiratory tract is denoted by the upper airways, comprising the oral cavity, larynx, and pharynx. The corresponding electrical elements are then denoted by a resistance R_{UA}, an inductance L_{UA} and a capacitance C_{UA} (see Fig. 7.31). Since we make use of recurrent properties as given by (5.4), the initial values of the recurrent ladder network, R_{UA}, L_{UA}, C_{UA}, are not known and they need to be included in the identification as unknown parameters. Next, using the recurrent ratios from (5.4) combined with the geometrical ratios from (5.1)–(5.3), the impedances Zl_m and Zt_m can be calculated.

We refer to the identified impedance Z_{REC} as the inverse of the admittance from (5.17). Similarly, we refer to the identified impedance from 7.15 as Z_{PAR}.

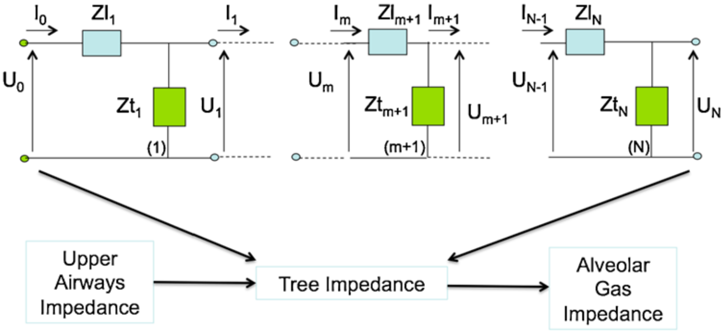

Fig. 7.31 Re-visited ladder network model to accommodate the upper airway segment

The best fit of $Z_{\mathrm{REC}}(j\omega)$ and $Z_{\mathrm{PAR}}(j\omega)$, respectively, is given by searching for the minimum value of the cost function:

$$J = \frac{1}{N_p} \sum_{\Omega_i}^{N_p} \left[(\mathrm{Re} - \hat{r})^2 + (\mathrm{Im} - \hat{x})^2 \right] \tag{7.16}$$

where $\mathrm{Re} = real(Z_r)$ and $\mathrm{Im} = imag(Z_r)$ with Z_r from (3.8), $\hat{r}$ and $\hat{x}$ are the estimated real and imaginary parts, Ω_i represents the set of sampling points in the frequency domain, and N_p the number of samples. The total error E_T between complex data and its estimate has been calculated as in (3.12).

7.4.2 Evaluation on Healthy Adults

The volunteers tested for their high frequency respiratory impedance characteristic are listed in Table 7.15 by means of their biometric values.

Figures 7.32, 7.33 depict the calculated impedance for the 31 volunteers using (3.8) by means of its complex representation and equivalent Bode plots. The values for the impedance are corresponding to similar measurements performed in the same frequency interval in adults [39]. The red line denotes the averaged impedance data from all 31 volunteers. After 70 Hz, there is increased noise amount, due to the fixed sampling period (1 ms). However, we are measuring long data intervals (30–40 seconds), such that the effects in the frequency response values are minimal.

Next step was to perform identification on each data set in the frequency interval from 7–250 Hz, resulting in identified values for the ladder network in a recurrent form Z_{REC}. More precisely, the ladder network has resistance, inductance, and capacitance terms, in a gamma form, with ratios for each parameter as in Chap. 5. The number of compartments in the ladder network has been set to $N = 24$, according to lung morphology [163, 164]. The initial values for the ladder network model were: $R_{\mathrm{UA}} = 0.001$ (kPa s/l), $C_{\mathrm{UA}} = 0.001$ (l/kPa), $L_{\mathrm{UA}} = 0.001$ (kPa s^2/l), $\lambda = 2.46$, $\chi = 0.54$, $\alpha = 1.15$. There were statistically significant results identified

Table 7.15 Biometric values of the volunteers. Notice that two volunteers are outliers, denoted pA and pB and they are not taken into account when mean and standard deviation values are calculated

Subject	Gender	Age (years)	Weight (kg)	Height (cm)
1	m	31	65	160
2	m	28	68	165
3	m	28	68	165
4	m	23	89	190
5	m	24	70	170
6	m	30	72	180
7	m	30	72	180
8	m	23	74	182
9	f	30	70	173
10	f	31	70	170
11	m	24	70	160
12	m	25	71	160
13	m	26	80	197
14	m	29	90	186
15	m	30	90	186
16	m	23	65	179
17	m	29	64	160
18	m	22	59	174
19	m	22	71	183
20	f	24	54	167
21	m	22	75	180
22	m	28	73	179
23	f	23	50	164
24	f	27	50	158
25	f	22	56	161
26	m	22	70	181
27	m	27	75	181
28	m	28	76	181
29	f	30	65	160
Mean ± std	–	26 ± 3	70 ± 10	173 ± 10
pA	m	55	80	170
pB	m	60	83	170

only for the recurrent ratios, given in Table 7.16. The other identified parameters are given in Fig. 7.34 by means of boxplots.

Next, we applied identification on the same data for the parametric impedance model Z_{PAR} from (7.15). The results of the identification are given in Fig. 7.35 by means of boxplots (volunteers pA and pB not included here). Figure 7.36 shows a typical identification result, all other identification results being similar. There were

Fig. 7.32 Respiratory impedance calculated from the 31 volunteers by means of its complex representations; *line* denotes the corresponding averaged values

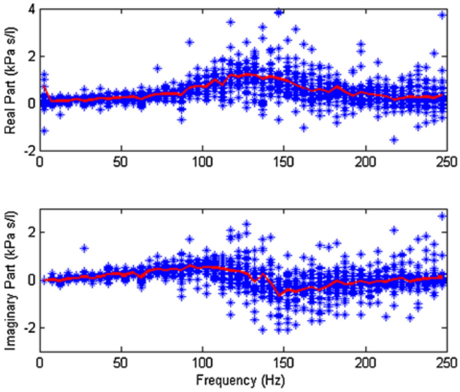

Fig. 7.33 Respiratory impedance calculated from the 31 volunteers by means of its modulus-phase representations; *line* denotes the corresponding averaged values

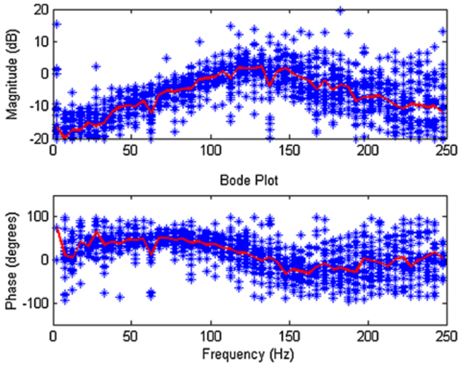

Fig. 7.34 Estimated parameters of the Z_{REC} impedance model. Units are, respectively: R, R_{ua} (kPa s/L); L, L_{ua} (kPa s^2/L); C, C_{ua} (L/kPa)

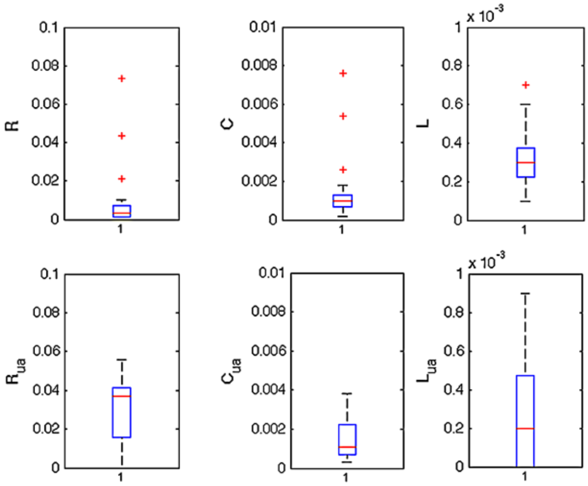

Table 7.16 Identified recurrent ratio values for the ladder network model Z_{REC} in the 7–250 Hz frequency interval; std: standard deviation. CI: 95 % confidence intervals. Notice that two volunteers are outliers with respect to age, weight, and height, they are denoted as pA and pB and they are not taken into account when mean and standard deviation values are calculated

Subject	λ	χ	α
1	2.66	0.70	1.34
2	2.24	0.52	1.40
3	1.96	0.57	1.32
4	0.60	0.62	1.28
5	2.08	0.56	1.22
6	2.05	0.68	1.33
7	2.12	0.55	1.20
8	2.30	0.56	1.20
9	2.17	0.56	1.34
10	2.17	0.57	1.33
11	1.94	0.58	1.21
12	1.95	0.60	1.29
13	0.019	0.60	1.29
14	0.10	0.57	1.21
15	2.19	0.59	1.30
16	2.01	0.55	1.15
17	2.25	0.51	1.31
18	1.96	0.56	1.24
19	0.96	0.59	1.21
20	2.07	0.55	1.17
21	2.01	0.52	1.28
22	1.98	0.62	1.18
23	2.06	0.56	1.21
24	0.77	0.56	1.10
25	2.02	0.58	1.26
26	2.04	0.54	1.29
27	0.53	0.67	1.26
28	1.68	0.54	0.96
29	1.98	0.60	1.18
Mean ± std 1.75 ± 0.69	0.58 ± 0.04	1.24 ± 0.08	
CI-min	1.70	0.54	1.20
CI-max	2.08	0.60	1.27
pA	2.19	0.67	1.26
pB	1.17	0.57	1.27

no statistically significant differences between the errors provided by the estimated parametric models ($p < 0.89$). Figure 7.37 shows the boxplots for the errors between Z_{REC} and Z_{PAR}, respectively.

Fig. 7.35 Estimated parameters of the Z_{PAR} impedance model. Units are, respectively: R_p, R_t, R_{aw} (kPa s/L); L_t, L_{aw} (kPa s^2/L); C_g, C_m, C_t, C_{aw} (L/kPa)

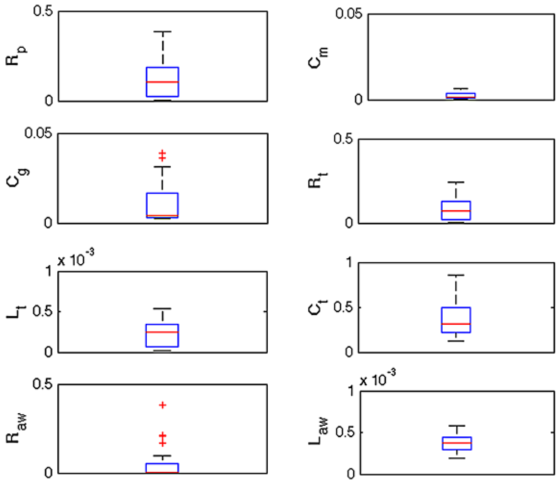

Fig. 7.36 Respiratory impedance by means of its complex representations; squares denote the estimated Z_{REC} impedance values; *stars* denote the measured impedance with (3.8), *bold line* denotes the estimated Z_{PAR} impedance values. This illustrative example is given for patient "22" from Table 7.15

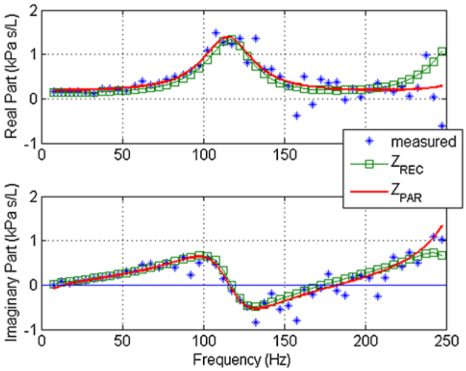

Fig. 7.37 Boxplot for the total errors provided by the two identified parametric models Z_{PAR} and Z_{REC}, respectively. There were no statistically significant differences ($p < 0.89$)

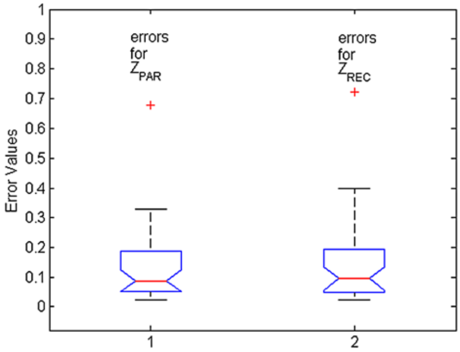

From the identified recurrent ratios, one can calculate the fractional order of the ladder network, using (5.25). The values are given in Fig. 7.38 as a boxplot showing the median value and the outliers. In order to check the variability of the fractional-

Fig. 7.38 Boxplot for the fractional-order values *n* identified from the 31 volunteers

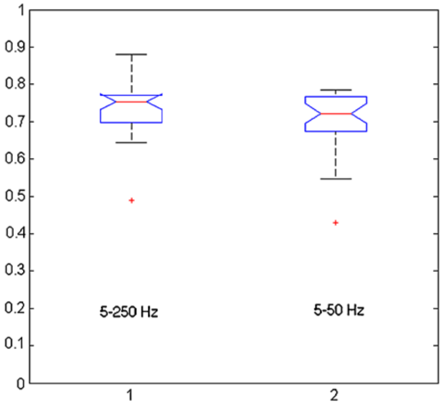

Fig. 7.39 The original Z_{PAR} impedance (*bold line*) as identified for patient "22" from Table 7.15 and the modified impedance (*stars*) with twofold increased R_{ts} (denoted in figure as "test case")

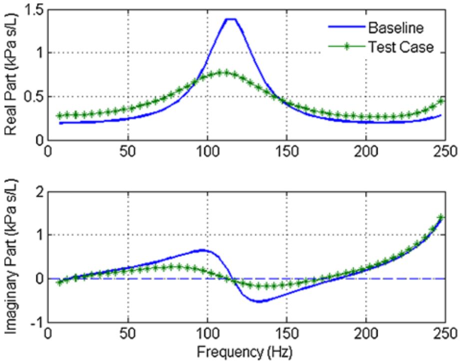

order parameter with frequency, we re-identify the ladder network model in the range 5–50 Hz, and we obtained a new fractional-order value, depicted in Fig. 7.38 in the right-column. There was no statistically significant difference between the two identified sets ($p < 0.7$). This validates the expected theoretical result that the fractional-order value is independent on the frequency.

Further on, the sensitivity of the fractional-order value to changes in mechanical parameters has been evaluated by using Z_{PAR} with modified R_{ts} increased twofold, and fitting Z_{REC} to it. Figure 7.39 shows the original Z_{PAR} impedance identified for patient "22" from Table 7.15 and the modified impedance (denoted in figure as "test case"). To the modified impedance (i.e. test-case impedance) we have fitted the model of Z_{REC} as shown in Fig. 7.40 and obtained the following parameter values: $R_{ua} = 1.3e^{-7}$ (kPa s/L); $L_{ua} = 0.0017$ (kPa s^2/L); $C_{ua} = 0.0034$ (L/kPa); $R = 0.098$ (kPa s/L); $L = 0.0005$ (kPa s^2/L); $C = 0.0016$ (L/kPa); $\lambda = 1.10$; $\chi = 0.52$; $\alpha = 1.10$ and total error $E_t = 0.03$. The simulated increase in tissue resistance is reflected by an overall increase in the airway resistance value and modified recurrent ratio values. The resulting fractional-order value is then calculated from the identified recurrent ratios using (5.38), it following that $n = 0.19$. This implies that our proposed model is able to capture variations in the respiratory parameters and the fractional-order value is a suitable parameter for classification.

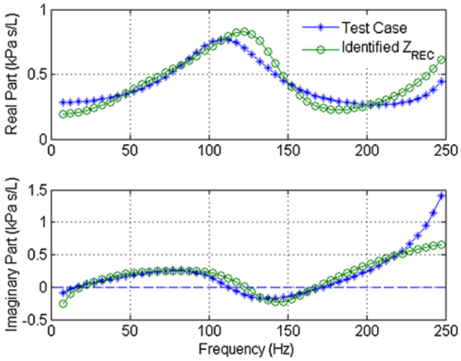

Fig. 7.40 Identified Z_{REC} impedance (*circles*) fitted to the test-case impedance data (*stars*)

7.4.3 Relation to Physiology and Pathology

The measured impedance values in healthy subjects and the corresponding resonance/anti-resonance peak values are qualitatively and quantitatively comparable to those reported in [39, 78, 79]. Both impedance models evaluated here were able to capture the frequency-dependence of the respiratory mechanics at high frequencies.

The idea of multiple parallel tubes to model the respiratory tree at high frequencies from [39] is here re-visited by means of a recurrent ladder network Z_{REC}. The ladder network model Z_{REC} captures well the variations with frequency in the impedance in all investigated patients and the identified model parameter values are within reasonable values from clinical insight [112]. One should keep in mind that the estimated ladder network coefficients are based on recurrent relations and the fact that this recurrence leads to the constant-phase behavior in the impedance data is an intrinsic property of such models [31, 56–58]. Even if these ladder network elements are then replaced by fractional-order elements, the convergence remains valid [118]. These findings support the theoretical insights on prior ladder network developments and are in line with morphometry of the respiratory system [31, 39]. The upper airway resistance values R_{ua} are similar to those identified in [79]. The identified upper airway compliance C_{ua} values are slightly lower for the Z_{REC} than the values reported in [79].

The identified model parameters of Z_{PAR} are close to those reported in [39] for the model with bronchial elasticity and similar to those reported in [79].

The values for the fractional order calculated from the identified recurrent ratios ($n = 0.78$) are very close to previously reported values in [71] for healthy subjects by means of a lumped FO parameter model (average value $n = 0.79$). It is remarkable that a very close FO value (average value $n = 0.8$) has been obtained in [11] when respiratory impedance has been evaluated at low frequencies in lambs. This suggests once again experimentally what has been theoretically shown in [70, 76, 118], i.e. that the recurrent ladder network converges to a lumped fractional-order model, whose fractional order is independent of frequency [105].

Since in [154, 155] it was illustrated that the respiratory impedance at high frequency is subject to bias originating from the nose clip, we re-identified the recurrent ladder network model Z_{REC} in the 5–50 Hz frequency range. The two identified data sets are illustrated in Fig. 7.38 and there were no statistically significant differences between them ($p < 0.7$). We conclude that the fractional-order index is independent of frequency, hence it is a reliable parameter to quantify the fractal properties of the human respiratory system. There can also be speculated that age does not seem to introduce difference in the results—as observed from the two introduced outliers pA and pB from Table 7.16. However, further studies will have to confirm this claim in detail.

Intuitively, we expect that changes in resistance and compliance values of the airways and respiratory tissue will affect the recurrent ratios. This has been shown in previous section by a simple yet efficient example on the “test-case” impedance, resulting in a different identified value for the FO parameter n. Consequently, we expect that the value of the fractional order will be sensitive to changes originated from different respiratory pathologies. This is also supported by our prior study on the impulse response of fractional-order models identified from healthy and pathologic data, which gave different pressure–volume dynamics [75] and other works [55]. There is also evidence in the literature showing that morphometric changes occur in the airways with pathology and thus we have reasons to believe that our claim is well justified [51, 84, 156].

There are several limitations present in this modeling approach. A first limitation is that the model lacks the characterization of diffusion phenomena. However, in our model we include a gas compression compartment to account for the gas compliance phenomena. It is also questionable whether diffusion phenomena are important at high frequency, since it is a slow process mainly observable at low frequencies.

Perhaps the most significant limitation in this study is the fact that we assume a symmetric tree, whereas the asymmetrical representation is more realistic [54, 65]. It is significant to note that the self-similarity is related to the optimality of ventilation [66, 91] and that asymmetry exists in the healthy lung as well, whereas a diseased lung contains significant heterogeneities and the optimality conditions are not fulfilled anymore. However, even the asymmetric representation of the Horsfield structure [65] has a high degree of self-similarity and, therefore, our model results are fairly reasonable. The major errors which may occur in this study are determined by the heterogeneity of the human lung and the inter-subject variability that can affect the recurrent values. However, these values are reported in several studies and they have offered a good basis for investigations [91, 97, 163, 164]. Although the airway tree of the human lung shows considerable irregularity, there exists a systematic reduction of airway size [167]. It was demonstrated that the airway tree in different species shows a common fractal structure, in spite of some gross differences in airway morphology [63]. On the other hand, it is indeed interesting to quantify changes in the results if the degree of asymmetry in the respiratory tree (which is scarcely discussed in literature) is taken into account. In our opinion, the case of asymmetry requires a separate study, since both the ‘uncertainty’ in the morphology of lungs from inter-patient variability and the asymmetry resulting from disease effects (e.g., COPD, cancer, etc.) can be discussed. We also suspect that the asymmetry may be self-similar over certain regions, leading thus to a multi-fractal spatial distribution.

7.5 Summarizing Thoughts

In this chapter, we evaluated the impedance in its non-parametric model form and its parametric model form over several frequency intervals. It turns out that no generic model can cope with the strongly varying, frequency-dependent, impedance values. However, the parameters of the proposed models are all linked to anatomical, morphological, and structural features in the respiratory system, so there is a link to physiology.

Next research directions may evaluate which of these models are most sensitive to airway changes and which of these are sensitive to tissue changes. Consequently, further studies may reveal directions for developing strategies to select the model according to the clinical target.

Chapter 8
Time Domain: Breathing Dynamics and Fractal Dimension

8.1 From Frequency Response to Time Response

8.1.1 Calculating the Impulse Response of the Lungs

In the previous section, we have seen that fractional order models of the impedance can be fitted on the frequency response (3.8) of the respiratory system in a given frequency band. However, these models cannot be used directly to simulate the time response of the respiratory system (e.g. impulse response). A feasible solution is to use finite-dimensional transfer functions of integer order. A good overview of such feasible implementations is given in [105]. From these methods, we shall adopt in this chapter the classical method of pole-zero interpolation introduced by Oustaloup in early 1990s [118]. In the remainder of this paper, we shall refer to this method as the *Oustaloup filter*.

Oustaloup filter approximation to a fractional order differentiator is a widely used method in fractional calculus. A generalized Oustaloup filter defined in the frequency band $[\omega_b, \omega_h]$ can be represented as

$$G(s) = K \prod_{k=1}^{N_{pz}} \frac{s+p}{s+z} \tag{8.1}$$

with p poles, z zeros, K a gain, and N_{pz} the number of pole-zero pairs (i.e. a design parameter). The poles, zeros, and gain can be calculated from:

$$p = \omega_b \cdot \omega_u^{2k-1-n/N_{pz}} \tag{8.2}$$

$$z = \omega_b \cdot \omega_u^{2k-1+n/N_{pz}} \tag{8.3}$$

$$K = \omega_h^n \tag{8.4}$$

with n the fractional order of the derivative s^n to be approximated and $\omega_u = \sqrt{\omega_h/\omega_b}$. The result will be a N_{pz}th integer order transfer function.

C.M. Ionescu, *The Human Respiratory System*, Series in BioEngineering,
DOI 10.1007/978-1-4471-5388-7_8, © Springer-Verlag London 2013

In this study, we have applied the approximation given by (8.1) for the s^{α_r} and the s^{β_r} coefficients from:

$$G(s) = L_r \cdot g_1 + \frac{1}{C_r \cdot g_2} \tag{8.5}$$

with g_1 and g_2 the integer order approximations for s^{α_r} and s^{β_r}, respectively.

The Fourier transform of a signal $x(t)$ in time is used to obtain the frequency representation of that signal [136]:

$$FT\{x\} = X(j\omega) = \int_{-\infty}^{\infty} x(t) e^{-j\omega t}\, dt \tag{8.6}$$

where $\omega = 2\pi f$ (rad/s) with f the frequency (Hz) and t is time (s). If we assume that x_k is a discrete sample of $x(t)$, we have the discrete Fourier transform (DFT):

$$DFT\{x\} = \sum_{k=0}^{N_k-1} x_k e^{-j\omega k T_s} \tag{8.7}$$

with k the sample number, T_s the sampling period and N_k the number of samples. Hence, the Fourier transform of a sequence of impulse functions, each of which is an element of the sample vector x, is equal to the DFT of x at each frequency where DFT is measured.

The inverse DFT is calculated as

$$x(t) = \frac{1}{2\pi} \int_{-\infty}^{\infty} X(j\omega) e^{j\omega t}\, d\omega \tag{8.8}$$

The result of (8.8) is the impulse response of the system whose frequency response is given by $X(j\omega)$.

It has been shown in Chap. 5 that the respiratory system can be successfully modeled by recurrent ladder networks which preserve the morphology and the anatomy. It was also shown that these ladder networks converge to a transfer function with fractional order operators. Since the fractal dynamics can be well modeled by power-law models (decay function), one may expect this property also from the respiratory system. We propose therefore to model the impulse response by the power-law model:

$$x(t) = A \cdot t^B \tag{8.9}$$

with A and B identified constants using a similar nonlinear least-squares algorithm as presented in Chap. 3 [21]. A Student t-test was used to derive the 95 % confidence intervals and analysis of variance (i.e. ANOVA test) was used to compare model parameters among the groups.

8.1.2 Implications in Pathology

The same groups of adults and children have been employed here as in the previous chapter. The estimated model parameter for (8.5) are given in Table 8.1 for all subjects by means of mean and standard deviation values, along with 95 % confidence

Table 8.1 Estimated and derived model parameters and modeling errors for all the investigated groups. Values are given as mean ± standard deviation; values in brackets indicate the corresponding 95 % confidence intervals

	L_r	$1/C_r$	α_r	β_r
Healthy adults	0.032 ± 0.029	1.59 ± 1.10	0.42 ± 0.08	0.75 ± 0.11
	(0.019, 0.045)	(1.09, 2.08)	(0.38, 0.47)	(0.70, 0.80)
COPD	0.016 ± 0.007	2.81 ± 1.45	0.56 ± 0.07	0.52 ± 0.10
	(0.013, 0.019)	(2.15, 3.47)	(0.53, 0.60)	(0.47, 0.56)
KS	0.0173 ± 0.012	2.47 ± 0.76	0.54 ± 0.05	0.55 ± 0.05
	(0.007, 0.02)	(1.85, 3.10)	(0.49, 0.58)	(0.50, 0.59)
Healthy children	0.11 ± 0.08	4.73 ± 2.73	0.32 ± 0.11	0.63 ± 0.16
	(0.06, 0.15)	(3.2, 6.2)	(0.26, 0.38)	(0.54, 0.72)
Asthma	0.13 ± 0.17	7.96 ± 3.16	0.32 ± 0.09	0.70 ± 0.13
	(0.03, 0.23)	(6.21, 9.7)	(0.27, 0.38)	(0.62, 0.77)
CF	0.07 ± 0.03	8.67 ± 4.63	0.38 ± 0.08	0.77 ± 0.15
	(0.05, 0.10)	(5.11, 12.23)	(0.31, 0.44)	(0.66, 0.89)

intervals. These model parameters are then used to calculate the frequency response in a wide range of frequencies. Statistically significant differences were observed in adults, between the healthy, COPD, and KS groups ($p < 0.01$) and, in children, between healthy, asthma, and CF groups ($p < 0.01$). There were no significant differences between H_C and A_C groups, due to prior inhaled medication ($p < 0.29$).

The tuning parameters for the Oustaloup filter were fitted in the frequency range 0–10^6 Hz, with 100 Hz frequency resolution, linearly spaced. The order of the filter set to $N_{pz} = 20$ gave good results for all frequency responses. An illustrative example is given in Fig. 8.1 by means of the Bode plot, with the corresponding 22nd order transfer function in the form of (8.1) with the gain

$$K = 245950.9486 \tag{8.10}$$

the denominator

$$\begin{aligned} &s^4\big(s + 4.759 \cdot 10^{-8}\big)\big(s + 3.369 \cdot 10^{-7}\big)\big(s + 2.385 \cdot 10^{-6}\big)\big(s + 1.688 \cdot 10^{-5}\big) \\ &\quad \times (s + 0.0001195)(s + 0.0008463)(s + 0.005991)(s + 0.04241)(s + 0.3003) \\ &\quad \times (s + 2.126)(s + 15.05)(s + 106.5)(s + 754.2)(s + 5339)(s + 37800) \\ &\quad \times \big(s + 2676 \cdot 10^{-5}\big)\big(s + 1.895 \cdot 10^{6}\big)\big(s + 1.111 \cdot 10^{7}\big) \end{aligned} \tag{8.11}$$

and the numerator

$$\begin{aligned} &s^2\big(s + 2.645 \cdot 10^{-8}\big)\big(s + 6.3 \cdot 10^{-8}\big)\big(s + 1.873 \cdot 10^{-7}\big)\big(s + 1.326 \cdot 10^{-6}\big) \\ &\quad \times \big(s + 9.386 \cdot 10^{-6}\big)\big(s + 6.645 \cdot 10^{-5}\big)(s + 0.0004704)(s + 0.00333) \end{aligned}$$

Fig. 8.1 An illustrative example of fitting the Oustaloup filter of order $N_{pz} = 20$ to the frequency response of the respiratory admittance in one patient

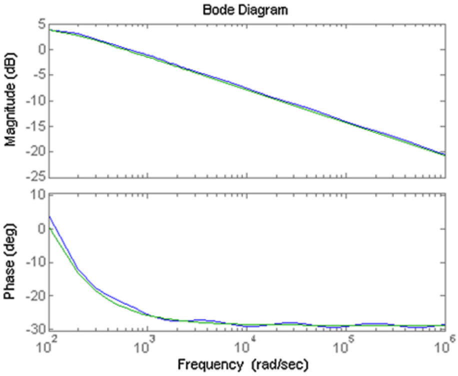

$$\begin{aligned}&\times (s+0.02358)(s+0.1669)(s+1.182)(s+8.366)(s+59.22)(s+419.3)\\&\times (s+2968)\left(s+2.101\cdot 10^4\right)\left(s+1.488\cdot 10^5\right)\left(s+1.053\cdot 10^6\right)\\&\times \left(s+7.456\cdot 10^6\right)\left(s+3.704\cdot 10^7\right)\end{aligned} \tag{8.12}$$

For the inverse DFT method, the same frequency response as for the Oustaloup filter was used. The results from Fig. 8.2 show that the same type of impulse response is obtained with either methods. Similar impulse responses are obtained for the other data sets. However, the Oustaloup filter is a high-order transfer function, containing coefficients which differ significantly in their magnitude. As such, the transfer function from (8.10)–(8.12) may not always pose numerical stability, since it contains coefficients which vary broadly in magnitude $[10^{-8}, 10^7]$. The inverse DFT is numerically stable by definition and can serve to simulate the output of the respiratory system for any input signal.

Figure 8.3 shows the log–log plots of the averaged values for impulse response in admittances for adults and for children groups, respectively. To the impulse response of each patient, a power-law model as given by (8.9) has been identified and its

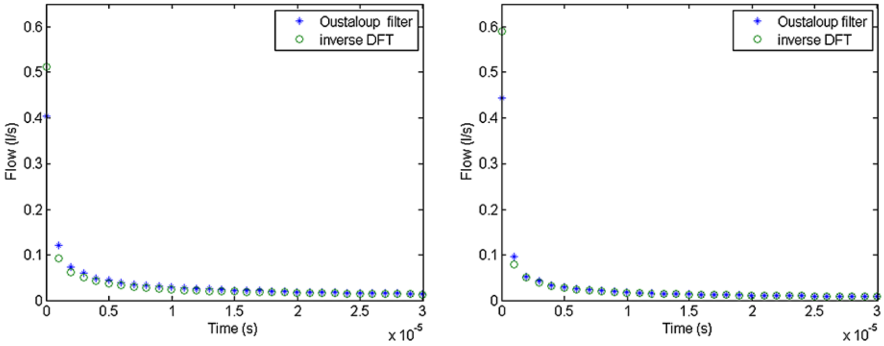

Fig. 8.2 Impulse responses for the adult healthy averaged data set (*left*) and for the healthy children averaged data set (*right*)

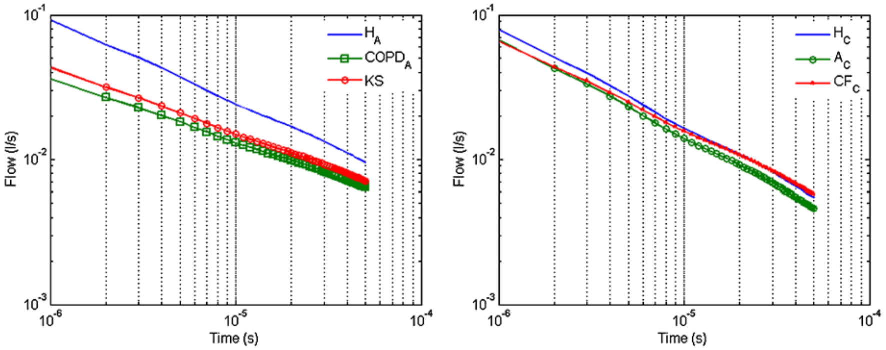

Fig. 8.3 Log-Log plot of the averaged impulse response of the admittance in adults (*left*) and in children (*right*)

Fig. 8.4 The locus of the identified A and B values from model (8.9)

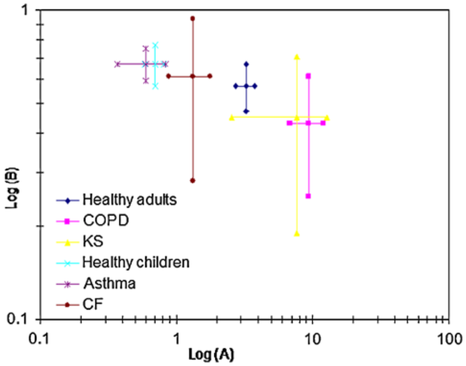

values are given in Table 8.2. The locus plot of the values from Table 8.2 is depicted by Fig. 8.4.

From the results presented in this paper, it is clear that the specificity of the respiratory disorders in $COPD_A$ and KS_A, respectively, has a significant impact on the fractal dynamics of the respiratory system ($p \ll 0.01$). However, the A_C group were controlled by means of medication, hence their lung function test was normal to the exam. This is often the case, since asthma does not manifest itself as a continuous phenomenon, mostly being triggered by external factors (i.e. allergens). Bearing these facts in mind, it is no surprising that the fractal dynamics in H_C and in A_C are similar ($p < 0.2$). In CF_C, there is no specificity in the manifestation of the disease with respect to respiratory airways and tissue, but its manifestation is overall the respiratory airways and tissue ($p \ll 0.01$).

From a practical point of view, the impulse response describes the dynamics of the respiratory airways and tissue. The results depicted in Fig. 8.2 show that with disease, the amplitude is diminished and the decay is accelerated, showing viscous effect (i.e. fibrosis of the tissue). In other words, in patients suffering from obstructive ($COPD_A$, A_C) or restrictive disease (KS_A), a much higher pressure (impulse amplitude and time interval) must be applied to obtain the same airflow as in healthy.

Table 8.2 Estimated power-law model parameters (8.9) for all the investigated groups, from the corresponding impulse response. Values are given as mean ± standard deviation; values in brackets indicate the 95 % confidence intervals

	$A \times 10^{-5}$	$-B$	$Res \times 10^{-5}$
Healthy adults	3.24 ± 0.51 (2.57, 4.93)	0.57 ± 0.10 (0.52, 0.61)	0.54 ± 0.16
COPD	9.43 ± 2.62 (7.65, 9.67)	0.43 ± 0.18 (0.39, 0.47)	0.05 ± 0.04
KS	7.68 ± 5.12 (7.05, 15.9)	0.45 ± 0.26 (0.41, 0.51)	0.09 ± 0.02
Healthy children	0.70 ± 0.11 (0.6, 0.9)	0.67 ± 0.10 (3.2, 6.2)	0.53 ± 0.15
Asthma	0.60 ± 0.23 (0.40, 1.78)	0.67 ± 0.08 (0.61, 0.73)	0.38 ± 0.12
CF	1.33 ± 0.45 (1.08, 1.44)	0.61 ± 0.33 (0.55, 0.68)	0.30 ± 0.19

We can therefore conclude that the impulse response can serve as an evaluation tool for respiratory dynamics and mechanical properties.

The results presented here indicate that both methods provide similar impulse response data. However, we may suggest that the inverse DFT is a more suitable alternative to the high-order transfer functions obtained using the classical Oustaloup filter. Additionally, a power-law model is fitted on the impulse response data, emphasizing once again the intrinsic fractal dynamics of the respiratory system.

8.2 Mapping the Impedance Values

8.2.1 Multi-dimensional Scaling

Multi-dimensional scaling (MDS) is a family of statistical techniques which attempt to discover the *hidden structure* in the available data [22]. MDS uses a matrix of proximities among the objects as input and produces an N-by-N mapping matrix of the output, given N objects for mapping. In other words, the MDS technique provides a geometric interpretation to (dis)similarity data and is a natural tool for mapping data sets in a low-dimensional space. Usually, by minimizing a loss function calculated for different possible configurations, a set of coordinates can be assigned to the envisaged objects, providing a functional meaning to the geometry of the map. The resulting map, or embedding, places objects that have similar attributes close to each other.

Various examples from technical and non-technical fields of applications can be found to use MDS as a mapping tool. The MDS has been applied to pilot performance data obtained during simulated air-to-air combat [127], where an adequate performance metric was developed to describe the complex interaction between position advantage and energy management.

Multi-dimensional scaling is also aimed to represent high-dimensional data in a low-dimensional space with preservation of the similarities between data points [47]. This reduction in dimensionality is crucial for analyzing and revealing the genuine structure hidden in the data. For noisy data, dimension reduction can effectively diminish the effect of noise on the embedded structure. For large data sets, dimension reduction can effectively overcome the information retrieval complexity. Thus, MDS techniques are used in many applications of data mining and gene network research [157, 160].

From the field of non-technical applications, the area of medicine seems to suit most the applicability of MDS, that is, the analysis of biomedical data in general. For medical image analysis, it is important to take advantage of the full range of information presented in an image, thus one has to consider distance and shape attributes [98, 166]. Separation between left and right brain sulci was developed using MDS for a new geometric representation [98]. Topography of functional brain spaces and cortico-cortical interactions was implemented through MDS [48], in order to transform anatomical space so that the distance between cortical areas is directly related to their functional connectivity. Similarly, MDS has been useful to provide an automatic method for classification of electroencephalogram (EEG) waveforms, in order to objectively detect changes in EEG recordings [60], with results in agreement with visual examination by trained physicians. Bearing in mind the success of previously reported results of MDS in various medical applications, we propose the use of MDS tools to provide a geometrical mapping of data from lung function tests in healthy subjects and in patients with respiratory disorders.

There are a manifold of techniques available to cluster data for classification purposes. These vary in optimization algorithms, speed of convergence, visualization technique and complexity. However, the MDS-based algorithms have lower complexity and faster convergence when compared to other variants [16]. If a large number data points are available, methods for high-dimensional data may be more suitable than MDS, e.g. self-organizing maps [89]. They are based on neural networks and rely on feature analysis to reduce dimensionality. In this paper, the dimension of our data is relatively low, hence the self-organizing feature maps are not employed. Moreover, they do not preserve distance information (i.e. only topological). The authors of [89] showed that a MDS-based tool is preferable for its trade off between complexity and ability to partition data sets. Moreover, MDS can process many types of data: nonnegative or negative, frequencies, correlations, ratings, etc. [14] and can optimally transform the data for better results. The main property of MDS that will be explored in this paper is that the distances between the points can be directly interpreted.

MDS is a generic name for a family of algorithms that construct a configuration of points in a low-dimensional space from information about inter-point distances measured in high-dimensional space [14]. The new geometrical configuration of points, which preserves the proximities of the high-dimensional space, facilitates the perception of data's underlying structure and often makes it much easier to understand. The problem addressed by MDS can be stated as follows: given n_i items in a m-dimensional space and an $n_i \times n_i$ matrix of proximity measures among the items, MDS produces a p_i-dimensional configuration X, $p_i \leq m$, representing the items such that the distances among the points in the new space reflect, with some degree of fidelity, the proximities in the data. The proximity measures the (dis)similarities among the items, and in general, it is a distance measure: the more similar two items are, the smaller their distance is. The Minkowski distance metric provides a general way to specify distance for quantitative data in a multi-dimensional space:

$$d_{ij} = \left(\sum_{k=1}^{m} w_k |x_{ik} - x_{jk}|^r \right)^{1/r} \tag{8.13}$$

where m is the number of dimensions, x_{ik} is the value of dimension k for object i and w_k is a weight. For $w_k = 1$, with $r = 2$, the metric equals the Euclidean distance metric, while $r = 1$ leads to the city-block (or Manhattan) metric. In practice, the Euclidean distance metric is generally used, but there are several other definitions that can be applied, including for binary data [22]. Typically MDS is used to transform the data into two or three dimensions for visualizing the result to uncover data's hidden structure, but any $p_i < m$ is also possible. The geometrical representation obtained with MDS is indeterminate with respect to translation, rotation, and reflection [47]. There are two forms of MDS, namely the metric MDS and the nonmetric MDS. The metric MDS uses the actual values of dissimilarities, while nonmetric MDS effectively uses only their ranks. Metric MDS assumes that the dissimilarities δ_{ij} calculated in the original m-dimensional data and distances d_{ij} in the p_i-dimensional space are related as follows:

$$d_{ij} \approx f(\delta_{ij}) \tag{8.14}$$

where f is a continuous monotonic function. Metric (scaling) refers to the type of transformation f of the dissimilarities and its form determines the MDS model. If $d_{ij} = \delta_{ij}$ (it means $f = 1$) and a Euclidean distance metric is used we obtain the classical (metric) MDS. In metric MDS the dissimilarities between all objects are known numbers and they are approximated by distances. Thus objects are mapped into a low-dimensional space, distances are calculated, and compared with the dissimilarities. Then objects are moved in such way that the fit becomes better, until an objective function (called stress function in the context of MDS) is minimized. In nonmetric MDS, the metric properties of f are relaxed but the rank order of the dissimilarities must be preserved. The transformation function f must obey the monotonicity constraint $d_{ij} < \delta_{rs} \rightarrow f(d_{ij}) = f(\delta_{rs})$ for all objects. The advantage of nonmetric MDS is that no assumptions need to be made about the underlying transformation function f. Therefore, it can be used in situations that only the rank order of dissimilarities is known (ordinal data). Additionally, it can be used in cases where there is incomplete information. In such cases, the configuration X is constructed from a subset of the distances, and, at the same time, the other (missing) distances are estimated by monotonic regression. In nonmetric MDS it is assumed that $d_{ij} \approx f(\delta_{ij})$, therefore $f(\delta_{ij})$ are often referred as the disparities [157] in contrast to the original dissimilarities δ_{ij}, on one hand, and the distances d_{ij} of the configuration space on the other hand. In this context, the disparity is a measure of how well the distance d_{ij} matches the dissimilarity δ_{ij}. There is no rigorous statistical method to evaluate the quality and the reliability of the results obtained by an MDS analysis. However, there are two methods often used for that purpose: the Shepard plot and the stress. The Shepard plot is a scatter plot of the dissimilarities and disparities against the distances, usually overlaid with a line having unitary slope. The plot provides a qualitative evaluation of the goodness of fit. On the other hand, the stress value gives a quantitative evaluation. Additionally, the stress plotted as a function of dimensionality can be used to estimate the adequate p_i-dimension. When the curve ceases to decrease significantly, the resulting "elbow" may correspond to a substantial improvement in fit.

In order to obtain the MDS mapping, the respiratory impedances from the same patient groups as presented in the previous chapter have been calculated using relation (3.8), for the 4 to 48 Hz frequency interval in increments of 2 Hz. As a result, we have the impedance for each patient consisting of a complex vector of real and imaginary parts, with 23 frequency points. Consequently, the distance between the real parts of the impedance Re, respectively the imaginary parts of the impedance Im, between various patients, can be calculated with some distance relations. We propose two such relations, as follows:

$$D_1 = \sqrt{\sum_{k=1}^{M1,M2} \left[(\mathrm{Re}_1 - \mathrm{Re}_2)^2 + (\mathrm{Im}_1 - \mathrm{Im}_2)^2\right]_k} \tag{8.15}$$

and

$$D_2 = \sqrt{\frac{\sum_{k=1}^{M1,M2}[(\mathrm{Re}_1 - \mathrm{Re}_2)^2 + (\mathrm{Im}_1 - \mathrm{Im}_2)^2]_k}{\sum_{k=1}^{M1,M2}[(\mathrm{Re}_1 + \mathrm{Re}_2)^2 + (\mathrm{Im}_1 + \mathrm{Im}_2)^2]_k}} \tag{8.16}$$

where both sums run over all distances between the patients in each group ($M1$, respectively, $M2$ are the total number of patients in each group used for calculating distance measurement). The $(\aleph M1 + \aleph M2) \times (\aleph M1 + \aleph M2)$ symmetric MDS matrix is constructed with the values resulting from the calculus of the corresponding distances, where $\aleph$ is the cardinal of the data set. The matrix can be visualized as a three-dimensional plot, which takes an $n_i \times n_i$ distance matrix D, and returns an $n_i \times p_i$ configuration matrix Y [101]. Rows of Y are the coordinates of n_i points in p-dimensional space for some $p_i < n_i$. When D is a Euclidean distance matrix, the distances between those points are given by D. The variable p_i is the dimension of the smallest space in which the n_i points whose inter-point distances are given by D can be embedded. One can specify D as either a full dissimilarity matrix form of D, or in upper triangle vector form (such as, e.g. the output by PDIST in Matlab). A full dissimilarity matrix must be real and symmetric, and have zeros along the diagonal and positive elements everywhere else. A dissimilarity matrix in upper triangle form

Fig. 8.5 Values for the respiratory impedance in adults with KS: kyphoscoliosis, COPD: chronic obstructive pulmonary disease and in H: healthy adults

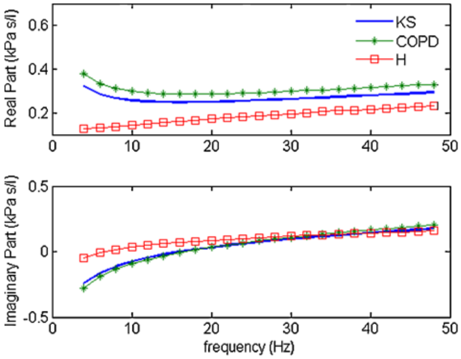

Fig. 8.6 Values for the respiratory impedance in children with A: asthma, CF: cystic fibrosis and in Hc: healthy children

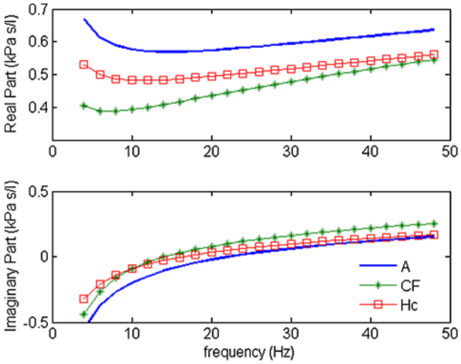

must have real, positive entries. One can also specify D as a full similarity matrix, with ones along the diagonal and all other elements less than 1. In this application we use the dissimilarity matrix form for D.

8.2.2 Classification Ability with Pathology

Illustrative, averaged values of respiratory impedance in adults with COPD, kyphoscoliosis, and healthy, are given in Fig. 8.5, by means of respective real and imaginary parts obtained with (3.8). Similarly, the respiratory impedance values in children are given in Fig. 8.6. Notice the differences in real and imaginary parts, leading to differences in the MDS scaling matrix.

Before proceeding to the MDS plots, first we shall present the analysis for stress and Shepard plots. The stress plots are always decreasing and they have a *knee*, i.e. a change in the velocity of decreasing. That knee is usually adopted as an engineering compromise for deciding the number of dimensions to adopt in the MDS plot. In the stress plots we have for the adults in Fig. 8.7-A, for (8.15), stress plot “knee” at $n_i = 3$ and in Fig. 8.7-B for (8.16), stress plot “knee” at $n_i = 2$. This suggests that (8.16) is “less demanding” in what concerns the MDS plot dimension, hence

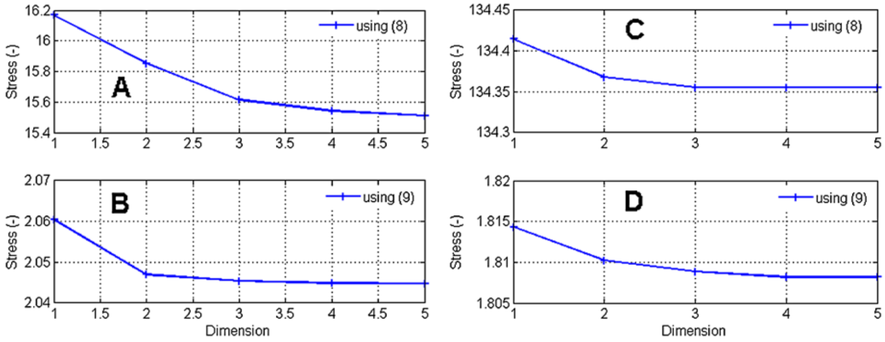

Fig. 8.7 Stress plots. The adult data set using (8.15) in plot **A** and using (8.16) in plot **B**. The children data set using (8.15) in plot **C** and using (8.16) in plot **D**

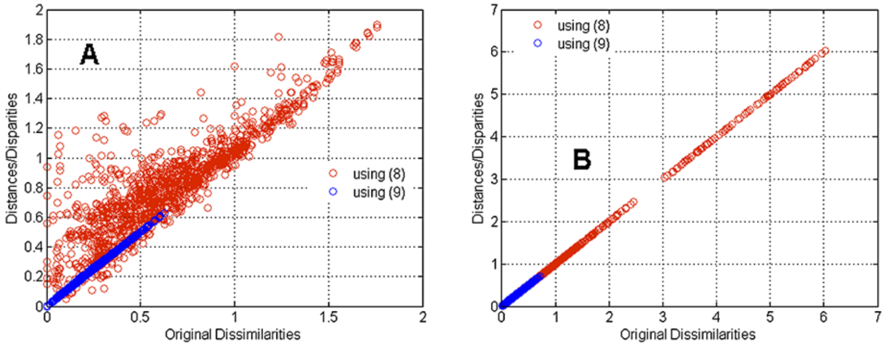

Fig. 8.8 Shepard plots for $n_i = 3$ with adult data set (plot **A**) and with children data set (plot **B**)

a low-dimension MDS plot. For children, in Fig. 8.7-C we see that for (8.15), the stress plot "knee" is at $n_i = 3$, while in Fig. 8.7-D for (8.16) the stress plot "knee" is at $n_i = 4$. In this case, the opposite situation arises: that (8.16) is more demanding. For the sake of uniformity, we shall choose $n_i = 3$ for all MDS plots.

The Shepard plots are depicted in Figs. 8.8-A and 8.8-B for (8.15) and (8.16), in adults and children, respectively. A Shepard plot is considered valid when the dots follow the 45 degree line. For example, if the dots present a low dispersion but following a curve (instead of the 45 degree line), it suggests that some nonlinear relation exists. Usually, the Shepard plots are better the higher the dimension, but "stabilize" for the n_i value obtained from the stress plot. That is why the stress and the Shepard plots are usually "redundant". From both figures we conclude that (8.16) delivers better dispersion than (8.15).

With the impedance data at hand, one can now assess the information from the MDS plots for $n_i = 3$. The mapping obtained with the MDS for relations (8.15) are given in Figs. 8.9–8.10 for the comparison between healthy adults and those with COPD and KS; respectively in Figs. 8.11–8.12 for the comparison between healthy

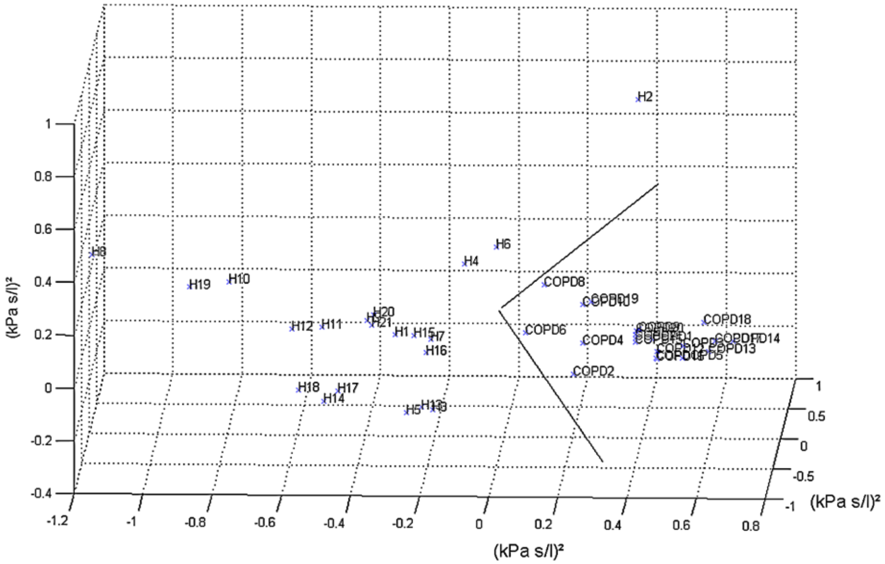

Fig. 8.9 In adults: MDS plot, using expression (8.15), for healthy (H) vs. chronic obstructive pulmonary disease (COPD), providing a perfect separation between the groups

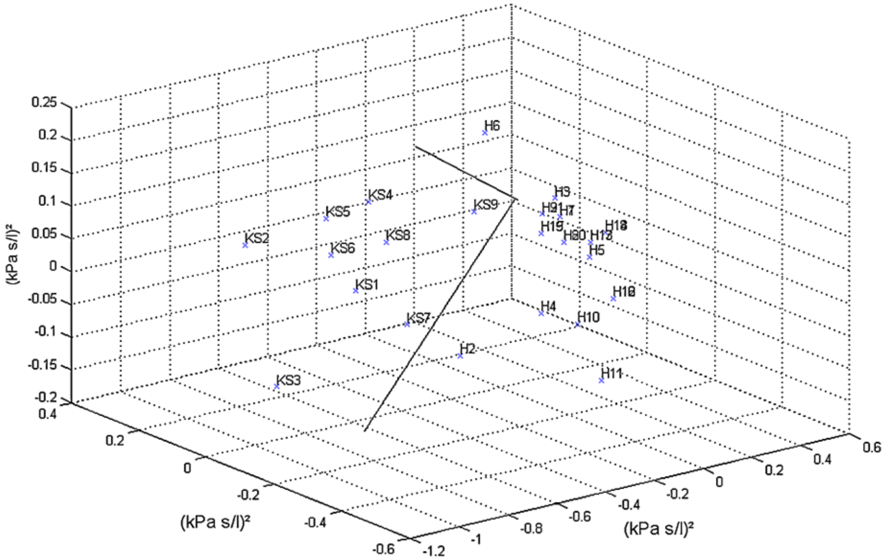

Fig. 8.10 In adults: MDS plot, using expression (8.15), for healthy (H) vs. kyphoscoliosis (KS), providing a perfect separation between the groups

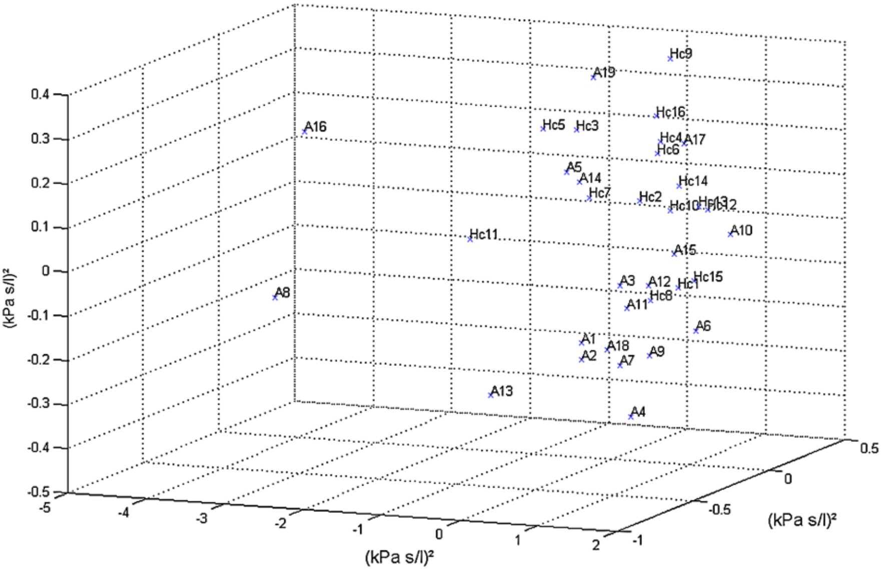

Fig. 8.11 In children: MDS plot, using expression (8.15), for healthy (Hc) vs. asthma (A); not a clear separation due to controlled asthma medication prior to the lung function test

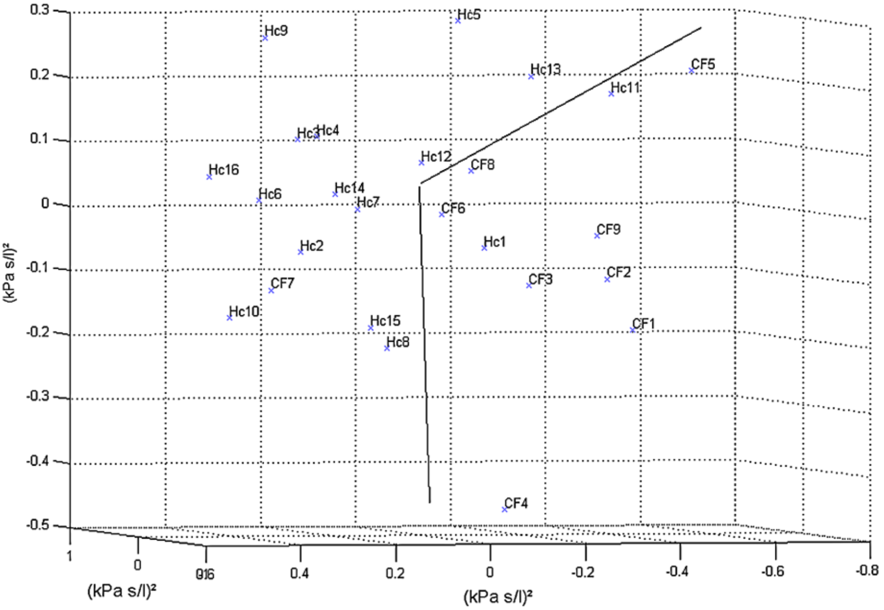

Fig. 8.12 In children: MDS plot, using expression (8.15), for healthy (Hc) vs. cystic fibrosis (CF); relatively good separation, with 1–2 outliers

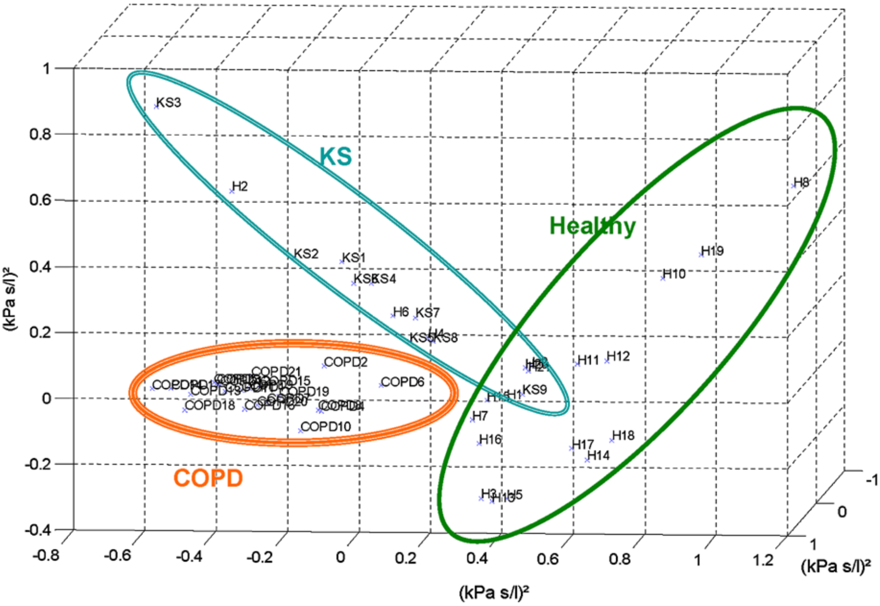

Fig. 8.13 The MDS results for the adults, using (8.15), providing good separation between the groups

children and those with asthma and CF. Similar results are obtained with relation (8.16).

In Fig. 8.13, one can observe the MDS plot using all three groups of adults (healthy, COPD, KS) in one matrix. A clear separation between these groups is obtained using (8.15), but not when using (8.16). The choice of distance metrics is therefore important when more than two groups are compared.

Further on, the mapping obtained with the MDS for relations (8.15) is given in Fig. 8.14, respectively for (8.16) in Fig. 8.15, for all three children groups (healthy, asthma, and cystic fibrosis).

Dendrograms are often used for displaying relationships among clusters. A dendrogram shows the multi-dimensional distances between objects in a tree-like structure. Objects which are closest to each other in the multi-dimensional data space are connected by a horizontal line, forming a cluster which can be regarded as a "new" object. The new cluster and the remaining original data are again searched for the closest pair, and so on. The distance of the particular pair of objects (or clusters) is reflected in the height of the horizontal line. Therefore, for comparison with MDS, using the same measure (8.15), the corresponding dendrograms for adults and children are given in Figs. 8.16 and 8.17, respectively. From all possible variations, the dendrogram using an unweighted average method provided reasonable clustering results. It is worth noticing that when applied in paired-sets, the dendrogram clustering is more homogeneous and can be easily applied to clinical use.

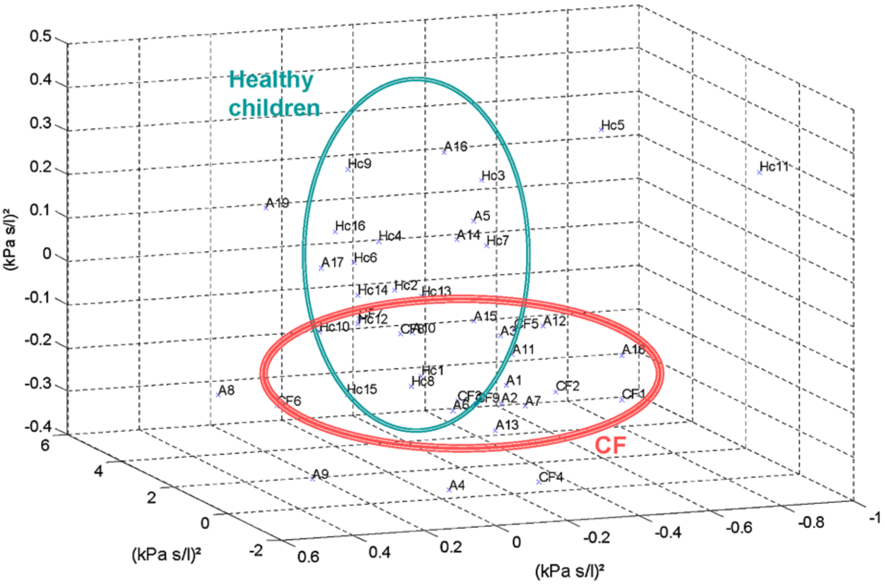

Fig. 8.14 The MDS results for the first sum, in children, thus using (8.15)

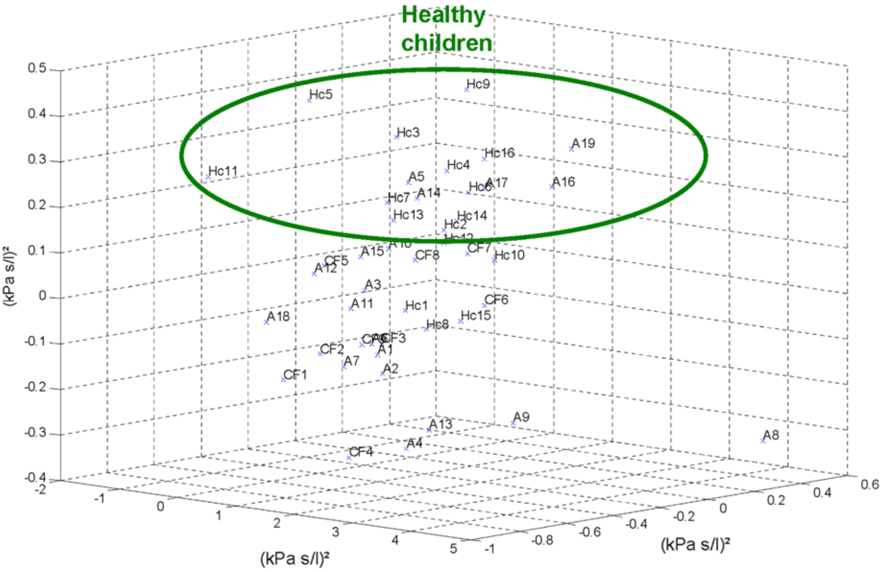

Fig. 8.15 The MDS results for the second sum, in children, thus using (8.16)

The frequency where the imaginary part of the impedance $\mathrm{Im}(Z_r) = 0$ is called the resonance frequency F_{res} and it depends on the balance between the different kind of mechanical properties (elastic, inertial). This then allows for differentiating

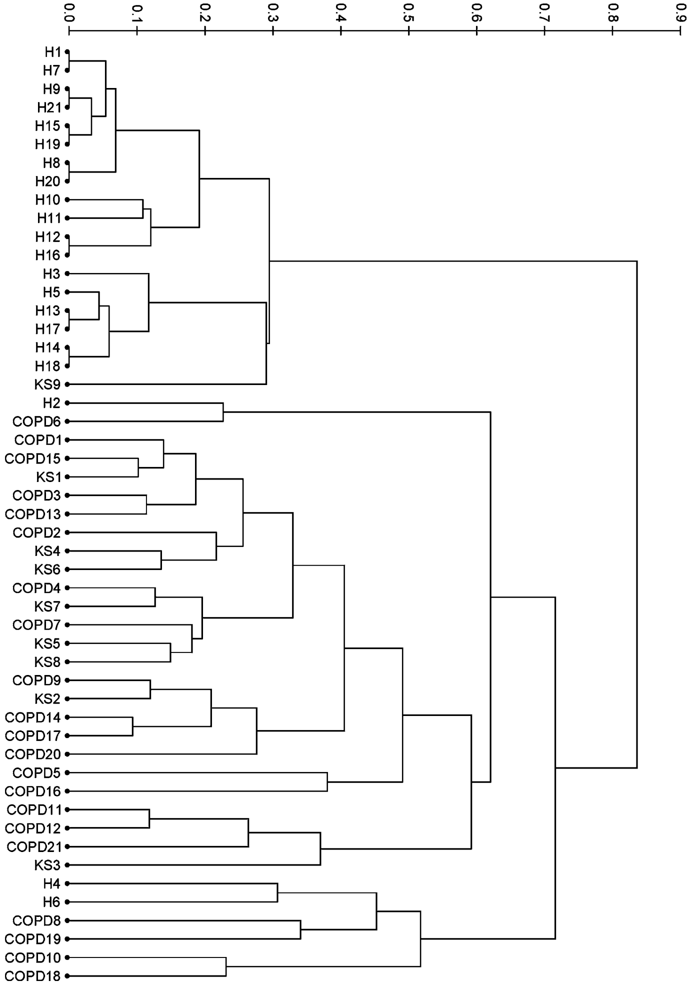

Fig. 8.16 The dendrogram tree clustering for the adult data set using (8.15), in healthy (H), chronic obstructive pulmonary disease (COPD) and kyphoscoliosis (KS)

between healthy and pathologic cases, since the resonance frequency changes significantly from typically 8 Hz for a healthy adult to 14 Hz for a patient with mild airway obstruction, and about 20 Hz in cases of severe obstruction [116]. The values obtained for the respiratory impedance data and resonant frequency have been compared with reported values from literature. We found that the values were very close to those reported in literature, namely for healthy adults [116]; for COPD [6]; for asthmatic children [17]; for cystic fibrosis [15, 35]; for healthy children [33] and for kyphoscoliosis [103]. Moreover, the impedance values and shape were significantly close to those identified with several parametric models, such as in [29, 69].

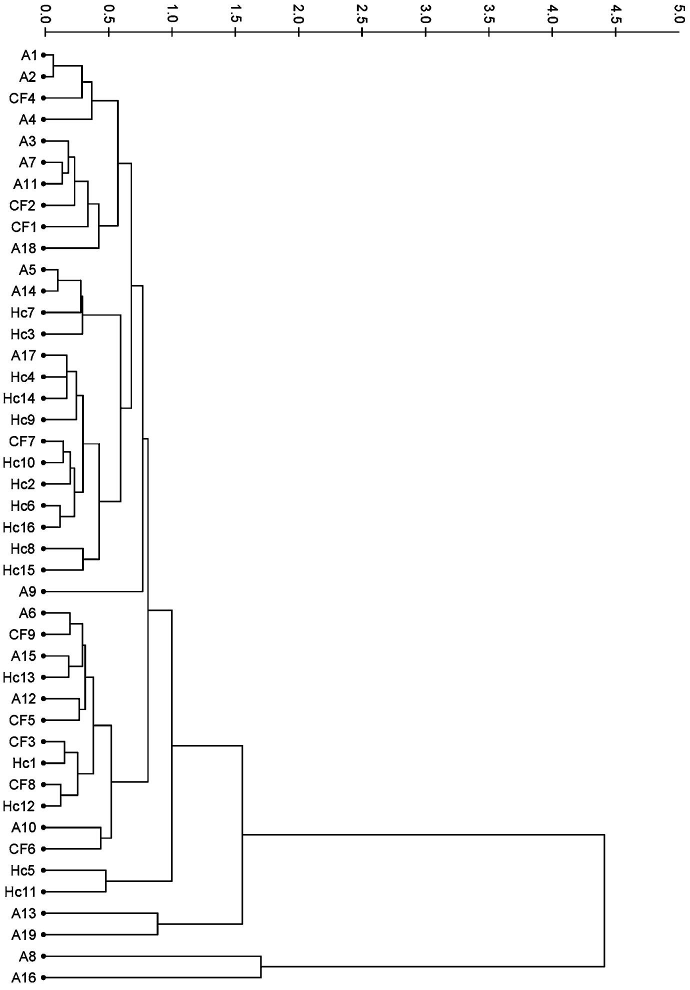

Fig. 8.17 The dendrogram tree clustering for the children data set using (8.15), in healthy (Hc), asthma (A) and cystic fibrosis (CF)

Additionally, we also looked at the real part of impedance values at 6 Hz, i.e. $R6$, which were also close to the reported and expected values from literature.

Before analyzing the MDS results, it is necessary to understand the nature of the respiratory restrictions presented by these groups of patients. Normal quiet breathing (such as during the forced oscillation technique lung function test) is accomplished by contraction of the diaphragm, the parasternal muscles and the scaleni. During inspiration, the diaphragm pulls the lower surfaces of the lung downwards. Expiration results from simple relaxation of these muscles. Changes in the elastic recoil of the lungs (more, or less, stiffness) will affect their normal function, in particular total lung volume and pressure–volume relationships.

Some measurements are performed during forced inspirations and forced expirations, that is, the spirometry lung function test. A person's vital capacity can be measured by a spirometer. In combination with other physiological measurements, the vital capacity (VC) can help making a diagnosis of the underlying lung disease. Vital capacity is the maximum amount of air a person can expel from the lungs after a maximum inspiration. It is equal to the inspiratory reserve volume plus the tidal volume plus the expiratory reserve volume. Force vital capacity (FVC) is the maximum volume of air that a person can exhale after maximum inhalation. Another important measure during spirometry is the forced expired volume in one second (FEV_1). The FEV_1/FVC ratio is used in the diagnosis of obstructive and restrictive lung disease, and normal values are approximately 80 %. In obstructive lung disease, the FEV_1 is reduced due to obstruction to air escape. Thus, the FEV_1/FVC ratio will be reduced. In restrictive lung disease, the FEV_1 and FVC are equally reduced due to fibrosis or other lung pathology (not obstructive pathology). Thus, the FEV_1/FVC ratio should be approximately normal. From the above, we observe that the spirometric values of the adults and children given in tables from Chap. 7 are in agreement.

From Fig. 8.13 we notice that the decision of using one or another distance form is important for the mapping representation. With the sum given by (8.15) the separation between groups is possible, whereas using (8.16) it becomes impossible to strictly separate between groups. One can clearly distinguish separated high density nuclei for each of the three groups: healthy, COPD, and KS. This means that it is possible to classify between these groups by means of MDS, given the suitable distance measure. Some COPD outliers are present, denoting marked progress of the obstructive disease, whereas majority of the KS objects lie fairly close to the nuclei of COPD. The reason for this similitude is that, although being a restrictive disease, KS affects in a similar manner the airway resistance. In spite of having different origins, airway resistance increases in both COPD and KS. In a similar manner, the compliance is lower in both COPD and KS. Nevertheless, different balance between these mechanical properties will place an object in the MDS map closer or further from the nucleus of the group. This is usually the case with significant pathologic restrictions, hence a more pronounced manifestation of the disease. Our results suggest that MDS is able to distinguish between restrictive (KS) and obstructive (COPD) pathologies, for clinical classification purposes. Moreover, the corresponding dendrogram tree from Fig. 8.16 supports this conclusion, by similar clustering.

In children, from Figs. 8.14–8.15 we can observe that some of the asthma patients were fairly close to the healthy subjects nucleus. The underlying reason for this result is that these asthma patients were controlled with specific medication, with intake prior to the lung function test. Hence, no significant differences from the healthy group can be seen, i.e. false 'healthy points'. The other asthma patients, who had exacerbations and a pronounced respiratory restriction, are either partially controlled, or did not take the medication prior to the exam. As far as cystic fibrosis is concerned, due to the nature of the disease, which affects in general the organism and not only the respiratory system, a clear separation could not be made from the other objects in the MDS map. Although well grouped, the nuclei of the CF lie within the surface of the other two groups (healthy children and asthma). Our results suggest that MDS may not be able to distinguish between pathologies with similar manifestations (both asthma and cystic fibrosis show presence of mucus, etc.). In children, the difficulty of diagnostic remains more pronounced than in adults. This conclusion is supported by Fig. 8.17 depicting the corresponding dendrogram tree.

8.3 Revealing the Hidden Information in Breathing at Rest

8.3.1 Pressure–Volume Loops, Work of Breathing and Fractal Dimension

A delay differential equation is a description where the evolution of a system at a certain time, depends on the state of the system at an earlier time. Such a relation is usually graphically analyzed by means of phase-plots. Hence, intuitively, there must exist a relationship between the information extracted from the phase-plots and fractional calculus. This motivates our interest in evaluating the dynamic patterns of the breathing, since it may provide useful insight into relating the changes in airway structure and tissue properties with the changes in the respiratory dynamics.

The pseudo-phase space is used to analyze signals with nonlinear behavior. For the two-dimensional case it is called pseudo-phase plane (PPP) [104]. To reconstruct the PPP it is necessary to find the adequate time lag between the signal and one delayed image of the original signal. Since PPP proved successful in various technical applications, we propose the use of PPP tools to analyze data from lung function tests in healthy subjects and in patients with respiratory disorders. The novelty of the proposed methodology is to combine the information from PPP with the corresponding fractal dimension computed using the box-counting method. In this way, the fractal dynamics of the respiratory system can be assessed and further analyzed.

One of the most common clinical features extracted from lung function tests is the air-pressure and the airflow variation during forced breathing or during breathing at rest. A standard measure of the work of breathing in lung function analysis is obtained by means of pressure–volume loops acquired during spirometry (i.e. by means of forced breathing maneuvers).

In clinical terms, the air-pressure and air-volume variations in one breathing cycle plotted against each other form a closed loop known as the PV loop [112]. The area inside this loop, and the slope of the axis of the minimal-to-maximal points in the PV loop are used to evaluate the respiratory mechanics of the patient. The interpretation of the PV loop is then made with respect to inspiratory and expiratory parameters, such as airflow resistance and work of breathing.

The PV loops are defined by

$$Area = \int_0^T V(t)\,dP(t) = \int_0^T P(t)\,dV(t) \tag{8.17}$$

with $P(t)$ the pressure and $V(t)$ the volume at time instants t. The airflow is related to the air volume by $Q(t) = dV(t)/dt$, and using this in (8.17) we find that the area is the integral of the power:

$$Area = \int_0^T P(t)Q(t)\,dt \tag{8.18}$$

which is by definition the work (energy) of breathing to perform the cycle over the period T. With disease, the work of breathing is increased and the ratio between peak pressure and peak volume is altered. However, for the purpose of this study, the area within the PV loop is of interest to us within a geometrical context. The volume has been obtained by integrating the measured airflow signal.

Usually, it is not possible to sense all the states in a system during the experimental study of its dynamics. The classical phase plane analysis provides information upon the dynamics of a system by means of one measured output and its derivative. However, other signals may be used to plot the phase dynamics, and these plans are then called *pseudo*-phase planes. The PPP reconstruction mitigates some lack of information about the system [31, 90]. The goal of the pseudo-phase space reconstruction is to view the signal in a higher-dimensional space taking a sample measurement of its history. In order to achieve the phase space, the proper time lag T_d for the delay measurements and the adequate dimension $d \in N$ (N natural numbers) of the space must be determined. In the pseudo-phase space, the measured signal $s(t)$ forms the pseudo-vector $y(t)$ according to

$$y(t) = \bigl[s(t), s(t + T_d), \ldots, s\bigl(t + (d - 1)T_d\bigr)\bigr] \tag{8.19}$$

The vector $y(t)$ can be plotted in a d-dimensional space forming a curve in the pseudo-phase space. There is a one-to-one relationship between the data in the pseudo-phase space and the associated data in the true state space. If $d = 2$ we have a two-dimensional time delay space (i.e. the pseudo-phase plane). Therefore, using the shifted signal instead of its derivative will not affect substantially the result, since the signal $\{s(t), s(t+T_d)\}$ is related by a time-shift with the model $\{s(t), \dot{s}(t)\}$. More precisely, the signal $\dot{s}(t)$ is calculated using the sampling period of the measurements, whereas $s(t + T_d)$ requires a time delay value. In resume, the PPP preserves the properties of the state space representation, and characterizes the system dynamics.

Among other methods to extract PPP [104], the method of time-delays is the most common method. Several techniques have been proposed to choose an appropriate time delay [90]. Usually the average mutual information (I_{av}) is referred as the preferred alternative to select the proper time delay T_d [31]. For the application presented in this study, we found that I_{av} presents a certain degree of noise and oscillations. Consequently, in order to use I_{av} in our study, an algorithm must be applied for smoothing the function values. Nevertheless, practice reveals that in some cases it is difficult to find the first minimum of I_{av} due to noise. Hence, a simpler, low-complexity alternative solution is proposed to select the best delay T_d based on the autocorrelation of the breathing signal [31].

A better value for T_d is the value that corresponds to the first local minimum of the mutual information. On the other hand, the mutual information is a measure of how much information can be predicted about one time series point giving full information about the other. The values of T_d at which the mutual information has a local minimum are equivalent to the values of T_d at which the logarithm of the correlation sum has a local minimum. Optimal time delay values based on the linear Pearson correlation function is a straightforward and low computational method adopted in our experiments.

Since the value of the correlation is between -1 and 1, in order to have only positive values, we will use its squared value.

From the correlation function, the first local minimum is detected and denoted as the delay value T_d. Consequently, the PPP two-dimensional plot results from plotting the breathing pressure signal $P(t)$ on the x-axis (in volts) and the shifted breathing pressure signal $P(t + T_d)$ on the y-axis (in volts).

The area inside the PV loop, and the slope of the axis of the minimal-to-maximal points in the PV loop are used to evaluate the respiratory mechanics of the patient. The interpretation of the PV loop is then made with respect to inspiratory and expiratory parameters, such as airflow resistance and work of breathing.

In the phase plane representation, we have

$$Area = \int_0^T P(t) \cdot P(t + T_d)\, dt \tag{8.20}$$

with $P(t)$ the breathing pressure signal and T_d the time delay estimated for each patient. One may notice that (8.20) is nothing else but the definition of the correlation function of two signals in time [136]. Since pressure and volume are related, the position of the air in the lungs is determined by each of these signals. Assuming that the pressure is a measure of the position of the air in the lungs, its delayed component is also related to the position. In this framework, we conclude that the PPP plot provides information on the position of air in the lungs between two time instants.

As given in the introductory chapter, the fractal dimension F_d is a quantity that gives an indication of how completely a spatial representation appears to fill the space. There are many specific methods to compute the fractal dimension. The most popular and simple methods are the Hausdorff dimension and box-counting dimension [5]. The box-counting method is an iterative method. For each box size value $\varepsilon_{\mathrm{FD}}$, follows a corresponding number of boxes $N(\varepsilon_{\mathrm{FD}})$ which will be needed in order to cover the area of the PPP loop. At the next iteration, another (bigger) size of the box is assumed and again used to cover the area in the PPP loop. The sequence of box-sizes and their corresponding total number used covering the area of the PPP loop will yield a straight line on a log–log graph:

$$F_d = \frac{\ln[N(\varepsilon_{\mathrm{FD}})] - \ln(C)}{\ln(1/\varepsilon_{\mathrm{FD}})} \tag{8.21}$$

where C is a constant related to the total area, $N(\varepsilon_{\mathrm{FD}})$ represents the minimal number of covering cells (e.g., boxes) of size $\varepsilon_{\mathrm{FD}}$ required to cover the PPP graph. The slope of the straight line in the log–log plane provides the estimate of the fractal dimension F_d:

$$N(\varepsilon_{\mathrm{FD}}) = C(1/\varepsilon_{\mathrm{FD}})^{F_d} \tag{8.22}$$

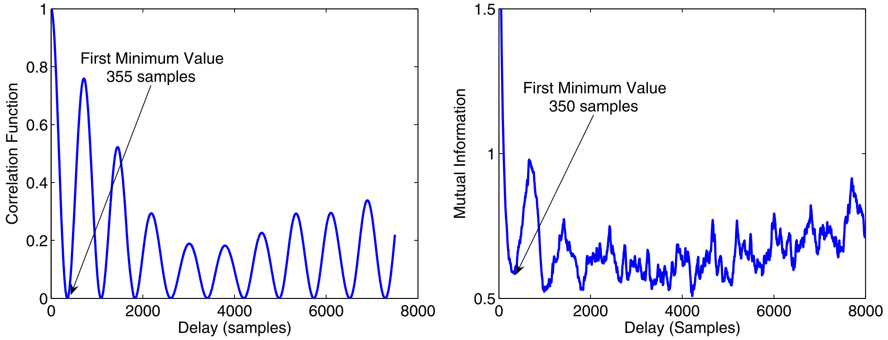

Fig. 8.18 Illustrative example for a healthy adult. (*Left*) the correlation function (time delay: 355 samples); (*right*) the mutual information (time delay: 350 samples)

Since we have a straight line in the log–log plot, from theoretical principles of fractional calculus it follows that a power-law model can be fitted to each group of patients [126], allowing deriving a model for each pathology:

$$C = A \cdot F_d^B \tag{8.23}$$

with A and B identified constants.

8.3.2 *Relations with Pathology*

For each measured set of signals, we have extracted the breathing signal from the pressure and flow signals by means of filtering. The volume was obtained by integrating the flow and the pressure–volume loops were plotted for the entire signal length.

From the breathing signal extracted from the pressure signal, the time delay value T_d was determined via the Pearson correlation function. For the sake of completeness, the mutual information has also been calculated to check that similar time delay values are obtained as with the correlation function (e.g. 355 and 350 samples, respectively). An illustrative example for a healthy patient is given in Fig. 8.18. Next, based on the extracted time delay value, the PPP plot can be obtained. The corresponding values for the time delay are given in Table 8.3.

Figure 8.19 represents the evaluation of the obtained values for the time delay by means of ANOVA tests (p was considered statistically significant for values lower than 0.05). Statistically significant variations have been observed between the adult groups ($p \ll 0.001$) and the children groups ($p < 0.0155$). These delay values were also verified against the biometric values of each group in order to determine if any correlation was present. The corresponding trends are given in Fig. 8.20 for age. Similar results were obtained for height and weight, respectively. The dependency of the delay values with the biometric values has not been observed consistently in all the evaluated groups.

Table 8.3 Time delay in samples; values are given as mean ± standard deviation; values in brackets indicate the corresponding 95 % confidence intervals

	Mean ± std	Confidence intervals
Healthy adults	545 ± 185	(487, 603)
COPD	798 ± 208	(733, 863)
Kyphoscoliosis	352 ± 50	(330, 373)
Healthy children	373 ± 96	(339, 407)
Asthma	336 ± 93	(308, 365)
Cystic fibrosis	377 ± 96	(345, 408)

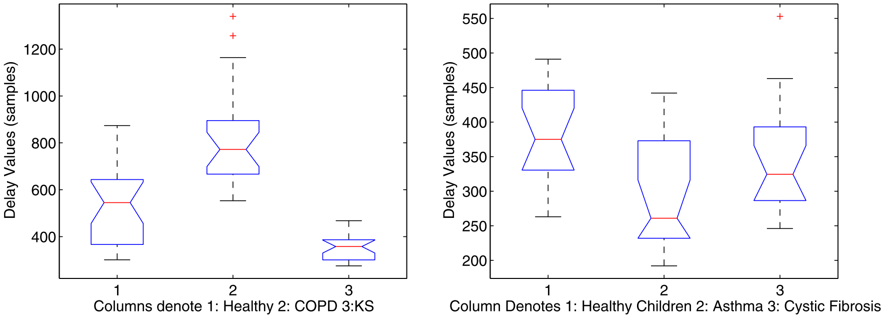

Fig. 8.19 ANOVA test for the calculated delay values: (*left*) the adult groups ($p \ll 0.001$); (*right*) the children groups ($p < 0.0155$)

Fig. 8.20 Dependence of delay values with age in each group

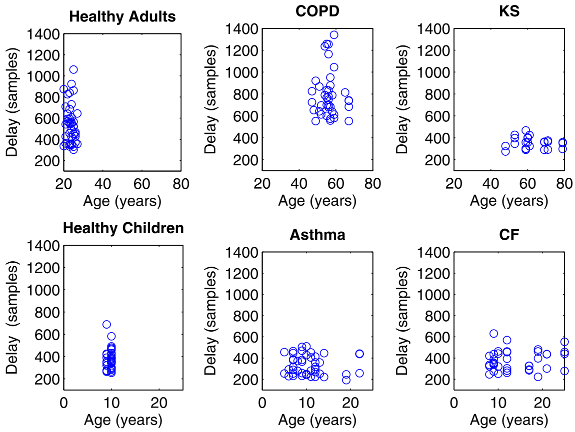

8.3.3 *Fractal Dimension and Identification of Power-Law Trends*

On each PV loop and PPP plot from each patient, the box-counting method was applied to obtain the fractal dimension F_d and the constant C for each patient. The models are identified for each set of measurements using the least-squares algorithm [136]. Consequently, the box-counting values $N(\varepsilon)$ and the box-sizes $1/\varepsilon$

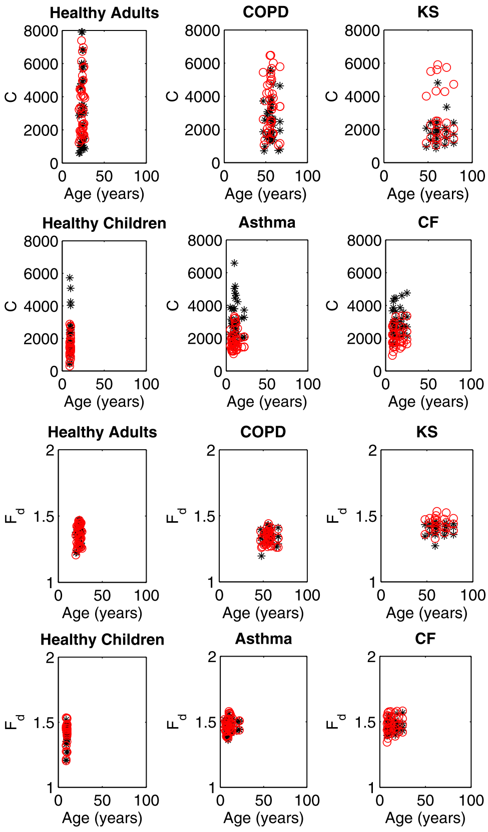

Fig. 8.21 The dependency with age for (*top half*) the constant C and (*bottom half*) the fractal dimension F_d. *Blue stars* denote the data extracted from PPP plots, while the *red circles* denote the data extracted from the PV plots

values are obtained for each patient, in each data set. The resulting data has been analyzed against biometric values in order to verify dependence, and an illustrative example is given in Fig. 8.21, for the age dependence. We found no consistent dependency with age, height, and weight, respectively.

Next, the trends of the fractal dimension calculated for each group are given in Fig. 8.22 by means of PV loops, and in Fig. 8.23 by means of PPP loops, respectively. Finally, the loci of the identified power-law model parameters from relation (8.23) are given in Fig. 8.24 and the values are listed in Table 8.4.

In its most simple representation, the respiratory system can be represented as a series connection of a resistance R_e and a compliance C_e. It assumes patient's respiratory muscles inactive and the external equipment is driving the flow into the lungs [53, 112, 125]. The driving pressure $P(t)$ generates flow $Q(t)$ across the resistance and the volume $V(t)$ changes in the compliance. If $P_r(t)$ and $P_e(t)$ are the resistive and elastic pressure drops, respectively, we have

$$R_r = \frac{P_r(t)}{Q(t)}; \qquad C_r = \frac{V(t)}{P_e(t)} \quad \text{and} \quad P(t) = P_e(t) + P_r(t). \tag{8.24}$$

Fig. 8.22 The information extracted for each patient in terms of C and F_d from the PV plots

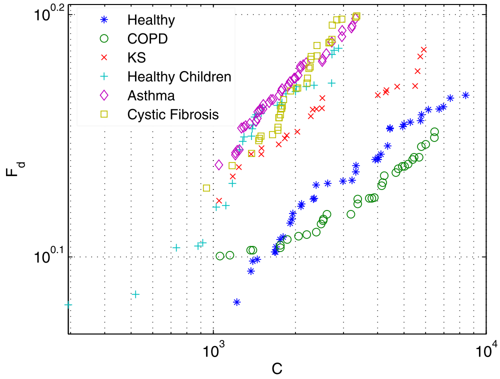

Fig. 8.23 The information extracted for each patient in terms of C and F_d from the PPP plots

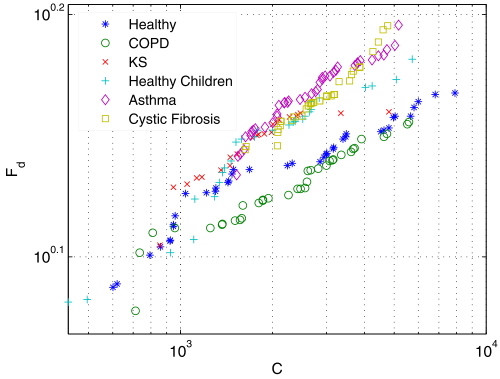

We have as a result

$$P(t) = R_r \cdot Q(t) + \frac{V(t)}{C_r} \tag{8.25}$$

This represents the first order equation in the motion-equation for a single compartment model of the respiratory system: a single balloon with compliance C_r on a pipeline with a resistance R_r. This system can be studied using the exponential decay of volume $V(t)$ as resulting from a step input V_0: $V(t) = V_0 e^{-t/\tau}$, where t is time and τ is the time constant which characterizes the system, denoted by the product of $R_r C_r$ [116].

In the representation of the PPP plots, we have the breathing signal expressed as pressure and its time-delayed derivative. From (8.25) can be observed that there exists a relation between pressure and flow ($Q(t) = dV/dt$). In clinical terms, the pressure–volume loop during one breathing period is able to tell the clinician something about the dynamic compliance of the respiratory system and its work. The area enclosed by the PV loop is called the physiologic work of breathing, denoting the resistive work performed by the patient to overcome the resistance present in the airways [134].

Table 8.4 Fitted power-law models (8.23) for each group of data. COPD: chronic obstructive pulmonary disease. KS: kyphoscoliosis. CF: cystic fibrosis

DATA source	A PV/PPP	B PV/PPP
Healthy adults	0.632/0.848	0.094/0.062
COPD	0.752/0.795	0.069/0.068
KS	0.882/0.844	0.062/0.067
Healthy children	0.557/0.704	0.127/0.090
Asthma	0.624/0.739	0.114/0.087
CF	0.478/0.640	0.147/0.104

As already explained in previous chapters, during cycling loading, the stress that develops in the viscoelastic body (respiratory tissue) displays:

- a component in phase with strain, which is the elastic stress contributing to the storage modulus E_S (elastance); and
- a component out of phase with strain, corresponding to the viscous dissipation and contributing to the loss modulus E_D (damping).

In [9, 26] was shown that the respiratory system can be indeed modeled as a combination of series RC elements in a cascade arrangement of consecutive airways, by using their mechanical analogue representation, springs K_{rs} and dashpots B_{rs}. In this mechanical model, it follows that the pressure–volume relationship equivalent to the stress–strain relationship is given by

$$P(t) = \frac{K_{rs}\ell_{rs}}{A_{rs}} V(t) + \frac{B_{rs}\ell_{rs}}{A_{rs}} \frac{dV(t)}{dt} \tag{8.26}$$

with P the air-pressure, V the air volume, ℓ_{rs} and A_{rs} the changes in length and area of airways during the breathing cycle, and K_{rs}, B_{rs} the constants of the spring and dashpot, respectively [26]. This relation suggests that the PPP loop is a measure

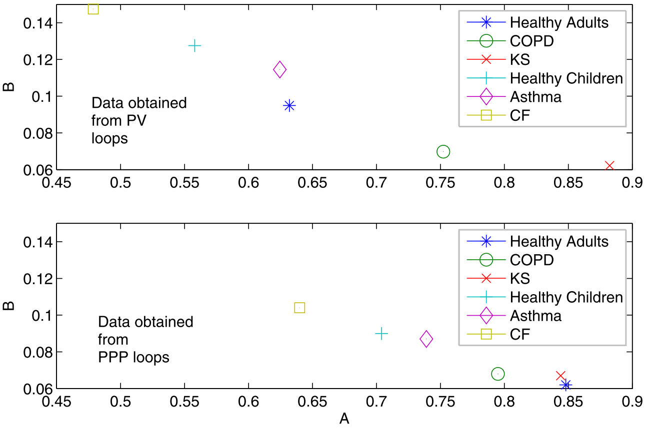

Fig. 8.24 The plot of the identified A and B values from model (8.23) for each set of data

of the mechanical properties in the lung parenchyma and airways during breathing. The respiratory mechanical properties have been shown to be related to the structure of the lungs, which consequently is altered by pathology [9, 87].

Normal quiet breathing (such as during the forced oscillation technique lung function test) is accomplished by contraction of the diaphragm, the parasternal muscles and the scaleni. During inspiration, the diaphragm pulls the lower surfaces of the lung downwards. Expiration results from simple relaxation of these muscles. Changes in the elastic recoil of the lungs (more, or less, stiffness) will affect their normal function, in particular total lung volume and pressure–volume relationships.

It has been recognized that the structure of the respiratory tree is strongly related to that of fractal structures [164]. Moreover, it has been shown that the particular dichotomous structure is a necessity for optimality with respect to total volume and resistance [66, 164]. The morphology of the human tree provides maximal efficiency in assuring air distribution with minimal viscous dissipation. The geometrical and morphological structure of the healthy lung has been shown to lead to lumped models of fractional order derivatives and integrals [70], which are by definition models for systems with long-memory properties (e.g. the respiratory system).

In [99], it has been shown that the structure and its bifurcating geometry plays an important role in ventilation. Assuming a ratio h between diameter and length between two consecutive airway generations—the homothety factor—the authors have shown that the volume and pressure drop can be written as

$$V_N = V_0\left[1+\sum_{i=1}^{N}\left(2h^3\right)^i\right] \tag{8.27}$$

and

$$\Delta P_N = R_0\bar{Q}\left[1+\sum_{i=1}^{N}\frac{1}{(2h^3)^i}\right] \tag{8.28}$$

respectively, with $\bar{Q}$ the global airflow, R_0 and V_0 some initial values for resistance and volume, i the airway generation number and N the total number of airway generations in the respiratory tree. The validity of these relations has been shown for the lower part of the bronchial tree (i.e. generations 6–16). Since the same factor $(2h^3)^i$ appears in both equations, there is an interplay between pressure and volume values. The fractal dimension in terms of lung structure is given by

$$FD_s = \frac{\log 2}{\log(1/h)}. \tag{8.29}$$

For a realistic respiratory tree, the assumption of a fractal structure does not hold. Nevertheless, it has been shown that although the structure is random, with different reduction ratios in a dichotomous bifurcation, the total resistance is given by

$$R_N = R_0\left[1+\sum_{i=1}^{N}\left(\frac{1}{h_1^3+h_2^3}\right)^i\right] \tag{8.30}$$

with h_1 and h_2 the homothety factors for the left and right branch, respectively. The critical value for the lungs is given by $h = 0.85$, corresponding to a low resistance and volume higher than necessary [164]. This value is higher than the value $h = 0.79$ for the symmetric model [99]. The relation (8.30) gives the homothety factor of $h = 0.76$, which is close to that given by the symmetrical structure model. Hence, it follows that the resistance depends on the structure and *not on the degree of symmetry*. Since the value of $0.85 > 0.79$, it follows that the design of the lungs is made with a safety margin for breathing in conditions of bronchial constriction [99].

The structural changes in the respiratory tree will change the value of the homothety factor h and one can analyze the dynamics of the respiratory tree in terms of pressure and volume variations. If the homothety factor decreases from 'optimal' then an increase in the pressure drop will occur (higher effort to breath). If the homothety factor increases from 'optimal', the resistance is small, i.e. the volume will increase for lower pressure drop values.

In asthma, the inner diameters of the bronchioli, and not their lengths, are reduced. In this case, the airway ducts are no longer homothetic and the diameter and length of the sequential bronchioles are altered. This implies that the pressure drop is given by

$$\Delta P_N = R_0 \bar{Q} \left[1 + \sum_{i=1}^{N} \frac{1}{2^i} \frac{h_1}{(h_d^4)^i} \right] \tag{8.31}$$

with h_1 the length reduction ratio, h_d the diameter reduction ratio. The nonlinear effect of the constriction is more pronounced, since a small reduction in h_d will have a manifold effect in the total tree resistance.

The fractal dimension extracted from the PV and PPP loops is indirectly related to the structure of the respiratory tree, since it quantifies the work of breathing, a measure of the combined effect of pressure and volume. This implies that indirectly, the proposed methods in this paper offer a measure of the degree of homothety in the lungs. In other words, we indirectly evaluate the degree of optimality in the respiratory process.

From Table 8.4, we observe that the values identified from mapping the information obtained in the PV loops provide more consistent results than those given by the PPP plots. Indeed, from Fig. 8.24, one can observe that the identified values for (8.23) are more dispersed in the context of PV loop, allowing a clearer separation between the groups. The data for the adults and the children do not overlap, thus the validity of the results is supported. In terms of the A parameter, its value for the adult group seems to be correlated directly with the airway resistance. Its values are increasing with COPD and KS, which corresponds to the clinical pathology. For the children group, its values are close to each other for healthy and asthma. We suspect the reason might be the medication taken by the asthmatic patients, which had mostly normal-to-the-exam spirometric values (i.e. controlled asthma). The values for the children with pulmonary cystic fibrosis were lower than in healthy, indicating a lower resistance, either by means of lower pressure drop, either by means of higher volume. In terms of the B parameter, its value seems to be correlated inversely with the resistance, or, directly with the volume. The values in COPD and KS were lower, indicating lower volumes, which corresponds to the clinical pathology. In children, the values of healthy and asthma were again close to each other, while in cystic fibrosis patients the values were higher (i.e. higher values). We conclude that the values for the CF group might be subject to the weight and height biometric parameters.

One of the limitations of the study is that the groups of subjects and patients were not equally balanced in terms of male/female distribution, hence dependency with gender was not determined. Similarly, dependency may exist for the adult groups in terms of age. The healthy adult group had an averaged age value significantly lower than those diagnosed with COPD and KS. The dependency with height and weight was not consistently observed in all groups, hence we could not conclude whether or not these biometric parameters will influence our results. However, even if this is the case, the seminal ideas presented in this work still hold, in the sense that there exists a link between changes in the structure and dynamic patterns in the breathing.

We have also concluded that the PV loop provides better results than PPP loop in terms of separation of the groups. However, the PV loop requires the recording of two signals: pressure and flow, or similarly, pressure, and volume. In the context of FOT, there is a 25-fold difference in the cost of pressure sensors and flow sensors. Therefore, measuring only one signal may be an interesting approach to support the use of PPP plots instead of PV plots. The advantage would be that if the pressure is available (i.e. the cheapest measurement), then the delayed derivative of pressure can be used to plot the PPP.

From a clinical standpoint, it is clear that one of the proposed parameters (i.e. A) is related to the resistive components of the breathing dynamics as extracted from the PPP loops. However, we do not yet have a parameter which characterizes the elastic components. Also, there is no information as to how the inhomogeneities in the lung affect the results of the PPP loops. We conclude that in order to provide a concise interpretation and mapping the short-term breathing dynamics by means of PPP plots, a bigger database of patients should be analyzed.

8.4 Summary

Following the theoretical basis laid in the first chapters of this book and the frequency domain identification from previous chapter, it was only natural to apply our knowledge in the time domain. First, the link between fractional order parametric models and time response has been achieved by calculating the impulse response of the respiratory system. It was shown that this response varies in healthy volunteers and in patients diagnosed with breathing impairment. Next, we employed the notions of fractal dimension and pseudo-phase plot and correlate them to the dynamics of the breathing. Again, the link to power-law and implicit fractal dynamics has been made and results were analyzed over several groups of patients. All these investigations have been performed in the context of linear systems. The next chapter in this book will tackle the problem from the nonlinear dynamics point of view in order to excerpt new information from the system.

Chapter 9
Non-linear Effects in the Respiratory Impedance

9.1 The Principles of Detection of Non-linear Distortions in a Non-linear System

This section addresses two problems: (i) the problem of breathing interference with the excitation signal and (ii) the detection of non-linear contributions in the measured signals. The common solution to these problems is the optimization of the excitation signal, further detailed hereafter.

9.1.1 Reducing the Breathing Interference

In the standard use of the FOT, the excitation signal (i.e. with frequencies from 4 Hz to 48 Hz) lies well above the breathing frequency (i.e. around 0.3 Hz), which enables high-pass filtering as a separation technique for the useful signals to be processed. Also, harmonics of the breathing frequency become small in amplitude as the frequency increases, such that the estimation of the impedance using standard estimation methods as explained in Chap. 3 poses no problem. However, when frequencies closer to the breathing are used in the excitation signal, the breathing of the patient must be modeled in order to provide a good separation of the overlapping frequencies. The challenges in this modeling step are manifold: the breathing is a non-stationary, time varying signal, whose frequency and amplitude may vary in time. In addition, the corresponding harmonics are overlapping with the excited frequencies. In the remainder of this work, it is assumed that the breathing frequency F_0 remains fixed during the measurement time, which is in fact a reasonable assumption.

The following is an algorithm which estimates the breathing of the patient from measured offline data [170]. Consider that the real breathing signal $b(t)$ has the following form (i denotes here the harmonics of the breathing frequency F_0, going

C.M. Ionescu, *The Human Respiratory System*, Series in BioEngineering,
DOI 10.1007/978-1-4471-5388-7_9, © Springer-Verlag London 2013

from 1 to k, with $k = 5$):

$$b(t) = \sum_{i=1}^{k} A_i(t)\sin[2\pi i F_0 t] + B_i(t)\cos[2\pi i F_0 t] + rez(t) \tag{9.1}$$

with $rez(t)$ denoting the residual values.

First, the matrix Φ_i corresponding to the ith harmonic is defined by

$$\Phi_i = \begin{bmatrix} \sin(T_s i\omega_0)(T_s)^0 & \cos(T_s i\omega_0)(T_s)^0 & \cdots & \sin(T_s i\omega_0)(T_s)^\beta & \cos(T_s i\omega_0)(T_s)^\beta \\ \sin(2T_s i\omega_0)(2T_s)^0 & \cos(2T_s i\omega_0)(2T_s)^0 & \cdots & \sin(2T_s i\omega_0)(2T_s)^\beta & \cos(2T_s i\omega_0)(2T_s)^\beta \\ \vdots & \vdots & \vdots & \vdots & \vdots \\ \sin(nT_s i\omega_0)(nT_s)^0 & \cos(nT_s i\omega_0)(nT_s)^0 & \cdots & \sin(nT_s i\omega_0)(nT_s)^\beta & \cos(nT_s i\omega_0)(nT_s)^\beta \end{bmatrix} \tag{9.2}$$

where

- $\omega_0 = 2\pi F_0$, with F_0 the breathing frequency
- T_s is the sampling period ($T_s = 1$ ms)
- n is the sample used for estimation (in our case, a 40 seconds measurement at $T_s = 1$ ms sampling period will result in a total number of samples of $N = 40.000$)
- i is the breathing harmonic with $i = 1, \ldots, k$, with $k = 5$ (the first five harmonics were considered to be most significant in terms of amplitude) and
- β is the order of the estimated polynomial $A_i(t)$ or $B_i(t)$.

The matrix is then completed for each harmonic (without accounting for modulation effects), resulting in

$$\Phi = [\Phi_1 \quad \Phi_2 \quad \cdots \quad \Phi_k] \tag{9.3}$$

where k is the total number of harmonics which are estimated ($k = 5$). Then one estimates the parameters in a vector Θ:

$$\begin{aligned} \Theta_i &= [A_{1i} \quad B_{1i} \quad \cdots \quad A_{pi} \quad B_{pi}] \\ \Theta &= [\Theta_1 \quad \Theta_2 \quad \cdots \quad \Theta_k]^T \end{aligned} \tag{9.4}$$

It follows that the reconstruction of the breathing is given by

$$b(n) = \Phi \cdot \Theta \tag{9.5}$$

The least square estimate of Θ is then given by

$$\hat{\Theta} = \left(\Phi^T \Phi\right)^{-1} \Phi^T \, b(n) \tag{9.6}$$

The estimation of the signal $b(t)$ will be represented as $\hat{b}(t)$. The aim is to minimize the cost function:

$$J = \frac{1}{N} \sum_{n=0}^{N-1} \left[b(n) - \hat{b}(n)\right]^2 \tag{9.7}$$

Notice that if the breathing frequency F_0 is perfectly known, the estimation is straightforward. However, if the baseline frequency is not well known, then also the harmonics are erroneously estimated [41, 111]. Therefore, the baseline frequency needs to be estimated as well, resulting in a non-linear least squares problem [124, 138]. In addition, a higher polynomial degree β can lead to numerical instability of the convergence matrix from (9.3). The numerical conditioning can be improved by making the values dimensionless, i.e. introducing the variable:

$$t' = \frac{t}{N \cdot T_s} \tag{9.8}$$

Additionally, one can introduce a diagonal matrix S:

$$\begin{aligned} \hat{b}(n) &= \varPhi \cdot \varTheta \\ &= \varPhi \cdot S \cdot S^{-1} \cdot \varTheta \\ &= \varPhi' \cdot \varTheta' \end{aligned} \tag{9.9}$$

with $\varPhi' = \varPhi \cdot S$ and $\varTheta' = S^{-1} \cdot \varTheta$. The matrix S is a diagonal matrix, with the diagonal elements the Root Mean Squared values calculated per each column, which can be depicted as

$$\varPhi = \begin{bmatrix} s_{11} & & 0 \\ & \ddots & \\ 0 & & s_{pk} \end{bmatrix} \tag{9.10}$$

To determine F_0, we make use of the FFT-interpolation method. The method is simplified for the case of a frequency F_0 surrounded by two integer multiples of the spectrum S_{xx} for the resolution frequency (f_0) [52]:

$$\begin{aligned} f_1 &= \max(S_{xx}) \\ \delta &= \frac{2\frac{f_1+f_0}{f_1} - 1}{\frac{f_1+f_0}{f_1} + 1} \\ \hat{F}_0 &= (f_1 - f_0) + \delta \cdot (f_0) \end{aligned} \tag{9.11}$$

The optimized excitation signal is an odd random phase multisine defined as:

$$U_{\text{FOT}} = \sum_{k=0}^{109} A_k \sin\bigl(2\pi(2k+1) f_0 t + \phi_k\bigr) \tag{9.12}$$

with

- frequency interval from 0.1 to 21.9 Hz
- frequency resolution f_0 of 0.1 Hz
- only odd harmonics

- only harmonics which are not overlapping with the first five breathing harmonics are used
- equal amplitude A_k for all excited harmonics
- the phase ϕ_k uniformly distributed between $[0, 2\pi]$
- one so-called *detection line* for each group of four excited odd harmonics is not excited in order to check for odd non-linear distortion.

This algorithm has been broadly detailed elsewhere [77, 136]. The flowchart for the measurement procedure can be summarized as follows:

- estimate the fundamental breathing frequency,
- make the excitation signal taking into account the information from the previous step and
- filter the measured data and perform further signal processing (i.e. non-linear distortions detection algorithm).

9.1.2 Non-linear Distortions

The standard procedure to obtain the impulse response $g(t)$ of a linear system is based on the correlation analysis:

$$R_{yu}(t) = g(t) * R_{uu}(t) \tag{9.13}$$

with $u(t)$ the input signal, $y(t)$ the output signal and $*$ denoting the convolution product. $R_{yu}(t)$ and $R_{uu}(t)$ are the cross- and auto-correlations, respectively:

$$\begin{aligned} R_{yu}(\tau) &= E\big\{y(t)u(t-\tau)\big\} \\ R_{uu}(\tau) &= E\big\{u(t)u(t-\tau)\big\} \end{aligned} \tag{9.14}$$

with τ the shift interval. Applying Fourier transform to (9.13) results in

$$G(j\omega) = \frac{S_{\mathrm{YU}}(j\omega)}{S_{\mathrm{UU}}(j\omega)} \tag{9.15}$$

where the cross-spectrum $S_{\mathrm{YU}}(j\omega)$, the auto-spectrum $S_{\mathrm{UU}}(j\omega)$, and the frequency response function (FRF) $G(j\omega)$ are the Fourier transforms of $R_{\mathrm{YU}}(t)$, $R_{\mathrm{UU}}(t)$ and $g(t)$, respectively.

The Best Linear Approximation (BLA) [136, 137] of a non-linear system $g_{\mathrm{BLA}}(t)$ minimizes the mean squared error (MSE) between the real output of a non-linear system $y(t) - E\{y(t)\}$ and the output of a linear model approximation $g_{\mathrm{BLA}}(t) * (u(t) - E\{u(t)\})$:

$$E\Big\{\big\|\big(y(t) - E\big\{y(t)\big\}\big) - g_{\mathrm{BLA}}(t) * \big(u(t) - E\big\{u(t)\big\}\big)\big\|^2\Big\} \tag{9.16}$$

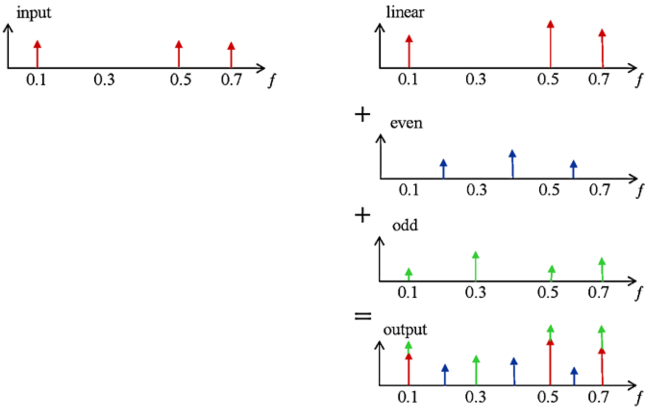

Fig. 9.1 A schematic representation of the input–output contributions

where E denotes the expected value with respect to realizations of the input. In the frequency domain, the solution to the optimization problem from (9.16) is given by

$$\hat{G}_{\mathrm{BLA}}(j\omega) = \frac{\hat{S}_{\mathrm{YU}}(j\omega)}{\hat{S}_{\mathrm{UU}}(j\omega)} \tag{9.17}$$

where the cross-spectrum $\hat{S}_{\mathrm{YU}}(j\omega)$, the auto-spectrum $\hat{S}_{\mathrm{UU}}(j\omega)$, and the FRF $\hat{G}_{\mathrm{BLA}}(j\omega)$ are the Fourier transforms of $R_{yu}(t)$, $R_{uu}(t)$ and $g_{\mathrm{BLA}}(t)$, respectively. In practice, this relation is simplified for periodical signals as:

$$\hat{G}_{\mathrm{BLA}}(j\omega_k) = \frac{1}{M}\sum_{m=1}^{M} \frac{Y^{[m]}(k)}{U^{[m]}(k)} \tag{9.18}$$

where the notation $X^{[m]}(k)$ has been used to describe the DFT spectrum of the mth multisinus realization. The estimation of BLA, $\hat{G}_{\mathrm{BLA}}$, described by relation (9.18) can be re-written as:

$$\hat{G}_{\mathrm{BLA}}(j\omega_k) = G_{\mathrm{BLA}}(j\omega_k) + G_S(j\omega_k) + N_G(j\omega_k) \tag{9.19}$$

where G_S is the non-linear noise term ($E\{G_S\} = 0$) and N_G is the measurement noise. The non-linear stochastic contribution G_S depends on the power spectrum and the power distribution of the input signal, as well as on the even and odd non-linear contributions. The effect of G_S can be reduced by averaging the measurements over several multisine realizations (i.e. multiple measurements m of the same system, with different inputs of same amplitude distribution, but different random phase realization in (9.12)). The effect of N_G can be reduced by measuring longer records (i.e. larger number of periods p during each measurement).

In Fig. 9.1, the underpinning principle of detecting these non-linearities is represented.

In time domain, the output $y(t)$ of a non-linear system can be written as:

$$y(t) = g_{\mathrm{BLA}}(t) * u(t) + y_s(t) \tag{9.20}$$

where $g_{\mathrm{BLA}}(t)$ is the impulse response of the linear BLA, and $y_s(t)$ is the term in the output signal as a result of the stochastic non-linear distortion.

Given that $n_y(t)$ is a stochastic process and $y_s(t)$ is a periodical signal dependent on the realization $r(t)$, the FRF of the mth realization and pth period, $G^{[m,p]}(j\omega_k)$ can be described as [136]

$$G^{[m,p]}(j\omega_k) = \frac{Y^{[m,p]}(k)}{U_0^{[m]}(k)} = G_{\mathrm{BLA}}(j\omega_k) + \frac{Y_S^{[m]}(k)}{U_0^{[m]}(k)} + \frac{N_Y^{[m,p]}(k)}{U_0^{[m]}(k)} \tag{9.21}$$

where $X^{[m,p]}(k)$ is the DFT spectrum of the pth period of the mth multisine realization and $\hat{X}^{[m]}$ is the estimated spectrum of the mth multisine realization.

Consequently, one can estimate the BLA, the variance of the stochastic non-linear distortions and the noise variance, using

$$\begin{aligned} \hat{G}^{[m]}(j\omega_k) &= \frac{1}{P}\sum_{p=1}^{P} G^{[m,p]}(j\omega_k) \\ \hat{G}_{\mathrm{BLA}}(j\omega_k) &= \frac{1}{M}\sum_{m=1}^{M} \hat{G}^{[m]}(j\omega_k) \end{aligned} \tag{9.22}$$

$$\begin{aligned} \hat{\sigma}^2_{\hat{G}^{[m]}}(k) &= \sum_{p=1}^{P} \frac{|G^{[m,p]}(j\omega_k) - \hat{G}^{[m]}(j\omega_k)|^2}{P(P-1)} \\ \hat{\sigma}^2_{\hat{G}_{\mathrm{BLA}}}(k) &= \sum_{m=1}^{M} \frac{|G^{[m]}(j\omega_k) - \hat{G}_{\mathrm{BLA}}(j\omega_k)|^2}{M(M-1)} \end{aligned} \tag{9.23}$$

$$\hat{\sigma}^2_{\hat{G}_{\mathrm{BLA},n}}(k) = \frac{1}{M^2}\sum_{m=1}^{M} \hat{\sigma}^2_{\hat{G}^{[m]}}(k) \tag{9.24}$$

$$\mathrm{var}\big(G_S(j\omega_k)\big) \approx M\big(\hat{\sigma}^2_{\hat{G}_{\mathrm{BLA}}}(k) - \hat{\sigma}^2_{\hat{G}_{\mathrm{BLA},n}}(k)\big) \tag{9.25}$$

where $\hat{G}_{\mathrm{BLA}}(j\omega_k)$ is the estimated BLA, $\hat{\sigma}^2_{\hat{G}_{\mathrm{BLA}}}(k)$ is the estimated total variance (stochastic non-linear variance + noise variance) averaged over the m realizations, $\hat{\sigma}^2_{\hat{G}_{\mathrm{BLA},n}}(k)$ is the estimated noise variance averaged over the m experiments and $\mathrm{var}(G_S(j\omega_k))$ the variance of the stochastic non-linear distortion with respect to one multisine realization. This estimations can be done for odd and even frequencies separately, depending on the selection of ω_k.

The total variance and noise variance are averaged over the m experiments and provide insight into the reliability of the FRF measurements over m different multisine realizations. The variance of the stochastic non-linear distortion with respect to

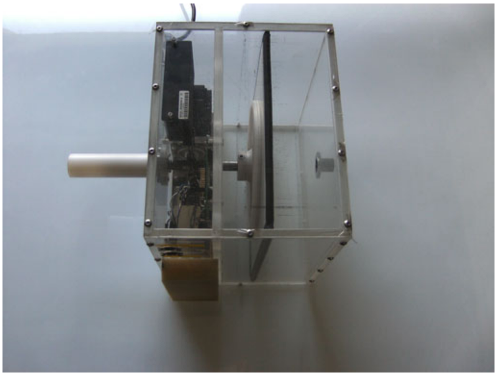

Fig. 9.2 Photo of the lab prototype, only the mechanical box. The tubing segment connecting to the patient is not shown

one realization provides insight into the amount of non-linear distortion in the system. A comprehensive description of these methods and a manifold of illustrative examples are given in [136].

9.2 Non-linear Effects from Measuring Device

The measurements of the signals analyzed in this paper have been performed using the device depicted in Fig. 9.2: the commercial FOT standard setup, assessing respiratory mechanics in the range from 4 Hz to 48 Hz and a laboratory prototype developed to measure a lower range of frequencies, namely 0.625 Hz to 22 Hz. The low-frequency multisine in the prototype allows excitation of respiratory tissue at frequencies where viscoelastic properties become important and relevant for clinical insight.

The loudspeaker-based device from Fig. 3.1 was used as a reference for building the lab prototype. To create a multisine with a frequency range below 4 Hz with a pressure excitation signal of a sufficient amplitude, it is necessary to find an alternative actuator for the loudspeaker and build a lab prototype device. The presented solution in this chapter is a pneumatic piston with an internal air-volume of approximately 8.4 liters, as in Fig. 9.2. This pneumatic piston is connected to a round marionette, further connected through a gear to a stepper motor. By using a stepper motor the device is able to reach a sufficient level of volume resolution, which is necessary to create the desired multisine input signal. The large volume allows to reliably create the desired multisine with a peak-to-peak amplitude of 0.35 kPa, or a sinusoidal pressure wave of 0.35 kPa from 0.625 Hz onwards (a lower limit for the excited frequency originated with the trade-off between device size and expected performance).

During the measurements, the patient wears a nose clip (nc) and keeps the cheeks firmly supported. Before starting the measurements, the frequency response of the transducers (PT)—SensorTechnics HCLA 12X53B—and of the pneumotachograph (PN)—Hans Rudolph 4830 series from 0–400 L/min—are calibrated with a known

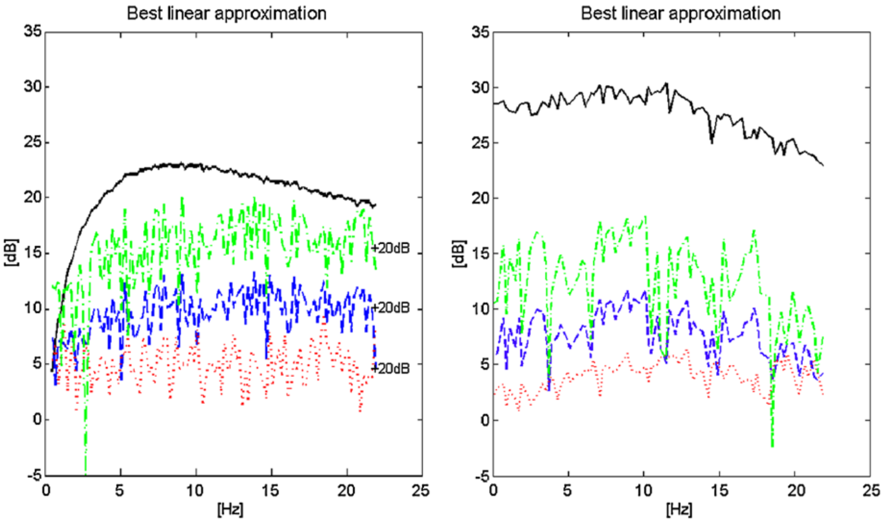

Fig. 9.3 BLA of the (*left*) commercial device and (*right*) prototype device. *Bold black line*: BLA; *blue dashed line*: total variance (noise + stochastic non-linear distortion); *red dotted line*: noise variance; *green dash-dot line*: variance of the stochastic non-linear distortion with respect to one multisine realization. The values of the noise and variance in (*left*) are +20 dB enhanced for clarity of observation (same Y-scale)

impedance (i.e. a calibration tube). The measurement of air pressure P and air flow $Q = dV/dt$ (with V as the air volume) during the FOT lung function test is done at the mouth of the patient. The FOT lung function tests were performed according to the recommendations described in [116]. The FOT excitation signal was kept within a range of a peak-to-peak size of 0.1–0.3 kPa, in order to ensure patient comfort and safety.

The BLA of both the commercial and the prototype devices are given in Fig. 9.3. Notice the noise lines in Fig. 9.3-(left) are increased with 20 dB for illustrative purposes only. In Fig. 9.3-(right), a significant improvement is done with respect to the power of the low-frequency signal generator, namely an increase in amplitude with 10 dB and a flat amplitude curve at low frequencies in the BLA. The drawback is the relatively high noise amplitudes. From this it follows that the noise in the prototype is about 20 dB higher, partly due to the less amount of tubing between the actuator and the mouthpiece and mechanical friction. The improved prototype device can send reliably a multisine excitation as low as 0.625 Hz, as shown by Fig. 9.4. The prototype has been further analyzed both experimentally and theoretically.

In order to validate the correctness of the measurement, a known impedance is required. A calibration tube with the characteristics shown in Fig. 9.5 has been measured by means of the prototype device, and the impedance results are given in Fig. 9.6. The tube has been simply added to the device at the same position where the mouthpiece is placed. The theoretical impedance has been also calculated, in order to validate the measured data. The systematic difference in amplitude between the

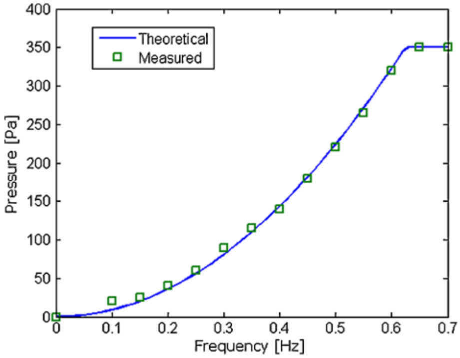

Fig. 9.4 Theoretical and measured characteristic between pressure signal amplitude and frequency in the proposed prototype device

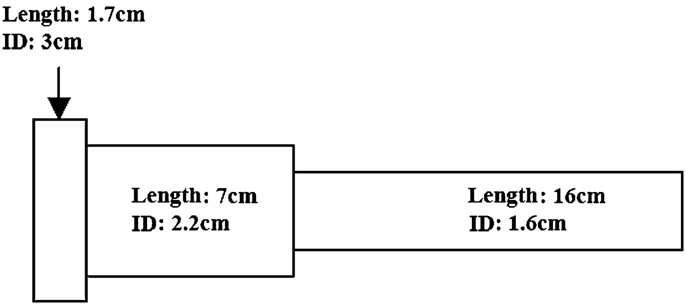

Fig. 9.5 Schematic representation of the calibration tube. ID: inner diameter

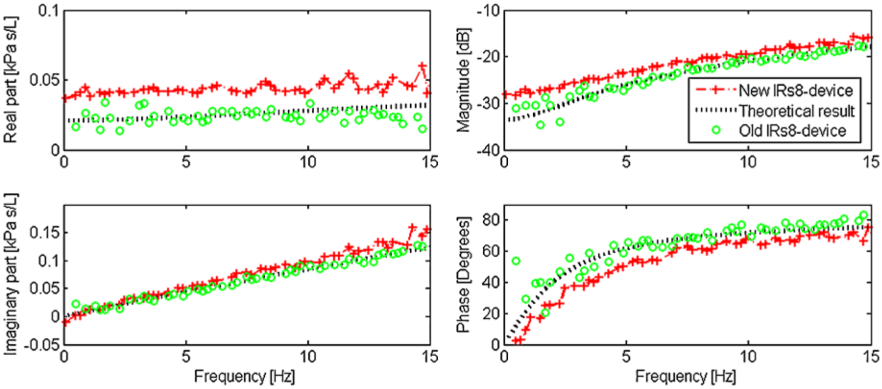

Fig. 9.6 Impedance of the calibration tube by means of complex and Bode representations. *Red dotted line* denotes the prototype with the first version of the excitation signal. *Green line*: prototype device, optimized signal with higher resolution at lower frequencies. *Black line*: theoretical impedance

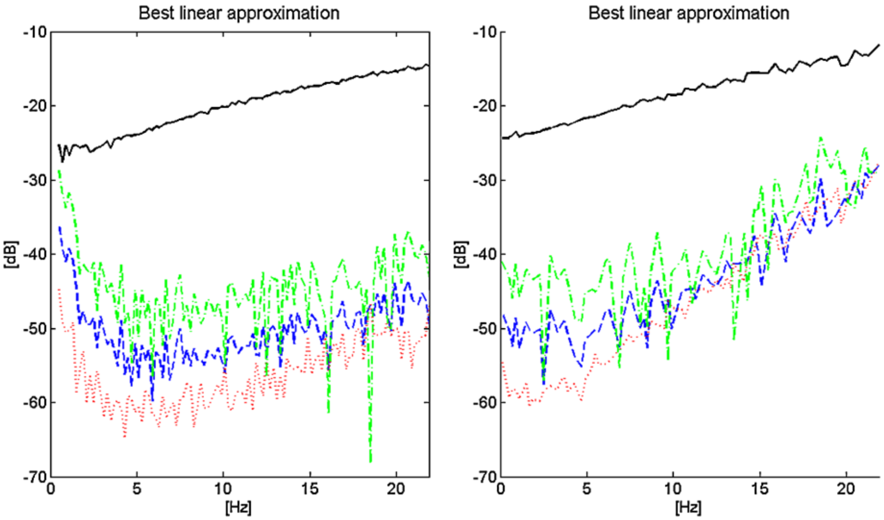

Fig. 9.7 BLA of the calibration tube: *left* the commercial device, *right* the prototype device. *Bold black line*: BLA; *blue dashed line*: total variance (noise + stochastic non-linear distortion); *red dotted line*: noise variance; *green dash-dot line*: variance of the stochastic non-linear distortion with respect to one multisine realization

commercial and the prototype device is due to difference in tubing length between the actuator and the mouthpiece.

Next, the BLA of the calibration tube has been estimated, and Fig. 9.7 shows a significant improvement by reducing the noise and non-linear contributions below 4 Hz. Although the prototype has higher level of noise at higher frequencies, this is not significant, since we do not intend to use the device for high frequencies. For the evaluation of the non-linear distortions present in the respiratory system, the measured non-linear distortions from the generator alone will be taken into account for correcting the final result in measured volunteers.

9.3 Clinical Markers for Quantifying Non-linear Effects

In order to quantify these non-linear contributions, let us introduce the following index:

$$T = \frac{P_{\text{even}} + P_{\text{odd}}}{P_{\text{exc}}} \cdot \frac{U_{\text{exc}}}{U_{\text{even}} + U_{\text{odd}}} \tag{9.26}$$

where each variable is the sum of the absolute values of all the contributions in pressure signal and input flow signal, respectively, at the even non-excited frequencies, the odd non-excited frequencies and the excited odd frequencies. Only the corrected output pressure has been taken into account when calculating (9.26).

This index expresses a relative ratio of the contributions at the non-excited frequency points, with respect to the contributions at the excited frequency points. Furthermore, it gives a relative measure of the gain between contributions in the input and in the output of the system. Since this is a non-linear system whose output depends on the input, the choice for this relative measure is technically sound.

9.4 Non-linear Effects Originated with Pathology

The non-linear distortions introduced in the input signal due to the device itself are corrected in the measured pressure before calculating the BLA or the respiratory impedance of the volunteers. This is done using the BLA of the device itself and (9.21). For the signal processing part, we used $m = 6$ realizations, $p = 3$ intervals and $n = 5000$ samples.

Figure 9.8 shows the results obtained for a patient diagnosed with cystic fibrosis, a patient diagnosed with asthma and a healthy volunteer. One can observe that the non-excited even harmonics are relatively high in asthma. In order to make a statistical analysis, one can characterize the non-linear distortions present in the calculated even and odd contributions using the index T from (9.26). The results are depicted in Fig. 9.9 by means of boxplots and a significant difference has been found between the two groups ($p < 0.0107$). No significant difference has been found between the asthma and cystic fibrosis groups, perhaps due to small dataset.

One may conclude that the non-linear distortions tend to be significantly increased in patients diagnosed with respiratory disease than in healthy subjects. From clinical insight, this is indeed a valid conclusion (recall here structural changes discussed in Chap. 2). The respiratory system affected by cystic fibrosis is filled with viscous secretions which will change the heterogeneous appearance of the tissues and introduce non-linear effects originated with turbulent flow, viscoelasticity, excessive inflammation, and clogged airways. The respiratory system affected by asthma is subject to airway hyperresponsiveness leading to airway chronic inflammation. This affects the airway remodeling, changing air-flow dynamics and hence introducing non-linear effects from turbulent flow, airway obstruction, airway muscle fibrosis etc. In both cases, changes in structure and morphology will change the non-linear behavior of the respiratory system, hence the values of the proposed index will change as well.

As a preliminary study, the information gathered in this work is crucial in the further development and implementation of measuring devices and algorithms to measure low-frequency respiratory impedance in a non-invasive and simple manner, without requiring breathing maneuvers or complex respiratory tests. Although this preliminary evaluation was performed on a limited number of volunteers, it suggests that measuring non-linear contributions is beneficial to gather insight into the evolution of respiratory diseases. The fact that respiratory mechanics at low frequencies have inherent information on the viscoelastic properties of airways and tissue is motivating the development of signal processing algorithms which can cancel the

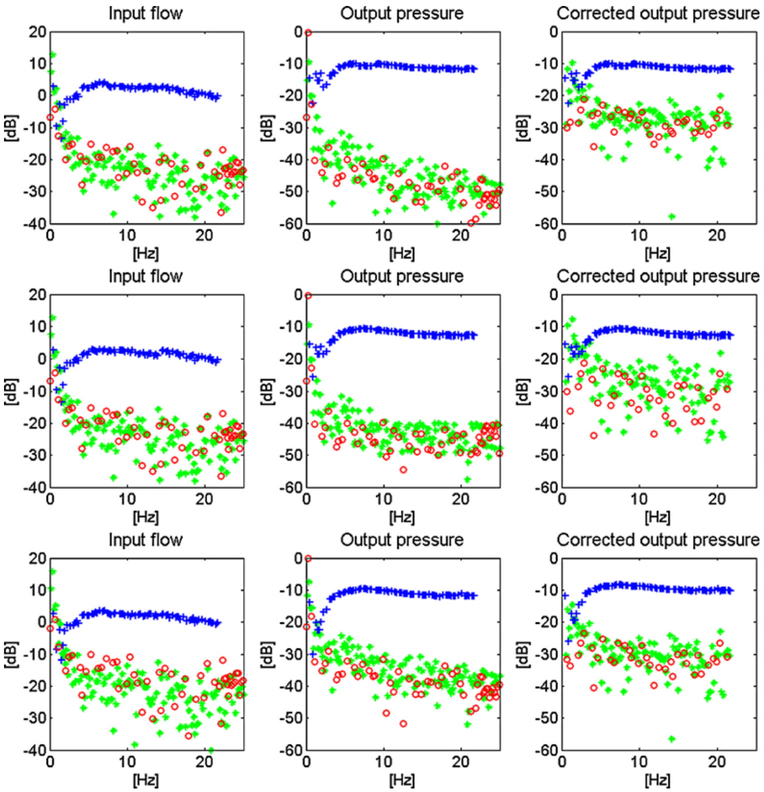

Fig. 9.8 Input (*left column*), output (*middle column*) and corrected DFT spectrum for non-linear contributions (*right column*) of a **cystic fibrosis** (*top row*), **asthma** (*middle row*) and a **healthy** volunteer (*bottom row*). *Blue* '+': excited odd harmonics; *red* 'o': non-excited odd harmonics; *green* '*': non-excited even harmonics

Fig. 9.9 The boxplot of the two groups of volunteers; significant difference is observed ($p < 0.0107$)

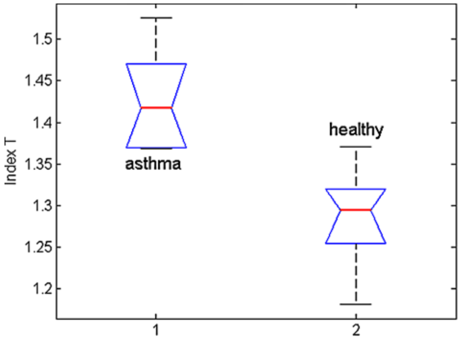

interference with the breathing of the patient. The challenge is that the amplitude and frequency of the breathing signal may vary within the measurement and from one measurement to another, making the detection lines prone to biased values. The results obtained in these initial steps are a proof of concept which motivates further development of the FOT device and detection algorithm.

9.5 Detecting Non-linear Distortions at Low Frequencies

Having the proof of concept available from previous sections in this chapter, the motivation to look at lower frequencies, where viscoelasticity plays an important role, becomes justified. However, we are facing two problems at this turn-point:

- according to Fig. 9.4, the mechanical device from Fig. 9.2 can only reliably excite frequencies as low as 0.6 Hz;
- the lower one tries to investigate the respiratory impedance, the closer one comes to the breathing frequency of the individual under test.

Consequently, a different approach was necessary to endeavor this objective, further detailed in the remainder of this chapter.

9.5.1 Prototype Device with Feedforward Compensation

In order to tackle the drawback of the loudspeaker (i.e. limitation in the lower frequency band) and of the mechanical setup (i.e. noise, friction), a device for applying FOT was designed by means of air-fans. The picture of the setup and its elements are shown in Fig. 9.10. The setup consists of two fans which are forcing the air through a PVC tube. The fans are driven by a pulse width modulated signal generated by a PIC 18F4550 microcontroller. Pressure and flow at the mouthpiece can be obtained using two pressure sensors and a pneumotachograph, similarly to the other FOT devices. The excitation pressure signal is kept below a peak-to-peak variation of 0.2 kPa at the airway opening as recommended in [116].

The fans create turbulences, which result in increased measurement noise. To reduce these turbulences [128], the PVC tube is filled with thin tubes (i.e. cocktail straws) of 3 mm diameter whereas the middle part of the tube is left empty to preserve a good air supply for the subject. The measured pressure values are quantized within the pressure sensors and transmitted to the microcontroller.

Two complementary compensation methods are used to suppress the linear dynamic behavior, the non-linear distortions generated by the measurement system and the disturbances introduced by the breathing of the patient. Firstly, a feedforward compensation of the excitation signal is proposed to suppress the non-linear distortions and the linear dynamic behavior of the measurement system. The feedforward compensation of the measurement system has two goals. The feedforward signal is generated in such a way that the bandwidth of the generated pressure signal is larger than the bandwidth of the measurement system. Additionally, the non-linear distortions are suppressed by use of an iterative scheme. Secondly, the residual dynamic

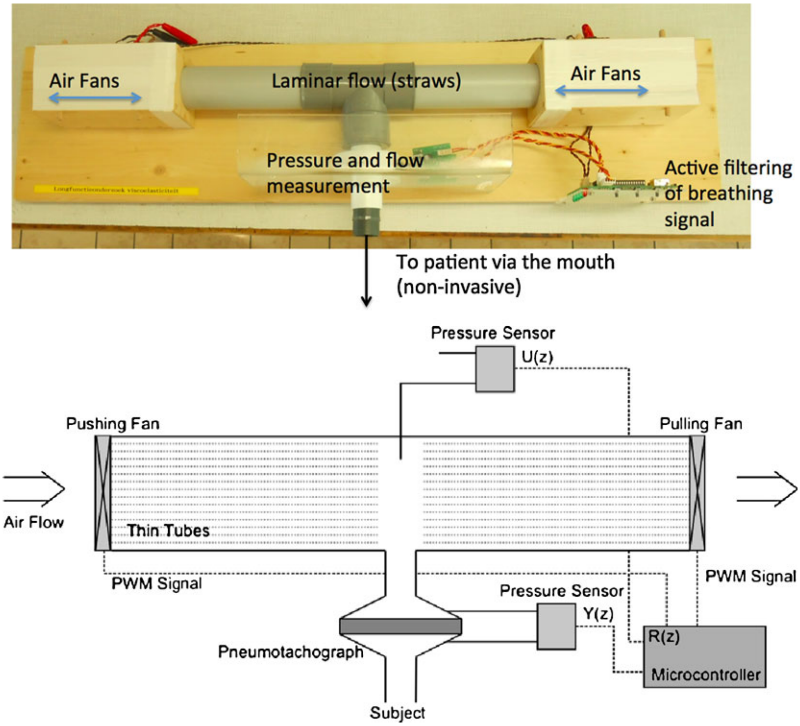

Fig. 9.10 Photo and schematic setup of the novel FOT device for low-frequency impedance measurement

non-linear distortions (after the feedforward compensation) and the disturbances resulting from the subjects breathing are suppressed by a feedback control loop, a simple proportional-integral (PI) control.

By applying these compensations, one can excite the respiratory properties of the patient with a random phase multisine with a random harmonic grid and a flat power spectrum in the frequency band 0.1–5 Hz. By use of a flat power spectrum, a constant SNR can be obtained over the whole frequency band, as observed from Fig. 9.11. More details about the design of multisine signals for frequency domain identification can be found in [136].

9.5.2 Respiratory Impedance at Low Frequencies

With the novel device available, measurements have been performed on healthy children, adults, and diagnosed patients with asthma and with COPD. The biometric data for the healthy groups are given in Table 9.1, whereas those for the diagnosed groups are given in Table 9.2. The COPD is further classified according to the GOLD standard in several levels of disease severity, as given in Table 9.3.

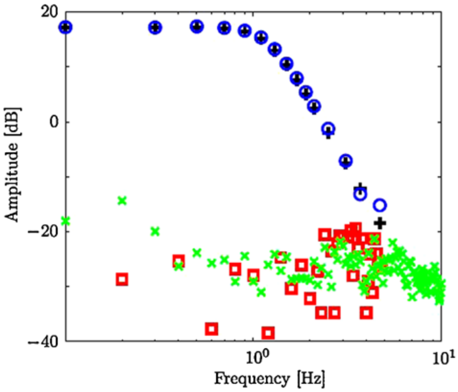

Fig. 9.11 Amplitude spectrum of generated pressure signals: the wanted signal (+), generated pressure on excited lines (○), generated pressure on the in-band non-excited frequency lines (□) and the sample variance (x)

Table 9.1 Biometric parameters of the investigated healthy subjects. Values are given as mean with standard deviations

	14-years (20)	17-years (158)	Adults (20)	Elders (5)
Male/female	1/19	96/61	8/12	3/2
Age (yrs)	14 ± 0.3	17 ± 0.6	30 ± 6.3	54 ± 1.4
Height (m)	1.63 ± 0.05	1.74 ± 0.08	1.73 ± 0.08	1.74 ± 0.04
Weight (kg)	48 ± 8	62 ± 9	68 ± 9	75 ± 10
BMI	18 ± 2	20 ± 2	22 ± 3	24 ± 3
Smoking	0	9	3	2

Table 9.2 Biometric and spirometric parameters of the investigated diagnosed subjects. Values are given as mean with standard deviations

	Asthma (9)	COPD (13)
Female/male	6/3	4/9
Age (yrs)	52 ± 14	66 ± 12
Height (m)	1.68 ± 0.05	1.67 ± 0.04
Weight (kg)	70 ± 11	80 ± 13
BMI	25 ± 5	28 ± 4
FEV1 % pred	67 ± 18	46 ± 8

Table 9.3 Biometric and spirometric parameters of the investigated COPD subjects divided according to GOLD classification. Values are given as mean with standard deviations

	GOLD II (5)	GOLD III (6)	GOLD IV (2)
Male/female	3/2	5/1	2/0
Age (yrs)	58 ± 12	65 ± 8	68 ± 6
Height (m)	1.74 ± 0.08	1.73 ± 0.08	1.74 ± 0.04
Weight (kg)	62 ± 9	68 ± 9	75 ± 10
BMI	25 ± 2	28 ± 3	29 ± 3
FEV1 % pred	67 ± 8	42 ± 6	27 ± 4

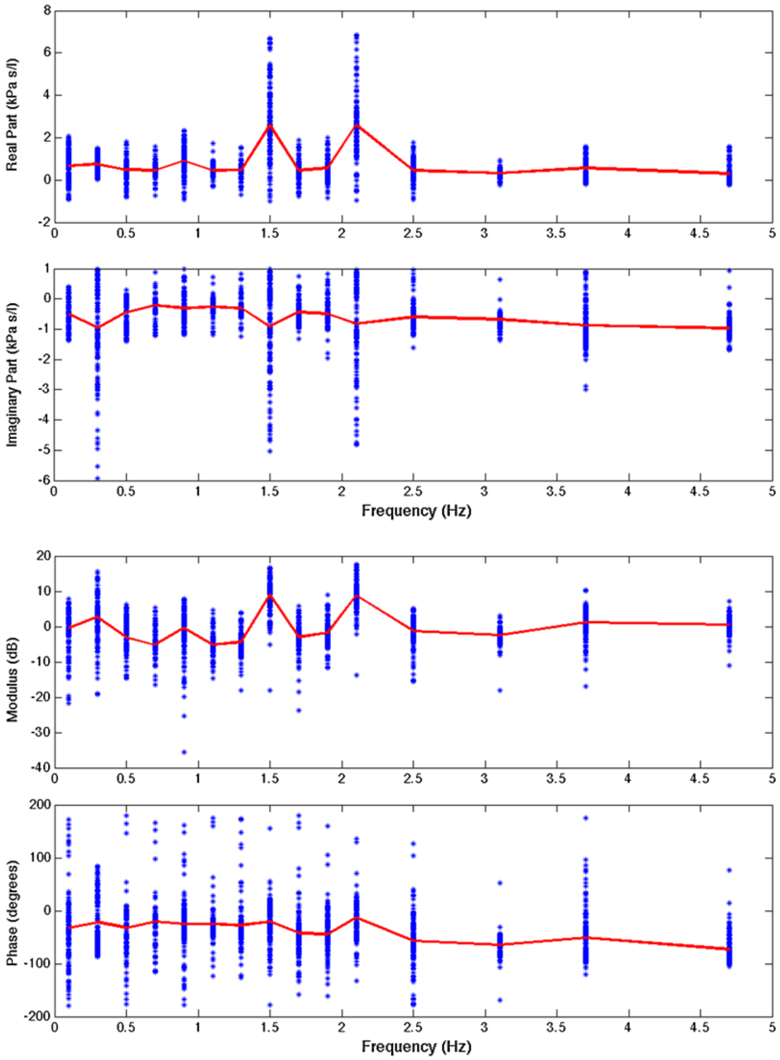

Fig. 9.12 Impedance in its complex representation and its equivalent Bode plot for healthy group #1. The *stars* denote estimated impedance using (3.8), while a *continuous line* denotes the averaged values

The respiratory impedance has been estimated by means of (3.8) and depicted by means of its complex representation and its equivalent Bode plot. For healthy groups, the impedance is given in Figs. 9.12, 9.13, 9.14, 9.15, and for the diagnosed groups, the impedance is depicted in Figs. 9.16–9.17. Their values have been successfully validated with reference values from (7.12).

The distribution, median, and confidence intervals of the impedance values at each excited frequency points are given in Figs. 9.18, 9.19, 9.20 and 9.21 for healthy,

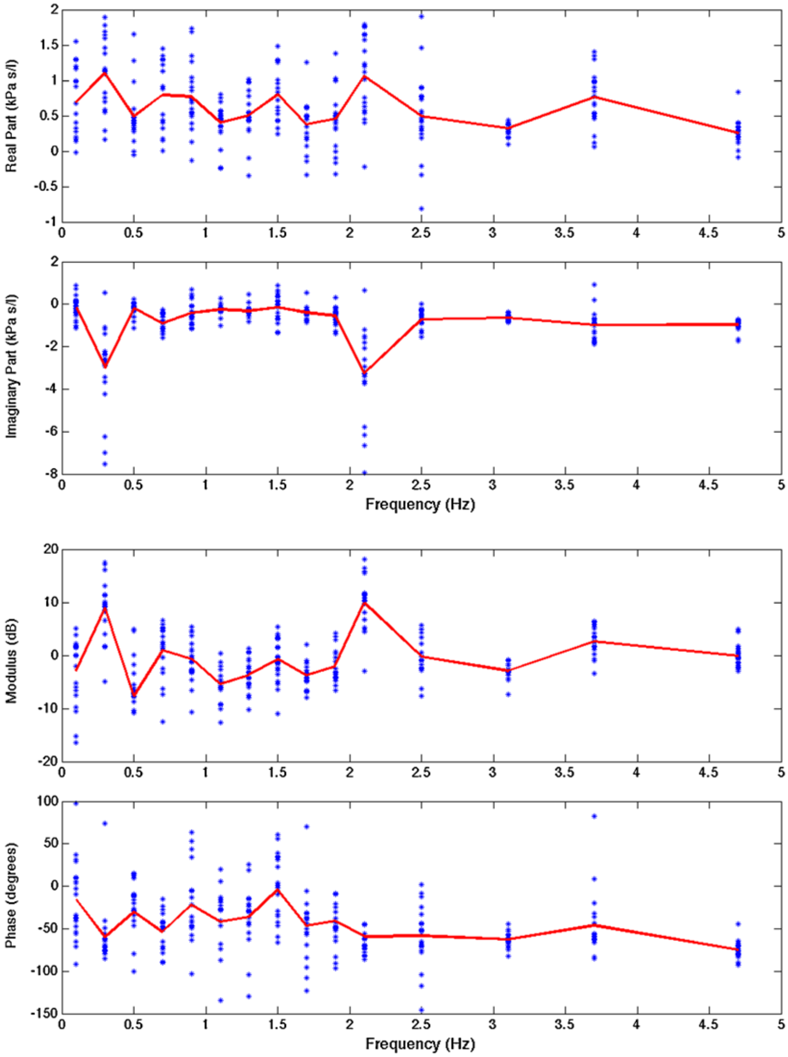

Fig. 9.13 Impedance in its complex representation and its equivalent Bode plot for healthy group #2. The *stars* denote estimated impedance using (3.8), while a *continuous line* denotes the averaged values

respectively, Figs. 9.22–9.23 for diagnosed patients, by means of boxplot representation.

The impedance values have been validated successfully against the reference values from [33, 121, 122]. Impedance values for both healthy and COPD patients are similar to those reported in [40, 92, 94].

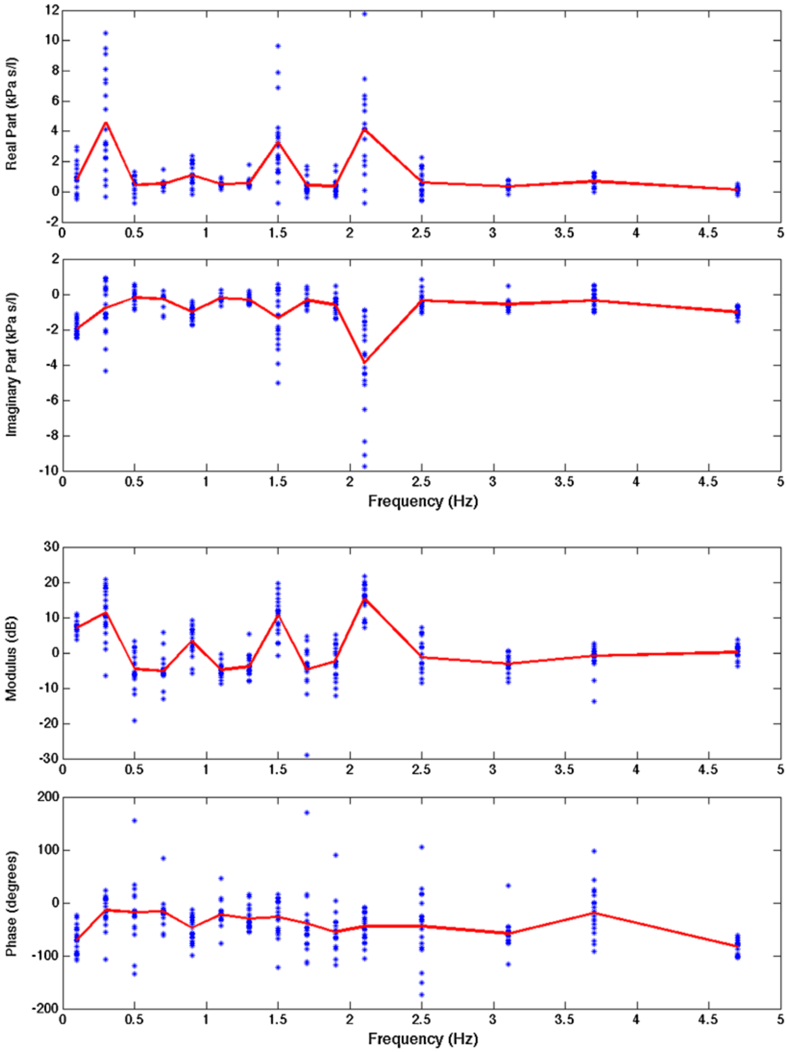

Fig. 9.14 Impedance in its complex representation and its equivalent Bode plot for healthy group #3. The *stars* denote estimated impedance using (3.8), while a *continuous line* denotes the averaged values

9.5.3 Non-linear Distortions at Low Frequencies

Similar to the measurements described previously in this chapter, the available information allows us to calculate the index from (9.26) in order to quantify the amount of non-linear distortions coming from the airways and lung tissue. The results are given in Fig. 9.24 for the healthy groups and in Fig. 9.25 for the diagnosed groups, by means of boxplots. In both cases, statistically significant differences have been

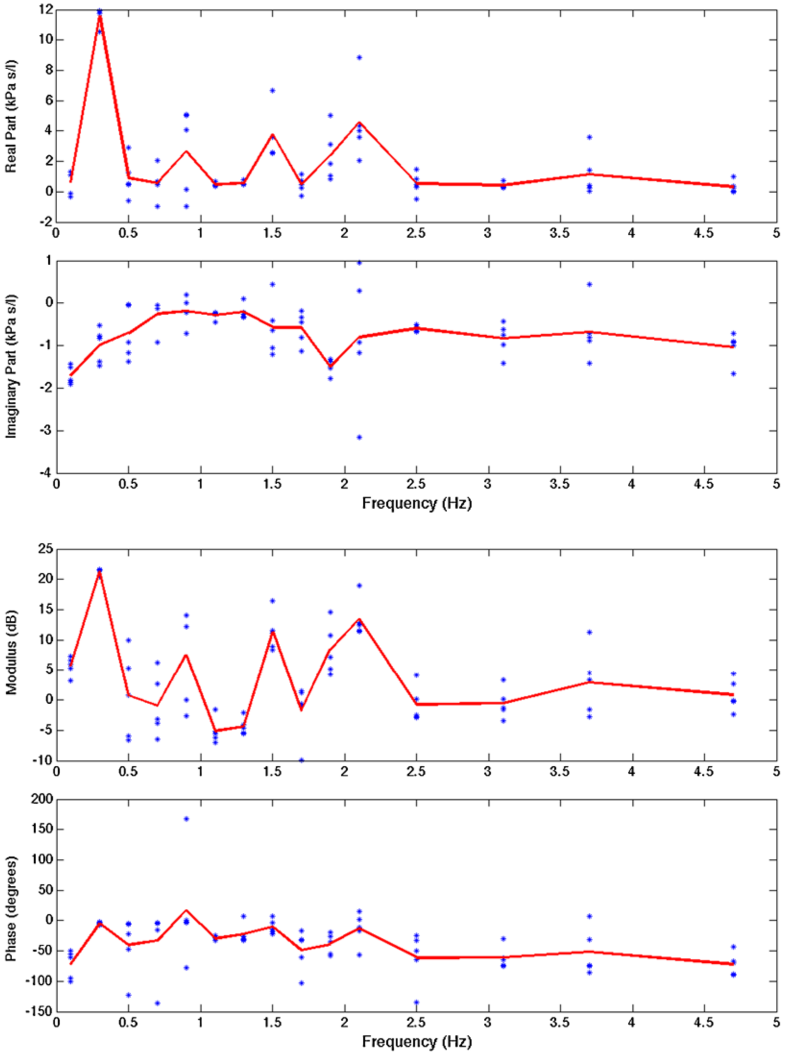

Fig. 9.15 Impedance in its complex representation and its equivalent Bode plot for healthy group #4. The *stars* denote estimated impedance using (3.8), while a *continuous line* denotes the averaged values

observed. The values for the confidence intervals of the index in these groups are given in Table 9.4.

For the healthy groups, these differences are due to variations in the biometric data, i.e. with increasing age, the development of the respiratory system with it inherent changes in structure and morphology will affect the non-linear dynamics, hence the non-linear distortions will vary as well. For the diagnosed groups, the marked changes in structure and morphology is indeed the origin for such variations

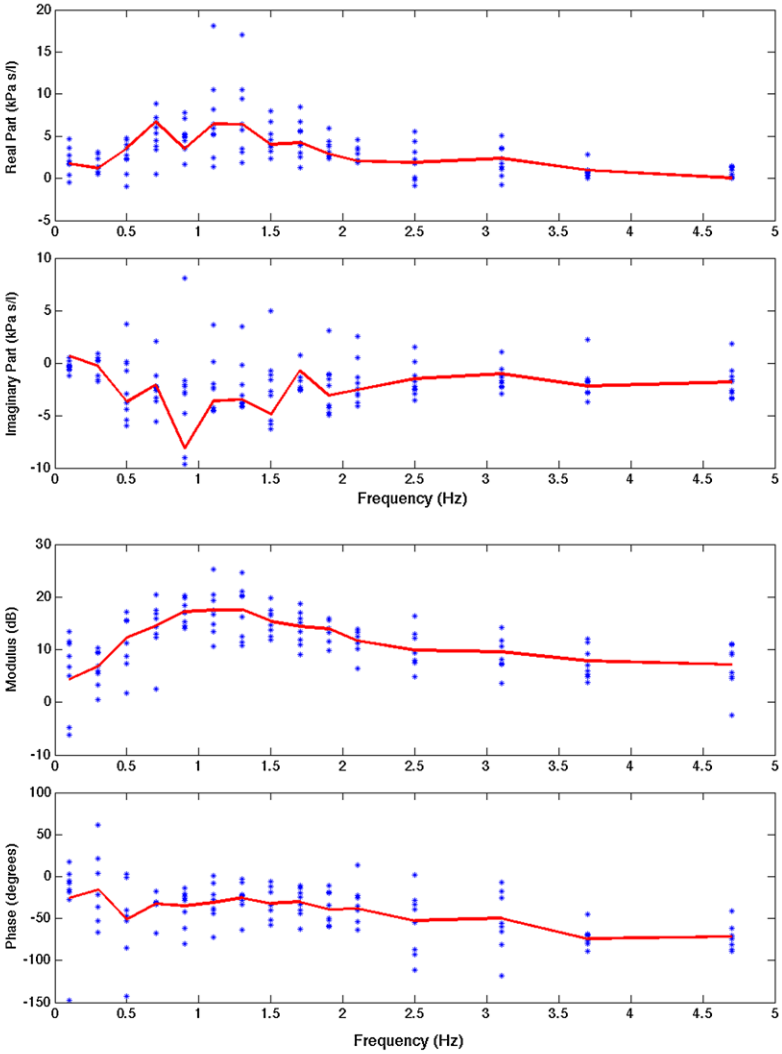

Fig. 9.16 Impedance in its complex representation and its equivalent Bode plot for the asthma diagnosed group. The *stars* denote estimated impedance using (3.8), while a *continuous line* denotes the averaged values

in non-linear dynamics and consequently the variations in the non-linear contributions. This suggests that the proposed index to quantify non-linear distortions is indeed a valuable tool for diagnosis and follow-up. Of course, a larger population database needs to be explored for diagnosed patients in order to provide reference values.

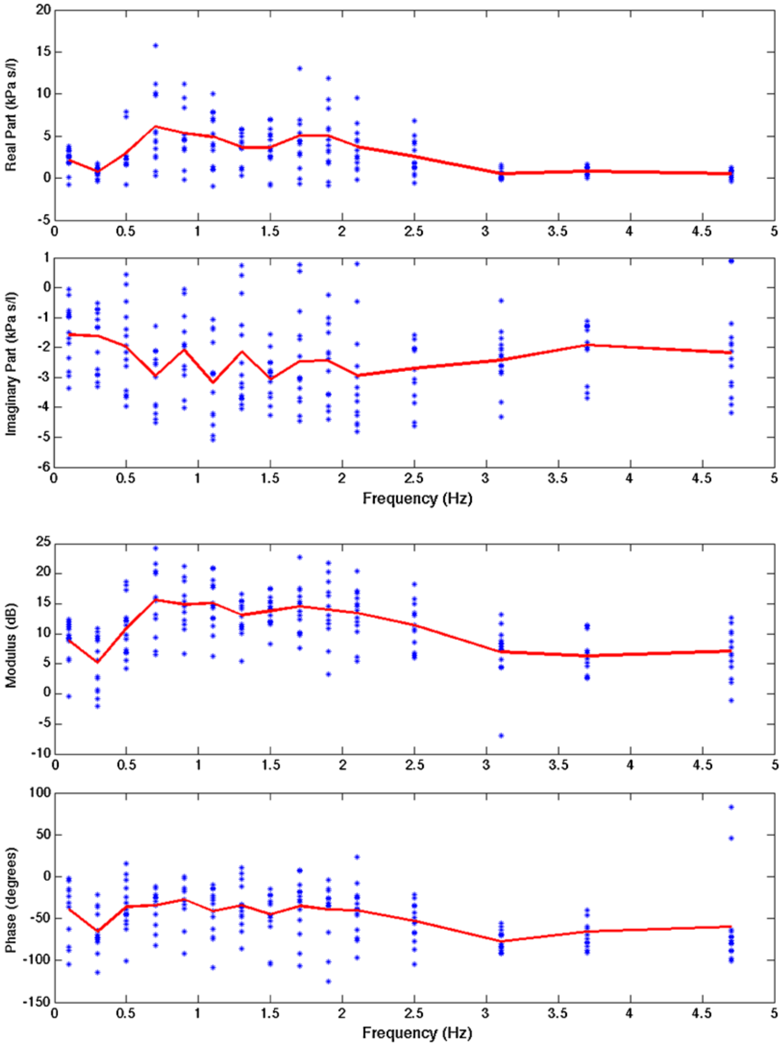

Fig. 9.17 Impedance in its complex representation and its equivalent Bode plot for the COPD diagnosed group. The *stars* denote estimated impedance using (3.8), while a *continuous line* denotes the averaged values

To verify if the T index changes by COPD severity, the subdivision of the COPD patients according to the GOLD classification is used. Although the number of patients is too low to provide a meaningful statistical difference, Fig. 9.26 shows a clear difference in the amount of non-linear distortions with gradual severity of the disease. This indeed delivers a proof of concept that non-linearity increases with disease severity ($p \ll 0.01$).

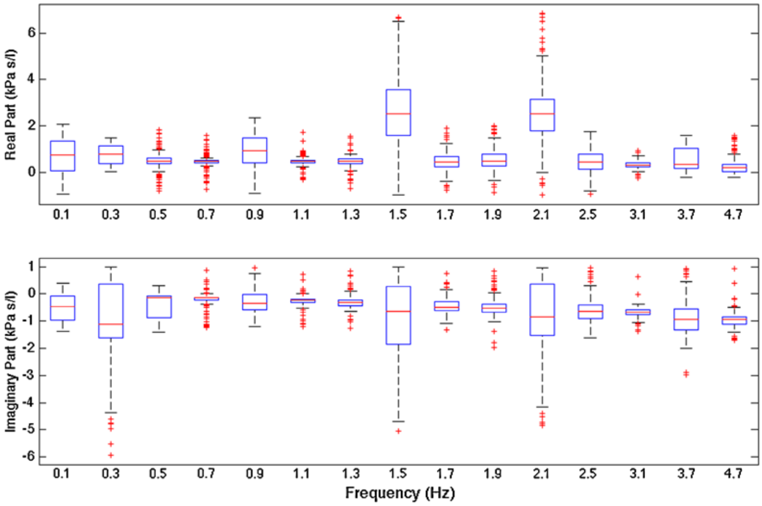

Fig. 9.18 Boxplot for healthy group #1

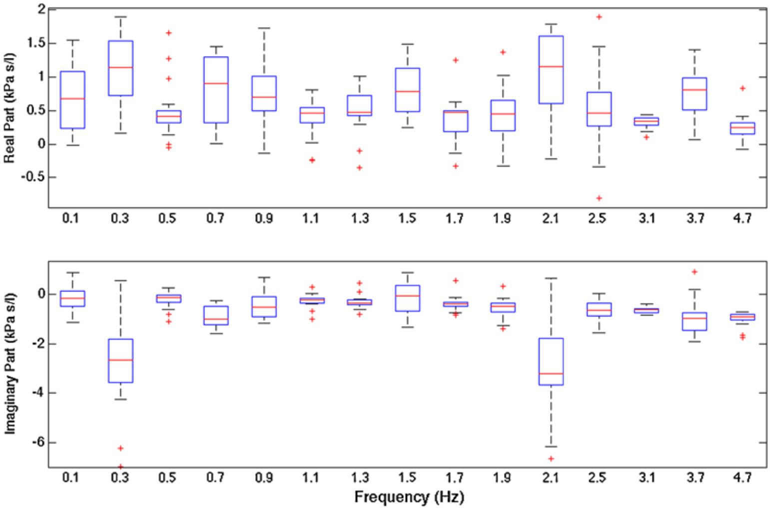

Fig. 9.19 Boxplot for healthy group #2

9.5.4 Relation to the FO Model Parameters

Apart from the non-parametric identification performed with (3.8), a parametric identification has been performed for the FO model structure from (7.5). The identified values are given in Table 9.5. There were no statistically significant differences between the asthma and COPD diagnosed groups in the parameters of the FO model. When the additional G_r, H_r and η_r parameters were calculated as in (7.6)–(7.7) and

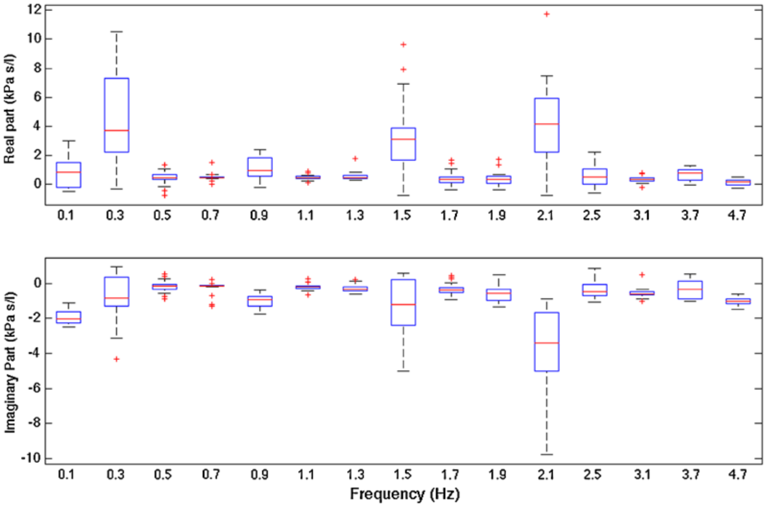

Fig. 9.20 Boxplot for healthy group #3

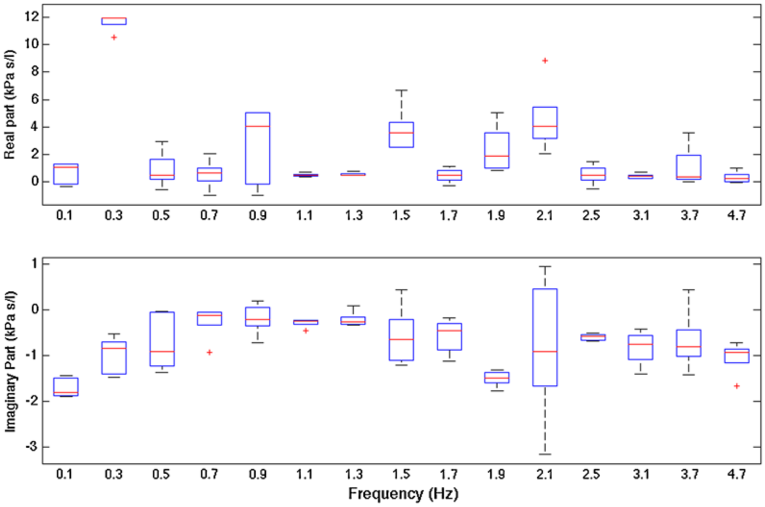

Fig. 9.21 Boxplot for healthy group #4

given in Table 9.6, no statistically significant differences have been observed either. One possible explanation might be the low number of patients measured. Another explanation might be the fact that the compensation from the device for the breathing effects is not perfect, hence breathing effects might still be present.

Next step was to check whether a relation exists between the heterogeneity factor η_r and the non-linear distortions index T. Figures 9.27 and 9.28 depict these two factors.

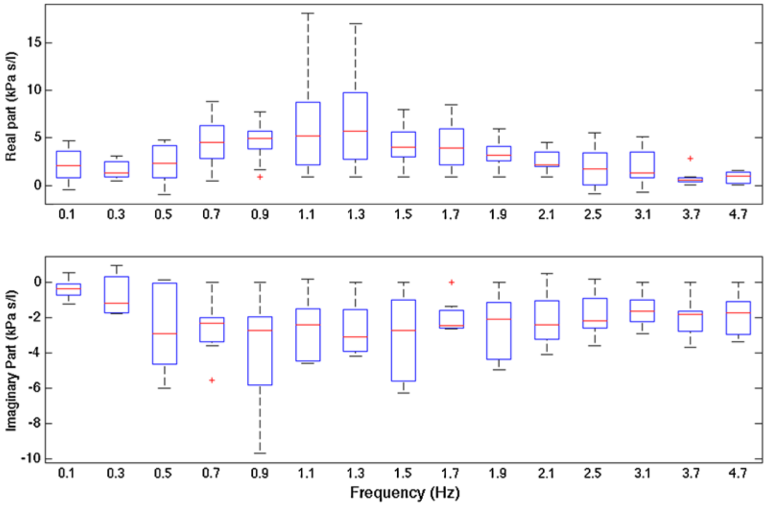

Fig. 9.22 Boxplot for the asthma diagnosed group

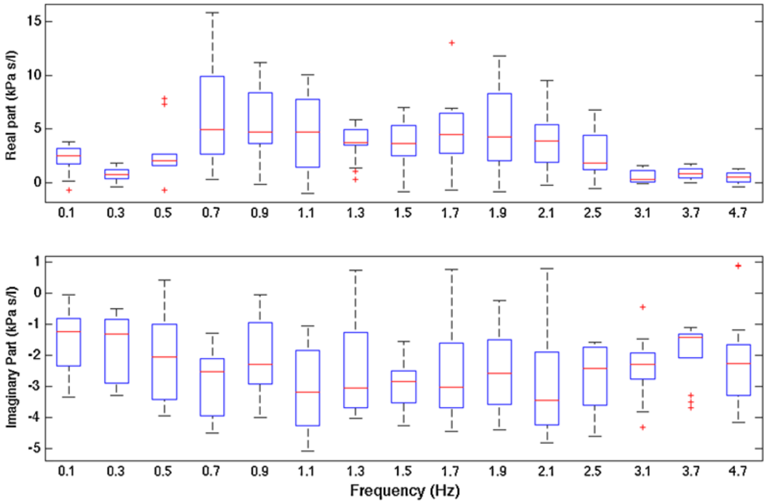

Fig. 9.23 Boxplot for the COPD diagnosed group

Although the results obtained cannot lead to a definite conclusion, they suggest that both FO models and proposed non-linear distortion index have great potential in characterizing mechanical properties of the lungs at low frequencies. Further serious and industrious efforts are necessary to broaden the horizons of applicability of FOT in clinical use.

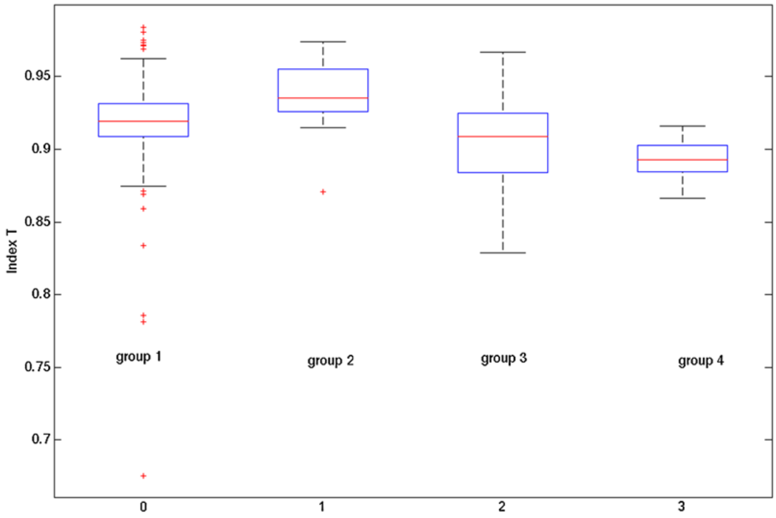

Fig. 9.24 Boxplot for the non-linear distortions in the healthy groups; there is a significant difference between groups ($p < 0.0046$)

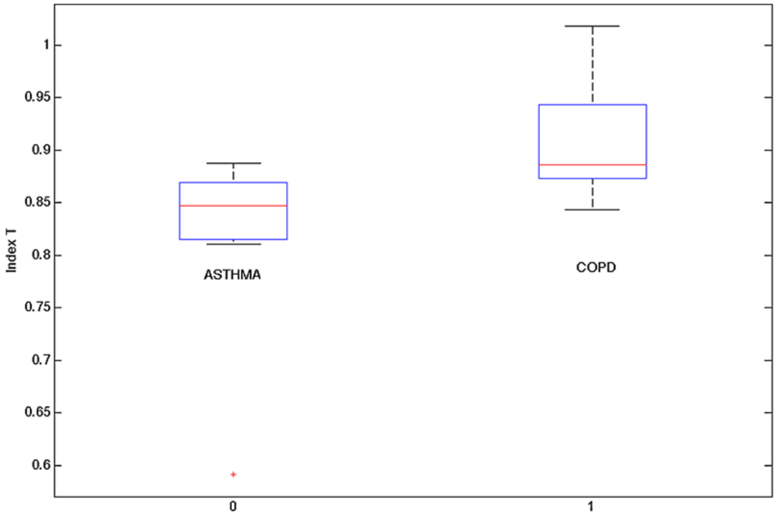

Fig. 9.25 Boxplot for the non-linear distortions in the asthma and COPD diagnosed groups; there is a significant difference between groups ($p < 0.0113$)

9.6 Summary

In this final chapter, some of the most revolutionary ideas with respect to analyzing respiratory system have been put forward to the reader. The non-linear effects in the respiratory signals and in the related measurement instrumentation during FOT tests

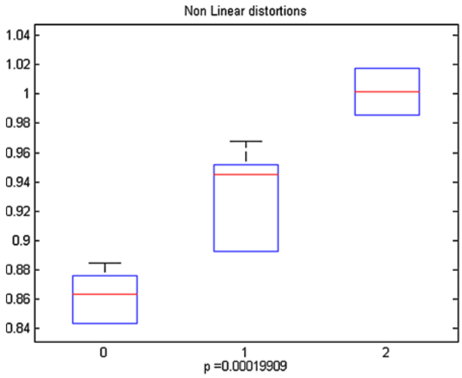

Fig. 9.26 Boxplot for the non-linear distortions within COPD group for various groups classified according to GOLD; from left to right: GOLD II, GOLD III and GOLD IV; there is a significant difference between groups ($p \ll 0.01$)

Table 9.4 Confidence intervals for the calculated non-linear distortions index T in the measured groups. Std denotes standard deviation

Group	Min	Max	Mean	Std
Healthy Group #1	0.9127	0.9231	0.9179	0.0333
Healthy Group #2	0.9260	0.9472	0.9366	0.0277
Healthy Group #3	0.8885	0.9200	0.9043	0.0336
Healthy Group #4	0.8707	0.9147	0.8927	0.0177
Diagnosed Asthma	0.7518	0.8900	0.8209	0.0899
Diagnosed COPD	0.8728	0.9301	0.9014	0.0496

Table 9.5 Confidence intervals for the identified FO model parameters in the measured groups

Group	L_r	$D = 1/C_r$	α_r	β_r
Healthy Group #1	0.2314–0.3132	5.1519–5.6028	0.1610–0.2314	0.6401–0.6945
Healthy Group #2	0.0311–0.1189	4.7797–6.2203	0.0558–0.2442	0.6150–0.7250
Healthy Group #3	0.0410–0.2490	5.3760–8.1240	0.2069–0.5831	0.4966–0.6334
Healthy Group #4	0.1986–0.5886	4.1782–5.7865	0.0690–1.0690	0.2717–0.6483
Diagnosed Asthma	0.0129–0.2562	12.0768–27.9232	0.3640–1.0137	0.4506–0.7716
Diagnosed COPD	0.0123–0.0834	11.5293–31.3279	0.2804–0.8196	0.4273–0.7013

Table 9.6 Confidence intervals for the derived parameters in the measured groups

Group	G_r	H_r	η_r
Healthy Group #1	0.5700–0.7118	0.8747–0.9512	0.5748–0.6953
Healthy Group #2	0.4526–0.6904	0.8436–1.0384	0.4805–0.7040
Healthy Group #3	0.8384–1.3536	1.0561–1.4818	0.6885–1.0960
Healthy Group #4	0.5470–2.1637	0.8991–1.2089	0.5791–1.9109
Diagnosed Asthma	1.3880–4.8148	2.2091–5.1828	0.4083–1.1916
Diagnosed COPD	1.7624–3.5918	2.1089–4.8446	0.6073–1.4115

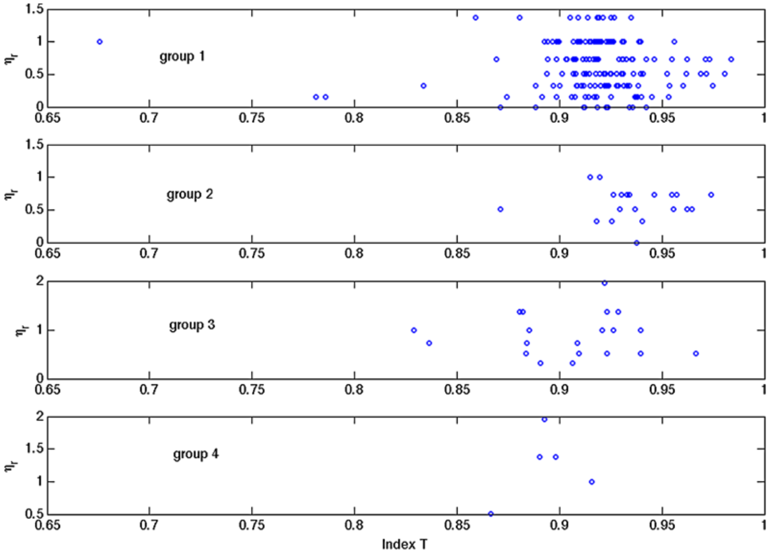

Fig. 9.27 Relation between the index of non-linear distortions T and the heterogeneity factor η_r in the healthy groups

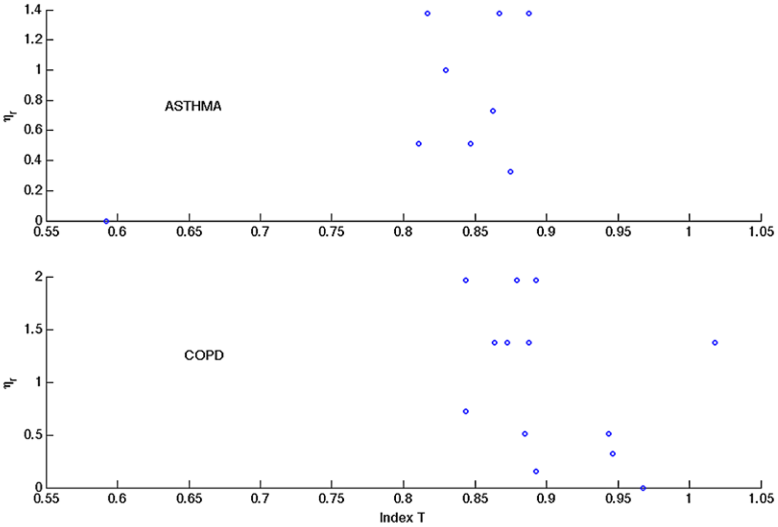

Fig. 9.28 Relation between the index of non-linear distortions T and the heterogeneity factor η_r in the asthma and COPD diagnosed groups

have been acknowledged. The pioneering principle of sending detection lines in the frequency domain for characterizing odd and even non-linear contributions from a non-linear system are introduced to the reader. Two detection methods are presented: a robust method based on multiple measurements and a fast method based on a single measurement. The non-linear effects have been quantified by means of a novel evaluation index. Observations of variations in this novel index values in groups of asthma patients, COPD patients and healthy volunteers have suggested that non-linear dynamic response of the lungs change with the type of disease. Furthermore, the link between the non-linear distortions and the lumped fractional order model parameters are introduced, thus completing the puzzle of this book.

Chapter 10
Conclusions

10.1 Main Results

In this book, the airway tree geometry and morphology was addressed to find the origins of the fractional order appearance in impedance models of the respiratory system. These models pose the characteristic of having a constant phase over a frequency interval, suggesting a frequency independent mechanical efficiency of the lungs (i.e. constant-phase models). After a careful investigation on the existing models from literature for the input impedance, we conclude that the fractional order models may outperform integer-order models in certain frequency intervals. Hence, the natural question arises: *why?*

The work in this book is based on two characteristics of the respiratory system:

1. the geometrical structure, using the intrinsic recurrence of the respiratory tree and
2. the tissue structure, using the viscoelastic properties of lung parenchyma.

A mathematical model has been developed using the Navier–Stokes equations and Womersley theory, leading to a relation between the air pressure and airflow in the airways, with respect to lung geometry, morphology and airway wall (visco)elasticity. Further on, following the two characteristics of the respiratory system, two analogues have been derived from this mathematical model:

1. an electrical analogue, based on the recurrent geometrical structure of the lung, and
2. a mechanical analogue, based on tissue viscoelasticity.

Next, it was shown that the electrical analogue leads to an equivalent structure of the respiratory tree, namely a ladder network. If approached with classic integer-order modeling, it results in a very high-order impedance model. However, a con-

C.M. Ionescu, *The Human Respiratory System*, Series in BioEngineering,
DOI 10.1007/978-1-4471-5388-7_10,

vergence analysis reveals that this recurrent ladder network can be well approximated by a low-order lumped impedance model containing a FO, over a limited range of frequencies. Similarly, we have shown that the mechanical analogue leads also to a ladder structure, whose low-order lumped model also contains fractional orders.

Therefore, a theoretical basis has been set onto which FO models arise. Furthermore, the book explains and provides supportive data to claim that FO lumped impedance models are able to classify between healthy groups of subjects and several pathologies: Chronic Obstructive Pulmonary Disease, asthma, cystic fibrosis and kyphoscoliosis. Some typical indices from the literature, which were derived from the identified model parameters, as well as several novel indices, are discussed for each of the groups in relation to the specific lung pathology. The results show good agreement with physiology and pathology of the lungs in all investigated groups.

Apart from the frequency domain, the book contains also information about the time domain signals. In this line of thought, the impulse response, pressure–volume loops and multidimensional scaling tools are employed to analyze the breathing dynamics and their relation to fractals.

The work presented in this book provides a mathematical basis for the phenomena observed in the results coming from the experimental data. We describe a physiologically consistent approach to model the respiratory tree and show the appearance of the fractional order impedance model and its typical constant-phase characteristic. Rather than dealing with a specific case study, the modeling approach presents a general method which can be applied in many other similar systems (e.g. leaves, circulatory system, liver, intestines, brain). Although recurrence is linked to symmetry of the tree, we consider also the case when symmetry is not present, showing that the constant-phase behavior is still present, hence justifying once again the use of fractional order models.

The overall aim of the work bundled in this book is to provide a theoretical and experimental basis of the information on the respiratory impedance extracted by means of the forced oscillation technique lung function test. Although it has both merit and simplicity, this lung function test is not a routinely used in clinical practice. I believe and I hope that this book will provide the necessary proof of added value necessary for taking the steps towards standardization.

Apart from this, a major goal of this book is to bring forward the existence of several emerging tools from fractional calculus in the biomedical engineering community. Although the content of the book is not focusing on the concepts of fractional calculus, it provides a mere introduction which suffices to assist the reader in this quest. The growing interest coming from the engineering community into these emerging tools motivates all researchers at large to stay abreast latest applications. On the other hand, biologists and doctors are encouraged to embrace these concepts in order to achieve progress in their endeavor to understand the human body and its features.

10.2 Important Directions for Research

10.2.1 Relating the Fractional Order Parameter Values to Pathology

It is significant to recognize the importance of relating the fractional order model parameter values to the specific changes occurring in lung pathology. Since these fractional orders are related to the physiology of the lungs, they give insight in the changes occurring in the structure and morphology of the airways with the gradual changes in the disease.

For instance, it has been shown that the fractional order arises from the recurrence ratio of the resistance and compliance per level. Most of the obstructive and restrictive lung disorders have a crucial impact on the overall resistance and compliance of the lungs, hence it is clear that changes in these properties will lead to changes in the values obtained for the fractional orders.

10.2.2 Low Frequency Measurements

In this book, a broad range of frequencies have been covered in terms of respiratory impedance. However, the most interesting for analysis of changes in the tissue with disease evolution is the 0.1–1 Hz frequency band. Therefore, one needs to measure closer to the breathing frequency. This will then bias the estimates due to the high noise level coming from the breathing signal itself. Hence, an interesting research direction is that of improving the low frequency identification presented in this book, in the presence of nonlinear distortions coming from the breathing of the patient. This can be achieved by developing adaptive filtering methods for canceling non-stationary effects from the breathing of the individual under test. Eventually, changes in the device components and setup may also be beneficial for improving the overall performance.

Appendix
Useful Notes on Fractional Calculus

In this appendix, some useful concepts from fractional calculus will be presented for the reader. For more details, the reader is encouraged to read more comprehensive works on this topic [105, 118, 126, 129, 146, 147, 149, 150].

We will start by introducing some basic functions. The gamma function is intrinsically tied to fractional calculus by definition. The simplest interpretation of the gamma function is the generalization of the factorial for all real numbers. The definition of the gamma function is given by

$$\Gamma(z) = \int_0^\infty e^{-u} u^{z-1} du, \quad \text{for all } z \in R \tag{A.1}$$

The 'beauty' of the gamma function can be found in its properties:

$$\begin{aligned} \Gamma(z+1) &= z\Gamma(z) \\ \Gamma(z) &= (z-1)! \end{aligned} \tag{A.2}$$

The consequence of this relation for integer values of z is the definition for factorial. Using the gamma function we can also define the function $\Phi(t)$, which later will become useful for showing alternate forms of the fractional integral:

$$\phi_\alpha(t) = \frac{t_+^{\alpha-1}}{\Gamma(\alpha)} \tag{A.3}$$

Also known as the Euler Integral of the First Kind, the Beta Function is in important relationship in fractional calculus. Its solution not is only defined through the use of multiple Gamma Functions, but furthermore shares a form that is characteristically similar to the Fractional Integral/Derivative of many functions, particularly polynomials of the form t^α and the Mittag–Leffer Function:

$$\begin{aligned} B(p,q) &= \int_0^1 (1-u)^{p-1} uq - 1\, du \\ &= \frac{\Gamma(p)\Gamma(q)}{\Gamma(p+q)} = B(q,p), \quad \text{where } p,q \in R_+ \end{aligned} \tag{A.4}$$

C.M. Ionescu, *The Human Respiratory System*, Series in BioEngineering,
DOI 10.1007/978-1-4471-5388-7,

The Laplace Transform is a function transformation commonly used in the solution of complicated differential equations. With the Laplace transform it is frequently possible to avoid working with equations of different differential order directly by translating the problem into a domain where the solution presents itself algebraically. The formal definition of the Laplace transform is given as

$$\mathscr{L}\{f(t)\} = \int_0^\infty e^{-st} f(t)\,dt = \tilde{f}(s) \tag{A.5}$$

The Laplace Transform of the function $f(t)$ is said to exist if the above definition is a convergent integral. The requirement for this is that $f(t)$ does not grow at a rate higher than the rate at which the exponential term e^{-st} decreases.

Another commonly used function is the Laplace convolution:

$$f(t) * g(t) = \int_0^t f(t-\tau)g(\tau)\,d\tau = g(t) * f(t) \tag{A.6}$$

The convolution of two function in the domain of t is sometimes complicated to resolve; however, in the Laplace domain (s), the convolution results in the simple function multiplication:

$$\mathscr{L}\{f(t) * g(t)\} = \tilde{f}(s)\tilde{g}(s) \tag{A.7}$$

One final important property of the Laplace transform that should be addressed is the Laplace transform of a derivative of integer order n of the function $f(t)$, given by

$$\mathscr{L}\{f^n(t)\} = s^n \tilde{f}(s) - \sum_{k=0}^{n-1} s^{n-k-1} f^{(0)} = s^n \tilde{f}(s) - \sum_{k=0}^{n-1} s^k f^{(n-k-1)}(0) \tag{A.8}$$

The Mittag–Leffer function is an important function that finds widespread use in the world of fractional calculus. Just as the exponential naturally arises out of the solution to integer order differential equations, the Mittag–Leffer function plays an analogous role in the solution of non-integer order differential equations. In fact, the exponential function itself is a very specific form, one of an infinite set, of this seemingly ubiquitous function. The standard definition of the Mittag–Leffer is

$$E_\alpha(z) = \sum_{k=0}^{\infty} \frac{z^k}{\Gamma(\alpha k + 1)}, \quad \alpha > 0 \tag{A.9}$$

The exponential function corresponds to $\alpha = 1$. It is also common to represent the Mittag–Leffer function in two arguments, α and β, hence:

$$E_{\alpha\beta}(z) = \sum_{k=0}^{\infty} \frac{z^k}{\Gamma(\alpha k + \beta)}, \quad \alpha > 0,\ \beta > 0 \tag{A.10}$$

The common formulation for the fractional integral can be derived directly from a traditional expression of the repeated integration of a function. This approach is commonly referred to as the Riemann–Liouville approach:

$$\underbrace{\int .....\int_0^t}_{n} f(\tau)\,\underbrace{d\tau.....d\tau}_{n} = \frac{1}{(n-1)!}\int_0^t (t-\tau)^{n-1} f(\tau)\,d\tau \tag{A.11}$$

which demonstrates the formula usually attributed to Cauchy for evaluating the nth integration of the function $f(t)$. For the abbreviated representation of this formula, we introduce the operator J^n such as shown in:

$$J^n f(t) = f_n(t) = \frac{1}{(n-1)!}\int_0^t (t-\tau)^{n-1} f(\tau)\,d\tau \tag{A.12}$$

Often, one will also find another operator, D^{-n}, used in place of J^n. While they represent the same formulation of the repeated integral function, and can be seen as interchangeable, one will find that the us of D^{-n} may become misleading, especially when multiple operators are used in combination. For direct use in (A.11), n is restricted to be an integer. The primary restriction is the use of the factorial which in essence has no meaning for non-integer values. The gamma function is, however, an analytic expansion of the factorial for all reals, and thus can be used in place of the factorial as in (A.2). Hence, by replacing the factorial expression for its gamma function equivalent, we can generalize (A.12) for all $\alpha \in R$, as shown in:

$$J^\alpha f(t) = f_\infty(t) = \frac{1}{\Gamma(\alpha)}\int_0^t (t-\tau)^{\alpha-1} f(\tau)\,d\tau \tag{A.13}$$

It is also possible to formulate a definition for the fractional-order derivative using the definition already obtained for the analogous integral. Consider a differentiation of order $\alpha = 1 = 2$; $\alpha \in R_+$. Now, we select an integer m such that $m-1 < \alpha < m$. Given these numbers, we now have two possible ways to define the derivative. The first definition, which we will call the Left Hand Definition is

$$f(n) = \begin{cases} D^\alpha f(t) = \frac{d^m}{dt^m}\left[\frac{1}{\Gamma(m-\alpha)}\int_0^t \frac{f(\tau)}{(t-\tau)^{(\alpha+1-m)}}\,d\tau\right] & m-1<\alpha<m \\ \frac{d^m}{dt^m} f(t), & \alpha = m \end{cases} \tag{A.14}$$

The second method, referred to here as the Right Hand Definition, is

$$f(n) = \left\{\begin{array}{ll} D_*^\alpha f(t) := \frac{1}{\Gamma(m-\alpha)}\int_0^t \frac{f^{(m)}}{(t-\tau)^{(\alpha+1-m)}}d\tau & m-1<\alpha<m \\ \frac{d^m}{dt^m} f(t), & \alpha = m \end{array}\right\} \tag{A.15}$$

Unlike the Riemann–Liouville approach, which derives its definition from the repeated integral, the Grunwald–Letnikov formulation approaches the problem from the derivative side. For this, we start from the fundamental definition a derivative:

$$f'(x) = \lim_{h\to 0}\frac{f(x+h)-f(x)}{h} \tag{A.16}$$

Applying this formula again, we can find the second derivative:

$$f''(x) = \lim_{h\to 0} \frac{f'(x+h) - f'(x)}{h}$$
$$= \lim_{h_1\to 0} \frac{\lim_{h_2\to 0} \frac{f(x+h_1+h_2)-f(x+h_1)}{h2} - \lim_{h_2\to 0} \frac{f(x+h_2)-f(x)}{h_2}}{h_1} \quad \text{(A.17)}$$

By choosing the same value of h, i.e. $h = h_1 = h_2$, the expression simplifies to

$$f''(x) = \lim_{h\to 0} \frac{f(x+2h) - 2f(x+h) + f(x)}{h^2} \quad \text{(A.18)}$$

For the nth derivative, this procedure can be consolidated into a summation. We introduce the operator d^n to represent the n-repetitions of the derivative:

$$d^n f(x) = \lim_{h\to 0} \frac{1}{h^n} \sum_{m=0}^{n} (-1)^m \binom{n}{m} f(x - mh) \quad \text{(A.19)}$$

This expression can be generalized for non-integer values for n with $\alpha \in R$ provided that the binomial coefficient be understood as using the Gamma Function in place of the standard factorial. Also, the upper limit of the summation (no longer the integer, n) goes to infinity as $\frac{t-1}{h}$ (where t and a are the upper and lower limits of differentiation, respectively). We are left with the generalized form of the Grunwald–Letnikov fractional derivative.

$$d^n f(x) = \lim_{h\to 0} \frac{1}{h^n} \sum_{m=0}^{\frac{t-a}{h}} (-1)^m \frac{\Gamma(\alpha+1)}{m!\Gamma(\alpha - m + 1)} f(x - mh) \quad \text{(A.20)}$$

It is obvious that, just as the Riemann–Liouville definition for the fractional integral could be used to define the fractional derivative, the above form of the GL derivative could be altered for use in an alternate definition of the fractional integral. The most natural alteration of this form is to consider the GL derivative for negative α. If we revert to the (A.19) form the most immediate problem is that ($\binom{-n}{m}$) is not defined using factorials. Expanded mathematically, ($\binom{-n}{m}$) is given by

$$\binom{-n}{m} = \frac{-n(-n-1)(-n-2)(-n-3)\cdots(-n-m+1)}{m!} \quad \text{(A.21)}$$

This form can be rewritten as

$$\binom{-n}{m} = (-1)^m \frac{-n(-n-1)(-n-2)(-n-3)\cdots(-n-m+1)}{m!}$$
$$= (-1)^m \frac{(n+m-1)!}{(n-1)!m!} \quad \text{(A.22)}$$

The factorial expression in (A.22) can be generalized for negative reals using the gamma function, thus

$$\binom{-\alpha}{m} = (-1)^m \frac{\Gamma(\alpha+m)}{\Gamma(\alpha)m!} \tag{A.23}$$

Using this relation we can now rewrite (A.20) for $-\alpha$ and thus are left with the Grunwald–Letnikov fractional integral:

$$d^{-\alpha} f(x) = \lim_{h\to 0} h^{\alpha} \sum_{m=0}^{\frac{t-a}{h}} \frac{\Gamma(\alpha+m)}{m!\Gamma(\alpha)} f(x-mh) \tag{A.24}$$

The we discuss the form of the Fractional Integral Equation:

$$\frac{1}{\Gamma(\alpha)} \int_t^0 \frac{u(\tau)}{(t-\tau)^{1-\alpha}} d\tau = f(t) \tag{A.25}$$

or equivalently:

$$J^{\alpha} u(t) = f(t) \tag{A.26}$$

The solution of this kind is

$$u(t) = D^{\alpha} f(t) \tag{A.27}$$

In the Laplace domain, integral equations of the first kind assume the form

$$J^{\alpha} u(t) = \Phi_{\alpha}(t) * u(t) \quad \Longrightarrow \quad \mathscr{L}\{\Phi_{\alpha}(t) * u(t)\} = \frac{\tilde{u}(s)}{s^{\alpha}} \tag{A.28}$$

which can be rewritten as

$$\tilde{u}(s) = s^{\alpha} \tilde{f}(s) = s\left[\frac{\tilde{f}(s)}{s^{1-\alpha}}\right] \tag{A.29}$$

or as:

$$\tilde{u}(s) = s^{\alpha} \tilde{f}(s) \quad \Longrightarrow \quad \frac{1}{a^{1-\alpha}}\left[s\tilde{f}(s) - f(0)\right] + \frac{f(0)}{s^{1-\alpha}} \tag{A.30}$$

Inverting the first form back into the time domain, we get

$$u(t) = \frac{1}{\Gamma(1-\alpha)} \frac{d}{dt} \int_0^t \frac{f(\tau)}{(t-\tau)^{\alpha}} d\tau = f(t) \tag{A.31}$$

which is equivalent to solution of the equation with the Left Hand Definition. The second form can be similarly inverted to yield

$$u(t) = \frac{1}{\Gamma(1-\alpha)} \int_0^t \frac{f'(\tau)}{(t-\tau)^{\alpha}} d\tau = f(t) + f(0) \frac{t^{-\alpha}}{\Gamma(1-\alpha)} \tag{A.32}$$

The first element of this result is the Right Hand Definition, but as mentioned above, one must include a remainder term that is dependent on the value of the function at 0.

In classic linear ODEs, there are typically two forms:

$$u'(t) = -u(t) + q(t) \tag{A.33}$$

and

$$u''(t) = -u(t) + q(t) \tag{A.34}$$

Similarly, one may use the previously introduced definitions to obtain Linear Fractional ODEs, which can be represented as follows:

$$D_*^\alpha u(t) = D^\alpha \left(u(t) - \sum_{k=0}^{m-1} \frac{t^k}{k!} u^{(k)}(0) \right) = -u(t) + q(t) \tag{A.35}$$

Note the use of the Right Hand Definition in this definition. As was discussed above in the properties of the Right Hand Definition and Left Hand Definition, the choice to use this definition is based upon the ability to use integer order initial conditions in the solution of problems of this kind. The most straightforward means of solving (A.35) is by means of Laplace transform, and can be re-arranged as

$$s^\alpha \tilde{u}(s) = \sum_{k=0}^{m-1} s^{\alpha-k-1} u^{(k)}(0) = \tilde{u}(s) = \sum_{k=0}^{m-1} \frac{s^{\alpha-k-1}}{s^\alpha + 1} \tag{A.36}$$

The terms inside the sum can be rewritten

$$\frac{s^{\alpha-k-1}}{s^\alpha + 1} = \frac{1}{s^k} \frac{s^\alpha}{s^\alpha + 1} = \mathscr{L}\left\{ J^k E_\alpha\left(-t^\alpha\right) \right\} \tag{A.37}$$

and the terms

$$\frac{1}{s^\alpha + 1} = -\left(s \frac{s^{\alpha-1}}{s^\alpha + 1} - 1 \right) = \mathscr{L}\left\{ \frac{d}{dt}\left[E_\alpha\left(-t^\alpha\right) \right] \right\} \tag{A.38}$$

Finally, using both (A.37) and (A.38) to define the inverse Laplace transform, it is possible to transform (A.36) into an expression for $u(t)$, and thus define the solution to the fractional-order ODE:

$$u(t) = \sum_{k=0}^{m-1} J^k E_\alpha\left(-t^\alpha\right) u^{(k)}(0) - q(t) * E'_\alpha\left(-t^\alpha\right) \tag{A.39}$$

In this book, the time-domain definitions have not been used; instead a simpler form, that in the frequency domain, has been used. As the reader can see, the time-domain definitions are of significant complexity and appealing to mathematicians rather than pragmatic individuals. However, for the sake of completeness, these definitions have been included here, but a more comprehensive overview can be found in [105, 118, 126].

References

1. Abramowitz M, Stegun I (1972) Handbook of mathematical functions with formulas, graphs, and mathematical tables. Dover, New York
2. Adolfsson K, Enelund M, Olsson M (2005) On the fractional order model of viscoelasticity. Mech Time-Depend Mater 9:15–34
3. Avolio A (1980) A multibranched model of the human arterial system. Med Biol Eng Comput 18:709–718
4. Babik B, Asztalos T, Petak F, Deac Z, Hantos Z (2003) Changes in respiratory mechanics during cardiac surgery. Anesth Analg 96:1280–1287
5. Baker GL, Gollub JB (1996) Chaotic dynamics: an introduction, 2nd edn. Cambridge University Press, Cambridge
6. Barnes PJ (2000) Chronic obstructive pulmonary disease. N Engl J Med 343(4):269–280
7. Bates J, Allen G (2006) The estimation of lung mechanics parameters in the presence of pathology: a theoretical analysis. Ann Biomed Eng 34(3):384–392
8. Bates J (2007) A recruitment model of quasi-linear power-law stress adaptation in lung tissue. Ann Biomed Eng 35(7):1165–1174
9. Bates J (2009) Lung mechanics—an inverse modeling approach. Cambridge University Press, Cambridge
10. Battaglia J, Cois O, Puigsegur L, Oustaloup A (1989) Solving an inverse heat conduction problem using a non-integer identified model. Int J Heat Mass Transf 44:2671–2680
11. Beaulieu A, Bosse D, Micheau P, Avoine O, Praud J, Walti H (2012) Measurement of fractional order model parameters of respiratory mechanical impedance in total liquid ventilation. IEEE Trans Biomed Eng 59(2):323–331
12. Benson D, Tadjeran C, Meerschaert M, Farnham I, Pohll G (2004) Radial fractional-order dispersion through fractured rock. Water Resour Res 40(12):W12416. doi:10.1029/2004WR003314
13. Berg JM (ed) (2002) Biochemistry, 6th edn. Freeman, New York
14. Borg I, Groenen P (2005) Modern multidimensional scaling-theory and applications, 2nd edn. Springer, New York
15. Brennan S, Hall G, Horak F, Moeller A, Pitrez P, Franzmann A, Turner S, de Klerk N, Franklin P, Winfield K, Balding E, Stick S, Sly P (2005) Correlation of forced oscillation technique in preschool children with cystic fibrosis with pulmonary inflammation. Thorax 60:159–163
16. Bronstein M, Bronstein A, Kimmel R, Yavneh I (2006) Multigrid multidimensional scaling. Numer Linear Algebra Appl 13:149–171
17. Busse W, Lemanske R (2001) Asthma New Engl J Med 344(5):350–362
18. Carvalho AR, Zin W (2011) Respiratory system dynamical mechanical properties: modelling in time and frequency domain. Biophys Rev 3:71–84

C.M. Ionescu, *The Human Respiratory System*, Series in BioEngineering,
DOI 10.1007/978-1-4471-5388-7,

19. Cavalcanti J, Lopes A, Jansen J, Melo P (2006) Detection of changes in respiratory mechanics due to increasing degrees of airway obstruction in asthma by the forced oscillation technique. Respir Med 100:2207–2219
20. Chen Y-Q, Bhaskaran T, Xue D (2008) Practical tuning rule development for fractional order proportional and integral controllers. J Comput Nonlinear Dyn 3:021403
21. Coleman T, Li Y (1990) An interior trust region approach for nonlinear minimization subject to bounds. SIAM J Control Optim 6:418–445
22. Cox T, Cox M (2001) Multidimensional scaling, 2nd edn. Chapman & Hall/CRC, London. ISBN 1-58488-094-5
23. Craiem D, Armentano RL (2007) A fractional derivative model to describe arterial viscoelasticity. Biorheology 44:251–263
24. Daroczi B, Hantos Z (1982) An improved forced oscillatory estimation of respiratory impedance. Int J Bio-Med Comput 13:221–235
25. Delacourt C, Lorino H, Herve-Guillot M, Reinert P, Harf A, Housset B (2000) Use of forced oscillation technique to assess airway obstruction and reversibility in children. Am J Respir Crit Care Med 161(3):730–736
26. De Geeter N, Ionescu C, De Keyser R (2009) A mechanical model of soft biological tissue—an application to lung parenchyma. In: IEEE proc of the eng med biol comp, Minneapolis, USA, pp 2863–2866
27. Desager KN, Buhr W, Willemen M (1991) Measurement of total respiratory impedance in infants by the forced oscillation technique. J Appl Physiol 71:770–776
28. Di Mango AM, Lopes A, Jansen J, Melo P (2006) Changes in respiratory mechanics with increasing degrees of airway obstruction in COPD: detection by forced oscillation technique. Respir Med 100(3):399–410
29. Diong B, Nazeran H, Nava P, Goldman M (2007) Modelling human respiratory impedance. IEEE Eng Med Biol Mag 26(1):48–55
30. Doehring T, Freed A, Carew E, Vesely I (2005) Fractional order viscoelasticity of the aortic valve cusp: an alternative to quasilinear viscoelasticity. J Biomech Eng 127:708
31. Duarte F, Tenreiro Machado JA, Duarte G (2010) Dynamics of the Dow Jones and the NASDAQ stock indexes. Nonlinear Dyn 61(4):691–705
32. DuBois AB, Brody A, Lewis D, Brugges B (1956) Oscillation mechanics of lung and chest in man. J Appl Physiol 8:587–594
33. Duiverman E, Clement J, Van De Woestijne K, Neijens H, van den Bergh A, Kerrebijn K (1985) Forced oscillation technique: reference values for resistance and reactance over a frequency spectrum of 2–26 Hz in healthy children aged 2.3–12.5 years. Clin Respir Physiol 21:171–178
34. Elzbieta G, Rybaczuk M, Kedzia A (2005) Fractal models of circulatory system. Symmetrical and asymmetrical approach comparison. Chaos Solitons Fractals 24:707–715
35. Elizur A, Cannon C, Ferkol T (2008) Airway inflammation in cystic fibrosis. Chest 133(2):489–495
36. Evans TM, Rundell K, Beck K, Levine A, Baumann J (2006) Impulse oscillometry is sensitive to bronchoconstriction after eucapnic voluntary hyperventilation or exercise. J Asthma 43(1):49–55
37. Eke A, Herman P, Kocsis L, Kozak L (2002) Fractal characterization of complexity in temporal physiological signals. Physiol Meas 23:R1–R38
38. Fabbri LM, Romagnoli M, Corbetta L, Casoni G, Busljetic K, Turato G, Ligabue G, Ciaccia A, Saetta M, Papi A (2003) Differences in airway inflammation in patients with fixed airflow obstruction due to asthma or chronic obstructive pulmonary disease. Am J Respir Crit Care Med 167(3):418–424
39. Farre R, Peslin R, Oostveen E, Suki B, Duvivier C, Navajas D (1989) Human respiratory impedance from 8 to 256 Hz corrected for upper airway shunt. J Appl Physiol 67:1973–1981

40. Farre R, Ferrer M, Rotger M, Navajas D (1995) Servocontrolled generator to measure respiratory impedance from 0.25 to 26 Hz in ventilated patients at different PEEP levels. Eur Respir J 8:1222–1227
41. Franken H, Clément J, Cauberghs M, Van De Woestijne K (1981) Oscillating flow of a viscous compressible fluid through a rigid tube: a theoretical model. IEEE Trans Biomed Eng 28(5):416–420
42. Fredberg J, Stamenovic D (1989) On the imperfect elasticity of lung tissue. J Appl Physiol 67:2408–2419
43. Fredberg J, Jones K, Nathan M, Raboudi S, Prakash Y, Shore S, Butler J, Sieck G (1996) Friction in airway smooth muscle: mechanism, latch and implications in asthma. J Appl Physiol 81:2703–2712
44. Frey U, Suki B, Kraemer R, Jackson A (1997) Human respiratory input impedance between 32 and 800 Hz, measured by interrupter technique and forced oscillations. J Appl Physiol 82:1018–1023
45. Frey U, Schibler A, Kraemer R (1995) Pressure oscillations after flow interruption in relation to lung mechanics. Respir Physiol 102:225–237
46. Frey U, Silverman M, Kraemer R, Jackson A (1998) High-frequency respiratory impedance measured by forced oscillation technique in infants. Am J Respir Crit Care Med 158:363–370
47. Fodor I (2002) A survey of dimension reduction techniques. Technical report, Center for Applied Scientific Computing, Lawrence Livermore National Laboratory
48. Friston K, Frith C, Fletcher P, Liddle P, Frackowiak R (1996) Functional topography: multidimensional scaling and functional connectivity in the brain. Cereb Cortex 6:156–164
49. Fung YC (1981) Biomechanics: mechanical properties of living tissues. Springer, New York
50. Gao J, Cao Y, Tung W-W, Hu J (2007) Multiscale analysis of complex time series. Wiley, New Jersey
51. Gillis H, Lutchen KR (1999) How heterogeneous bronchconstriction affects ventilation and pressure distributions in human lungs: a morphometric model. Ann Biomed Eng 27:14–22
52. Grandke T (1983) Interpolation algorithms for discrete Fourier transforms of weighted signals. IEEE Trans Instrum Meas 32:350–355
53. Guyton A (1986) In: Dreibelbis D (ed) Textbook of medical physiology. Saunders, Philadelphia
54. Habib R, Chalker R, Suki B, Jackson A (1994) Airway geometry and wall mechanical properties estimated from sub-glottal input impedance in humans. J Appl Physiol 77(1):441–451
55. Hanifi A, Goplen N, Matin M, Salters R, Alam R (2012) A linear parametric approach for analysis of mouse respiratory impedance. IEEE Trans Biomed Circuits Syst 6(3):287–294
56. Hantos Z, Daroczy B, Suki B, Galgoczy G, Csendes T (1986) Forced oscillatory impedance of the respiratory system at low frequencies. J Appl Phys 60(1):123–132
57. Hantos Z, Daroczy B, Suki B, Nagy S, Fredberg J (1992) Input impedance and peripheral inhomogeneity of dog lungs. J Appl Phys 72(1):168–178
58. Hantos Z, Adamicz A, Govaerts E, Daroczy B (1992) Mechanical impedances of lungs and chest wall in the cat. J Appl Phys 73(2):427–433
59. Harper P, Karman S, Pasterkamp H, Wodicka G (2001) An acoustic model of the respiratory tract. IEEE Trans Biomed Eng 48(5):543–549
60. Hernandez JL, Biscay R, Jimenez JC, Valdes P, Grave de Peralta R (1995) Measuring the dissimilarity between EEG recordings through a nonlinear dynamical system approach. Int J Bio-Med Comput 38:121–129
61. Hildebrandt J (1969) Comparison of mathematical models for cat lung and viscoelastic balloon derived by Laplace transform methods from pressure-volume data. Bull Math Biophys 31:651–667
62. Hildebrandt J (1970) Pressure-volume data of cat lung interpreted by a plastoelastic, linear viscoelastic model. J Appl Physiol 28(3):365–372
63. Hlastala M, Robertson T (1998) Complexity in structure and function of the lung. In: Lung biology in health and disease series, vol 121. Dekker, New York

64. Hogg J, Chu F, Utokaparch S et al (2004) The nature of small airway obstruction in chronic obstructive pulmonary disease. N Engl J Med 350(26):2645–2653
65. Horsfield K, Dart G, Olson D, Cumming G (1971) Models of the human bronchial tree. J Appl Physiol 31:207–217
66. Hou C, Gheorghiu S, Coppens MS, Huxley VH, Pfeifer P (2005) Gas diffusion through the fractal landscape of the lung. In: Losa, Merlini, Nonnenmacher (ed) Fractals in biology and medicine, vol IV. Birkhauser, Berlin
67. Ionescu C, De Keyser R (2003) A novel parametric model for the human respiratory system. In: Proc. of the IASTED int conf on modelling and simulation, Palm Springs, CA, USA, pp 246–251
68. Ionescu C, Chirita M (2008) Stress-strain properties of natural and biomimetical formed collagen constructs. Int J Technol Healthcare 16(6):437–444
69. Ionescu C, De Keyser R (2008) Parametric models for the human respiratory impedance. J Med Eng Technol 32(4):315–342
70. Ionescu C, Muntean I, Tenreiro-Machado J, De Keyser R, Abrudean M (2009) A theoretical study on modelling the respiratory tract with ladder networks by means of intrinsic fractal geometry. IEEE Trans Biomed Eng. doi:10.1109/TBME.2009.2030496
71. Ionescu C, Derom E, De Keyser R (2009) Assessment of respiratory mechanical properties with constant-phase models in healthy and COPD lungs. Comput Methods Programs Biomed. doi:10.1016/j.cmpb.2009.06.006
72. Ionescu C, De Keyser R (2009) Relations between fractional order model parameters and lung pathology in chronic obstructive pulmonary disease. IEEE Trans Biomed Eng 56(4):978–987
73. Ionescu C, Segers P, De Keyser R (2009) Mechanical properties of the respiratory system derived from morphologic insight. IEEE Trans Biomed Eng 56(4):949–959
74. Ionescu C, Tenreiro Machado JA (2010) Mechanical properties and impedance model for the branching network of the sapping system in the leaf of Hydrangea macrophylla. Nonlinear Dyn. doi:10.1007/s11071-009-9590-0
75. Ionescu C, Machado JT, De Keyser R (2011) Fractional-order impulse response of the respiratory system. Comput Math Appl 62(3):845–854
76. Ionescu C, De Keyser R, Sabatier J, Oustaloup A, Levron F (2011) Low frequency constant-phase behaviour in the respiratory impedance. Biomed Signal Process Control 6:197–208
77. Ionescu CM, Schoukens J, De Keyser R (2011) Detecting and analyzing non-linear effects in respiratory impedance measurements. In: Proceedings of the American control conference, San Francisco, USA, 29 June–01 July. 978-1-4577-0079-8, 5412-5417
78. Jabłoński I, Mroczka J (2009) Frequency domain identification of the respiratory system model during the interrupter technique. Measurement 42:390–398
79. Jabłoński I, Polak A, Mroczka J (2011) Preliminary study on the accuracy of respiratory input impedance measurement using the interrupter technique. Comput Methods Programs Biomed 101:115–125
80. Jesus I, Tenreiro Machado JA (2008) Development of fractional order capacitors based on electrolyte processes. Nonlinear Dyn. doi:10.1007/s11071-008-9377-8
81. Jesus I, Tenreiro J, Cuhna B (2008) Fractional electrical impedances in botanical elements. J Vib Control 14:1389–1402
82. Kaczka D, Dellaca R (2011) Oscillation mechanics of the respiratory system: applications to lung disease. Crit Rev Biomed Eng 39(4):337–359
83. Kundur P (1994) Power system stability and control. In: Balu NJ, Lauby MG (ed) Power system engineering. Mc Graw-Hill, New York
84. Lutchen KR, Gillis H (1997) The relation between airway morphometry and lung resistance and elastance during constriction: a modeling study. J Appl Physiol 83(4)
85. Lai S, Hyatt R (2000) Effect of age on elastic moduli. J Appl Physiol 89:163–168
86. Lande B, Mitzner W (2006) Analysis of lung parenchyma as a parametric porous medium. J Appl Physiol 101:926–933
87. Lakes RS (2009) Viscoelastic materials. Cambridge University Press, Cambridge

88. Lapperre T, Snoeck-Stroband JB, Gosman MME, Stolk J, Sont JK, Jansen DF, Kerstjens HAM, Postma DS, Sterk PJ (2004) Dissociation of lung function and airway inflammation in chronic obstructive pulmonary disease. Am J Respir Crit Care Med 170(5):499–504
89. Li J (2004) Visualization of high-dimensional data with relational perspective map. Inf Vis 3:45–59
90. Lima M, Tenreiro Machado JA, Crisóstomo M (2008) Pseudo phase plane, delay and fractional dynamics in robotic signals. J Eur Syst Autom 42(6–8):1037–1051. Special issue on fractional differentiation, Hermes
91. Losa G, Merlini D, Nonnenmacher T, Weibel E (2005) Fractals in biology and medicine, vol IV. Birkhauser, Basel
92. Lorx A, Szabo B, Hercsuth M, Penzes I, Hantos Z (2009) Low frequency assessment of airway and tissue mechanics in ventilated COPD patients. J Appl Physiol 107:1884–1892
93. Lutchen K, Costa K (1990) Physiological interpretation based on lumped element models fit to respiratory impedance data: use of forward—inverse model. IEEE Trans Biomed Eng 37(11):1076–1086
94. Ma B, Lutchen K (2006) An anatomically based hybrid computational model of the human lung and its application to low frequency oscillatory mechanics. Ann Biomed Eng 34(11):1691–1704
95. Magin RL (2006) Fractional Calculus in Bioengineering. Begell House Publishers
96. Maksym G, Bates J (1997) A distributed nonlinear model of lung tissue elasticity. J Appl Physiol 82(1):32–41
97. Mandelbrot B (1983) The fractal geometry of nature. Freeman, New York
98. Mani M, Srivastava A, Barillot C (2008) The labeling of cortical sulci using multidimensional scaling. Presented at MICCAI Workshop, Manifolds in Medical Imaging: metrics, learning and beyond, NY, USA, 9p
99. Mauroy B, Flloche M, Weibel ER, Sapoval (2004) An optimal bronchial tree may be dangerous. Nature 427(2):633–636
100. Mauroy B (2005) 3D hydrodynamics in the upper human bronchial tree: interplay between geometry and flow distribution. In: Losa, Merlini, Nonnenmacher (eds) Fractals in biology and medicine, vol IV. Birkhauser, Berlin
101. Mathworks—Matlab: Statistics Toolbox; v. 7.2 (2006). http://www.mathworks.com/products/statistics/
102. Mead J (1961) Mechanical properties of lungs. Physiol Rev 41:281–330
103. McCool F, Rochester D (2008) Non-muscular diseases of the chest wall. In: Fishman A (ed) Fishman's pulmonary disease and disorders, vol II. McGraw-Hill Medical, New York, pp 1541–1548
104. Moon FC (1987) Chaotic vibration. Wiley, New York
105. Monje CA, Chen YQ, Vinagre B, Xue D, Feliu V (2010) Fractional order systems and controls—fundamentals and applications. Advanced industrial control series. Springer, Berlin. ISBN 978-1-84996-334-3
106. Morris MJ, Deal LE, Bean DR (1999) Vocal cord dysfunction in patients with exertional dyspnea? Chest 116(6):1676–1682
107. Murray CD (1926) The physiological principle of minimum work applied to the angle of branching arteries. J Gen Physiol 9:835–841
108. Muntean I, Ionescu C, Nascu I (2009) A simulator for the respiratory tree in healthy subjects derived from continued fractions expansions. AIP Conf Proc 1117:225–231
109. Miller MR, Hankinson J, Brusasco V, Burgos F, Casaburi R, Coates A, Crapo R, Enright P, van der Grinten CPM, Gustafsson P, Jensen R, Johnson DC, MacIntyre N, McKay R, Navajas D, Pedersen OF, Pellegrino R, Viegi G, Wanger J (2005) Standardisation of spirometry. Eur Respir J 26:319–338. doi:10.1183/09031936.05.00034805
110. Navajas D, Farre R, Rotger M, Badia R, Puig-de-Morales M, Montserrata M (1998) Assessment of airflow obstruction during CPAP by means of forced oscillation in patients with sleep apnea. Am J Respir Crit Care Med 157(5):1526–1530

111. Navajas D, Farre R, Canet J, Rotger M, Sanchis J (1990) Respiratory input Impedance in anesthetized paralyzed patients. J Appl Physiol 69:1372–1379
112. Northrop R (2002) Non-invasive measurements and devices for diagnosis. CRC Press, Boca Raton
113. Oldham K, Spanier J (1974) The fractional calculus. Academic Press, London
114. Olson D, Dart G, Filley G (1970) Pressure drop and fluid flow regime of air inspired into the human lung. J Appl Physiol 28:482–494
115. Olufsen MS (2004) On deriving lumped models for blood flow and pressure in the systemic arteries. Math Biosci Eng 1(1):61–80
116. Oostveen E, Macleod D, Lorino H, Farre R, Hantos Z, Desager K, Marchal F (2003) The forced oscillation technique in clinical practice: methodology, recommendations and future developments. Eur Respir J 22:1026–1041
117. Oustaloup A, Cois O, Lannusse P, Melchior P, Moreau X, Sabatier J, Thomas JL (2000) A survey on the CRONE approach. In: Proc. of the IEEE conf on systems, signals and devices (SSD05), tutorial
118. Oustaloup A (1995) La derivation non-entière. Hermes, Paris (in French)
119. Pasker H, Peeters M, Genet P, Nemery N, Van De Woestijne K (1997) Short-term ventilatory effects in workers exposed to fumes containing zinc oxide: comparison of forced oscillation technique with spirometry. Eur Respir J 10:523–1529
120. Pedley T, Schroter R, Sudlow M (1971) Flow and pressure drop in systems of repeatedly branching tubes. J Fluid Mech 46(2):365–383
121. Peslin R, Duvivier C, Jardin P (1984) Upper airway walls impedance measured with head plethysmograph. J Appl Physiol: Respir, Environ Exercise Physiol 57(2):596–600
122. Peslin R, da Silva J, Chabot F, Duvivier C (1992) Respiratory mechanics studied by multiple linear regression in un-sedated ventilated patients. Eur Respir J 5:871–878
123. Petak F, Babik B, Asztalos T, Hall G, Deak Z, Sly P, Hantos Z (2003) Airway and tissue mechanics in anesthetized paralyzed children. Pediatr Pulmonol 35(3):169–176
124. Pintelon R, Schoukens J (1996) An improved sine-wave fitting procedure for characterizing data acquisition channels. IEEE Trans Instrum Meas 2(45):588–593
125. Pride NB (2001) Tests of forced expiration and inspiration. Clin Chest Med 22(4):599–622
126. Podlubny I (2001) Fractional differential equations. IEEE Press, New York
127. Polzella D, Reid G (1989) Multidimensional scaling analysis of simulated air combat maneuvering performance data. Aviat Space Environ Med February:141–144
128. Potter M, Wiggert D, Ramadan B (2011) Mechanics of fluids. Cengage Learning, Stamford
129. Rabei EM, Almayteh I, Muslih SI, Baleanu D (2008) Hamilton-Jacobi formulation of systems within caputoś fractional derivative. Phys Scr 77(1):015101
130. Ramus-Serment C, Moreau X, Nouillant M, Oustaloup A, Levron F (2002) Generalised approach on fractional response of fractal networks. Chaos Solitons Fractals 14:479–488
131. Reyes-Melo M, Martinez-Vega J, Guerrero-Salazar C, Ortiz-Mendez U (2004) Application of fractional calculus to modelling of relaxation phenomena of organic dielectric materials. In: IEEE proc int conf on solid dielectrics. 6 p
132. Rogers D, Doull I (2005) Physiological principles of airway clearance techniques used in the physiotherapy management of cystic fibrosis. Curr Pediatr 15:233–238
133. Romero PV, Sato J, Shardonofsky F, Bates J (1990) High frequency characteristics of respiratory mechanics determined by flow interruption. J Appl Physiol 69:1682–1688
134. Salazar E, Knowles J (1964) An analysis of pressure-volume characteristics of the lungs. J Appl Physiol 19:97–104
135. Sauret V, Goatman, Fleming J, Bailey A (1999) Semi-automated tabulation of the 3D topology and morphology of branching networks using CT: application to the airway tree. Phys Med Biol 44:1625–1638
136. Schoukens J, Pintelon R (2012) System identification. A frequency domain approach, 2nd edn. IEEE Press, New Jersey
137. Schoukens J, Pintelon R, Dobrowiecki T, Rolain Y (2005) Identification of linear systems with nonlinear distorsions. Automatica 41(3):491–504

138. Schoukens J, Rolain Y, Simon G, Pintelon R (2003) Fully automated spectral analysis of periodic signals. IEEE Trans Instrum Meas 52(4):1021–1024
139. Segers P, Stergiopulos N, Verdonck P, Verhoeven R (1997) Assessment of distributed arterial network models. Med Biol Eng Comput 35:729–736
140. Sly P, Hayden M, Petak F, Hantos Z (1996) Measurement of low frequency respiratory impedance in infants. Am J Respir Crit Care Med 156(4-part1):1172–1177
141. Smith HJ, Reinhold P, Goldman MD (2005) Forced oscillation technique and impulse oscillometry. Eur Respir Monogr 31:72–105
142. Suki B, Yuan H, Zhang Q, Lutchen K (1992) Partitioning of lung tissue response and inhomogeneous airway constriction at the airway opening. J Appl Phys 82:1349–1359
143. Suki B, Barabasi A, Lutchen K (1994) Lung tissue viscoelasticity: a mathematical framework and its molecular basis. J Appl Physiol 76(6):2749–2759
144. Suki B, Frey U (2003) Temporal dynamics of recurrent airway symptoms and cellular random walk. J Appl Physiol 95:2122–2127
145. Suki B, Bates J (2011) Lung tissue mechanics as an emergent phenomenon. J Appl Physiol 110:1111–1118
146. Tenreiro Machado JA (1997) Analysis and design of fractional-order digital control systems. Syst Anal Model Simul 27(2–3):107–122
147. Tenreiro Machado JA (1999) Fractional-order derivative approximations in discrete-time control systems. Syst Anal Model Simul 34:419–434
148. Tenreiro Machado JA, Jesus I (2004) Suggestion from the past? Fract Calc Appl Anal 7(4):403–407
149. Tenreiro Machado JA, Kiryakova V, Mainardi F (2011) Recent history of fractional calculus. Commun Nonlinear Sci Numer Simul 16(3):1140–1153
150. Tenreiro Machado JA (2011) And I say to myself: “What a fractional world!”. Fract Calc Appl Anal 14(4):635–654
151. Tenreiro Machado JA, Kiryakova V, Mainardi F (2013) Recent history of fractional calculus. Commun Nonlinear Sci Numer Simul 16(3):1140–1153
152. Tenreiro Machado J, Galhano AM, Trujillo JJ (2013) On development of fractional calculus during the last fifty years. Scientometrics. doi:10.1007/s11192-013-1032-6
153. Tgavalekos N, Venegas JG, Suki B, Lutchen K (2003) Relation between structure, function and imaging in a three-dimensional model of the lung. Ann Biomed Eng 31:363–373
154. Thamrin C, Finucane K, Singh B, Hantos Z, Sly P (2007) Volume dependence of high-frequency respiratory mechanics in healthy adults. Ann Biomed Eng 36(1):162–170
155. Thamrin C, Albu G, Sly P, Hantos Z (2009) Negative impact of the noseclip on high-frequency respiratory impedance measurements. Respir Physiol Neurobiol 165:115–118
156. Thorpe CW, Bates J (1997) Effect of stochastic heterogeneity on lung impedance during acute bronchoconstriction: a model analysis. J Appl Physiol 82:1616–1625
157. Tzeng J, Shing-Lu H, Hsiung-Li W (2008) Multidimensional scaling for large genomic data sets. BMC Bioinform 9:179. Open Access: http://www.biomedcentral.com/1471-2105/9/179
158. Van Noord J (1990) Oscillations mechanics of the respiratory system: clinical applications and modelling. Doctoral Thesis, 189 pp
159. Van De Woestijne K, Desager K, Duivermanand E, Marshall F (1994) Recommendations for measurement of respiratory input impedance by means of forced oscillation technique. Eur Respir Rev 4:235–237
160. Vernon S, Unger E, Dimulescu I, Rajeevan M, Reeves W (2002) Utility of the blood for gene expression profiling and biomarker discovery in chronic fatigue syndrome. Dis Markers 18:193–199
161. Vignola A, Paganin F, Capieu L, Scichilone N, Bellia M, Maakel L, Bellia V, Godard P, Bousquet J, Chanez P (2004) Airway remodeling assessed by sputum and high-resolution computer tomography in asthma and COPD. Eur Respir J 24:910–917

162. Yuan H, Kononov S, Cavalcante F, Lutchen K, Ingenito E, Suki B (2000) Effects of collagenase and elastase on the mechanical properties of lung tissue strips. J Appl Physiol 89(3):3–14
163. Weibel ER (1963) Morphometry of the human lung. Springer, Berlin
164. Weibel ER (2005) Mandelbrot's fractals and the geometry of life: a tribute to Benoit Mandelbrot on his 80th birthday. Losa, Merlini, Nonnenmacher (eds) Fractals in biology and medicine, vol IV. Birkhauser, Berlin
165. Welty J, Wicks C, Wilson R (1969) Fundamentals of momentum, heat and mass transfer. Wiley, New York
166. Welchew D, Honey D, Sharma T, Robbins T, Bullmore E (2002) Multidimensional scaling of integrated neurocognitive function and schizophrenia as a disconnexion disorder. NeuroImage 17:1227–1239
167. West B, Barghava V, Goldberger A (1986) Beyond the principle of similitude: renormalization of the bronchial tree. J Appl Physiol 60:1089–1097
168. Womersley JR (1957) An elastic tube theory of pulse transmission and oscillatory flow in mammalian arteries. Wright Air Development Center, Technical Report WADC-TR56-614
169. Zhang Q, Lutchen K, Suki B (1999) A frequency domain approach to nonlinear and structure identification for long memory systems: application to lung mechanics. Ann Biomed Eng 27:1–33
170. Zivanovic M, Schoukens J (2009) Time-variant harmonic signal modeling by using polynomial approximation and fully automated spectral analysis. In: Proc of the 17th European signal processing conference (EUSIPCO), Glasgow, UK, August, pp 899–903

Subject Index

C.M. Ionescu, *The Human Respiratory System*, Series in BioEngineering,
DOI 10.1007/978-1-4471-5388-7,